UNIVERSITY OF
LIVERPOOL

Solution-Processable Polymer Photocatalysts for Hydrogen Evolution from Water

Duncan J. Woods

August 2019

Thesis submitted in accordance with the requirements of the
University of Liverpool for the degree of Doctor of Philosophy

Solution-Processable Polymer Photocatalysts for Hydrogen Evolution from Water

Duncan Woods

Methods of storing renewable energy are urgently required to meet future energy demands. Photocatalytic hydrogen production from water represents an attractive method of storing solar energy for a diverse range of end-use applications. Semiconducting polymers are an emerging class of photocatalysts with eminently tunable structures and properties. However, the insolubility of most polymer photocatalysts limits processability and, therefore, opportunities to optimise the morphology of these materials for photocatalytic applications.

Processability was achieved with the introduction of solubilising side-chains, which were systematically varied in order to study their influence on the photocatalytic performance of polymers. It was found that high hydrogen evolution rates could be achieved by incorporating oligo(ethylene glycol) side-chains, which seem to promote interaction with water during photocatalysis as well as affording solubility in common organic solvents. The polymer backbone was also varied to further improve the performance of solution-processable polymer photocatalysts. A fluorene-based polymer, **FS-TEG**, was prepared that displayed high activity under visible light, with an external quantum efficiency of 10.0% at 420 nm.

Polymers were processed into a variety of forms, including photocatalytic films, both free-standing and cast on substrates. The substrate was varied to improve performance, with roughened glass slides found to achieve the highest areal hydrogen evolution rates. Photocatalytic polymers were also cast on planar substrates, which enabled precise control over film formation. Important parameters such as optimum film thicknesses for hydrogen evolution performance were subsequently established.

Processability also enabled facile preparation of composites and blends. Incorporation of a narrow band gap dye was shown to triple the hydrogen evolution rate of **FS-TEG** films while the formation of heterojunctions with inorganic photocatalysts also enhanced performance. The scope for fabricating composites of this kind is boundless and, in the long term, devices capable of overall water splitting that utilise these materials are envisaged.

Acknowledgements

First, I would like to thank Professor Andy Cooper for giving me the opportunity to conduct this work and for valuable supervision. Thanks also to my Research Coordinator Dr Reiner Sebastian Sprick for your guidance, support and encouragement throughout the completion of this thesis.

I would also like to thank all those I have collaborated with on this work, especially Sam, Drew and Jenny at Imperial College London, Charlotte and Alex at the University of Liverpool and Liam and Martijn at UCL. Your insights have helped shape this work and it would not have been possible without you. Thanks also to the EPSRC for providing funding for this research.

Thanks must also go to Cooper group members past and present for their help, advice and camaraderie in the AJ on Friday nights after a long week in the lab. There are truly too many to list but Ammar, Craig, Andy, Rach, Xiaoyan, Ai, Hui, Haofan, Christian, Jet, Chloe, Bonnie, Becky, Briggs, Linjiang, Marc, Tom Hasell, Meera, Balta and various Bens all deserve a mention. Special thanks to Rob Clowes for fixing all the instruments and Yang for helping with high throughput experiments (and for generally enlightening discussions).

Thanks also to Mr Chilli and MBox karaoke bar for hosting many memorable Cooper group outings. A special mention also to Mike, Ste, Annie and Jonesy for providing a distraction from lab work and to everyone who came to see us butcher that Ricky Martin cover over the years. More broadly, thanks to the people of Liverpool for your warmth, wit and for making this wonderful city feel like home.

Finally, I must thank my friends and family for everything they've done for me during the last four years. In particular, thanks to my parents for your continued love and support. And, last but not least, my incredible girlfriend Cath. I couldn't have done this without you.

List of Publications

D.J. Woods, R.S. Sprick, C.L. Smith, A.J. Cowan, and A.I. Cooper, *Advanced Energy Materials*, 2017, **7**, 1700479.

"**A Solution-Processable Polymer Photocatalyst for Hydrogen Evolution from Water**"

D. J. Woods, S. A. J. Hillman, D. Pearce, L. Wilbraham, L. Q. Flagg, W. Duffy, D. S. Ginger, I. McCulloch, M. A. Zwijnenburg, R. S. Sprick, J. Nelson, and A. I. Cooper, in preparation.

"**Side-Chain Tuning in Conjugated Polymer Photocatalysts for Hydrogen Production from Water**"

Y. Bai, D. J. Woods, L. Wilbraham, C. M. Aitchison, M. A. Zwijnenburg, R. S. Sprick, and A. I. Cooper

Incorporating Heteroatoms into Fluorene-type Conjugated Polymers for Enhanced Photocatalytic Hydrogen Production

S. A. J. Hillman, R. S. Sprick, X. Shi, M. Sachs, D. Pearce, D. J. Woods, A. A. Y. Guilbert, A. I. Cooper, J. R. Durrant, J. Nelson, in preparation

"**Mechanistic Limitations of Linear Conjugated Polymer Photocatalysts for Hydrogen Evolution from Water and the Deposition of Thin Films as a Microstructural Solution**"

R. S. Sprick, Y. Bai, A. A. Y. Guilbert, M. Zbiri, C. M. Aitchison, L. Wilbraham, Y. Yan, D. J. Woods, M. A. Zwijnenburg and A. I. Cooper, *Chem. Mater.*, 2019, **31**, 305–313.

"**Photocatalytic Hydrogen Evolution from Water Using Fluorene and Dibenzothiophene Sulfone-Conjugated Microporous and Linear Polymers**"

F. Carraro, K. Chapman, Z. Chen, M. Dincă, T. Easun, M. Eddaoudi, O. Farha, R. Forgan, L. Gagliardi, F. Haase, D. Harris, S. Kitagawa, J. Knichal, C. Lamberti, J. S. M. Lee, K. Leus, J. Li, W. Lin, G. Lloyd, J. R. Long, C. Lu, S. Ma, L. McHugh, J. P. H. Perez, M. Ranocchiari, N. Rosi, M. Rosseinsky, M. R. Ryder, V. Ting, M. Van Der Veen, P. Van Der Voort, D. Volkmer, A. Walsh, D. Woods and O. M. Yaghi, *Faraday Discuss.*, 2017, **201**, 369–394.

"**Catalysis in MOFs: General Discussion**"

T. Banerjee, T. Bennett, K. Butler, T. L. Easun, M. Eddaoudi, R. Forgan, L. Gagliardi, C. Hendon, M. Jorge, C. Lamberti, J. S. M. Lee, K. Leus, J. Li, W. Lin, M. Ranocchiari, N. Rosi, J. G. Santaclara, S. Shevlin, K. Svane, V. Ting, M. Van Der Veen, P. Van Der Voort, A. Walsh, D. Woods, O. M. Yaghi and G. Zhu, *Faraday Discuss.*, 2017, **201**, 87–99.

"**Electronic, Magnetic and Photophysical Properties of MOFs and COFs: General Discussion**"

Table of Contents

List of Abbreviations

ε	Molar extinction coefficient
λ_{exc}	Excitation wavelength
λ_{em}	Emssion maxima wavelength
µs-TAS	Microsecond-transient absorption spectroscopy
AA	L-Ascorbic acid
AFM	Atomic force microscopy
AM1.5G	Air mass 1.5 global filter
AQY	Apparent quantum yield
BEV	Battery electric vehicle
BHJ	Bulk heterojunction
C_3N_4	Carbon nitride
CA	Contact angle
CB	Conduction band
CMP	Conjugated microporous polymer
COF	Covalent organic framework
CTF	Covalent triazine-based framework
CV	Cyclic voltammetry
D	Debyes
DBTS	Dibenzo[*b*,*d*]thiophene sulfone
DEA	Diethylamine
DEG	Di(ethylene glycol)
DoE	Department of Energy
DSSC	Dye-sensitised solar cells
DVS	Dynamic water vapour isotherms
EA	Ethylamine
EA	Electron affinity of photocatalyst's ground state
EA*	Electron affinity of photocatalyst's excited state
EQE	External quantum efficiency
FCEV	Fuel cell electric vehicle
FP	Fluorene-phenylene copolymer
FS	Fluorene-dibenzo[*b*,*d*]thiophene sulfone copolymer
fs-TAS	Femtosecond-transient absorption spectroscopy
FT-IR	Fourier transform infrared
FTO	Fluorine-doped tin oxide

GC	Gas chromatography
GIXRD	Grazing incidence X-ray diffraction
GO	Graphene oxide
HOMO	Highest occupied molecular orbital
HTS	High throughput screening
ICP-MS	Inductively coupled plasma-mass spectrometry
ICP-OES	Inductively coupled plasma-optical emission spectrometry
IP	Ionisation potential of photocatalyst's ground state
IP*	Ionisation potential of photocatalyst's excited state
LHV	Low heating value
LUMO	Lowest unoccupied molecular orbital
MALDI-TOF MS	Matrix-assisted laser desorption/ionization high-resolution time-of-flight mass spectrometry
MD	Molecular dynamics
M_n	Number-average molecular weight
M_w	Weight-average molecular weight
Na(detc)	Sodium diethyldithiocarbamate
$Ni(dtc)_2$	Nickel(II) dibutyldithiocarbamate
NMR	Nuclear magnetic resonance
NP	Nanoparticles
O.D.	Optical density
OEG	Oligo(ethylene glycol)
OFET	Organic field-effect transistor
OPV	Organic photovoltaic
OTS	*N*-octadecyltrichlorosilane
P3HT	Poly(3-hexylthiophene)
PDI	Polydispersity index
PDot	Polymer dot
PEM	Proton exchange membrane
PESA	Photoelectron spectroscopy in air
PFO	Poly(9,9-di-n-octylfluorenyl-2,7-diyl)
PIA	Photoinduced absorption
PXRD	Powder X-ray diffraction
PV	Photovoltaic
QCM	Quartz crystal microbalance gravimetry
RGO	Reduced graphene oxide

SAM	Self-assembled monolayer
SEM	Scanning electron microscopy
SHE	Standard hydrogen electrode
SMR	Steam methane reforming
STH	Solar-to-hydrogen
$T_{50\%}$	Time for 50% of photoinduced absorption at *ca.* 1 ps to decay by 50%
TAS	Transient absorption spectroscopy
T_d	Thermal decomposition temperature (at which 5% weight loss of original mass occurs)
(TD)-DFT	Time-dependent density functional theory
TEA	Triethylamine
TEAR	Triethylamine radical
TeEG	Tetra(ethylene glycol)
TEG	Tri(ethylene glycol)
TEOA	Triethanolamine
TGA	Thermogravimetric analysis
UPS	Ultraviolet photoelectron spectroscopy
UV	Ultraviolet
UV-vis	Ultraviolet-visible
VB	Valence band
WGS	Water-gas shift

List of Figures

List of Tables

Chapter 1

Introduction

"I'd put my money on the Sun and solar energy. What a source of power! I hope we don't have to wait until oil and coal run out before we tackle that."

Thomas Edison, 1931[1]

Avoiding the potentially catastrophic effects of significant climate change is perhaps the defining challenge of our time. The Paris Agreement stipulates that global warming must be kept "well below" 2 degrees Celsius within the next century, relative to pre-industrial levels.[2] Achieving this in the face of a growing global population with ever-increasing energy demands[3] necessitates the urgent development of scalable low-carbon energy generation.

Over 80% of the world's energy is currently produced by the combustion of fossil fuels.[4] There is widespread consensus that this reliance on fossil fuels must be ended and that a transition towards renewable sources of energy such as solar and wind power is necessary if the Paris Agreement is to be honoured. The abundance of these resources is without question; enough solar energy falls on the Earth's surface in one hour and 25 minutes to satisfy the needs of our current population for an entire year.[5] The amount of electricity generated from renewable sources has risen significantly in recent years and is set to increase. However, the disparity in peak output and demand times coupled with the intermittency of these energy sources dictates the need for on-grid energy storage to effectively utilise this electricity.

Batteries could be used to store electricity generated from renewable means. However, the cost of batteries may be prohibitively expensive to store energy on the scale required.[6] An alternative strategy is to store energy in the form of molecular bonds. Dihydrogen molecules (hydrogen henceforth) represent the most attractive molecular energy carrier as they possess the highest gravimetric energy of any chemical. Surplus electricity could be transformed into hydrogen and later used in a variety of applications including transportation and heating.[7] Alternatively, locally abundant renewable energy sources could be used to produce hydrogen directly. For instance, sunlight can be directly converted to hydrogen by using solar energy to 'split' water into hydrogen and oxygen molecules. So-called photocatalytic water splitting is one method of achieving this. The discovery of cheap, efficient and sustainable photocatalysts for this application could revolutionise energy supply on a global scale and help to avert the impending climatological and energy crises.[8]

1.1 Applications of Hydrogen

1.1.1 The "Hydrogen Economy"

The term "hydrogen economy" was first coined in 1970 to describe the potentially transformative effect of hydrogen on our global energy landscape.[9] Hydrogen is a flexible energy carrier that can be transformed into various forms of energy. For instance, hydrogen can be burned directly to produce heat or combined with oxygen in fuel cells to generate an electric current, with water the only by-product in both cases. In this vision of a hydrogen economy, energy would take the form of either electricity or hydrogen and therefore no greenhouse gases would be emitted at the point of use.[10] The versatility of hydrogen means it could facilitate decarbonisation across a diverse range of industries as well as playing a central role in future energy infrastructure (**Figure 1.1**).

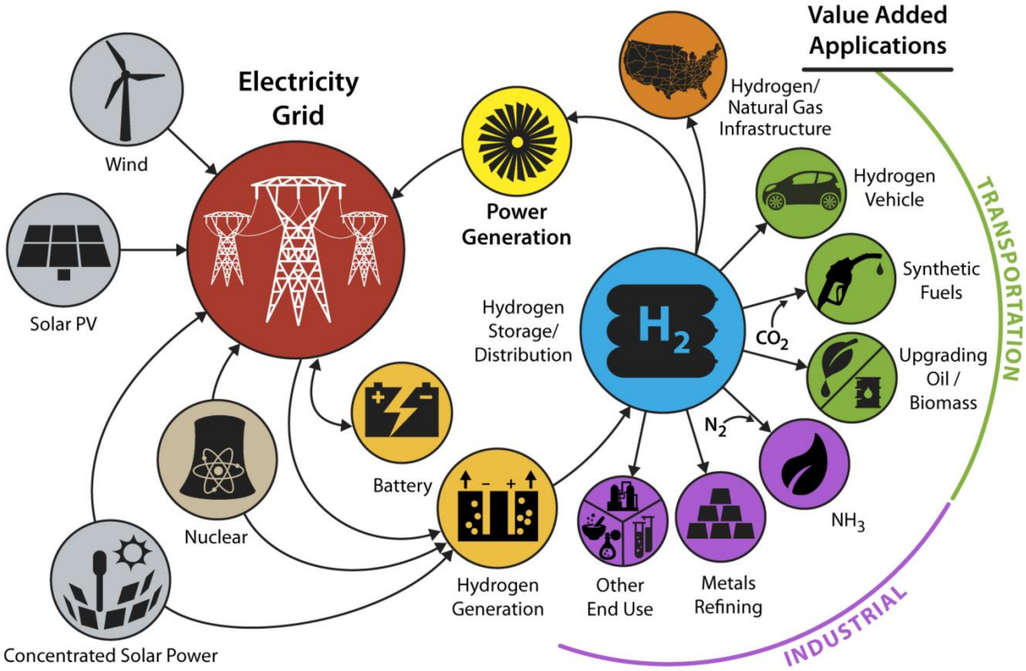

Figure 1.1. Image showing how H$_2$ could play a central role in a future energy system. Figure reprinted from US DoE presentation.[11]

Hydrogen is expected to find widespread application in the transportation sector. The sale of petrol and diesel cars will be banned from 2040 by the UK government and so vehicles that run on alternative fuels are urgently required. The light weight of hydrogen and clean emissions of hydrogen fuel cells make hydrogen an attractive candidate.[10] Automobiles powered by hydrogen—hydrogen fuel cell electric vehicles

(FCEVs)—have already entered mass production,[12] although consumer adoption is likely to be slow due to the initial high cost and lack of refuelling infrastructure. While sales of FCEVs for personal use are expected to increase,[13] hydrogen is likely to find more immediate application in public transportation as governments strive to meet imposed emissions and air pollution targets. For example, as diesel-powered trains are phased out, the introduction of fuel cell-powered trains represent a viable alternative to electrification of the routes they previously operated on. The first hydrogen-powered trains entered into passenger service in these circumstances in Germany in 2018.[14]

Transportation of freight is one application to which hydrogen is particularly suited. While sales of battery-powered electric vehicles (BEVs) for personal transportation have surged in recent years,[15] adoption of EVs for transportation of freight has been slow. This is because of their long charging times and limited ranges due to the weight compound effect associated with batteries.[16] Long-range FCEVs on the other hand, are able to fully recharge in minutes and are typically significantly lighter and cheaper than BEVs capable of achieving equivalent distances (**Figure 1.2**). These commercially attractive characteristics have recently led to the introduction of pilot schemes such as the forthcoming deployment of Kenworth T680 trucks fitted with Toyota hydrogen fuel cells across the USA.[17,18]

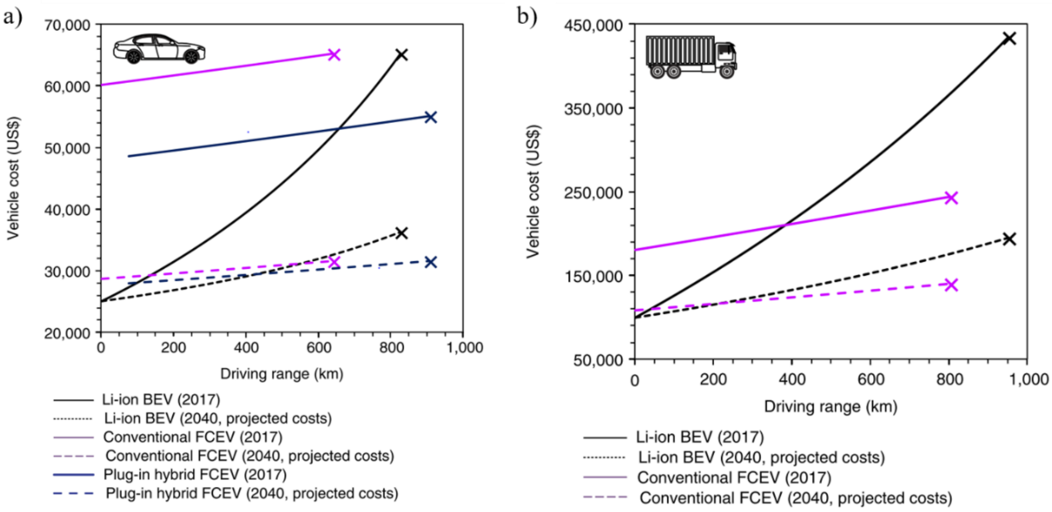

Figure 1.2. Vehicle cost as a function of driving range for Li-ion battery (BEVs), hydrogen fuel-cell vehicles (FCEVs) and plug-in hybrid FCEVs for **a)** mid-size vehicles and **b)** semi-trailer trucks (Figure adapted from literature with permission).[12]

Hydrogen can also be used as an alternative to natural gas in households and industries. When burned, it releases no greenhouse gases and produces more energy per unit of mass than any other fuel; hydrogen has a low heating value (LHV) 2.4, 2.8 and 4 times higher than methane, petrol and coal respectively.[19] This further underlines the versatility of hydrogen as an energy carrier.

Of course, a number of challenges associated with hydrogen must first be addressed if this flexibility is to be utilised. Most notably, efficient, sustainable and cheap methods of hydrogen production are required (as discussed further in **Chapter 1.2.2**). Storage is another key obstacle to overcome. Although hydrogen has the highest gravimetric density of any fuel, its low ambient temperature density means it has a low energy per unit volume. Advanced methods that can store hydrogen in a more energy-dense fashion are therefore required. Pressurising or liquefying H_2 are not considered to be economically viable so investigations into suitable materials which can store hydrogen either by physi- or chemisorption are ongoing.[20] Making hydrogen attractive to consumers is a further challenge due to historic safety concerns.

In spite of these sizeable obstacles, projects are already in progress that demonstrate how hydrogen can play an important role in the future energy mix. For example, the Port of Los Angeles has secured funding to become a zero emission hydrogen-based complex where vehicles run on hydrogen produced on-site from locally abundant renewable resources.[21] The realisation of the vision of a full-scale hydrogen economy will of course require significant investment and implementation of infrastructure that is likely to take several decades. Regardless, demand for hydrogen is already high as it is an important chemical industrially with a host of wide-ranging applications.

1.1.2 Current Applications

A major use of H_2 is in the production of ammonia using the Haber-Bosch process. This process, which involves the fixation of nitrogen under high temperatures and pressures, is the most common method of ammonia production. The high demand for ammonia in agriculture for use in fertilisers means that this industrial process accounts for around 50% of the 50 million metric tonnes of hydrogen currently produced annually.[22,23]

Hydrogen is also used extensively in the petrochemical industry in the process of oil refining. The technique of hydrocracking involves the hydrogenation of high molecular weight hydrocarbon feedstock in the presence of a catalyst. This results in the removal of impurities and the production of high-value, low-molecular weight products such as petrol, diesel, LPG and kerosene.[24]

Alternatively, an abundant supply of hydrogen could enable us to produce these hydrocarbons in more sustainable ways than extracting them from fossil fuels. For instance, in Iceland, renewably-sourced hydrogen is being combined with captured carbon dioxide to produce methanol with a 90% lower carbon footprint than methanol obtained from fossil fuels.[25,26] A diverse range of other applications for hydrogen include metal refining and hydrogenation of oils and fats while liquid hydrogen is also used as a coolant in electrical generators and as a rocket propellant.[22]

1.2 Hydrogen Production Methods

Hydrogen is evidently an important chemical in industry, and its increasing use in transportation and energy storage applications mean demand is only set to increase. However, current methods of production are generally unsatisfactory for a low-carbon future. This is because 96% of hydrogen is currently produced from fossil fuels (**Figure 1.3**).[27–30]

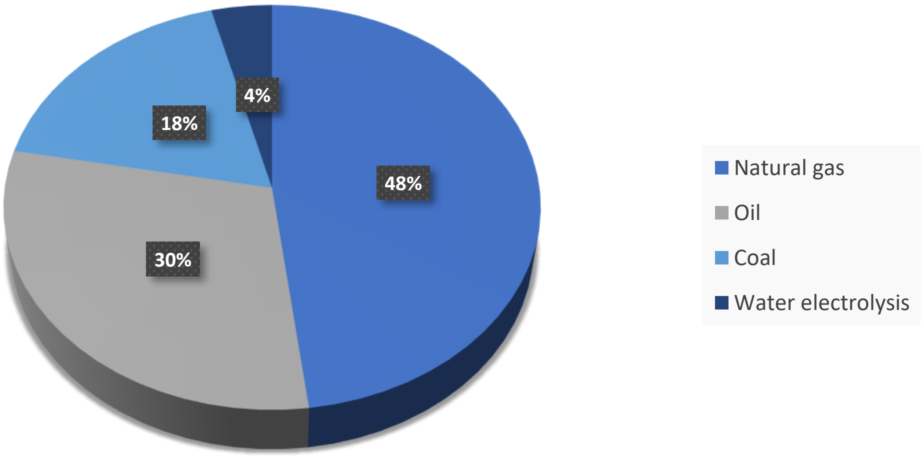

Figure 1.3. Current sources of hydrogen production.[31]

1.2.1 Hydrogen Production from Fossil Fuels

1.2.1.1 Steam Reforming

Steam reforming of hydrocarbons involves the conversion of hydrocarbon fuels into a hydrogen-rich gaseous mixture using steam. The most commonly used hydrocarbon for this process is methane; steam methane reforming (SMR) alone accounts for 48% of global hydrogen production.[31] SMR involves the following reactions:

$$CH_4 + H_2O \rightarrow CO + 3\ H_2 \tag{1.1}$$

$$CO + H_2O \rightarrow CO_2 + H_2 \tag{1.2}$$

The methane reforming reaction (**Reaction 1.1**) is highly endothermic ($\Delta H = +\ 206.1$ kJ mol^{-1}) and must therefore be carried out in the presence of a catalyst at high temperatures and pressures (700-950 °C, up to 3.5 MPa).[29] Following reforming, the gas mixture passes through a heat recovery step and into a reactor where the carbon monoxide reacts with further steam to produce more hydrogen in what is known as the water-gas shift (WGS) reaction (**Reaction 1.2**). This is a highly efficient (>80%)[23,31], low cost process and has therefore become the *de facto* method of hydrogen production on an industrial scale.

1.2.1.2 Partial Oxidation

Catalytic partial oxidation involves the reaction of a ratio of fuel and air that results in incomplete combustion (**Reaction 1.3**). This means that the reaction is exothermic rather than endothermic like SMR.

$$C_nH_m + \frac{n}{2}\ O_2 \rightarrow n\ CO + \frac{m}{2}\ H_2 \tag{1.3}$$

Although it has a lower hydrogen yield than the steam reforming process, partial oxidation avoids the need for large amounts of expensive high temperature steam[32] and is also more sulfur-tolerant than steam reforming.[33] The partial oxidation of coal—or gasification, as it is also known—accounts for 18% of hydrogen production.[27]

1.2.1.3 Autothermal Reforming

In the autothermal reforming process, the endothermic steam reforming reaction is combined with exothermic partial oxidation resulting in an almost thermodynamically neutral, highly energy efficient process (**Reaction 1.4**). This method enables hydrogen to be produced on a larger scale but requires a source of oxygen which is expensive. Hydrogen is also produced at a lower yield than SMR.[31]

$$\mathrm{C_nH_m} + \frac{\mathrm{n}}{2}\ \mathrm{H_2O} + \frac{\mathrm{n}}{4}\ \mathrm{O_2} \rightarrow \mathrm{n\ CO} + \left(\frac{\mathrm{n}}{2} + \frac{\mathrm{m}}{2}\right) \mathrm{H_2} \tag{1.4}$$

The fossil fuel reforming processes outlined here have been optimised over many decades and have therefore become highly efficient. However, using these methods to produce hydrogen to store renewably-generated electricity, or to use as an alternative to hydrocarbon fuels in transportation, is clearly counter-intuitive. While capture and sequestration of emitted carbon dioxide is possible, this adds significant costs and the long-term efficacy of this technology remains uncertain.[34]

1.2.1.4 Hydrocarbon Pyrolysis

Hydrogen can also be produced by the thermal decomposition, or pyrolysis, of hydrocarbons in the absence of air and water (**Reaction 1.5**).

$$\mathrm{C_nH_m} \rightarrow \mathrm{n\ C} + \frac{\mathrm{m}}{2}\ \mathrm{H_2} \tag{1.5}$$

This process has the notable advantage of avoiding the production of carbon dioxide as a by-product and has therefore been proposed as a possible stepping stone in the transition to hydrogen production from renewable sources.[35] In fact, the sustainability of this process can be improved by using biomass as a renewable feedstock.

1.2.2 Hydrogen Production from Renewable Energy Sources

1.2.2.1 Biomass

Biomass is the umbrella term given to organic material derived from a wide range of plant and animal sources. Hydrogen production from biomass can be broadly grouped into thermochemical and biological processes.[29]

1.2.2.1.1 Thermochemical Methods of Hydrogen Production from Biomass

Thermochemical methods are analogous to the methods used for fossil fuels discussed previously. Although the use of these methods for hydrogen production from biomass still results in the emission of greenhouse gases, the consumption of carbon dioxide by the plant feedstock in photosynthesis means the processes are considered to have low net emissions.[36]

The most common thermochemical methods are pyrolysis and gasification. The chemically diverse nature of biomass means a mixture of products are formed in solid, liquid and gaseous phases upon pyrolysis and several complex purification steps are therefore necessary.[33] Biomass gasification, carried out in the presence of steam or air, results in the formation of more gaseous products and is considered to be a more economically viable and environment-friendly route to large scale hydrogen production than pyrolysis[31,37] Biomass gasification is expected to become cost-competitive with SMR and, therefore, an important method of hydrogen production in the coming decades.[34,37]

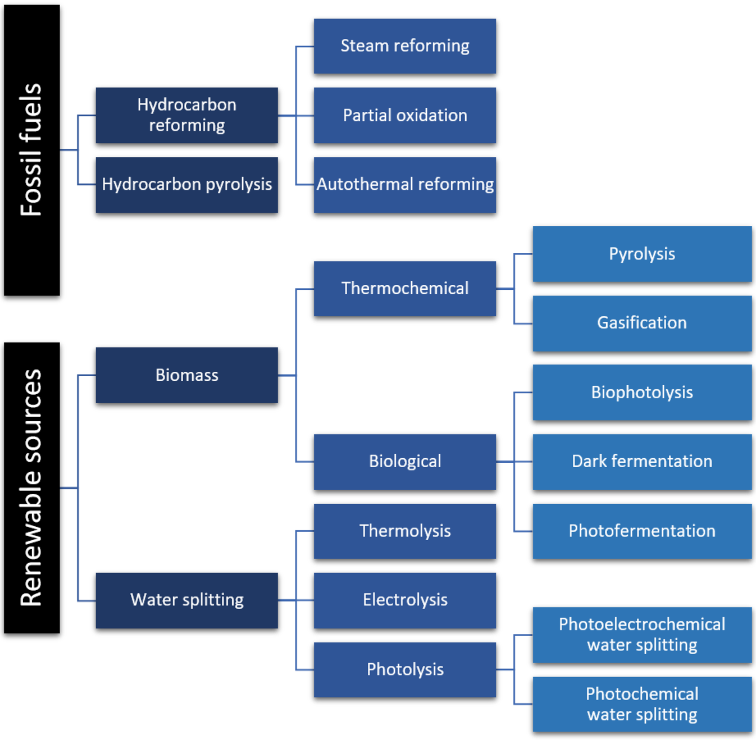

Figure 1.4. Overview of methods of hydrogen production Adapted from literature.[29]

1.2.2.1.2 Biological Methods of Hydrogen Production from Biomass

Hydrogen can also be produced from biomass using bacteria and algae that contain hydrogen-producing enzymes such as hydrogenase and nitrogenase. This approach is considered to be more environmentally benign and less energy-intensive than the thermochemical routes described previously. In biophotolysis, the photosynthetic systems of microorganisms use sunlight to produce hydrogen and oxygen from water with no greenhouse gas emissions.[38] However this process also takes place with a poor solar energy conversion efficiency.[39]

Alternatively the fermentation of biomass can produce hydrogen in the absence of water. For example, nitrogenase enzymes use solar energy to produce hydrogen in anaerobic conditions although this process typically operates with low solar energy conversion efficiencies and requires large, complex photobioreactors.[37] Anaerobic microalgae and bacteria can also produce hydrogen in the absence of solar energy; a process known as "dark" fermentation which is expected to be cheaper and less technologically complex.[28] Set-ups comprising sequential photofermentation and dark fermentation reactors have been proposed to boost efficiency.[40] This technology is still in its infancy though, and real-world feasibility has yet to be proven.

Hydrogen production from biomass has the potential to become a major source of hydrogen. This is especially true in areas with large amounts of agricultural waste such as California where a new facility utilising biomass is set to become the first to produce hydrogen from renewable energy on a megawatt scale.[41] However, it is doubtful that this approach is sufficiently scalable to fulfil the requirements of a hydrogen-based economy. The development of more efficient and scalable methods of hydrogen production remains a priority.

1.2.2.2 Water Splitting

'Splitting' water into its constituent elements is viewed as an elegant approach to hydrogen production as it is essentially the reverse of the reaction that takes place in a fuel cell. Dioxygen molecules (oxygen henceforth) are formed as the only by-product from this process. The abundance of water means that an efficient cost-competitive method of water splitting could kick-start the hydrogen economy. Water splitting is energetically unfavourable ($\Delta G = + 237$ kJ mol^{-1})[42] and therefore requires the input of a significant amount of energy. Several methodologies are being developed that use heat, electricity, solar energy, or a combination of these energy sources to split water in order to produce hydrogen.

1.2.2.2.1 Water Thermolysis

The high Gibbs energy of the water splitting reaction means that thermal dissociation of water requires temperatures in excess of 2500 °C and is therefore not practical.[29] Lower temperatures can however facilitate water splitting by driving a series of reactions that result in the production of hydrogen; for example, a two-step process in which SnO_2 is thermally reduced to SnO (**Reaction 1.6**) which can then perform water splitting, resulting in the regeneration of SnO_2 (**Reaction 1.7**).

$$\mathrm{SnO_2 \rightarrow SnO + \tfrac{1}{2}\, O_2} \tag{1.6}$$

$$\mathrm{SnO + H_2O \rightarrow SnO_2 + H_2} \tag{1.7}$$

Reaction 1.6 requires a temperature of 1500 °C when the partial pressure of oxygen in the carrier gas is reduced while **Reaction 1.7** proceeds at around 600 °C.[43] Although still high, these temperatures could be attained using waste heat from nuclear reactors or by using mirrors to concentrate solar energy[29] and thermochemical water splitting has been identified as having an especially low environmental impact.[28] However, the high temperatures required mean that the durability of both reagents and reactors is likely to be prohibitive[44] while high capital costs also represent an obstacle to commercial application.[29]

1.2.2.2.2 Water Electrolysis

A more established technique, electrolysis involves passing an electric current through water to split it into its constituent elements. An electrolysis unit consists of an anode and a cathode immersed in an electrolyte. Applying a current results in hydrogen production at the cathode while oxygen is simultaneously produced at the anode. **Reactions 1.8** and **1.9** are the half-reactions that take place at the anode and cathode respectively in a proton exchange membrane (PEM) electrolyser.

$$\mathrm{2\,H_2O \rightarrow O_2 + 4\,H^+ + 4\,e^-} \tag{1.8}$$

$$\mathrm{4\,H^+ + 4\,e^- \rightarrow 2\,H_2} \tag{1.9}$$

Naturally, the sustainability of this approach depends on the electricity source. Surplus electricity from renewable sources could be used to produce hydrogen onsite. For instance, photovoltaic (PV) cells can be used in conjunction with an electrolyser to convert solar energy to hydrogen during the day when demand for electricity is low, as illustrated in **Figure 1.5a**. The hydrogen can then be used in a fuel cell in the evening when demand for energy is highest.

Electrolysis currently accounts for just 3.9% of hydrogen production[45] as the cost of this technology has been considered prohibitive.[28] However, electrolysis is becoming more attractive as the cost of both renewable energy and electrolysers decrease. Hydrogen from water electrolysis is now cost-competitive with hydrogen derived from fossil fuels in niche applications and is expected to be competitive on an industrial scale within a decade.[46]

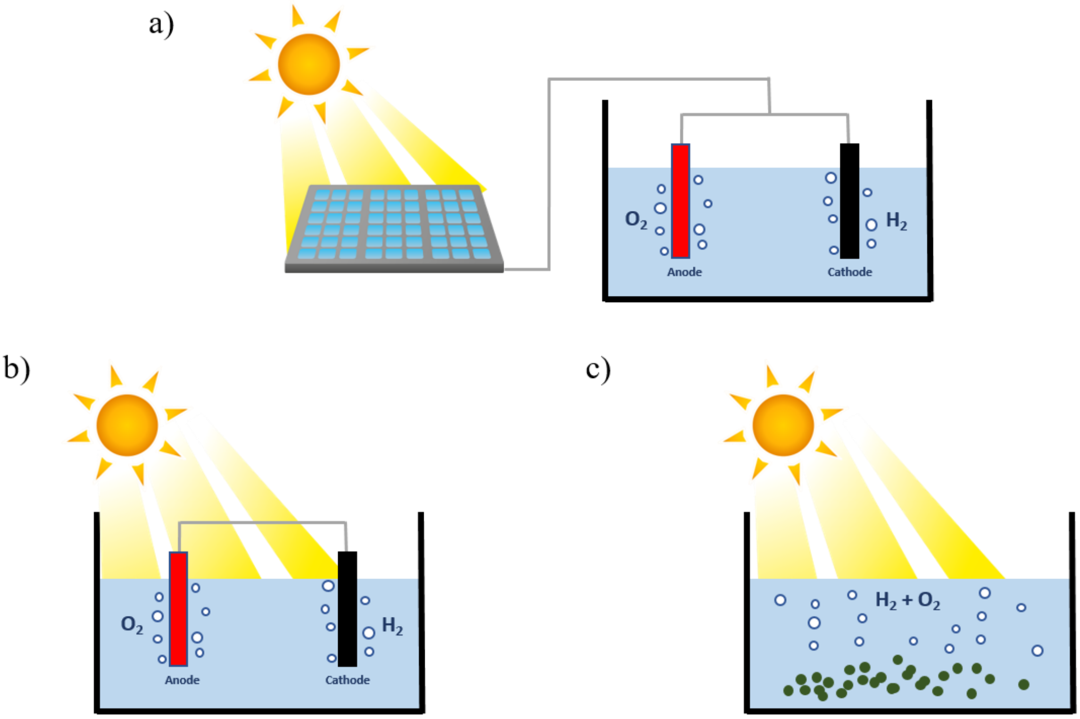

Figure 1.5. Schematic illustrations of hydrogen production by **a)** PV-electrolysis, **b)** photoelectrochemical water splitting and c) photochemical water splitting.

1.2.2.2.3 Photolysis

1.2.2.2.3.1 Photoelectrochemical Water Splitting

In photoelectrochemical (PEC) water splitting, the light-harvesting semiconducting materials are submerged in the electrolyte (**Figure 1.5b**). The PEC approach is theoretically more efficient than PV-electrolysis but demands stability of the semiconductors in the aqueous medium. The pioneering work of Fujishima and Honda in 1972 showed how overall water splitting (OWS) can be achieved using a rutile TiO_2 photoanode coupled with a platinum black cathode.[47] Irradiation of TiO_2 with photons of greater energy than the band gap results in excitation of electrons from the valence band (VB) to the conduction band (CB). The electrons then migrate towards the Pt cathode where they facilitate the proton reduction reaction to produce hydrogen while the holes participate in the water oxidation at the photoanode.[45] Charge extraction was achieved in this study by the application of an external bias.

Efficient separation of electron and holes is of critical importance in PEC devices. PEC water splitting can occur without the application of an external bias but takes place with much lower solar-to-hydrogen (STH) efficiencies due to the larger band gap that is required.[48] This can be circumvented by the use of dual-photoelectrode tandem devices in which two semiconductors are employed to maximise the generated photovoltage.[49] Recently, a record efficiency of 19.3% STH was achieved, approaching the theoretical upper limit of PEC devices.[50] However, the poor stability of the photocathode used in this study must be addressed and efficiency is still some way below PV-electrolysis systems with which 30% STH efficiency has recently been achieved.[51]

Significant recent advances in PV technology have led some to question whether PEC water splitting can ever compete with the PV-electrolysis method of hydrogen production.[52] Certainly, significant reductions in costs and improvements in stability are needed if PEC cells are to become commercially viable.

1.2.2.2.3.2 Photochemical Water Splitting

In photochemical water splitting both water oxidation and reduction reactions take place on the same semiconducting photocatalysts—or composites of photocatalysts—thus removing the need for wiring and therefore reducing associated losses in mass transport (**Figure 1.5c**). The technological simplicity of this approach also means that hydrogen production from direct photocatalysis is expected to be cheaper than both PV-electrolysis and PEC water splitting.[53] However, requirements for photocatalytic materials are stringent[54] and a complex multi-step processes must take place for photocatalytic water splitting to occur in a particulate system. The key stages of photochemical OWS are outlined in **Figure 1.6**, along with relevant properties of photocatalytic materials.

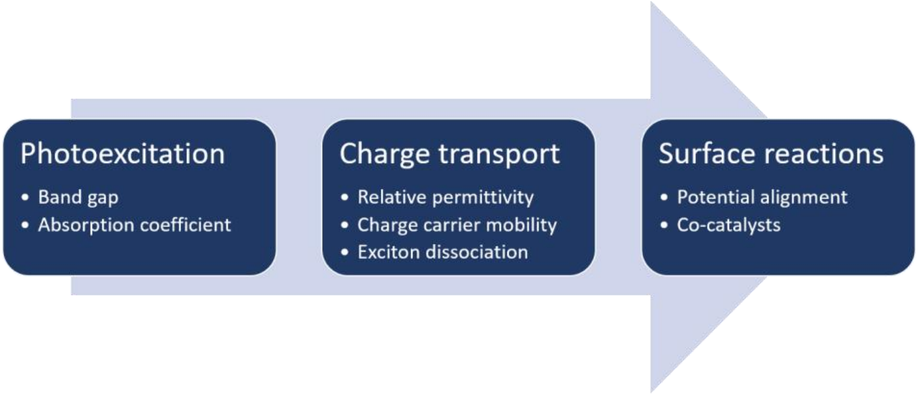

Figure 1.6. Steps involved in photocatalytic reactions and selected properties that influence these steps.

Absorption of a photon leads to excitation of an electron from the VB to the CB, resulting in the formation of an electron-hole pair, or exciton. Photocatalysts must have suitable band positions in relation to the water oxidation and reduction potentials. The size of the band gap is also critical. In principle, a band gap of 1.23 eV is sufficient to straddle the water splitting potentials although an overpotential is required to overcome the energetic barrier to water oxidation and so materials with band gaps in excess of 2.0 eV are typically employed (**Figure 1.7a**).[55] However, wide band gap materials are inefficient harvesters of solar energy; light with wavelengths below 400 nm represents only 4% of the solar spectrum.[56] Z-schemes, in which the two half-reactions take place on different semiconductors, have therefore attracted interest as they permit the use of materials with narrower band gaps that can therefore harness a greater amount of visible light (**Figure 1.7b**).

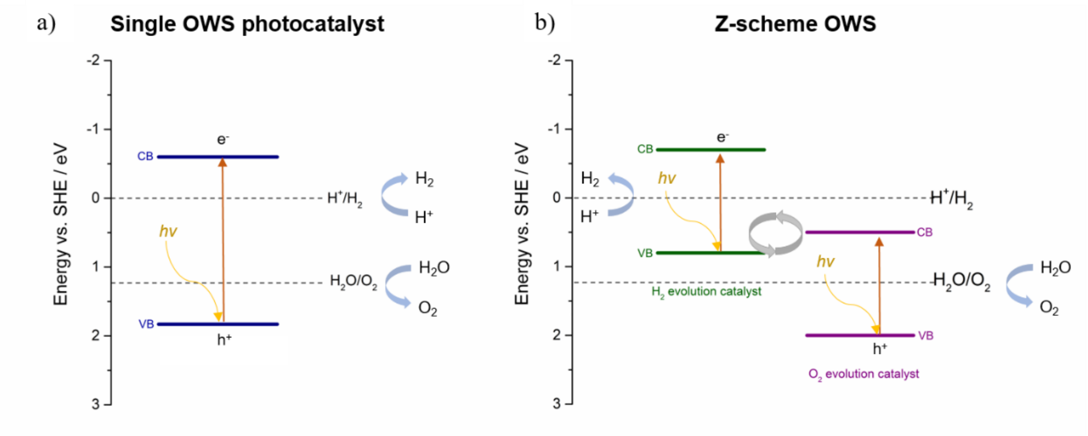

Figure 1.7. Band structure representations of OWS by **a)** a single photocatalyst and **b)** a Z-scheme system involving a two-step excitation process and electron transfer between hydrogen and oxygen-evolving photocatalysts.

In a Z-scheme system, photoexcitation occurs in both a hydrogen-evolving and oxygen-evolving catalyst. Holes from the CB of the hydrogen-evolving material are transferred to the VB of the oxygen-evolving catalyst while electrons from the oxygen-evolving catalyst pass in the other direction, with electron transfer between the two often facilitated by a redox mediator.[57] The use of electron mediators can reduce performance because of backward reactions involving the redox couples taking place.[58] However, the fact that, in a Z-scheme, the hydrogen and oxygen-evolving species can be separated may be advantageous; the difficulty associated with separating the potentially explosive mixture of hydrogen and oxygen is a widely acknowledged shortcoming of single particulate OWS systems.[59] Z-scheme photocatalytic systems will be discussed in greater detail in **Chapter 4**.

Following photoexcitation of a semiconductor, excitons are formed. Depending on the longevity and mobility of these excitons, they can then either dissociate to form free charges in the bulk material or migrate to the solid-liquid interface before dissociating. The rate of exciton dissociation is heavily dependent on the effective masses of charge carriers and relative permittivity of the photocatalyst, with both properties determined by the material's electronic structure.[60] The high relative permittivities of most inorganic materials mean excitons typically dissociate readily in these materials. However, in organic semiconductors, holes and electrons are much more strongly bound and these excitons are therefore expected to migrate to the photocatalyst surface before dissociating.[61,62] In order for photocatalytic reactions to occur, migration of excitons or free charge carriers to the surface must take place before relaxation back to the ground state, either by fluorescence or non-radiative decay, can occur. Photocatalytic applications therefore demand semiconductors with long excited state lifetimes and high charge carrier mobilities.[42]

Upon migration of charge carriers to the solid-liquid interface, surface reactions must finally take place. As previously discussed, this requires the ionisation potential and electron affinity of the excited state of the photocatalyst to straddle the redox potentials of the desired half-reactions. Co-catalysts are often loaded onto photocatalysts to provide active sites for these redox reactions by trapping charge carriers. However, while these co-catalyst particles enhance the rate of photocatalytic reactions, they can also catalyse the water-forming back-reaction of H_2 and O_2.[63,64] To mitigate this, 'core-shell' co-catalyst particles have been developed. These particles consist of noble metal 'cores' encased by 'shells' that act as membranes to prevent permeation of dissolved oxygen molecules to the noble metal.[65]

However, OWS remains a challenge, mainly as a result of the sluggish kinetics of the four-electron water oxidation reaction (**Reaction 1.8**), which is considered a "kinetic bottleneck" of water splitting.[66] It is therefore common to initially develop new materials by studying the individual half-reactions. This is achieved with the use of sacrificial reagents which rapidly scavenge either holes or electrons upon their formation and enable the aptitude of a photocatalyst for a specific half-reaction to be studied.[67]

The choice of sacrificial reagent can significantly affect performance. Low oxidation potentials and high relative permittivities are desirable properties for sacrificial electron donors.[68] Tertiary amines like triethylamine (TEA) and triethanolamine (TEOA) are commonly used because of the irreversibility of their degradation pathways.[67] TEA will be used in the majority of cases in this thesis, with the sequence of reactions outlined below hypothesised to take place (**Reactions 1.10-1.16**).[69] Briefly, TEA scavenges holes from the excitonic state of the photocatalyst (**Reaction 1.11**) thus enabling the excited electron to persist and participate in the proton reduction half-reaction (**Reaction 1.15**). Meanwhile, TEA itself degrades to diethylamine and ethanaldehyde (**Reactions 1.12**, **1.13** and **1.16**).

$$\text{Photocatalyst} \rightarrow \text{Photocatalyst}^* \tag{1.10}$$

$$\text{Photocatalyst}^* + \text{TEA} \rightarrow \text{Photocatalyst}^{\bullet -} + \text{TEA}^{\bullet +} \tag{1.11}$$

$$\text{TEA}^{\bullet +} \xrightarrow{-\text{H}^+} \text{Et}_2\text{NC}^{\bullet}\text{HCH}_3 \tag{1.12}$$

$$\text{Et}_2\text{NC}^{\bullet}\text{HCH}_3 \rightarrow \text{Et}_2\text{NC}^{+}\text{HCH}_3 + \text{e}^- \tag{1.13}$$

$$\text{Photocatalyst}^{\bullet -} \rightarrow \text{Photocatalyst} + \text{e}^- \tag{1.14}$$

$$2\ \text{H}_2\text{O} \xrightarrow{2\text{e}^-} \text{H}_2 + 2\ \text{OH}^- \tag{1.15}$$

$$\text{Et}_2\text{NC}^{+}\text{HCH}_3 \xrightarrow{\text{OH}^-} \text{Et}_2\text{NH} + \text{CH}_3\text{CHO} \tag{1.16}$$

As well as the previously discussed optical and electronic factors, additional properties such as high photostability and resistance to water corrosion are also essential in photocatalytic materials.[70] Furthermore, it is believed that a high surface area may be beneficial to maximise the interface between the photocatalyst and water.[71] Recent studies have also shown the wettability of particulate photocatalysts to be crucial.[72–74] Determining the relative influence of a single property on photocatalytic performance is difficult as changing one property often impacts another. Some important parameters may also yet to be discovered, although high throughput screenings of properties are underway that are intended to reveal these.[75]

In spite of the many obstacles that must be overcome, photochemical water splitting is still considered to be a goal worth pursuing. The scalability of this approach means that it is expected to be an economically viable source of hydrogen if STH efficiencies in the region of 5-10% can be achieved.[53,76,77] Inorganic materials have been the subject of the majority of research in this field and have therefore come closest to achieving this target.

1.3 Materials for Photocatalytic Water Splitting

1.3.1 Inorganic Photocatalysts

The first instance of water splitting from particulate photocatalysts followed soon after the landmark report on PEC water splitting by Fujishima and Honda.[47] Since then, a host of inorganic materials have been investigated as potential photocatalysts for both the hydrogen- and oxygen-evolution reactions. These have been detailed in several comprehensive reviews.[78–80] Inorganic materials commonly used for the hydrogen evolution reaction include chalcogenides and metal oxides like cadmium sulfide (CdS), cadmium selenide (CdSe), titanium dioxide (TiO_2) and strontium titanate ($SrTiO_3$). Unmmodified, these materials typically exhibit poor activity under visible and near infra-red light due to their low-lying VBs.[81,82]

However, performance has been improved by incorporating dopants, forming composites and adding co-catalysts. The introduction of metal ion dopants in inorganic materials can introduce energy levels between the VB and CB while the addition of non-metal ions can shift the VB edge upwards to narrow the band gap. Both of these approaches have been shown to improve activity under visible light irradiation.[78] The formation of composite materials can alternatively enhance performance by promoting charge carrier separation. For instance, a composite of the anatase and rutile forms of TiO_2 outperforms the individual components.[83]

The addition of co-catalysts can also encourage separation of electrons and holes and inhibit charge recombination. Particles of noble metals like platinum, rhodium, ruthenium and gold are thought to behave as electron traps and therefore act as active sites for proton reduction. Conversely, hole-trapping transition metal oxides are often employed as co-catalysts for oxygen evolution.[70] These co-catalysts play a vital role in photocatalytic reactions; the hydrogen evolution rate of TiO_2 has been shown to scale with the amount of Pt deposited[84] while the size and morphology of co-catalyst particles has been shown to dramatically affect photocatalytic performance.[85] The field has also benefited from recent advances in nanoscience.[55] Incorporation of nanometre-sized semiconductor particles known as quantum dots (QDs) into photocatalytic systems has become commonplace, owing to their excellent light harvesting properties.[86] Together, these strategies have enabled the fabrication of highly elaborate structures, such as CdS nanorods with embedded platinum and CdSe

QDs which have recently achieved 100% photon-to-hydrogen conversion efficiency at λ = 455 nm in sacrificial conditions.[87]

Overall water splitting (OWS) has also been achieved with a host of inorganic systems. The wide band gaps of some inorganic semiconductors makes them capable of OWS under UV light without modification. Evolution of hydrogen and oxygen from water in a stoichiometric ratio by anatase TiO_2 powder was first reported in 1977, although the amounts produced were low (0.80 µmol H_2, 0.39 µmol O_2).[88] OWS has since been reported by a multitude of titanates, tantalates and niobates, amongst others,[79] with efficiencies improved using the strategies described previously. The highest STH efficiencies achieved by Z-scheme systems are around 1%.[89] However, it is expected that STH efficiencies in the region of 5% are required to make these systems commercially viable.[90]

A major drawback of inorganic materials is that, individually, they typically exhibit poor photocatalytic activity under visible light. Composites of lower band gap materials have therefore been fabricated in an effort to harvest a greater portion of the solar spectrum and thereby achieve OWS at higher STH efficiencies. Recently, a composite of Ta_3N_5 nanorods with $KTaO_3$ and a Rh/Cr_2O_5 co-catalyst was shown to split water under visible light irradiation, although the STH efficiency was low (0.014%).[91] Visible light performance has also been improved by the construction of Z-schemes of hydrogen-evolving photocatalysts like $SrTiO_3$ with oxygen-evolving materials with deeper-lying band structures, such as tungsten oxide (WO_3) and bismuth vanadate ($BiVO_4$).[77] The concept of a Z-scheme using inorganic semiconductors was first introduced in 1979[92] since when numerous Z-schemes have been reported.[57] Typically, these systems require redox shuttles to mediate electron transfer between the two photocatalysts although OWS has been achieved in their absence.[93]

The limited tunability of these materials is expected to make attainment of the 5% STH target challenging. Moreover, reservations persist over the long-term stability of inorganic systems,[94] as well as their reliance on precious metal co-catalysts. In recent years, organic photocatalysts have attracted increased attention due to a number of advantageous properties.

1.3.2 Organic Photocatalysts

The discovery of a host of aryl-aryl coupling reactions during the 21st century has led to the use of π-conjugated organic polymers in electronic applications.[95] The earth-abundance of the constituent elements of organic materials is viewed as a key advantage.[96] Moreover, the diversity of monomeric building blocks that can be utilised in the aforementioned cross-coupling reactions ensures that far greater structural tunability is possible than for inorganic materials. This ability to systematically modify polymer structure allows for the fine-tuning of key properties such as size and position of the band gap and, therefore, optimisation for photocatalytic applications.

Instead of the conduction and valence bands of inorganic materials, the electronic properties of organic semiconductors must be considered in terms of molecular orbitals, in particular the highest occupied molecular orbital (HOMO) and lowest unoccupied molecular orbital (LUMO). The energies of these orbitals correspond to the energies required to remove or add an electron to or from the material; respectively the ionisation potential (IP) and electron affinity (EA). The potentials associated with the exciton (IP* and EA*) are typically narrower than the ground state potentials but should also straddle the water splitting potentials.[97]

Hydrogen evolution rates of organic photocatalysts are typically lower than inorganic systems. This can partly be attributed to the comparative infancy of the field although organic materials do also possess some inherent limitations. Polymers typically exhibit low relative permittivities which means excitons do not dissociate as readily as in inorganic materials.[97,98] Lower charge carrier mobilities, stemming from greater structural disorder, are also considered to be an “Achilles heel” of polymers.[98] However, the aforementioned tunability of polymer structures means that these limitations can be methodically addressed.

1.3.2.1 Carbon Nitrides

Carbon nitrides (C_3N_4) are a class of polymeric materials prepared by the condensation of nitrogen-rich monomers, such as melamine and urea, at high temperatures. The idealised C_3N_4 structure consists of linked *s*-triazine or heptazine (tri-*s*-triazine) units (**Figure 1.8**) although exact structures are often unknown and are likely to contain mixtures of these units and other structural defects.[99] In 2009, the discovery of these materials’ ability to evolve hydrogen in the presence of a sacrificial electron donor sparked the surge of interest in polymeric semiconductors for hydrogen production.[100] C_3N_4 materials boast a number of desirable properties for photocatalytic applications, including good thermal and chemical stability and optimal band structure. Computational studies have confirmed the suitability of C_3N_4 band positions for both proton reduction and water oxidation.[99]

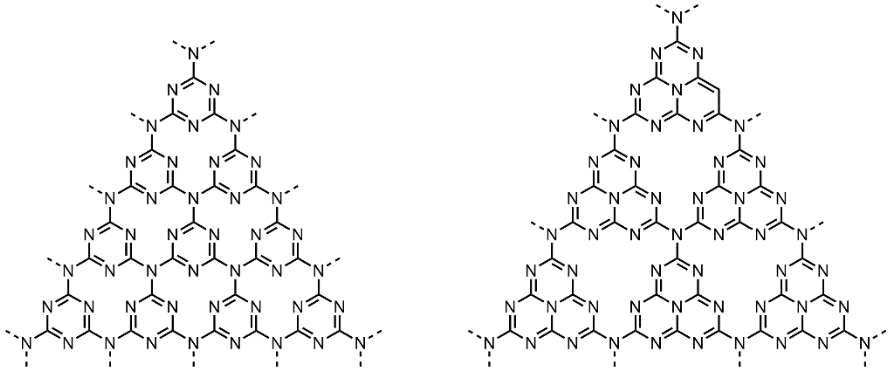

Triazine C_3N_4 **Heptazine C_3N_4**

Figure 1.8. Chemical structures of C_3N_4 consisting of linked units of **a)** triazine and **b)** heptazine.

C_3N_4 has been the most widely studied organic photocatalyst to date and the subject of a wealth of research that has been detailed in recent reviews.[101–103] Significant improvements in hydrogen evolution activity have been achieved, mainly through the addition of co-catalysts and by controlling morphology. In particular, improving crystallinity has been found to enhance the performance of C_3N_4.[103] A post-synthesis ionothermal treatment, in which eutectic salt mixtures are used to improve structural order, resulted in the formation of highly ordered C_3N_4 with an AQY of 60% at $\lambda = 420$ nm.[62,104] Stoichiometric overall water splitting has also been reported from crystalline C_3N_4 made using this method, albeit with added platinum and cobalt co-catalysts.[105,106] The formation of composites is another commonly used strategy to improve photocatalytic performance by encouraging charge separation.[107–112] Recently, overall water splitting from a purely organic nanocomposite with carbon nanodots has been reported.[113]

Although carbon nitrides possess attractive traits for photocatalytic applications, these materials share many of the drawbacks of inorganic photocatalysts. Most notably, for the context of the present thesis, carbon nitrides are insoluble in common organic solvents.[a] As with inorganic catalysts, this can present challenges in terms of processing and characterisation and the exact structure of most C_3N_4 materials is therefore unknown. Furthermore, while C_3N_4 can be produced from inexpensive starting materials the synthesis usually involves high temperatures and offers limited scope for systematic alteration of structure and properties. This has led to a reliance on heavy metal co-catalysts and incorporation of dopants to achieve desirable properties such as increased light absorption in the visible region.[114] There is thus a need for organic frameworks in which greater structural control and variety can be achieved.[115]

1.3.2.2 Conjugated Microporous Polymers

Conjugated microporous polymers (CMPs) combine high surface areas with semiconducting properties, thereby offering distinct advantages over non-porous materials. First prepared in 2007,[116] these networks have been researched for a wide range of functions.[117,118] Conjugation is maintained throughout the 3-D networks and properties such as pore size,[119] fluorescence[120] and optical gaps[121] can be controlled by varying monomer feedstock ratios. CMPs are characteristically amorphous as they are synthesised by thermodynamically-controlled, irreversible reactions.

CMPs were first investigated as photocatalysts for hydrogen evolution in 2015.[122] In this study, the ratio of benzene and pyrene units in CMP networks was systematically varied by statistical copolymerisation, enabling optimisation of the optical gap for photocatalytic performance. Meanwhile, recent studies have suggested that the porosity of CMPs may be beneficial for photocatalysis. The porosity of a dibenzo[*b*,*d*]thiophene sulfone-containing CMP enabled higher water uptake than an equivalent linear polymer which seemed to permit increased hydrogen evolution.[73]

Incorporation of alkyne moieties into the linker units of CMPs has been shown to increase their performances under visible light by lowering the LUMO.[123] Composites of 2-D CMP nanosheets containing alkyne functionalities (**Figure 1.9**) were recently reported to be capable of stoichiometric overall water splitting.[124]

---

[a] C_3N_4 has recently been shown to dissolve in acid.[175]

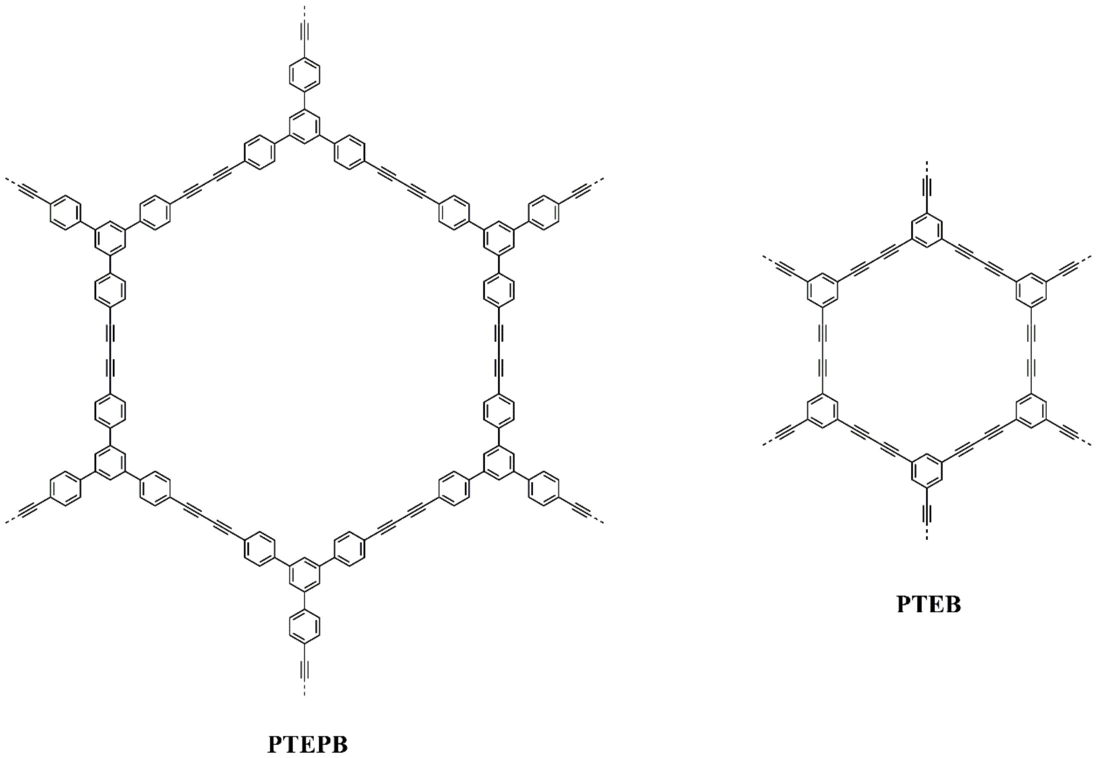

Figure 1.9. Chemical structures of CMP nanosheets synthesised from 1,3,5-tris-(4-ethynylphenyl)-benzene **(PTEPB)** and 1,3,5-triethynylbenzene **(PTEB)**.[124]

1.3.2.3 Covalent Triazine-Based Frameworks

Covalent triazine-based frameworks (CTFs) incorporate the highly active and stable triazine motif found in C_3N_4 materials into porous 2-D networks. In doing so they combine many of the advantageous properties of CMPs and C_3N_4. Triazines are connected by variable aromatic linkers to extend their π-conjugation and enable synthetic modularity. Unlike CMPs, CTFs are prepared by ionothermal syntheses catalysed by Lewis acids such as $ZnCl_2$ or trifluoromethanesulfonic acid.[125]

Appreciable rates of hydrogen evolution has been observed from a number of CTFs, generally when platinum co-catalysts are added.[121-123] Furthermore, as with C_3N_4, CTFs typically possess HOMOs and LUMOs that straddle the water-splitting half reaction potentials.[129] Oxygen evolution has recently been observed from **CTF-1** (**Figure 1.10a**) with an apparent quantum efficiency (AQE) of 3.8% at 420 nm.[130] However, concurrent stoichiometric OWS has yet to be observed.

Like CMPs, CTFs are generally amorphous,[115] which may limit charge carrier mobilities and, consequently limit photocatalytic performance.[70] Organic frameworks of greater crystallinity have therefore attracted attention in recent years.

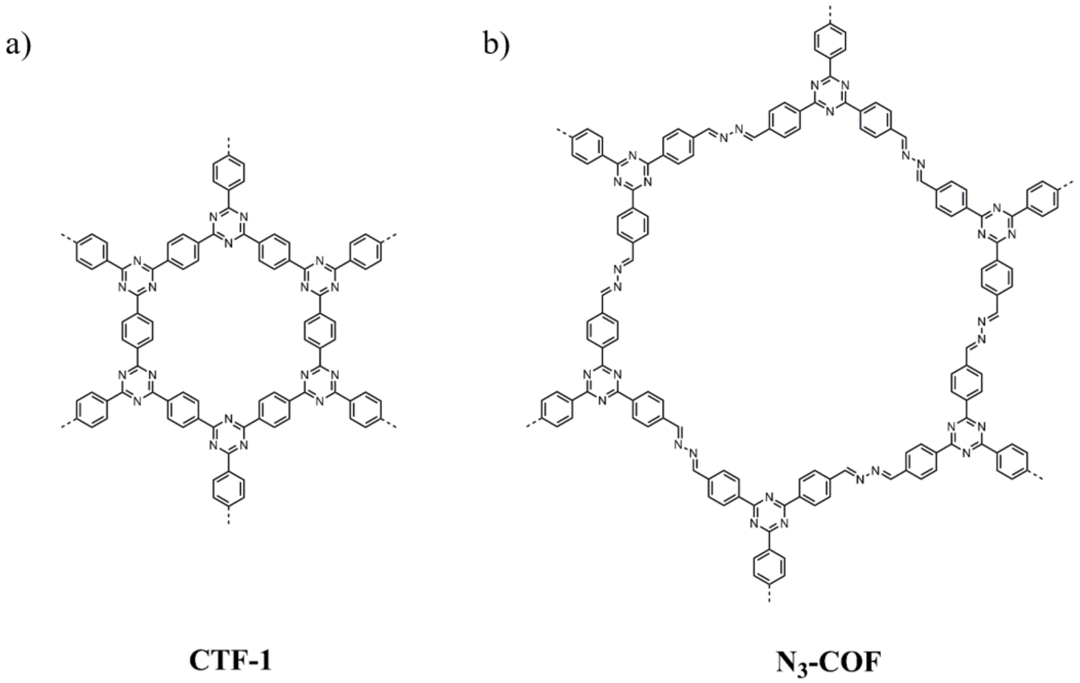

Figure 1.10. Chemical structures of **a) CTF-1**[127] and **b) N_3-COF**.[131]

1.3.2.4 Covalent Organic Frameworks

Covalent organic frameworks (COFs) are typically highly stable, can possess both micro- and mesoporosity and present unique opportunities for precise synthetic control.[125] The reversibility of the Schiff base reactions used to prepare COFs enables the formation of highly crystalline networks with uniform pore structures. As envisaged in the landmark report by Yaghi *et al* in 2005,[132] this crystallinity, coupled with the almost limitless scope for variation of building blocks, opens up the possibility of designing and optimising COFs for a broad range of applications. The photocatalytic capability of COFs was first reported in 2014 when hydrazone-based COFs were found to evolve hydrogen in sacrificial conditions.[131] Inspired by C_3N_4 and CTFs, hydrogen evolution rates were enhanced by incorporation of azine units into 2-D COFs like **N_3-COF** (**Figure 1.10b**).[131]

The channels within these frameworks are thought to enable intimate contact with added dyes and co-catalysts. Usually platinum is added as a co-catalyst to boost the performance of COFs.[115] However, addition of a molecular cobaloxine co-catalyst recently enabled higher performance than Pt-loaded analogues.[133] Meanwhile, a high hydrogen evolution rate of 16.3 mmol g^{-1} h^{-1} under visible light irradiation has been achieved with the assistance of a near-infrared-absorbing dye.[134]

However, as with other porous organic networks, the practicality of COFs is limited by the inability to post-synthetically process these materials. Several efforts have been made to form films of COFs despite the insolubility of these frameworks.[135] These strategies include synthesising directly on substrates or at liquid interfaces or alternatively using post-synthesis exfoliation and delamination techniques. However, the scalability of such approaches is questionable[136] and the use of solution-processable polymers should enable much greater control over morphology.

1.3.2.5 Linear Polymers

Poly(*p*-phenylene) (**PPP**, **Figure 1.11**) and oligo(*p*-phenylenes) were the first reported organic photocatalysts in 1985[137] and 1991[69] although these reports went largely unnoticed until the breakthrough C_3N_4 study in 2009.[100] In the intervening years, vast progress has been made in developing semiconducting linear polymers for electronic applications like organic photovoltaics (OPVs)[138], organic field effect transistors (OFETs)[139] and organic light-emitting diodes (OLEDs).[140] The requirements of photocatalysts are of course different, but the wealth of research that has been conducted on the optical and electronic properties of these polymers for other applications can be used to develop this class of polymers for photocatalytic applications.

An obvious potential drawback of one-dimensional chains of conjugated polymers in comparison to the previously discussed 2-D and 3-D networks is their lower surface areas. However, although porosity is expected to be beneficial, linear polymers have displayed hydrogen evolution performance comparable to[73] and, in some instances,[141] even higher than structurally analogous network polymers. In the latter study, the increased performance of a linear phenylene-benzothiadiazole polymer (**B-BT-1,4**, **Figure 1.11**) was attributed to improved charge transporting behaviour. Some linear conjugated polymers have amongst the highest reported hydrogen evolution rates in the field of polymer photocatalysis (**Table 1.1**) although it should be noted that the different set-ups and conditions used for photocatalysis make direct comparisons difficult.[142]

Table 1.1. Optical gaps, photocatalytic hydrogen evolution rates (HERs) and external quantum efficiencies (EQEs) of selected linear photocatalysts. UV + visible light = λ > 295 nm, visible light = λ > 420 nm unless stated.

Polymer	Optical gap / eV	HER UV + visible light / mmol g^{-1} h^{-1}	HER Visible light / mmol g^{-1} h^{-1}	EQE / % (λ)	Ref.
PPP[i]	2.9	0.105	-	<0.04 (290 nm)	137
P12[ii]	2.42	0.545	0.420	1.4 (420 nm)	143
PTh-c[iii]	~1.94	-	2.8	-	144
P28[ii]	2.45	0.960	1.34	6.7 (420 nm)	145
PyPm[iv]	2.32	0.374	-	1.1 (420 nm)	146
B-BT-1,4[v]	1.64	-	0.308[i]	2.4 (420 nm)	141
B-BT-1,4-E[v]	2.11	-	0.355	3.7 (420 nm)	123
P7[ii]	2.73	-	1.49	7.2 (420 nm)	147
P10[ii]	2.62	-	3.26	11.6 (420 nm)	148
P10-e[vi]	2.66	29.5	14.5	5.8 (420 nm)	149

[i] **PPP** (20 mg) in 4 mL 50 vol.% diethylamine in water, measured over 4 hours irradiation by a 300 W mercury light source (UV light = λ > 290 nm)

[ii] **P12**, **P28**, **P7** and **P10** (25 mg) in water/methanol/TEA (1:1:1, 25mL) with irradiation by a 300 W Xe light source.

[iii] **PTh-c** (5.0 mg) in 100 mL aqueous solution of 0.1 M ascorbic acid in a closed gas circulation system with irradiation by a 300 W Xe light source

[iv] **PyPm** (50 mg) with 3 wt% Pt was suspended in 100 mL water containing 20 vol% triethanolamine under UV–Vis light (UV light = λ > 300 nm)

[v] **B-BT-1,4** and **B-BT-1,4-E** (30 mg) with 3 wt.% Pt co-catalyst in 30 mL 10 vol.% TEOA/H_2O irradiated by a 300W Xe-lamp.

[vi] **P10-e** (0.1 mg mL^{-1}) in aqueous/methanol/triethylamine (1 : 1 : 1, 25 mL, aqueous phase containing water : toluene (9 : 1), SDS surfactant (10 mg mL^{-1}) and Na_2CO_3 (3.5 mg mL^{-1}) with irradiation by a 300 W Xe light source.

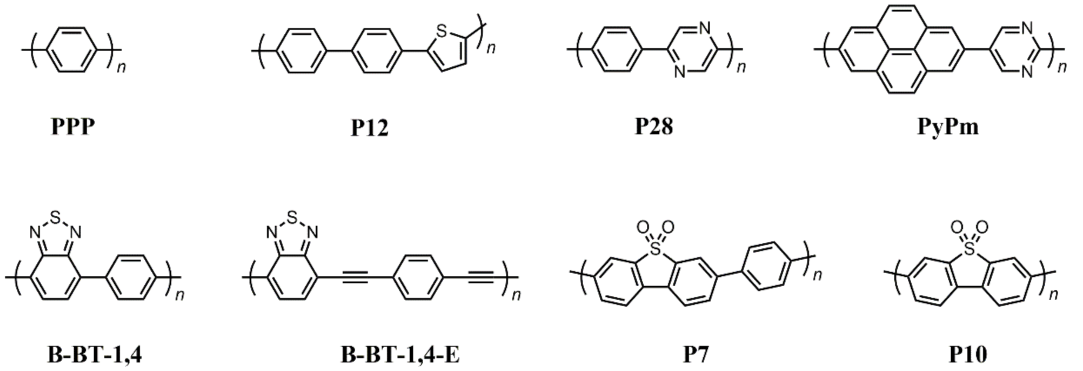

Figure 1.11. Chemical structures of selected linear photocatalysts.

PPP suffers from poor visible light activity as a result of its wide band gap.[146] The optical properties of **PPP** have therefore been tuned by incorporating other functionalities into the polymer backbone. Incorporation of thiophene units improved visible light absorption although a trade-off with reduced thermodynamic driving force for the half-reactions was observed at higher thiophene contents.[143] A polymer with 33% thiophene content (**P12**, **Figure 1.11**) was found to have highest performance (EQE = 1.4% at 420 nm). The need for an overpotential for sacrificial donor oxidation was again demonstrated when nitrogen-containing heterocycles were introduced into a **PPP** backbone.[145] The incorporation of nitrogen atoms resulted in a lowering of IP, thereby increasing the driving force for TEA oxidation, resulting in an EQE of 6.7% for **P28** (**Figure 1.11**) at 420 nm. Nitrogen-containing heterocycles have also been co-polymerised with pyrene units, again resulting in enhanced hydrogen evolution rates (**PyPm**, **Figure 1.11**).[146] Incorporating alkyne functionalities represents another strategy for narrowing the optical gap and thereby increasing the photocatalytic performance of linear polymers, including the previously discussed **B-BT-1,4** (**B-BT-1,4-E**, **Figure 1.11**).[123]

Hydrophilicity also appears to be a key factor in determining the performance of these materials. A copolymer of phenylene with dibenzo[*b,d*]thiophene sulfone, (**P7**, **Figure 1.11**) was found to significantly outperform **PPP** (92.0 vs. 3.9 µmol h^{-1}).[147] This was initially attributed to planarisation of the polymer backbone although the polarity of dibenzo[*b,d*]thiophene sulfone has since been identified as significant.[74] A combination of molecular dynamics (MD) simulations and spectroscopic measurements of transient species revealed that the high water content surrounding the polar dibenzo[*b,d*]thiophene sulfone units may increase photocatalytic rates by stabilising the polymer anion and accelerating charge transfer. In this study, a homopolymer of dibenzo[*b*,*d*]thiophene sulfone (**P10**, **Figure 1.11**) was found to significantly outperform **P7**, with an EQE of 11.6% at 420 nm.[74] The performance of **P10** has been further enhanced by preparing the polymer as nanoparticles *via* an emulsion polymerisation route (**P10-e**, **Table 1.1**).[149]

A key advantage of linear polymers is that they can easily be made to be processable in common organic solvents with the incorporation of solubilising side-chains. Solubilising groups can be added into network polymers but may limit porosity by obstructing pores and this has therefore been the subject of limited research. Solution-processable CMPs have been reported although these are actually discrete branched chains rather than truly extended networks.[150] By contrast, a wealth of solution-processable linear polymers have been prepared.[151] These have been used to fabricate intricate electronic devices[152] with a degree of precision that is extremely challenging with insoluble materials.

The preparation of solution-processable polymer photocatalysts has the potential to further our understanding of photocatalytic materials by enabling hitherto inaccessible characterisation techniques while simultaneously expanding processing opportunities. To date, only a handful of solution-processable linear polymer photocatalysts have been reported.[69,105,153–159] In the majority of these studies, polymers are processed into the form of nanoparticles, while recently blends of solution-processable polyfluorenes have been encapsulated in nanomicelles.[156] These studies indicate the morphological control made possible by solubility and provide motivation for further investigation into these materials.

1.4 Experimental Techniques

Characterisation of materials in this thesis will require the use of standard techniques such as powder X-ray diffraction (PXRD), thermogravimetric analysis (TGA), gel permeation chromatography (GPC), UV-vis absorption spectroscopy and photoluminescence (PL) spectroscopy. These techniques are commonly used in the field and will therefore not be outlined in great detail.

However, factors such as band positions and the lifetimes of photoinduced charge carriers are also likely to affect photocatalytic performance. Probing these properties requires the use of more specialist techniques which will now be outlined in greater detail. A high throughput methodology, which may be useful for systematic variation of parameters in large-scale studies, will also be presented.

1.4.1 Transient Absorption Spectroscopy

Transient absorption spectroscopy (TAS) is an effective method for studying charge carrier dynamics on ultrafast timescales.[160] TAS is a 'pump-probe' technique in which the material being investigated is excited from the ground state using a specific wavelength before a second 'probe' wavelength is applied (**Figure 1.12**). In doing so, the absorption spectrum of the excited state is obtained. Laser light sources are typically used for photoexcitation of the samples and the observable timescales are therefore limited by the frequency of the laser pulse.

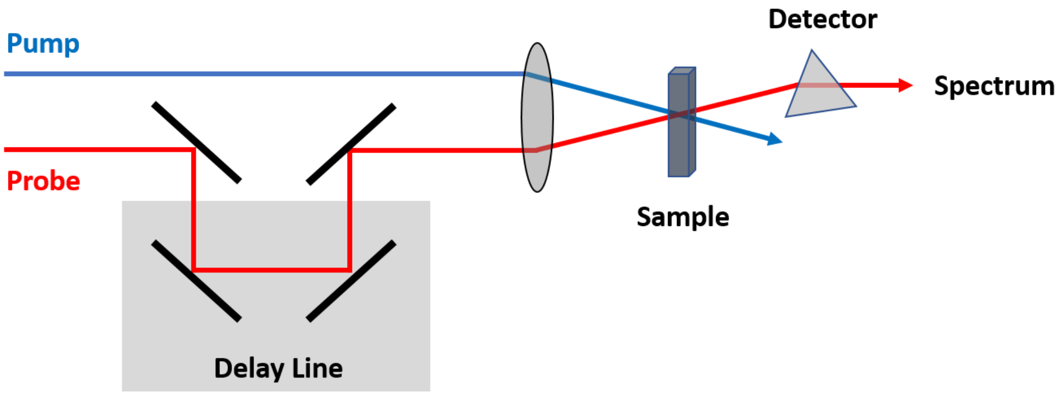

Figure 1.12. Schematic representation of transient absorption spectroscopy experimental set-up.

Transient absorption is quantified in terms of the change in optical density (ΔO.D.) of the probe beam before and after passing through the sample. ΔO.D. is calculated using **Equation 1.1**, where I_0 is the spectral intensity of the probe pulse in front of the sample and I is the intensity of the probe pulse having passed through the sample. The time at which the sample is probed can be controlled using the time delay line, shown in **Figure 1.12**. Varying the time, t, across a range of wavelengths, λ, results in essentially two-dimensional plots of transient absorption kinetics that enable identification of excited state species and their lifetimes.

$$\Delta \mathrm{O.D.}(\mathrm{t}, \lambda) = \log \frac{I_0}{I(\mathrm{t}, \lambda)} \qquad \textbf{(Eq. 1.1)}$$

In the context of photocatalysis, TAS can allow us to follow the generation and dissociation of excitons as well as quenching of excited states in the presence of sacrificial reagents. Commonly observed long-lived features in the TAS spectra of polymers include polarons; radical ionic species that are the prototypical charge carriers in semiconducting organic polymers.[161] Negative features are also typically observed in TAS spectra due to the ground state bleaching effect caused by photoluminescence from the excited state.[162]

TAS is typically used to probe charge carrier dynamics on both the microsecond (μs) and, more recently,[163] femtosecond (fs) timescales. fs-TAS enables initially-generated states to be observed while longer-lived species, which persist on the timescales at which proton reduction is expected to occur, can be studied using μs-TAS. Both techniques will be applied to the study of transient excited states of polymer photocatalysts in this thesis.

TAS is often used in conjunction with spectroelectrochemistry (SEC) measurements.[164] In SEC measurements, an electrical potential is applied to a sample whilst its physical properties are spectroscopically monitored *in situ*.[165] Monitoring the UV-vis spectra of oxidised or reduced samples can verify the nature of long-lived features present in TAS spectra.

1.4.2 Photoelectron Spectroscopy in Air

Photoelectron spectroscopy in air (PESA) is a useful technique for measuring the energy levels of organic materials.[166] These properties can also be probed using techniques such as cyclic voltammetry (CV) and ultraviolet photoelectron spectroscopy (UPS). However, the operating windows of these methods are limited by solvent stability and the values obtained can differ from those observed in practical device cconditions.[167,168] Values obtained by PESA have, on the other hand, been experimentally corroborated.[169,170]

In PESA experiments, films of semiconductors in ambient conditions are bombarded with a monochromatic UV light source, generating photoelectrons that in turn ionises oxygen molecules in the air. The resultant singlet oxygen molecules ($^1O_2$) are then detected by an open counter.[171] The incident photon energy is gradually increased until a threshold is reached above which the photoelectron yield begins to increase linearly (**Figure 1.13**). This threshold corresponds to the IP of the semiconductor in ambient conditions.

The obtained IP values can be used in conjunction with optical gaps obtained from UV-vis spectrometry to estimate the EA of materials.[169] The resultant band structure can be used to determine the suitability of materials for photocatalytic hydrogen evolution and assist in the design of composite materials for this application.

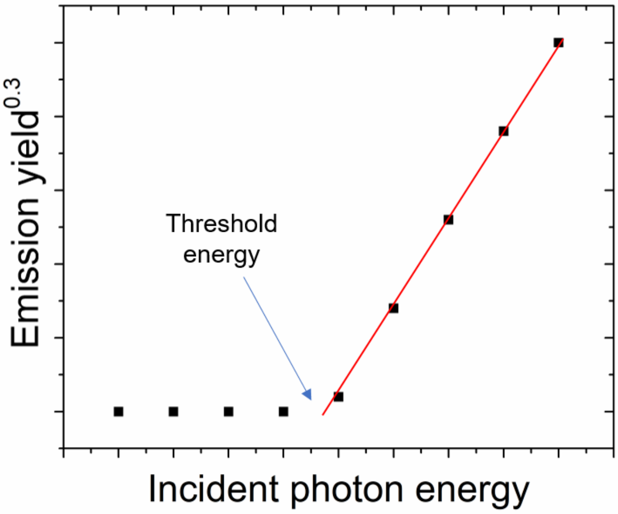

Figure 1.13. Typical plot obtained from PESA with the threshold energy, corresponding to the ionisation potential of the material being studied, indicated.

1.4.3 High Throughput Screening of Photocatalytic Performance

In this thesis, hydrogen evolution rates are typically measured using kinetic runs in which photocatalytic performance is monitored over the course of a number of hours with regular measurement of evolved gases by gas chromatography reliant on manual injections. However, some investigations require multiple photocatalytic experiments to be performed in parallel with a number of parameters varied. In these experiments, sample preparation and measurement of photocatalytic performance can be tedious and time-consuming and therefore limit experimental output.

Experiments can alternatively make use of a recently developed high throughput screening (HTS) approach which utilises automated equipment in order to measure the photocatalytic performance of 48 samples at once.[75] The following HTS workflow will be used in some instances:

1) Samples are weighed into glass vials and placed in a Chemspeed Technologies Sweigher (**Figure 1.14a**).
2) Liquids are then automatically dispensed in inert conditions, before vials are capped and crimped.
3) Samples are then sonicated to ensure dispersion and irradiated using a solar simulator with sedimentation prevented with the use of a rocking and rolling device (**Figure 1.14b**).
4) Evolved gases are finally detected with an automatically injecting gas chromatograph.

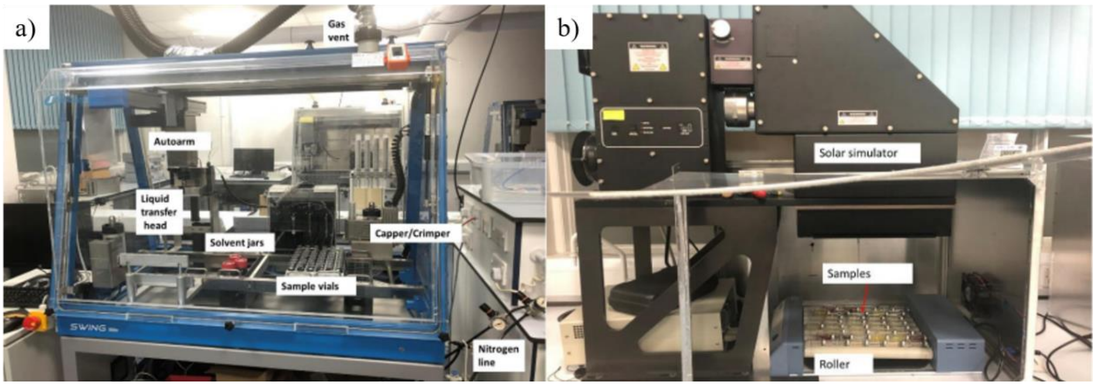

Figure 1.14. Image of **a)** Chemspeed Sweigher for liquid dispension and vial capping and crimping and **b)** solar simulator with rocking and rolling sample holder. Adapted from literature with permission from the author.[75]

1.5 Project Aims

The core aim of this thesis is to prepare solution-processable polymer photocatalysts for the evolution of hydrogen from water. As previously discussed, few examples of solution-processable photocatalysts exist in literature[69,105,153–157] and the potential benefits of dissolution remain largely unexplored.

The appeal of solution-processability is twofold. First, characterisation techniques that require sample solubility can be used to investigate properties and further our understanding of the key factors that determine photocatalytic activity. For example, the molecular weight of solution-processable polymers can be studied using gel permeation chromatography (GPC). Dissolution also enables techniques to study optical properties; molar extinction coefficients can be obtained using polymer solutions while ionisation potentials can be determined by performing PESA on polymer films. Meanwhile, soluble polymers can be straightforwardly characterised by nuclear magnetic resonance (NMR) spectroscopy whereas previous studies in this field have relied on more complex and time-consuming solid state NMR spectroscopy.[129,147,172]

Secondly, solution-processability can enable the morphologies of polymers to be optimised for photocatalytic applications. The vast majority of photocatalytic hydrogen evolution experiments performed to date involve particles suspended in aqueous mixtures.[90] These, often micron-sized,[149] particles are unlikely to be optimised for photocatalytic performance as migration of photogenerated charge carriers in the centre of these particles to the surface is improbable.

Different morphologies may therefore enable more efficient use of photocatalytic materials. For instance, films of TiO_2 were recently found to be 11-12 times more active for hydrogen evolution than the equivalent amount of unprocessed powder.[173] While films[134] and nanoparticles[149] of insoluble polymer photocatalysts have been prepared, solubility would undoubtedly enable more precise control over morphology and it can be no coincidence that the vast majority of polymers used in OPV devices are solution-processable.[138] The crudeness of photocatalytic suspensions is apparent when viewed alongside the latest complex multi-layered OPV devices.[152] Ultimately, the preparation of similarly intricately processed devices that are optimised for overall water splitting is envisaged.

In this study, processability will be afforded by the incorporation of solubilising side-chains into linear polymers. The choice of side-chain has been shown to have a significant impact on the performance of polymers in other electronic applications.[174] In **Chapter 2**, the influence of solubilising side-chains on electronic and physical properties, as well as the photocatalytic activities, of these polymers will be investigated. These will be studied using characterisation techniques, described previously, that are not possible with inorganic systems. The influence of residual palladium and the effect of varying molecular weight on photocatalytic performance will furthermore be investigated.

A further aim of this project is to investigate methods of processing polymers in order to maximise their photocatalytic activities. Inspiration will be taken from the field of OPVs for the preparation of photocatalytically active thin films. The influence of factors such as substrate choice and film thickness will be studied. Other processing methods will also be considered with a view to eventual application. Key requirements for the effective harvesting of solar energy will be identified and used to direct the design of photoreactors based on processable polymers. This work will be detailed in **Chapter 3**.

The processability of the synthesised polymers also enables the facile fabrication of composite materials, which will be explored in **Chapter 4**. Attempts will be made to enhance photocatalytic performance by forming heterojunctions of the most active polymers with inorganic metal oxides. The success of these composite materials will be assessed by comparison of photocatalytic performance with the constituent materials and control composites.

1.6 References

1 J. Newton, *Uncommon Friends: Life with Thomas Edison, Henry Ford, Harvey Firestone, Alexis Carrel & Charles Lindbergh*, Thomson Learning; 1st Harvest/HBJ Ed edition, 1987.

2 The Paris Agreement, 2019 United Nations Framework Convention on Climate Change, Retrieved from https://unfccc.int/process-and-meetings/the-paris-agreement/the-paris-agreement, Date accessed: January 22nd, 2019.

3 BP Energy Outlook 2019 Edition, BP p.l.c. 2019. Retrieved from https://www.bp.com/content/dam/bp/business-sites/en/global/corporate/pdfs/energy-economics/energy-outlook/bp-energy-outlook-2019.pdf, Date accessed: February 16th, 2019.

4 Global Energy & CO2 Status Report, International Energy Agency, Retrieved from https://www.iea.org/geco/, Date accessed: January 6th, 2019.

5 Cédric Philibert, *Solar Energy Perspectives*, Organisation for Economic Co-operation and Development/International Energy Agency, 2011.

6 F. J. de Sisternes, J. D. Jenkins and A. Botterud, *Appl. Energy*, 2016, **175**, 368–379.

7 M. A. Pellow, C. J. M. Emmott, C. J. Barnhart and S. M. Benson, *Energy Environ. Sci.*, 2015, **8**, 1938–1952.

8 S. S. Penner, *Energy*, 2006, **31**, 33–43.

9 J. O. M. Bockris, *Int. J. Hydrogen Energy*, 2002, **27**, 731–740.

10 M. Ball and M. Weeda, *Int. J. Hydrogen Energy*, 2015, **40**, 7903–7919.

11 H2 at Scale: Deeply Decarbonizing our Energy System, Hydrogen and Fuel Cell Technical Advisory Committee, Retrieved from www.hydrogen.energy.gov/pdfs/htac_apr16_10_pivovar.pdf, Date accessed: January 8th 2019.

12 Z. P. Cano, *Nat. Energy*, 2018, **3**, 279–289.

13 C. E. Thomas, *Int. J. Hydrogen Energy*, 2009, **34**, 6005–6020.

14 World premiere: Alstom's hydrogen trains enter passenger service in Lower Saxony, Alstom, Retrieved from https://www.alstom.com/press-releases-news/2018/9/world-premiere-alstoms-hydrogen-trains-enter-passenger-service-lower, Date accessed: February 2nd, 2019.

15 Electric vehicle sales surge in UK as fuel prices rise, BBC News, Retrieved from https://www.bbc.co.uk/news/business-45419705, Date accessed: January 23rd, 2019.

16 C. E. Thomas, *Int. J. Hydrogen Energy*, 2009, **34**, 6005–6020.

17 Toyota and Kenworth Collaborate To Develop Zero Emission Trucks, Toyota Motor Corporation, Retrieved from https://pressroom.toyota.com/toyota-kenworth-collaborate-develop-zero-emission-trucks/, Date accessed: January 17th, 2019.

18 Anheuser-Busch Continues Leadership in Clean Energy, Places Order for 800 Hydrogen-Electric Powered Semi-Trucks with Nikola Motor CompanyNikola Corporation, Retrieved from https://nikolamotor.com/press_releases/anheuser-busch-continues-leadership-in-clean-energy-places-order-for-800-hydrogen-electric-powered-semi-trucks-with-nikola-motor-company-23, Date accessed March 17th 2019.

19 G. Marbán and T. Valdés-Solís, *Int. J. Hydrogen Energy*, 2007, **32**, 1625–1637.

20 J. Ren, N. M. Musyoka, H. W. Langmi, M. Mathe and S. Liao, *Int. J. Hydrogen Energy*,

2016, **42**, 289–311.

21 Port of Los Angeles preliminarily awarded $41 million from California air resources board to launch zero emissions hydrogen-fuel-cell-electric freight project. https://www.portoflosangeles.org/references/news_091418_carb_toyota, Date accessed: February 4th 2019.

22 R. A. M. Ramachandran, *Int. J. Hydrogen Energy*, 1998, **23**, 593–598.

23 W. C. Lattin and V. P. Utgikar, 2007, **32**, 3230–3237.

24 B. Viswanathan, *Energy sources: Fundamentals of chemical conversion processes and applications*, Newnes, 2017.

25 M. Kauw, R. M. J. Benders and C. Visser, *Energy*, 2015, **90**, 208–217.

26 M. Halper, *Renew. Energy Focus*, 2011, **12**, 56–58.

27 B. C. R. Ewan and R. W. K. Allen, *Int. J. Hydrogen Energy*, 2005, **30**, 809–819.

28 I. Dincer and C. Acar, *Int. J. Hydrogen Energy*, 2015, **40**, 11094–11111.

29 P. Nikolaidis and A. Poullikkas, *Renew. Sustain. Energy Rev.*, 2017, **67**, 597–611.

30 T. Uekert, M. F. Kuehnel, D. W. Wakerley and E. Reisner, *Energy Environ. Sci.*, 2018, **11**, 2853–2857.

31 T. da Silva Veras, T. S. Mozer, D. da Costa Rubim Messeder dos Santos and A. da Silva César, *Int. J. Hydrogen Energy*, 2017, **42**, 2018–2033.

32 R. M. Navarro, M. A. Peña and J. L. G. Fierro, *Chem. Rev.*, 2007, **107**, 3952–3991.

33 J. D. Holladay, J. Hu, D. L. King and Y. Wang, *Catal. Today*, 2009, **139**, 244–260.

34 H. Balat and E. Kirtay, *Int. J. Hydrogen Energy*, 2010, **35**, 7416–7426.

35 N. Z. Muradov and T. N. Veziroğlu, *Int. J. Hydrogen Energy*, 2005, **30**, 225–237.

36 Hydrogen Production: Biomass Gasification, United States Department of Energy, Retrieved from https://www.energy.gov/eere/fuelcells/hydrogen-production-biomass-gasification, Date accessed: January 18th, 2019.

37 M. Ni, D. Y. C. Leung, M. K. H. Leung and K. Sumathy, *Fuel Process. Technol.*, 2006, **87**, 461–472.

38 M. K. Lam and K. T. Lee, *Biohydrogen Production from Algae*, Elsevier B.V., 1st edn., 2013.

39 C. Ding, K. L. Yang and J. He, *Biological and fermentative production of hydrogen*, Elsevier Ltd, 2016.

40 K. Y. Show and D. J. Lee, *Bioreactor and Bioprocess Design for Biohydrogen Production*, Elsevier BV., 1st edn., 2013.

41 Toyota to Build the World's First Megawatt-Scale 100% Renewable Power and Hydrogen Generation Station, Toyotta Motor Corporation, Retrieved from https://global.toyota/en/newsroom/corporate/20132821.html, Date accessed: 17th January 2019.

42 R. M. Navarro Yerga, M. C. Alvarez-Galván, F. Vaquero, J. Arenales and J. L. G. Fierro, *Renew. Hydrog. Technol. Prod. Purification, Storage, Appl. Saf.*, 2013, 43–61.

43 R. R. Bhosale, A. Kumar and P. Sutar, *Energy Convers. Manag.*, 2017, **135**, 226–235.

44 Hydrogen Production: Thermochemical Water Splitting, United States Department of

Energy, Retrieved from https://www.energy.gov/eere/fuelcells/hydrogen-production-thermochemical-water-splitting, Date accessed: January 14th, 2019.

45 R. Singh and S. Dutta, *Fuel*, 2018, **220**, 607–620.

46 G. Glenk and S. Reichelstein, *Nat. Energy*, 2019, **4**, 216–222.

47 A. Fujishima and K. Honda, *Nature*, 1972, **238**, 37–38.

48 V. M. Aroutiounian, V. M. Arakelyan and G. E. Shahnazaryan, *Sol. Energy*, 2005, **78**, 581–592.

49 M. Ahmed and I. Dincer, *Int. J. Hydrogen Energy*, 2019, **44**, 2474–2507.

50 W. H. Cheng, M. H. Richter, M. M. May, J. Ohlmann, D. Lackner, F. Dimroth, T. Hannappel, H. A. Atwater and H. J. Lewerenz, *ACS Energy Lett.*, 2018, **3**, 1795–1800.

51 J. Jia, L. C. Seitz, J. D. Benck, Y. Huo, Y. Chen, J. W. D. Ng, T. Bilir, J. S. Harris and T. F. Jaramillo, *Nat. Commun.*, 2016, **7**, 1–6.

52 T. J. Jacobsson, *Energy Environ. Sci.*, 2018, **11**, 1977–1979.

53 B. A. Pinaud, J. D. Benck, L. C. Seitz, A. J. Forman, Z. Chen, T. G. Deutsch, B. D. James, K. N. Baum, G. N. Baum, S. Ardo, H. Wang, E. Miller and T. F. Jaramillo, *Energy Environ. Sci.*, 2013, **6**, 1983–2002.

54 M. Bowker, *Green Chem.*, 2011, **13**, 2235–2246.

55 P. V Kamat, *Acc. Chem. Res.*, 2017, **50**, 527–531.

56 P. Kumar, R. Boukherroub and K. Shankar, *J. Mater. Chem. A*, 2018, **6**, 12876–12931.

57 K. Maeda, *ACS Catal.*, 2013, **3**, 1486–1503.

58 S. Sun, T. Hisatomi, Q. Wang, S. Chen, G. Ma, J. Liu, S. Nandy, T. Minegishi, M. Katayama and K. Domen, *ACS Catal.*, 2018, **8**, 1690–1696.

59 T. Jafari, E. Moharreri, A. S. Amin, R. Miao, W. Song and S. L. Suib, *Molecules*, 2016, **21**, 900.

60 K. Takanabe, *ACS Catal.*, 2017, **7**, 8006–8022.

61 P. Guiglion, C. Butchosa and M. A. Zwijnenburg, *Macromol. Chem. Phys.*, 2016, **217**, 344–353.

62 G. Zhang, G. Li, Z.-A. Lan, L. Lin, A. Savateev, T. Heil, S. Zafeiratos, X. Wang and M. Antonietti, *Angew. Chemie Int. Ed.*, 2017, **56**, 13445–13449.

63 L. Samiolo, M. Valigi, D. Gazzoli and R. Amadelli, *Electrochim. Acta*, 2010, **55**, 7788–7795.

64 C. A. Bignozzi, *Topics in Current Chemistry: Photocatalysis*, Springer-Verlag Berlin Heidelberg, 2011.

65 K. Maeda, K. Teramura, D. Lu, N. Saito, Y. Inoue and K. Domen, *Angew. Chemie - Int. Ed.*, 2006, **45**, 7806–7809.

66 L. Yao, A. Rahmanudin, N. Guijarro and K. Sivula, *Adv. Energy Mater.*, 2018, **8**, 1802585.

67 Y. Pellegrin and F. Odobel, *Comptes Rendus Chim.*, 2017, **20**, 283–295.

68 M. Wang, S. Shen, L. Li, Z. Tang and J. Yang, *J. Mater. Sci.*, 2017, **52**, 5155–5164.

69 S. Matsuoka, H. Fujii, T. Yamada, C. Pac, A. Ishida, S. Takamuku, M. Kusaba, N. Nakashima and S. Yanagida, *J. Phys. Chem.*, 1991, **95**, 5802–5808.

70 S. Chen, T. Takata and K. Domen, *Nat. Rev. Mater.*, 2017, **2**, 17050.

71 A. G. Slater and A. I. Cooper, *Science (80-.).*, 2015, **348**, 8075.

72 D. J. Woods, R. S. Sprick, C. L. Smith, A. J. Cowan and A. I. Cooper, *Adv. Energy Mater.*, 2017, **7**, 1700479.

73 R. Sebastian Sprick, Y. Bai, A. A. Y Guilbert, M. Zbiri, C. M. Aitchison, L. Wilbraham, Y. Yan, D. J. Woods, M. A. Zwijnenburg and A. I. Cooper, *Chem. Mater.*, 2018, **31**, 305–313.

74 M. Sachs, R. S. Sprick, D. Pearce, S. A. J. Hillman, A. Monti, A. A. Y. Guilbert, N. J. Brownbill, S. Dimitrov, X. Shi, F. Blanc, M. A. Zwijnenburg, J. Nelson, J. R. Durrant and A. I. Cooper, *Nat. Commun.*, 2018, **9**, 4968.

75 Y. Bai, L. Wilbraham, B. J. Slater, M. A. Zwijnenburg, R. S. Sprick and A. I. Cooper, *J. Am. Chem. Soc.*, 2019, **141**, 9063–9071.

76 D. M. Fabian, S. Hu, N. Singh, F. A. Houle, T. Hisatomi, K. Domen, F. E. Osterloh and S. Ardo, *Energy Environ. Sci.*, 2015, **8**, 2825–2850.

77 Z. Wang, C. Li and K. Domen, *Chem. Soc. Rev.*, 2019, **48**, 2109–2125.

78 X. Chen, S. Shen, L. Guo and S. S. Mao, *Chem. Rev.*, 2010, **110**, 6503–6570.

79 J. Xing, W. Q. Fang, H. J. Zhao and H. G. Yang, *Chem. - An Asian J.*, 2012, **7**, 642–657.

80 F. E. Osterloh, *Chem. Soc. Rev.*, 2013, **42**, 2294–2320.

81 D. E. Scaife, *Sol. Energy*, 1980, **25**, 41–54.

82 R. Abe, *J. Photochem. Photobiol. C Photochem. Rev.*, 2010, **11**, 179–209.

83 D. O. Scanlon, C. W. Dunnill, J. Buckeridge, S. A. Shevlin, A. J. Logsdail, S. M. Woodley, C. R. A. Catlow, M. J. Powell, R. G. Palgrave, I. P. Parkin, G. W. Watson, T. W. Keal, P. Sherwood, A. Walsh and A. A. Sokol, *Nat. Mater.*, 2013, **12**, 798–801.

84 Z. Jiang, Z. Zhang, W. Shangguan, M. A. Isaacs, L. J. Durndell, C. M. A. Parlett and A. F. Lee, *Catal. Sci. Technol.*, 2016, **6**, 81–88.

85 D. Wang, Z.-P. Liu and W.-M. Yang, *ACS Catal.*, 2018, 7270–7278.

86 S. Rajaambal, K. Sivaranjani and C. S. Gopinath, *J. Chem. Sci.*, 2015, **127**, 33–47.

87 P. Kalisman, Y. Nakibli and L. Amirav, *Nano Lett.*, 2016, **16**, 1776−1781.

88 G. N. Schrauzer and T. D. Guth, *J. Am. Chem. Soc.*, 1977, **99**, 7189–7193.

89 Q. Wang, T. Hisatomi, Q. Jia, H. Tokudome, M. Zhong, C. Wang, Z. Pan, T. Takata, M. Nakabayashi, N. Shibata, Y. Li, I. D. Sharp, A. Kudo, T. Yamada and K. Domen, *Nat. Mater.*, 2016, **15**, 611–615.

90 T. Takata and K. Domen, *ACS Energy Lett.*, 2019, **4**, 542–549.

91 Z. Wang, Y. Inoue, T. Hisatomi, R. Ishikawa, Q. Wang, T. Takata, S. Chen, N. Shibata, Y. Ikuhara and K. Domen, *Nat. Catal.*, 2018, **1**, 756–763.

92 A. J. Bard, *J. Photochem.*, 1979, **10**, 59–75.

93 Y. Sasaki, *J. Phys. Chem. C*, 2009, **113**, 17536–17542.

94 T. Minegishi, H. Nishiyama, T. Hisatomi, M. Yoshida, H. Lyu, M. Katayama, K. Domen, Y. Goto, K. Asakura, Y. Sakata, T. Yamada, T. Higashi and T. Takata, *Chem. Sci.*, 2019, 3196–3201.

95 J. Hassan, M. Sévignon, C. Gozzi, E. Schulz and M. Lemaire, *Chem. Rev.*, 2002, **102**,

1359–1469.

96 P. Guiglion, C. Butchosa and M. A. Zwijnenburg, *J. Mater. Chem. A*, 2014, **2**, 11996.

97 P. Guiglion, C. Butchosa and M. A. Zwijnenburg, *Macromol. Chem. Phys.*, 2016, **217**, 344–353.

98 S. Shoaee, M. Stolterfoht and D. Neher, *Adv. Energy Mater.*, 2018, **8**, 1703355.

99 C. Butchosa, P. Guiglion and M. A. Zwijnenburg, *J. Phys. Chem. C*, 2014, **118**, 24833–24842.

100 X. Wang, K. Maeda, A. Thomas, K. Takanabe, G. Xin, J. M. Carlsson, K. Domen and M. Antonietti, *Nat. Mater.*, 2009, **8**, 76–80.

101 W.-J. Ong, L.-L. Tan, Y. H. Ng, S.-T. Yong and S.-P. Chai, *Chem. Rev.*, 2016, **116**, 7159–7329.

102 S. Cao, J. Low, J. Yu and M. Jaroniec, *Adv. Mater.*, 2015, **27**, 2150–2176.

103 L. Lin, Z. Yu and X. Wang, *Angew. Chemie - Int. Ed.*, 2019, **58**, 2–14.

104 G. Zhang, L. Lin, G. Li, Y. Zhang, A. Savateev, S. Zafeiratos, X. Wang and M. Antonietti, *Angew. Chemie Int. Ed.*, 2018, **57**, 9372–9376.

105 G. Zhang, Z.-A. Lan, L. Lin, S. Lin and X. Wang, *Chem. Sci.*, 2016, **7**, 3062–3066.

106 L. Lin, C. Wang, W. Ren, H. Ou, Y. Zhang and X. Wang, *Chem. Sci.*, 2017, **8**, 5506–5511.

107 H. Yan and H. Yang, *J. Alloys Compd.*, 2011, **509**, 26–29.

108 H. Wang, L. Zhang, Z. Chen, J. Hu, S. Li, Z. Wang, J. Liu and X. Wang, *Chem. Soc. Rev.*, 2014, **43**, 5234.

109 D. Ma, J. Wu, Y. Xin, Y. Sun, T. Ma and M. Gao, *Chem. Eng. J.*, 2016, **290**, 136–146.

110 X. Zhao, J. Yu, H. Cui and T. Wang, *J. Photochem. Photobiol. A Chem.*, 2017, **335**, 130–139.

111 W. Yu, J. Chen, T. Shang, L. Chen, L. Gu and T. Peng, *Appl. Catal. B Environ.*, 2017, **219**, 693–704.

112 Y. Tan, Z. Shu, J. Zhou, T. Li, W. Wang and Z. Zhao, *Appl. Catal. B Environ.*, 2018, **230**, 260–268.

113 J. Liu, Y. Liu, N. Liu, Y. Han, X. Zhang, H. Huang, Y. Lifshitz, S.-T. Lee, J. Zhong and Z. Kang, *Science (80-.).*, 2015, **347**, 970–974.

114 S. A. Shevlin and Z. X. Guo, *Chem. Mater.*, 2016, **28**, 7250–7256.

115 J. Tang, C. Pan, G. Yu, W. Zhang and C. Xu, *Front. Chem.*, 2018, **6**, 1–12.

116 J. X. Jiang, F. Su, A. Trewin, C. D. Wood, N. L. Campbell, H. Niu, C. Dickinson, A. Y. Ganin, M. J. Rosseinsky, Y. Z. Khimyak and A. I. Cooper, *Angew. Chemie - Int. Ed.*, 2007, **46**, 8574–8578.

117 A. I. Cooper, *Adv. Mater.*, 2009, **21**, 1291–1295.

118 Y. Xu, S. Jin, H. Xu, A. Nagai and D. Jiang, *Chem. Soc. Rev.*, 2013, **42**, 8012–8031.

119 J. X. Jiang, F. Su, A. Trewin, C. D. Wood, H. Niu, J. T. A. Jones, Y. Z. Khimyak and A. I. Cooper, *J. Am. Chem. Soc.*, 2008, **130**, 7710–7720.

120 J. Brandt, J. Schmidt, A. Thomas, J. D. Epping and J. Weber, *Polym. Chem.*, 2011, **2**, 1950–1952.

121 J. X. Jiang, A. Trewin, D. J. Adams and A. I. Cooper, *Chem. Sci.*, 2011, **2**, 1777–1781.

122 R. S. Sprick, J.-X. Jiang, B. Bonillo, S. Ren, T. Ratvijitvech, P. Guiglion, M. A. Zwijnenburg, D. J. Adams and A. I. Cooper, *J. Am. Chem. Soc.*, 2015, **137**, 3265–3270.

123 X. H. Zhang, X. P. Wang, J. Xiao, S. Y. Wang, D. K. Huang, X. Ding, Y. G. Xiang and H. Chen, *J. Catal.*, 2017, **350**, 64–71.

124 L. Wang, Y. Wan, Y. Ding, S. Wu, Y. Zhang, X. Zhang, G. Zhang, Y. Xiong, X. Wu, J. Yang and H. Xu, *Adv. Mater.*, 2017, 1702428.

125 V. S. Vyas, V. W. Lau and B. V Lotsch, *Chem. Mater.*, 2016, **28**, 5191–5204.

126 M. G. Schwab, M. Hamburger, X. Feng, J. Shu, H. W. Spiess, X. Wang, M. Antonietti and K. Müllen, *Chem. Commun.*, 2010, **46**, 8932–8934.

127 J. Bi, W. Fang, L. Li, J. Wang, S. Liang, Y. He, M. Liu and L. Wu, *Macromol. Rapid Commun.*, 2015, **36**, 1799–1805.

128 C. B. Meier, R. S. Sprick, A. Monti, P. Guiglion, J.-S. M. Lee, M. A. Zwijnenburg and A. I. Cooper, *Polymer (Guildf).*, 2017, **126**, 283–290.

129 K. Schwinghammer, S. Hug, M. B. Mesch, J. Senker and B. V Lotsch, *Energy Environ. Sci.*, 2015, **8**, 3345–3353.

130 J. Xie, S. A. Shevlin, Q. Ruan, S. J. A. Moniz, Y. Liu, X. Liu, Y. Li, C. C. Lau, Z. X. Guo and J. Tang, *Energy Environ. Sci.*, 2018, **11**, 1617–1624.

131 V. S. Vyas, F. Haase, L. Stegbauer, G. Savasci, F. Podjaski, C. Ochsenfeld and B. V Lotsch, *Nat. Commun.*, 2015, **6**, 8508.

132 N. W. Ockwig, A. P. Co, M. O. Keeffe, A. J. Matzger and O. M. Yaghi, 2005, **310**, 1166–1171.

133 T. Banerjee, F. Haase, G. Savasci, K. Gottschling, C. Ochsenfeld and B. V. Lotsch, *J. Am. Chem. Soc.*, 2017, **139**, 16228–16234.

134 X. Wang, L. Chen, S. Y. Chong, M. A. Little, Y. Wu, W.-H. Zhu, R. Clowes, Y. Yan, M. A. Zwijnenburg, R. Sebastian Sprick and A. I. Cooper, *Nat. Chem.*, 2018, **10**, 1180.

135 H. Wang, Z. Zeng, P. Xu, L. Li, G. Zeng, R. Xiao, Z. Tang, D. Huang, L. Tang, C. Lai, D. Jiang, Y. Liu, H. Yi, L. Qin, S. Ye, X. Ren and W. Tang, *Chem. Soc. Rev.*, 2019, **48**, 488–516.

136 N. Chaoui, M. Trunk, R. Dawson, J. Schmidt and A. Thomas, *Chem. Soc. Rev.*, 2017, **46**, 3302–3321.

137 S. Yanagida, A. Kabumoto, K. Mizumoto, C. Pac and K. Yoshino, *J. Chem. Soc. Chem. Commun.*, 1985, 474–475.

138 L. Dou, J. You, Z. Hong, Z. Xu, G. Li, R. A. Street and Y. Yang, *Adv. Mater.*, 2013, **25**, 6642–6671.

139 H. Kajii, K. Koiwai, Y. Hirose and Y. Ohmori, *Org. Electron. physics, Mater. Appl.*, 2010, **11**, 509–513.

140 X. Guo, M. Baumgarten and K. Müllen, *Prog. Polym. Sci.*, 2013, **38**, 1832–1908.

141 C. Yang, B. C. Ma, L. Zhang, S. Lin, S. Ghasimi, K. Landfester, K. A. I. Zhang and X. Wang, *Angew. Chemie - Int. Ed.*, 2016, **55**, 9202–9206.

142 M. Schwarze, D. Stellmach, M. Schröder, K. Kailasam, R. Reske, A. Thomas and R. Schomäcker, *Phys. Chem. Chem. Phys.*, 2013, **15**, 3466.

143 R. S. Sprick, C. M. Aitchison, E. Berardo, L. Turcani, L. Wilbraham, B. M. Alston, K. E.

Jelfs, M. A. Zwijnenburg and A. I. Cooper, *J. Mater. Chem. A*, 2018, **6**, 11994–12003.

144 X. Zong, X. Miao, S. Hua, L. An, X. Gao, W. Jiang, D. Qu, Z. Zhou, X. Liu and Z. Sun, *Appl. Catal. B Environ.*, 2017, **211**, 98–105.

145 R. S. Sprick, L. Wilbraham, Y. Bai, P. Guiglion, A. Monti, R. Clowes, A. I. Cooper and M. A. Zwijnenburg, *Chem. Mater.*, 2018, **30**, 5733–5742.

146 Z. Wang, N. Mao, Y. Zhao, T. Yang, F. Wang and J.-X. Jiang, *Polym. Bull.*, 2019, **76**, 3195–3206.

147 R. S. Sprick, B. Bonillo, R. Clowes, P. Guiglion, N. J. Brownbill, B. J. Slater, F. Blanc, M. A. Zwijnenburg, D. J. Adams and A. I. Cooper, *Angew. Chemie - Int. Ed.*, 2016, **55**, 1792–1796.

148 M. Sachs, R. S. Sprick, D. Pearce, S. J. Hillman, A. Monti, A. A. Y. Guilbert, N. J. Brownbill, S. Dimitrov, F. Blanc, M. A. Zwijnenburg, J. Nelson, J. R. Durrant and A. I. Cooper, *Nat. Commun.*, 2018, **9**, 4968.

149 C. M. Aitchison, R. S. Sprick and A. I. Cooper, *J. Mater. Chem. A*, 2019, 37–39.

150 G. Cheng, T. Hasell, A. Trewin, D. J. Adams and A. I. Cooper, *Angew. Chemie - Int. Ed.*, 2012, **51**, 12727–12731.

151 J. Mei and Z. Bao, *Chem. Mater.*, 2014, **26**, 604–615.

152 M. Li, K. Gao, X. Wan, Q. Zhang, B. Kan, R. Xia, F. Liu, X. Yang, H. Feng, W. Ni, Y. Wang, J. Peng, H. Zhang, Z. Liang, H. L. Yip, X. Peng, Y. Cao and Y. Chen, *Nat. Photonics*, 2017, **11**, 85–90.

153 P. B. Pati, G. Damas, L. Tian, D. Fernandes, L. Zhang, I. B. Pehlivan, T. Edvinsson, C. M. Araujo and H. Tian, *Energy Environ. Sci.*, 2017, **10**, 1372–1376.

154 A. Liu, C.-W. Tai, K. Holà and H. Tian, *J. Mater. Chem. A*, 2019, **7**, 4797–4803.

155 Z. Hu, Z. Wang, X. Zhang, H. Tang, X. Liu, F. Huang and Y. Cao, *iScience*, 2019, **13**, 33–42.

156 X. Zhang, F. Shen, Z. Hu, Y. Wu, H. Tang, J. Jia, X. Wang, F. Huang and Y. Cao, *ACS Sustain. Chem. Eng.*, 2019, **7**, 4128–4135.

157 J. Kosco, M. Sachs, R. Godin, M. Kirkus, L. Francas, M. Bidwell, M. Qureshi, D. Anjum, J. R. Durrant and I. McCulloch, *Adv. Energy Mater.*, 2018, **8**, 1802181.

158 C. Dai, M. Panahandeh-Fard, X. Gong, C. Xue and B. Liu, *Sol. RRL*, 2018, **3**, 1800255.

159 Z. Hu, X. Zhang, Q. Yin, X. Liu, X. fang Jiang, Z. Chen, X. Yang, F. Huang and Y. Cao, *Nano Energy*, 2019, **60**, 775–783.

160 H. Ohkita and S. Ito, *Polymer (Guildf).*, 2011, **52**, 4397–4417.

161 J. Rawson, P. J. Angiolillo and M. J. Therien, *Proc. Natl. Acad. Sci.*, 2015, **112**, 13779–13783.

162 F. Etzold, I. A. Howard, R. Mauer, M. Meister, T. D. Kim, K. S. Lee, N. S. Baek and F. Laquai, *J. Am. Chem. Soc.*, 2011, **133**, 9469–9479.

163 A. Maciejewski, R. Naskrecki, M. Lorenc, M. Ziolek, J. Karolczak, J. Kubicki, M. Matysiak and M. Szymanski, *J. Mol. Struct.*, 2000, **555**, 1–13.

164 U. B. Cappel, E. A. Gibson, A. Hagfeldt and G. Boschloo, *J. Phys. Chem. C*, 2009, **113**, 6275–6281.

165 W. Kaim and J. Fiedler, *Chem. Soc. Rev.*, 2009, **38**, 3373–3382.

166 M.Uda, *Jpn. J. Appl. Phys.*, 1985, **24**, 284.

167 R. J. Davis, M. T. Lloyd, S. R. Ferreira, M. J. Bruzek, S. E. Watkins, L. Lindell, P. Sehati, M. Fahlman, J. E. Anthony and J. W. P. Hsu, *J. Mater. Chem.*, 2011, **21**, 1721–1729.

168 A. Kahn, *Mater. Horiz.*, 2016, **3**, 7–10.

169 K. N. Winzenberg, P. Kemppinen, G. Fanchini, M. Bown, G. E. Collis, C. M. Forsyth, K. Hegedus, T. B. Singh and S. E. Watkins, *Chem. Mater.*, 2009, **21**, 5701–5703.

170 W. Zhang, J. Smith, R. Hamilton, M. Heeney, J. Kirkpatrick, K. Song, S. E. Watkins, T. Anthopoulos and I. McCulloch, *J. Am. Chem. Soc.*, 2009, **131**, 10814–10815.

171 H. Kirihata and M. Uda, *Rev. Sci. Instrum.*, 1981, **52**, 68–70.

172 K. Schwinghammer, M. B. Mesch, V. Duppel, C. Ziegler, J. Senker and B. V. Lotsch, *J. Am. Chem. Soc.*, 2014, **136**, 1730–1733.

173 N. Nalajala, K. K. Patra, P. A. Bharad and C. S. Gopinath, *RSC Adv.*, 2019, **9**, 6094–6100.

174 L. Yang, H. Zhou and W. You, *J. Phys. Chem. C*, 2010, **114**, 16793–16800.

175 C. Huang, J. Wen, Y. Shen, F. He, L. Mi, Z. Gan, J. Ma, S. Liu, H. Ma and Y. Zhang, *Chem. Sci.*, 2018, **9**, 7912–7915.

Chapter 2

Solution-Processable Polymer Photocatalysts

2.1. Contributions to this Chapter

All polymers were prepared by the thesis author except **FP-Hex**, **FP-EtHex**, **FP-Oct**, **FP-Dodec**, **FS-EtHex**, **FS-Oct**, **FS-Dodec**, **PFO** and **FS-1-5** polymers, which were prepared and characterised by Dr Reiner Sebastian Sprick. Dr Sprick also measured EQE for **FS-TEG** and nitrogen sorption for all polymers. SEM images were captured by Catherine Aitchison. TAS experiments in **Chapter 2.1.4** were performed by Charlotte Smith. All other TAS experiments were carried out by Sam Hillman who also performed AFM on the polymer films. QCM measurements were undertaken by Lucas Flagg. MD simulations were performed by Drew Pearce. Water sorption was measured by Rob Clowes. (TD)-DFT calculations were performed by Dr Liam Wilbraham and Dr Martijn Zwijenberg. PESA measurements were carried out by Dr Warren Duffy and Dr Jan Kosco.

2.2. Introducing Solubility in Carbazole-Phenylene Polymer Photocatalysts

An initial investigation was performed to probe the suitability of solution-processable polymers for photocatalytic hydrogen evolution. The polymer was based on the previously reported polymer (poly[(9*H*-carbazole-2,7-diyl)-1,4-phenylene]) (**P4**, **Table 2.1**) as it was shown to be photocatalytically active but not appreciably soluble in any common organic solvent.[1] Furthermore, the carbazole nitrogen in **P4** offers scope for alkylation to produce soluble analogues without disruption of the conjugated backbone. It was anticipated that solubility in organic solvents would be enabled by the addition of the 2-ethylhexyl side-chain, yielding the polymer **P8**. This side-chain was selected as branched alkyl chains generally afford greater solubility enhancements relative to equivalent linear chains.[2]

2.2.1 Synthesis

Polymer **P8** was synthesised *via* Suzuki–Miyaura polycondensation of 1,4-benzenediboronic acid bis(pinacol) ester and 2,7-dibromo-9-(2-ethylhexyl)-9*H*-carbazole, which was prepared using a literature procedure[3] (**Figure 2.1**). After 48 hours at 80 °C, the reaction mixture was extracted with toluene and the organic products were purified by Soxhlet extractions in methanol, acetone, and ethyl acetate to remove more polar unreacted monomers and low molecular weight by-products. A chloroform-soluble fraction of the 2-ethylhexyl-substituted polymer, **P8-s**, was then recovered by antisolvent precipitation from chloroform in methanol. A chloroform-insoluble fraction of the polymer, **P8-i**, was also obtained.

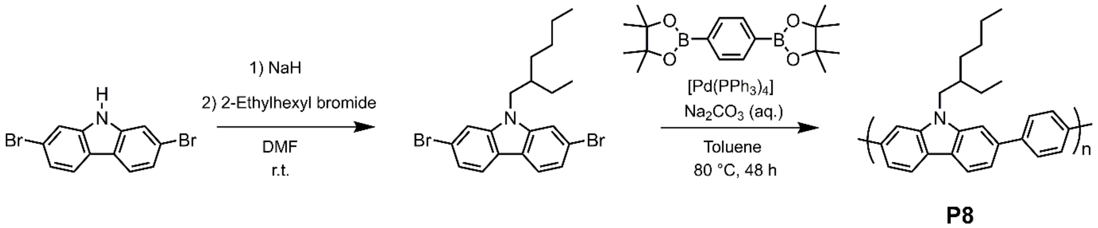

Figure 2.1. Stynthetic route to 2,7-dibromo-9-(2-ethylhexyl)-9H-carbazole monomer and polymerisation of **P8**.

The yields of **P8-s** and **P8-i** (9% and 84% respectively) indicate that a sole 2-ethylhexyl side-chain is not sufficient to afford appreciable solubility to this carbazole-phenylene co-polymer. Nevertheless, the partial solubility of **P8** enables a useful comparison of a solution-processable alkyl-substituted polymer (**P8-s**) with an insoluble substituted analogue (**P8-i**) as well as an unsubstituted insoluble analogue (**P4**) (**Table 2.1**).

Table 2.1. Structure of **P4**, **P8-s** and **P8-i** where **P8-s** is the soluble fraction obtained from Soxhlet extraction with chloroform.

Polymer	**P4**	**P8-s**	**P8-i**
Structure	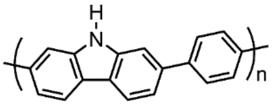	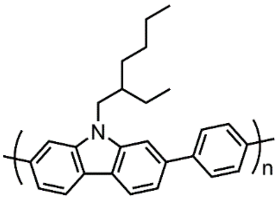	
Solubility in $CHCl_3$	✗	✓	✗

2.2.2 Characterisation

Fourier-transform infrared spectroscopy (FT-IR) demonstrated the presence of the expected alkyl C-H stretching signals (2800-3000 cm^{-1}) for both **P8-i** and **P8-s** (**Figure 2.2a**) while the unsubstituted carbazole N-H stretching signal that is present in the spectra of **P4** (3400-3500 cm^{-1}) was absent. In fact, the FT-IR spectra of **P8-i** and **P8-s** appear to be essentially identical suggesting that they have analogous structures and the difference in solubility may be attributed to differences in molecular weight. The solubility of **P8-s** allowed further characterisation of the polymer using ^{1}H NMR spectroscopy (**Figure 2.2b)**. This spectrum shows the aliphatic protons of the 2-ethylhexyl side-chain (1.4-1.7 ppm) as well as the aromatic signals (7.7-8.1 ppm) in the expected ratio. The molecular weight of **P8-s** was determined to be M_n = 1500 g mol^{-1} (M_w = 2100 g mol^{-1}, $Đ$ = 1.4) by performing gel permeation chromatography (GPC) calibrated against polystyrene standards. This corresponds to a chain length of approximately four repeating units (or eight monomer units).

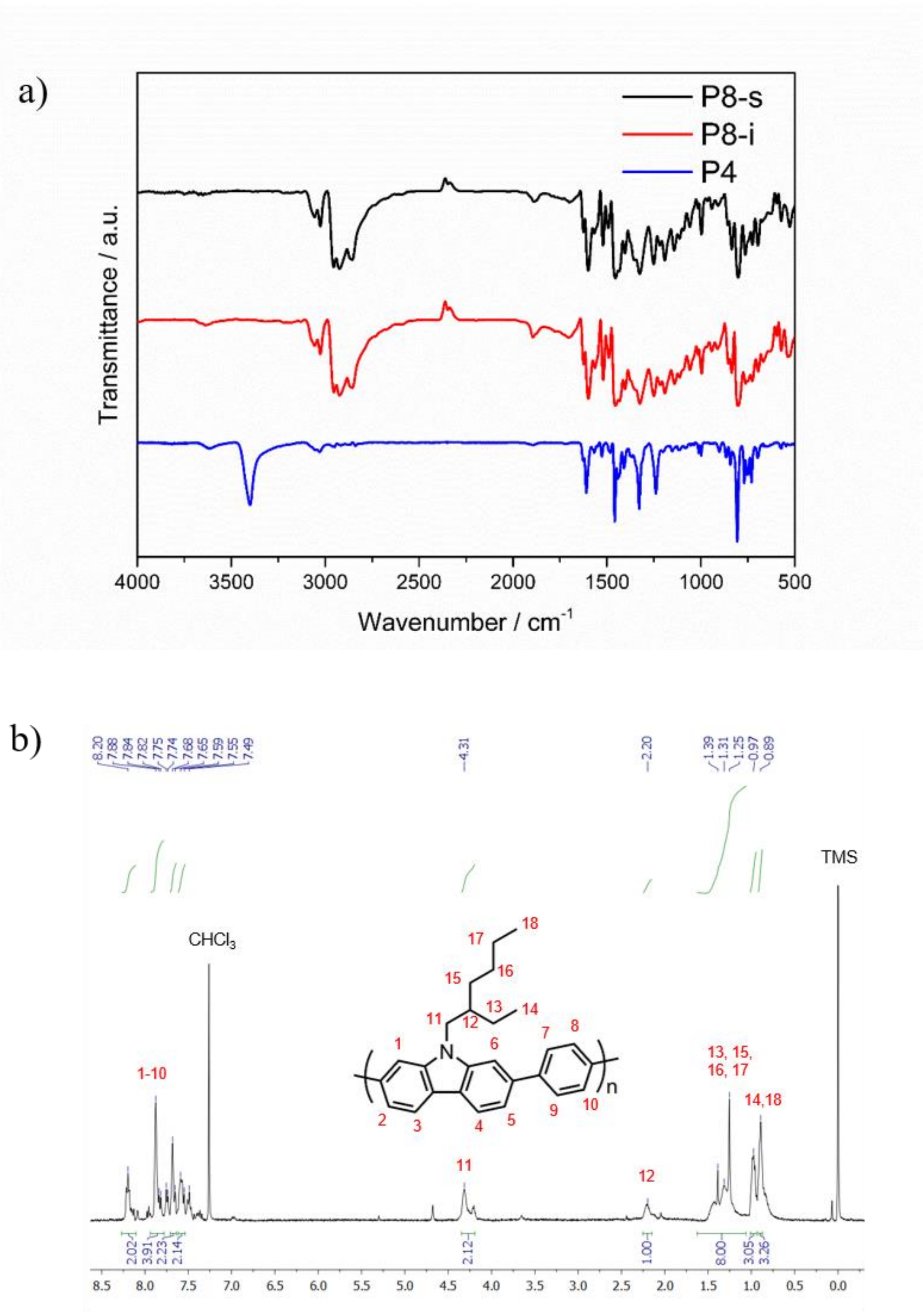

Figure 2.2 a) FT-IR spectrum of **P8-s**, **P8-i** and **P4**. **b)** ^{1}H NMR spectrum of **P8-s** in CDCl$_3$.

The optoelectronic properties of powdered polymers were studied by UV-vis and photoluminescence (PL) spectroscopy (**Figure 2.3a** and **b**). The absorption on-sets of **P8-s** and **P8-i** (2.71 and 2.77 eV respectively) are very similar to **P4** (2.72 eV). All polymers also exhibit similar emission profiles (λ_{em} = 465, 455 and 451 nm for **P4**, **P8-s** and **P8-i** respectively).

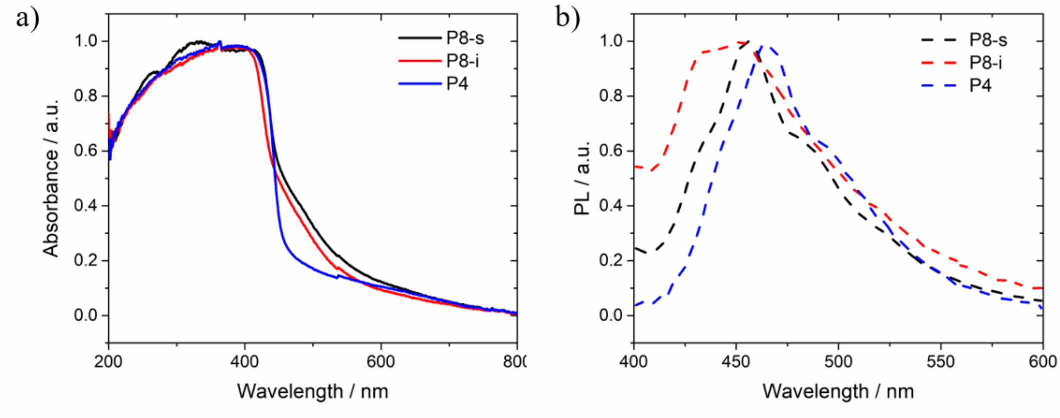

Figure 2.3 a) UV-vis and **b)** photoluminescence (PL) spectra of **P8-s**, **P8-i** and **P4** powders (λ_{exc} = 360 nm).

The solubility of **P8-s** enabled its optical properties to be studied in solution and cast as a film on a glass substrate (**Figure 2.4**). The UV-visible spectra of the **P8-s** film and powder are similar, as expected, with optical gaps of 2.79 and 2.71 eV respectively. The absorption profile of the polymer is significantly blue shifted in solution due to the loss of π-π stacking between polymer chains.[4] Similarly, the PL maxima of the polymer in solution (λ_{em} = 407 nm) is blue shifted compared to the film and powder (λ_{em} = 430 nm and 455 nm respectively).

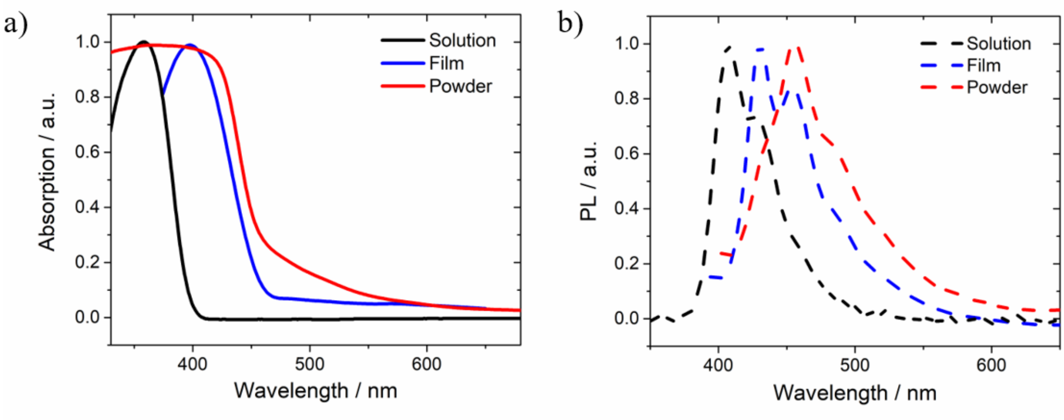

Figure 2.4 a) UV-vis and **b)** PL spectra of **P8-s** dissolved in chloroform, cast as a film and as a powder (λ_{exc} = 360 nm).

The powder X-ray diffraction (PXRD) patterns of ground samples of **P8-s** and **P8-i** both show some degree of crystallinity (**Figure 2.5a**) although they appear to be less crystalline than **P4**, presumably due to disruption of packing by the 2-ethylhexyl side-chains.[5] Thermogravimetric analysis (TGA) shows thermal decomposition temperatures (T_d = temperature at which 5% weight loss of initial mass occurs) of **P8-s** and **P8-i** to be 339 and 295 °C in air respectively (**Figure 2.5b**). These T_d values are somewhat lower than similar unsubstituted photocatalysts, including the analogue **P4** (T_d = 408 °C),[6,7] but are in the region typically observed for polyfluorenes bearing alkyl side-chains.[8,9] Previous investigations have also shown that introduction of alkyl side-chains can reduce the thermal stability of conjugated polymers.[10,11]

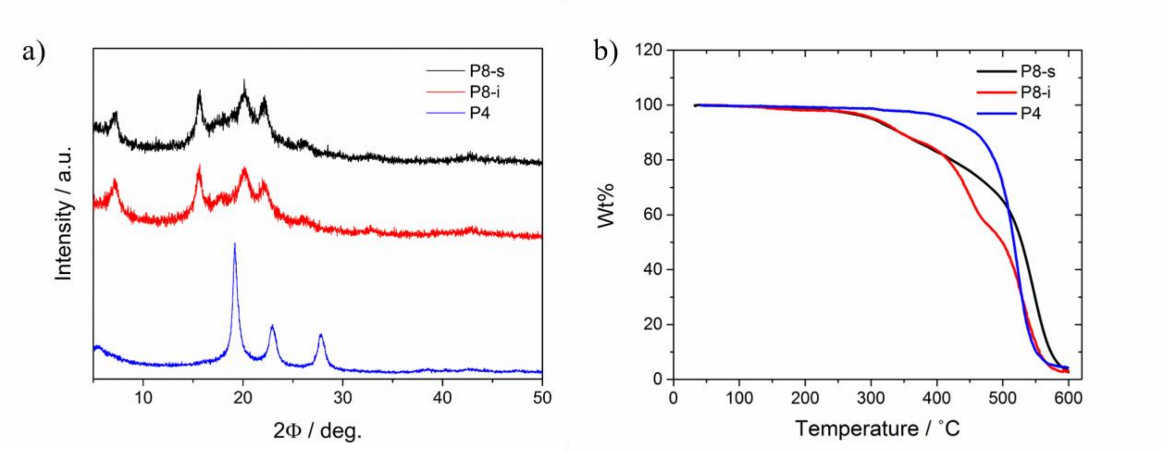

Figure 2.5 a) PXRD patterns of **P8-s**, **P8-i** and **P4** and **b)** TGA traces of **P8-s**, **P8-i** and **P4** in air with a heating rate of 10 °C min^{-1}.

The presence of residual palladium from the polycondensation reaction is an important property that should also be considered.[a] The level of residual palladium in the two fractions were found to be markedly different. Inductively Coupled Plasma-Optical Emission Spectrometry (ICP-OES) found Pd levels of 200 ppm and 5000 ppm for **P8-s** and **P8-i** respectively. This difference is likely to impact photocatalytic performance.[12]

---

[a] The influence of palladium content on photocatalytic performance will be discussed in greater detail in **Chapter 2.5.**

2.2.3 Photocatalytic Hydrogen Evolution Performance

Sacrificial conditions were used to study the ability of these materials to photocatalytically produce hydrogen from water. Triethylamine (TEA) was employed as a sacrificial electron donor as it has been previously used for **P4**.[1] A 1:1:1 water/methanol/TEA mixture was used for these photocatalysis experiments. Methanol was used as a co-solvent to promote miscibility of TEA with water (as TEA is not miscible with water above 5.5 g in 100 g at 20 °C).[13] Methanol should also improve dispersibility of the polymers, which are expected to be hydrophobic, in the aqueous reaction mixture.

P8-i powder photocatalytically evolves hydrogen from the water/methanol/TEA mixture at a rate of 21.5 μmol h^{-1} (860 μmol g^{-1} h^{-1}) under broadband irradiation (300W Xe light source, $\lambda > 295$ nm band pass filter), while powdered **P8-s** produced 13.6 μmol h^{-1} (544 μmol g^{-1} h^{-1}) under the same conditions in suspension (**Table 2.2**). It appears that introduction of the 2-ethylhexyl side-chain in **P8-i** and **P8-s** does not affect the hydrogen evolution rate greatly with respect to our previous insoluble polymer,[1] **P4**—indeed, the catalytic activity for **P8-i** is somewhat higher than for **P4** under broadband irradiation. While lower than **P8-i**, the activity of **P8-s** was comparable to commercially available C_3N_4 and TiO_2 under broadband irradiation and notably outperformed TiO_2 under visible light irradiation (**Table 2.2**).

Negligible hydrogen evolution was observed when methanol alone was used as a sacrificial electron donor and no hydrogen evolution was observed when a polymer was suspended in pure water (**P8-i**, **Figure 2.6a**). Acetonitrile could also be used as a co-solvent in the TEA/water mixture to facilitate a comparable rate of hydrogen evolution, showing that the photocatalytic reaction is not dependent on the presence of methanol.

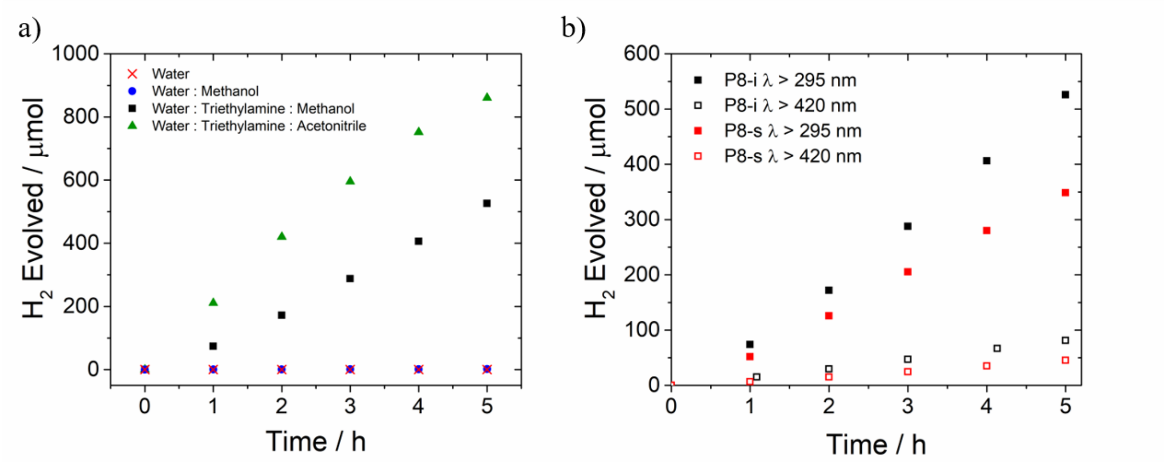

Figure 2.6 a) H_2 evolution runs of **P8-i** (25 mg) in water, water/methanol (1:1), water/methanol/TEA (1:1:1) and water/acetonitrile/TEA (1:1:1) under broadband irradiation; **b)** H_2 evolution runs of **P8-i** and **P8-s** (25 mg) in water/methanol/TEA (1:1:1) with the specified band pass filters.

P8-i evolves H_2 at a higher rate than **P8-s** under both broadband and visible light (300 W Xe light source, λ > 420 nm band pass filter) irradiation (**Figure 2.6b**, **Table 2.2**). This could be a consequence of higher palladium content or higher molecular weight of **P8-i** or a combination of these factors.[b] Regardless, the comparable photocatalytic performances of **P8-s** and **P8-i** implies that only limited effective conjugation lengths may be required to achieve good photocatalytic performance in linear polymers.

Table 2.2. Summary of solubility in chloroform, hydrogen evolution rates and optical gap[b] of **P8-s** and **P8-i** in comparison to **P4** and commercially available C_3N_4[24] and TiO_2.

Photocatalyst	**Solubility in $CHCl_3$**	**HER[i] λ > 420 nm / µmol h^{-1}**	**HER[i] λ > 295 nm / µmol h^{-1}**	**Optical gap[ii] / eV**
P4	Insoluble	5.6 (±0.2)	13.8 (±0.2)	2.72
P8-s	Soluble	1.8 (±0.03)	13.6 (±0.2)	2.71
P8-i	Insoluble	3.1 (±0.02)	21.5 (±0.1)	2.77
C_3N_4	Insoluble	2.7 (±0.1)	11.2 (±0.6)	2.70
TiO_2	Insoluble	0.1 (±0.003)	37.3 (±1.3)	3.13

[i] **P8-s**, **P8-i** and **P4**: 25 mg photocatalyst suspended in water/methanol/TEA solution, irradiated using 300 W Xe light source for 5 hours using the stated band pass filter (no additional Pt added). **C_3N_4** (Nicanite): 25 mg photocatalyst suspended in 10 vol. % triethanolamine in water loaded with 3 wt.% Pt. **TiO_2**: 25 mg photocatalyst suspended in water/methanol/TEA (1:1:1) with photodeposition of 1 wt.% Pt.

[ii] Calculated from the onset of the absorption spectrum.

---

[b] The influence of both palladium content and molecular weight on photocatalytic performance will be discussed in further detail in **Chapters 2.5.** and **2.6.** respectively.

Extended hydrogen evolution runs were performed for **P8-s** under visible and broadband irradiation and using a solar simulator (**Figure 2.7**). After 92.5 hours under broadband irradiation and with intermittent degassing, **P8-s** evolved 328 µmol of H_2. **P8-s** appears to remain photocatalytically active over the timescales studied here. A drop-off in performance is observed, especially when irradiated with UV light (**Figure 2.7a**). However, analysis of the polymer after 92.5 hours suspended in water/methanol/TEA under broadband irradiation shows that it appears to be structurally unaltered according to ^{1}H NMR, FT-IR, UV-vis and PL spectroscopy (**Figure 2.8**).

Crucially, the rate of hydrogen evolution under irradiation by a solar simulator is consistent over almost 100 hours (**Figure 2.7c**). When the hydrogen evolution rate decreased, activity could be partially recovered by replacing the aqueous mixture. This suggests that buildup of sacrificial reagent degradation products may account for the observed performance drop-off rather than polymer degradation. The fact that performance was not fully recovered is likely due to loss of polymer during the centrifugation process used to replace the mixture.

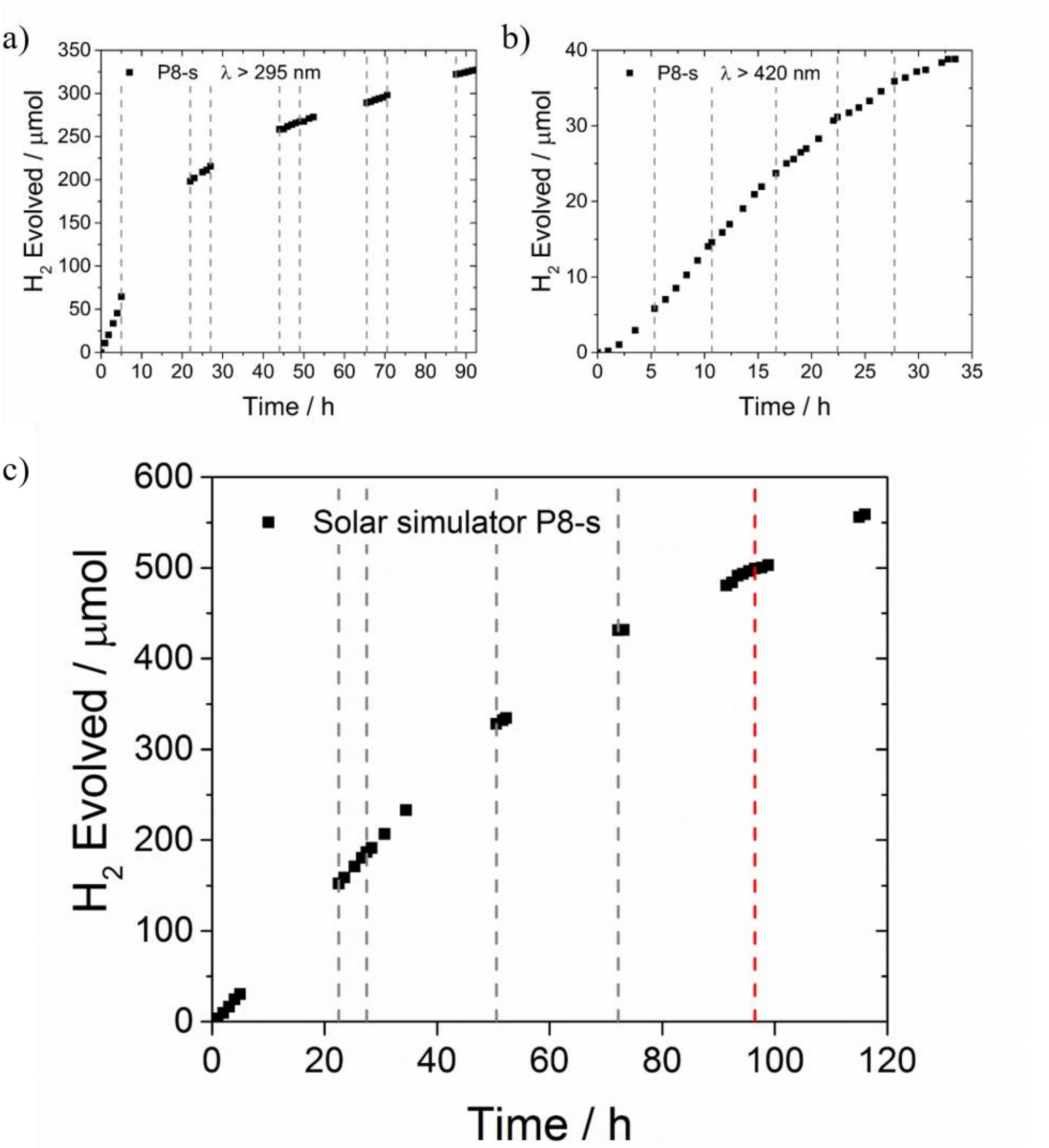

Figure 2.7. Extended H_2 evolution runs of of **P8-s** in water/methanol/TEA under **a)** broadband irradiation **b)** visible light iradiation and **c)** irradiation by a solar simulator (AM1.5G, 1 sun). Dashed black lines denote degassing of the mixture with N_2 while red lines denote replacement of the aqueous mixture.

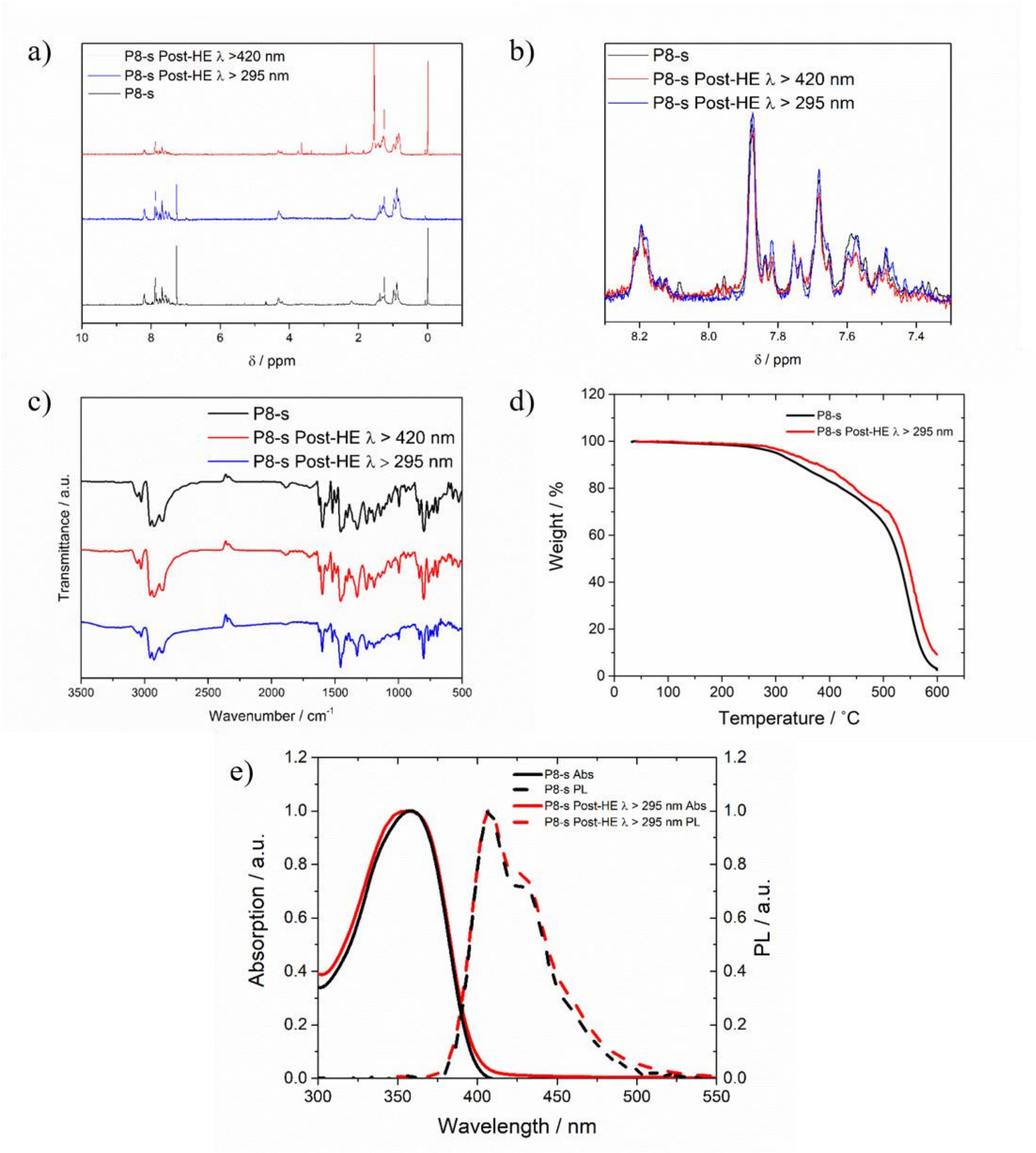

Figure 2.8 a) ^{1}H NMR spectra of **P8-s** before and after extened hydrogen evolution experiments in water/methanol/TEA under broadband and visible light irradiation; **b)** Enlarged aromatic region of ^{1}H NMR spectra; **c)** Transmission FT-IR spectra of **P8-s** before and after hydrogen evolution experiments under broadband irradiation for 92.5 hours and visible light irradiation for 33.5 hours in water/methanol/triethylamine mixtures; **d)** TGA traces of **P8-s** before and after hydrogen evolution experiments in a water/methanol/TEA mixture for 5 hours under broadband irradiation. TGA performed in air at a heating rate of 10 °C min^{-1}; **e)** UV-vis and photoluminescence spectra of **P8-s** in chloroform before and after hydrogen evolution in a triethylamine/water/methanol mixture for 92.5 hours under broadband irradiation.

The addition of heavy metal co-catalysts has previously improved the hydrogen evolution performance of polymers[14] and so could be used to boost the activity of **P8-s** in this case. Polymer performance is likely to depend on both the metal and amount of co-catalyst loaded onto the polymer. Finding optimised systems requires a number of experiments to be performed. A study of this kind therefore lends itself to the high throughput screening (HTS) methodology introduced in **Chapter 1.5.3**, which enables rapid modulation of these variables. A HTS with various metal co-catalysts at different loading was carried out with **P8-i** as this fraction was obtained in the highest yield. The co-catalysts were dispensed into vials containing pre-weighed polymer samples and loaded *in situ* by photodeposition, a process whereby metal ions are reduced by photogenerated electrons onto a semiconductor under irradiation.[15,16]

The photocatalytic performance of **P8-i** was tested with ruthenium, rhodium and platinum co-catalysts at 1 wt. %, 3 wt. % and 5 wt. %, loaded from rhodium (III) chloride, ruthenium (IV) oxide and chloroplatinic acid respectively (**Figure 2.9a)**. Interestingly, the addition of platinum, which has been shown to enhance the activity of a host of polymers,[17–19] appears to inhibit the photocatalytic activity of **P8-i** at the loadings studied here. It has been shown for TiO_2 that at high Pt loadings photocatalytic performance is reduced.[20] This is thought to be due to Pt shielding the polymer surface, decreasing light absorption by the polymer and, consequently, reducing the surface concentration of charge carriers. The fact that activity decreases with increasing Pt content from 1 wt. % to 3 wt. % for **P8-i** suggests this may be the case here and that a rate enhancement could be achieved with Pt loadings less than 1 wt. %.

The addition of 3 wt. % ruthenium resulted in the greatest increase in performance of **P8-i** in the HTS experiment. Kinetic runs were therefore performed with **P8-s** loaded with 3 wt. % ruthenium in an attempt to improve the performance of this solution-processable material (**Figure 2.9b)**. Photocatalytic activity was enhanced, particularly under visible light irradiation (from 74 ± 1 to 336 ± 5 μmol g^{-1} h^{-1}).

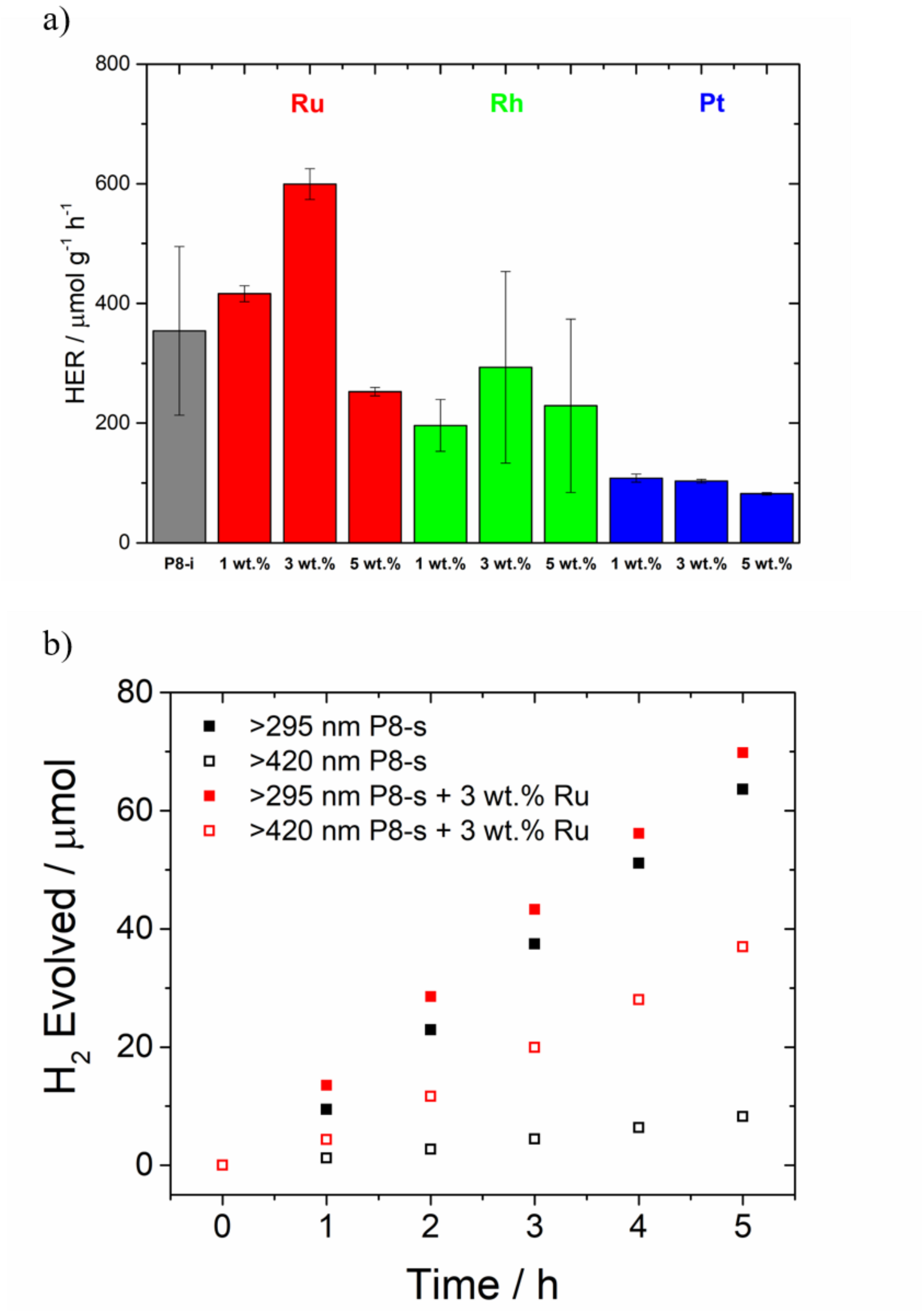

Figure 2.9 a) H_2 evolution rates of of **P8-i** loaded with ruthenium, rhodium and platinum co-catalysts at 1 wt. %, 3 wt. % and 5 wt. % in water/methanol/TEA over 5 hours irradiated with a solar simulator (AM1.5G, 1 sun). **b)** Kinetic traces of **P8-s** in water/methanol/TEA with no co-catalyst and 3 wt. % ruthenium cocatalyst under broadband and visible light irradiation.

2.2.4 Photophysical Measurements

Cast films of **P8-s** showed a low degree of scattering, thus enabling transient absorption spectroscopy (TAS) to be performed. These measurements can be useful in confirming observations from photocatalysis experiments and provide insights into the lifetimes of excited states, quenching and the role of solvents in the reaction mixture.

Figure 2.10 shows the femtosecond-TAS (fs-TAS) spectra of **P8-s** films on glass (λ_{exc} = 365 nm). In water, photoinduced absorptions (PIAs) are observed immediately after excitation at 525, 564 and 648 nm, with a broad feature at 740 nm on a similar timescale to the instrument response (around 0.6 ps, **Figure 2.10a**). These spectral features initially decay rapidly with a $t_{50\%}$—the time for 50% of the PIA at approximately 1 ps to decay by 50%—of around 2 ps. This results in a small PIA that persists beyond 3.1 ns, the maximum observable timeframe of this experiment (**Figure 2.10a** and **d**). A similar lifetime is observed in a water/methanol (1:1) mixture ($t_{50\%}$ ~ 4 ps, **Figure 2.10b**), supporting the observation from hydrogen evolution experiments (**Figure 2.6a**) that methanol alone does not act as a sacrificial electron donor for this material.

In contrast, in the presence of water, methanol and TEA (**Figure 2.10c**), the features at 525, 564 and 648 nm decay more rapidly. While these features decay, a broad feature grows in with a maximum at approximately 715 nm and a shoulder at 570 nm. The simultaneous formation of this feature and rapid decay of the 525 nm feature, and the dependence of this phenomenon on the presence of TEA, is shown in **Figure 2.10e**. The 715 nm feature displays a much longer lifetime ($t_{50\%}$ ~ 50 ps) in the presence of TEA than in water and water/methanol mixtures (**Figure 2.10d**).

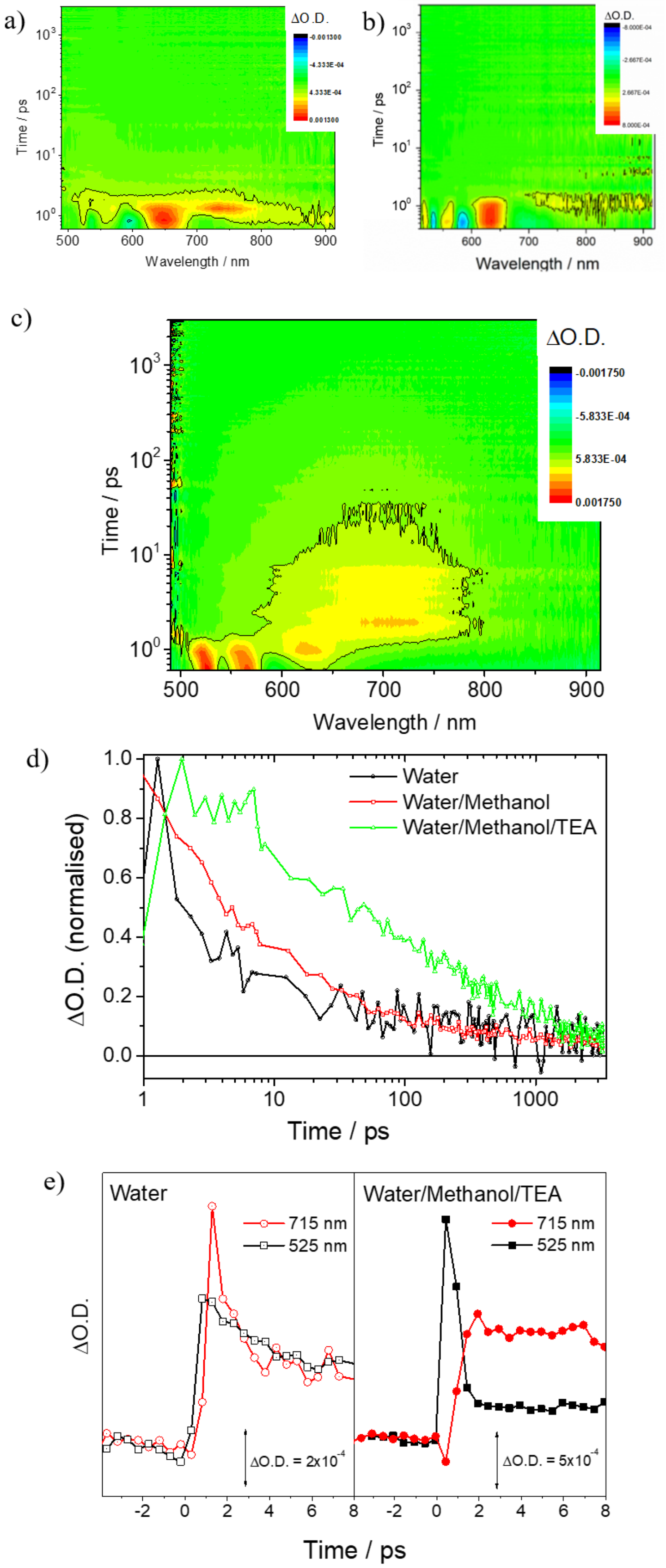

Figure 2.10. fs-TAS of **P8-s** in **a)** water, **b)** water/methanol (1:1) and **c)** water/methanol/TEA (1:1:1) with λ_{exc} = 365 nm in all cases; **d)** Kinetic traces recorded at 715 nm in each solvent mixture; **e)** Kinetic tracess recorded at 715 and 525 nm in water and water/methanol/TEA (1:1:1).

The persistence of the spectral feature at around 700 nm beyond 100 ps is shown with greater clarity in **Figure 2.11a**. In fact, this feature persists even beyond the maximum observable timescale of 3.1 ns (**Figure 2.11b)**. The long lifetime of this feature in the presence of an electron donor and its difference to reported spectra of positive polarons of similar polycarbazoles[21] implies that this is the polymer anion—or electron polaron—state,[22] formed after the polymer exciton is quenched by the sacrificial electron donor, TEA.

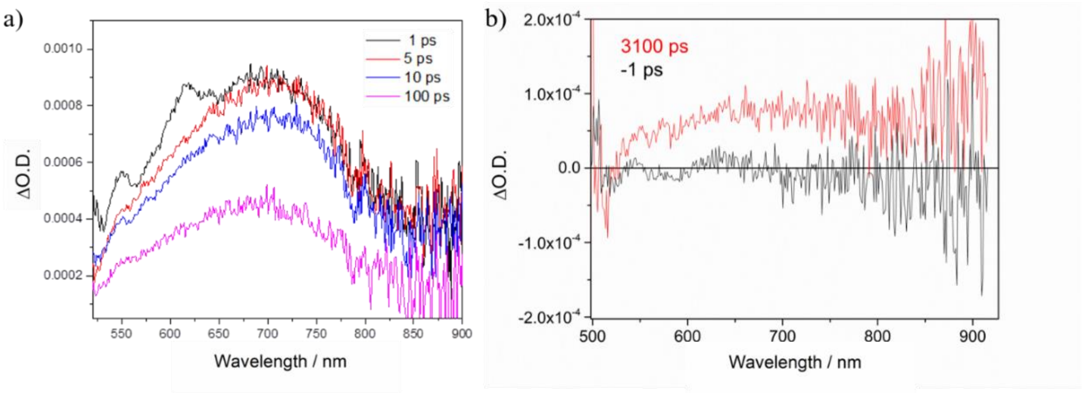

Figure 2.11. fs-TAS spectra of **P8-s** in water/methanol/TEA (1:1:1) mixture at **a)** 1 ps, 5 ps, 10 ps and 100 ps and **b)** -1 and 3100 ps (λ_{exc} = 365 nm).

2.2.5 Summary

In summary, an alkyl-substituted conjugated polymer photocatalyst was prepared that can be processed in solution. Despite its low molecular weight this material retains photocatalytic activity similar to unsubstituted **P4** and demonstrates good photostability. TAS provided insights into excited state dynamics and their timescales, allowing for understanding of the roles played by each component of the system. Furthermore, electron transfer was observed from the amine scavenger onto the excitonic species forming an electron polaron state. This study represents an important first step in the design of solution-processable polymer photocatalysts.

However, there are clearly areas for improvement in the design of these materials. First, the prohibitively low yield of **P8-s** could be addressed by increasing the number and size of solubilising side groups in the polymer structure. However, the impact of these side-chains on photocatalytic activity must also be considered given that performance must be improved if a STH efficiency of 10% is to be reached in future photocatalytic systems. A more systematic and comprehensive study on the effect of side-chain modification within a variety of polymer structures is required to fully assess the viability of solution-processable polymers as hydrogen evolution photocatalysts.

2.3. Side-Chain Variation in Solution-Processable Polymer Photocatalysts

2.3.1. Alkyl Side-Chain Variation in Polymer Photocatalysts

2.3.1.1. Alkyl Side-Chain Variation in Poly(carbazole-phenylene)s

The influence of the choice of solubilising group on photocatalytic performance of polycarbazole photocatalysts was investigated by preparing an analogous polymer to **P8**, **P9**, with a longer, unbranched hexadecyl side-chain (**Figure 2.12a**). **P9** was prepared using an identical method to **P8**. Despite the increased length of the solubilising side-chain, the yield of soluble material (**P9-s**) remained low (10%).

Once again, the photocatalytic performance of the soluble fraction, **P9-s**, was lower than that of the insoluble fraction, **P9-i**. Hydrogen evolution rates of **P9-s** and **P9-i** were found to be significantly lower than those of **P8-s** and **P8-i** under both broadband and visible light irradiation (**Figure 2.12 b** and **c**). This is also true when rates are normalised to the molecular weight of the repeating unit; i.e., accounting for the reduced proportion of conjugated polymer backbone when larger solubilising chains are present (see **Appendix**, **Table A-1**).

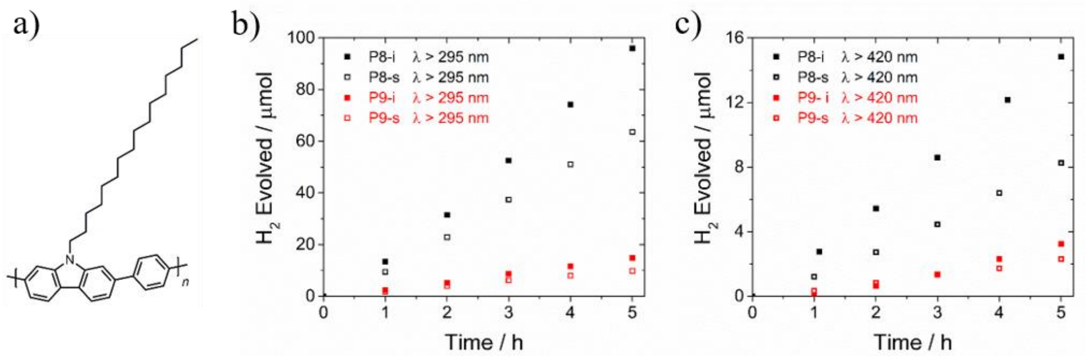

Figure 2.12. **a)** Structure of **P9**. H_2 evolution runs of **P8-i**, **P8-s**, **P9-i** and **P9-s** (25 mg) in water/methanol/TEA (1:1:1) under **b)** broadband irradiation and c**)** visible light irradiation (300 W Xe light source).

Contact angle measurements of water droplets with polymer films showed **P9-s** to be more hydrophobic than **P8-s** (**P8-s =** 97.4 ± 0.7˚, **P9-s** = 103.1 ± 0.9˚, **(Figure 2.12a** and **b**). The longer hexadecyl side-chain may therefore decrease the wettability and dispersibility of **P9-s** in the water/methanol/TEA mixture used for hydrogen evolution. Powder X-ray diffraction (PXRD) patterns showed **P9-s** and **P9-i** to be less crystalline than **P8-s** and **P8-i** (**Figure 2.13c)**, which may also account for their reduced hydrogen evolution rates.

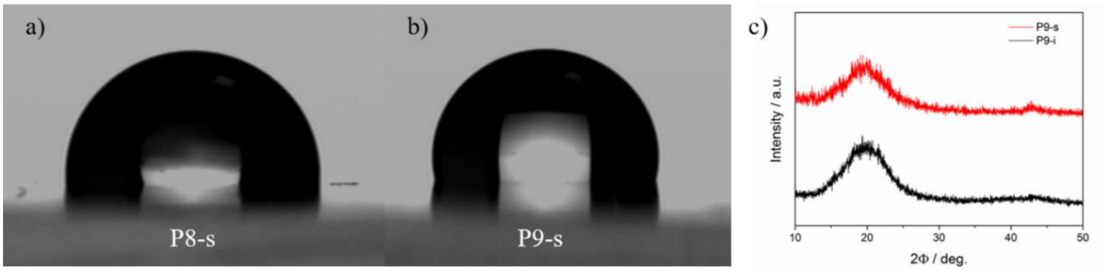

Figure 2.13. Water droplets on the surface of glass slides with drop-cast films of **a) P8-s** and **b) P9-s**. **c)** PXRD patterns of **P9-s** and **P9-i**.

This study suggests that longer side-chains may diminish photocatalytic activity by reducing wettability and crystallinity. However, the low yield of **P9-s** suggests the addition of more solubilising groups may be required to achieve higher yields of soluble material. It appears therefore that a trade-off between the amount of solubilising alkyl side-chain, the yield of soluble material and the photocatalytic performance of these polymers may be inevitable. Nevertheless, the preparation of series of polymers with systematically varied alkyl side-chains is required to confirm the influence of side-chain length on photocatalytic activity.

2.3.1.2. Alkyl Side-Chain Variation in Poly(fluorene-phenylene)s and Poly(fluorene-dibenzo[*b*,*d*]thiophene sulfone)s

Fluorenes are a commonly used structural motif in organic electronics.[23–26] The fluorene unit can be substituted with two solubilising groups at the bridgehead position thus enabling greater side-chain variation than singly-substituted carbazoles. The ease of substitution at the 2,7 positions also makes them ideal for polycondensation reactions[26] and a variety of alkyl-substituted dibromo- and diboronic acid/ester-functionalised fluorene monomers are now commercially available. These monomers were used to prepare two series of co-polymers with systematically modulated alkyl side-chains. Two series of polymers with fluorene-phenylene (**FP**) and fluorene-dibenzo[*b*,*d*]thiophene sulfone (**FS**) backbones were prepared. Di-*n*-hexyl- (**Hex**), di-2-ethylhexyl- (**EtHex**), di-*n*-octyl- (**Oct**) and di-*n*-dodecyl- (**Dodec)** substituted fluorenes were employed in the polymers in both series (**Figure 2.14**). Previously-reported insoluble dimethyl (**Me)**-substituted insoluble polymers were also included for comparison.[1,27]

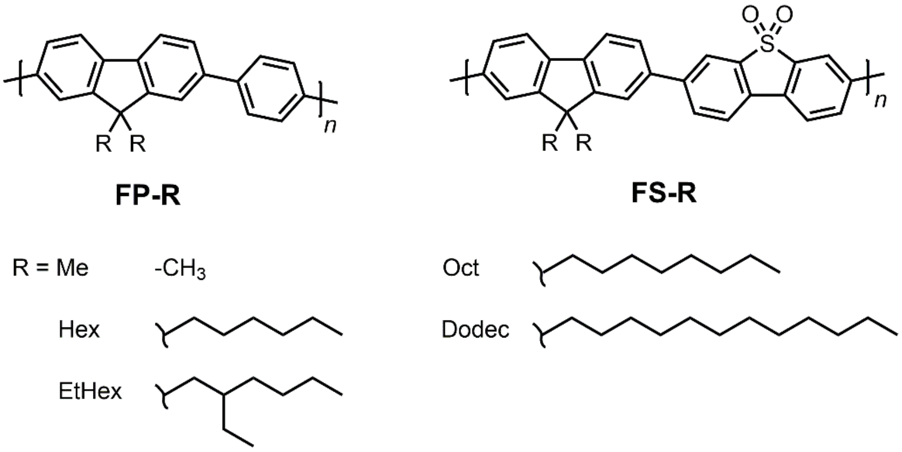

Figure 2.14. Structure of **FP-R** and **FS-R** polymers where R is the alkyl side-chain being varied as shown.

^{1}H NMR spectroscopy confirms the expected number of protons in the backbone and side-chains in the soluble polymers (**Figure 2.15**). The use of longer side-chains is expected to lead to enhanced molecular weight due to improved solubility in the reaction mixture preventing the ‘crashing out’ of oligomeric polymer chains.[28] However, Suzuki-Miyaura polycondensations are notoriously difficult to control[29] and no clear correlation between increased side-chain length and increased molecular weight was observed (**Table 2.3**). The yield of chloroform-soluble fractions of

FP-Hex, **FS-Hex**, and **FS-Oct** were low as insoluble products were also obtained although still notably higher than the carbazole-phenylene polymers discussed previously.

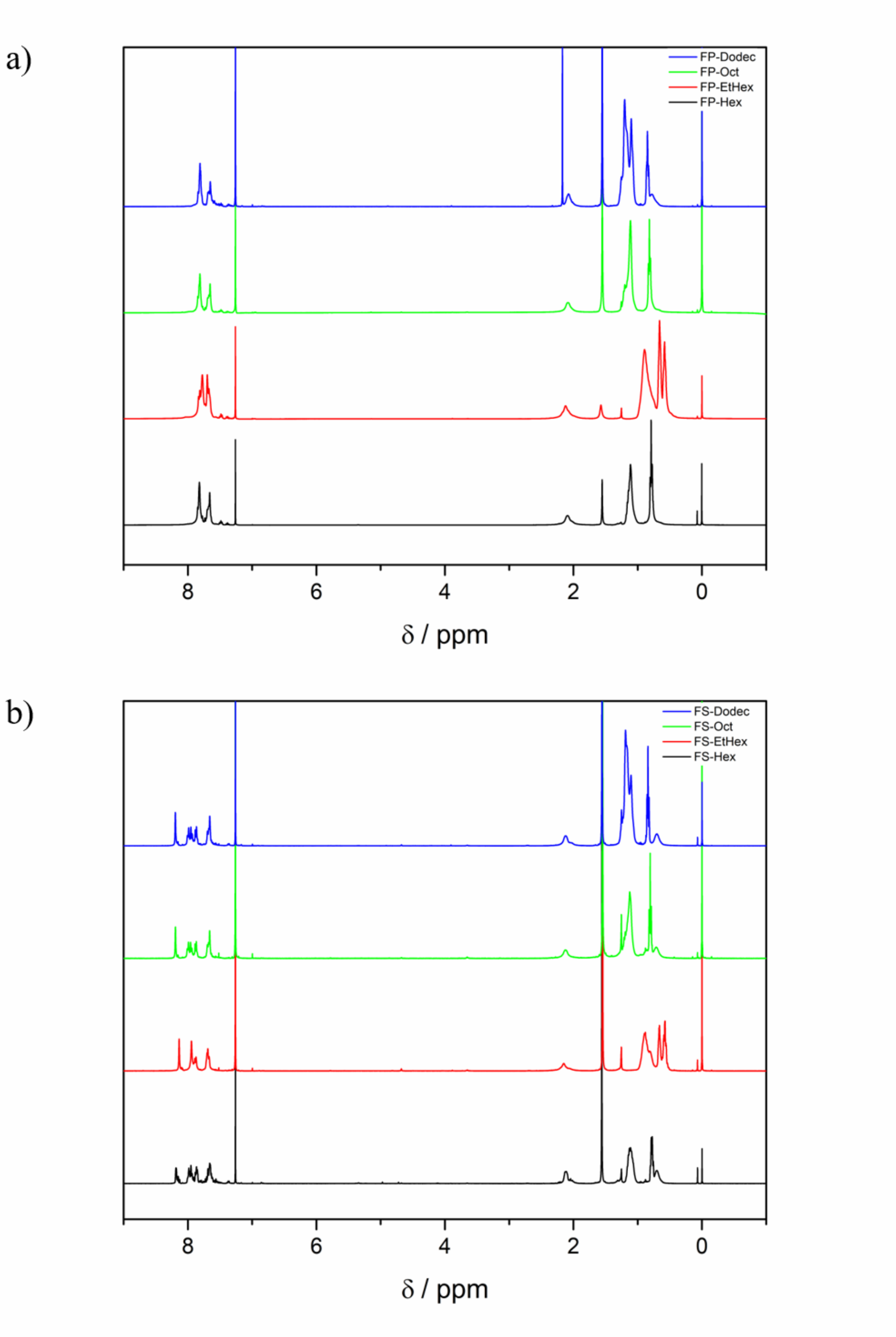

Figure 2.15. ^{1}H NMR spectra of **a) FP** and **b) FS** series of alkylated polymers in $CDCl_3$. Peaks of residual solvents correspond to chloroform (7.26 ppm), acetone (2.12 ppm) and water (1.56 ppm).

Table 2.3. Number- and weight-averaged molecular weights and polydispersity indices (Đ) obtained by GPC and yields of the **FP** and **FS** series of solubtion-processable polymers.

Polymer	**M_n / g mol^{-1}**	**M_w / g mol^{-1}**	***Đ***	**Yield / %**
FP-Hex	18,200	43,200	4.4	47
FP-EtHex	14,600	39,000	2.7	90
FP-Oct	16,300	57,900	3.6	72
FP-Dodec	6600	12,900	2.0	57
FS-Hex	3800	8200	2.2	50
FS-EtHex	19,000	36,900	1.9	63
FS-Oct	18,900	31,900	1.7	37
FS-Dodec	14,900	25,400	1.7	79

TGA shows that all alkylated polymers exhibit thermal stability up to temperatures in excess of 300 ˚C under air, when decomposition starts to occur (**Figure 2.16**). The **FP** series display a stepwise degradation with the size of the initial step consistent with the percentage of side-chain in the polymer, suggesting initial loss of side-chains. This is typically observed in polyfluorenes with solubilising side-chains.[8,9] Alkylated **FS** polymers display very similar degradation profiles to **FS-Me**. The thermal stability of these polymers confirms they are suitable for application in the mild temperatures required for photocatalytic hydrogen evolution.

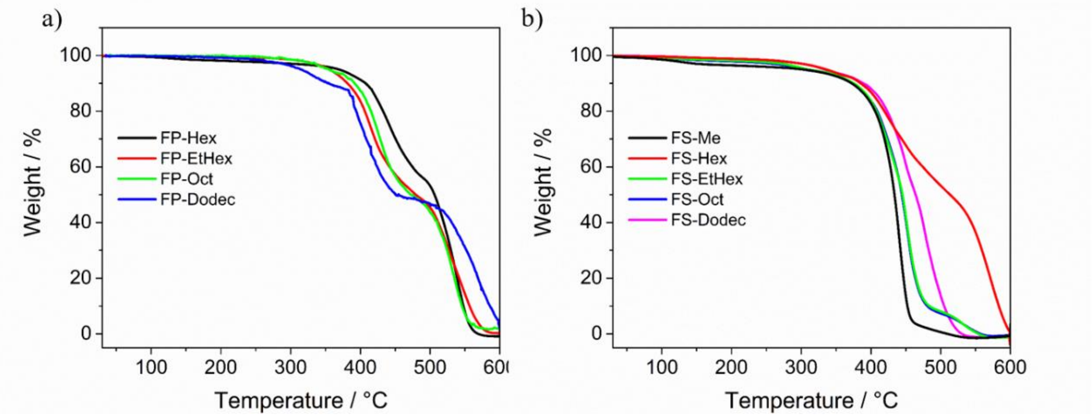

Figure 2.16. TGA traces **a) FP** and **b) FS** series of poylymers in air at a heating rate of 10 °C min^{-1}.

The UV-vis absorption profiles of the polymers in solution are virtually unaffected by the nature of the alkyl side-chain (**Figure 2.17a**, **Figure 2.18a**). Some variation in the absorption strength of the polymers was observed when molar extinction coefficients (ε) of the polymers were measured in solution ($\varepsilon_{\mathbf{FP}}$ = 2.5-4.2 × 10^5 m^2 mol^{-1}, $\varepsilon_{\mathbf{FS}}$ = 4.5–5.3 × 10^5 m^2 mol^{-1}, normalised to the molecular weight of the repeating unit). No clear relationship was observed between alkyl side-chain length and ε in the two series (**Appendix**, **Table A-1**) although the fact that **FS-Hex** has the lowest ε may be due to its lower molecular weight (approximately 14 monomer units) which is in the region of the effective conjugation length of polyfluorenes (approximately 12 units).[30]

As expected, the absorption spectra of these polymers as thin films (**Figure 2.17c**, **Figure 2.18c**) exhibit a slight bathochromic shift relative to the solutions[31] and again display minimal variation across both series. More variation is evident in the emission spectra of these films than in solution (**Figure 2.17d**, **Figure 2.18d**). The PL spectrum of **FP-EtHex** contains an emissive g-band between 500 and 600 nm that is not evident for the other polymers in the **FP** series. The emission band is also strongly evident in the PL spectrum of **FP-EtHex** powder. The variation in emissive properties in these series is likely to arise from differences in aggregation behaviour. This g-band was recently assigned to emission from H-aggregates or charge-transfer states in similar polyfluorene materials.[32]

The absorption spectra of the polymers in powdered form are broadened, presumably as a result of the variation of stacking arrangements caused by the disorderly packing of polymer chains in the solid state (**Figure 2.17e**, **Figure 2.18e)**.[31] The PXRD patterns confirm the amorphous nature of the majority of these polymers, although **FP-Me**, **FS-Me** and members of the **FS** series with shorter side-chains appear to have some limited long-range order (**Figure 2.19**).

SOLUTIONS

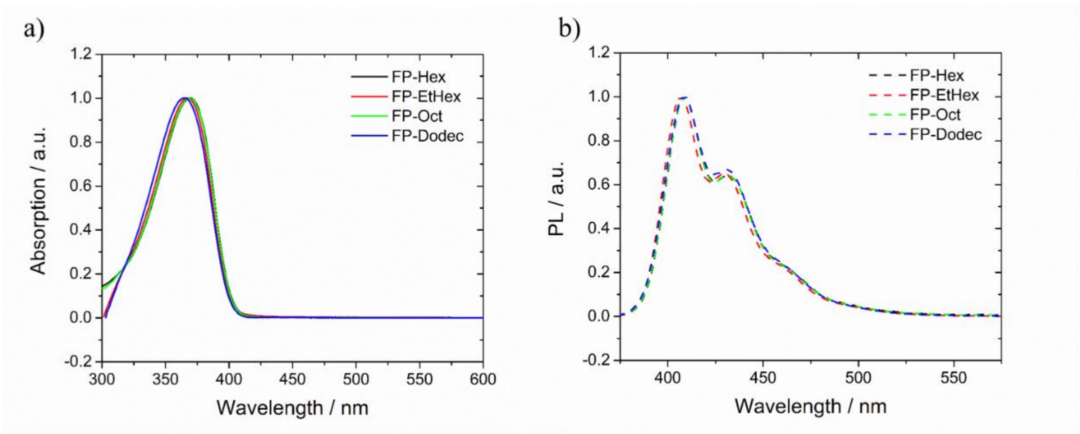

FILMS

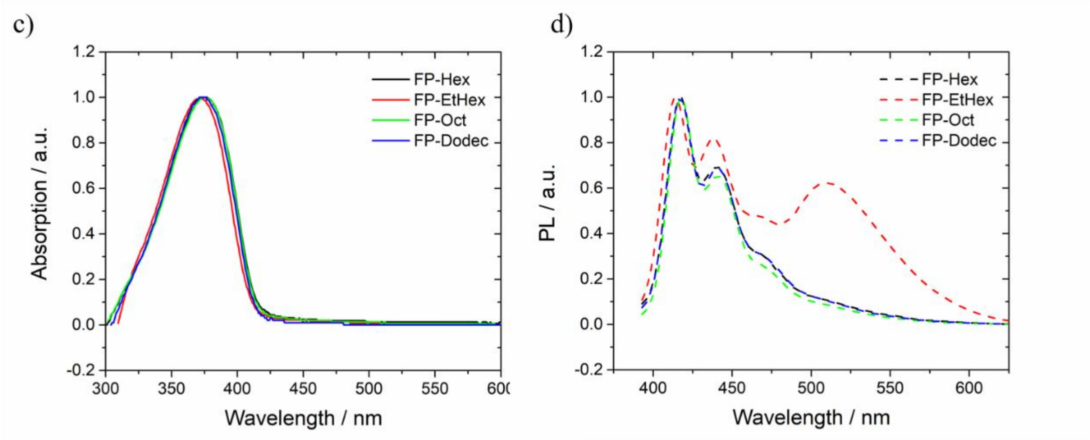

POWDERS

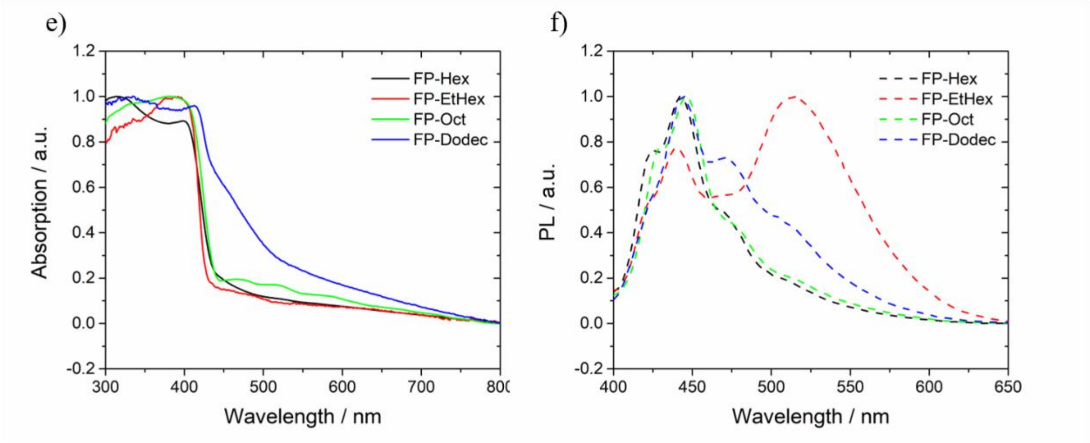

Figure 2.17. Normalised UV-vis and PL spectra of **FP** polymers dissolved in chloroform (**a** and **b**), cast as spin-coated films from chloroform on glass substrates (**c** and **d**) and as powders (**e** and **f**).

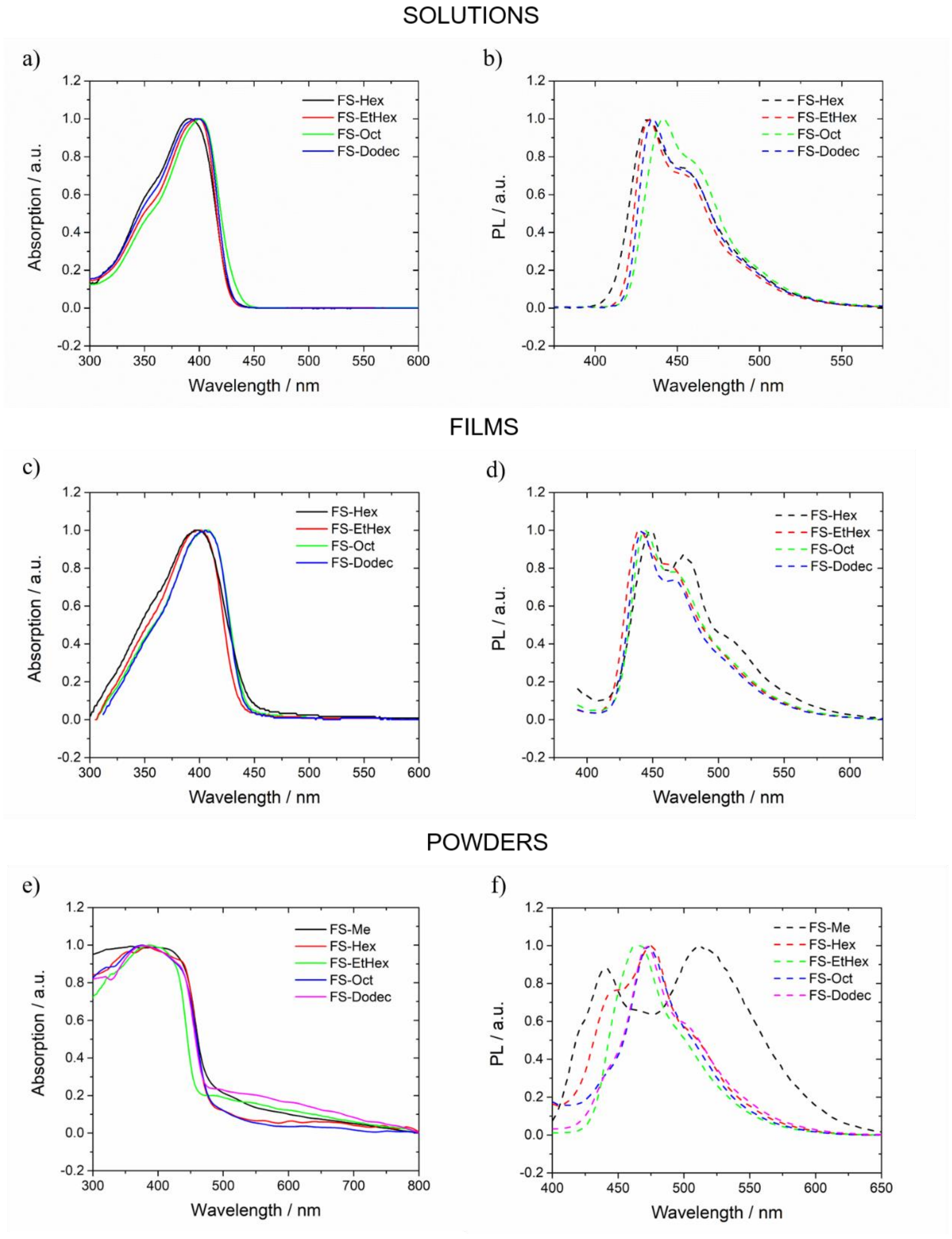

Figure 2.18. Normalised UV-vis and PL spectra of **FS** polymers dissolved in chloroform (**a** and **b**), cast as spin-coated films from chloroform on glass substrates (**c** and **d**) and as powders (**e** and **f**).

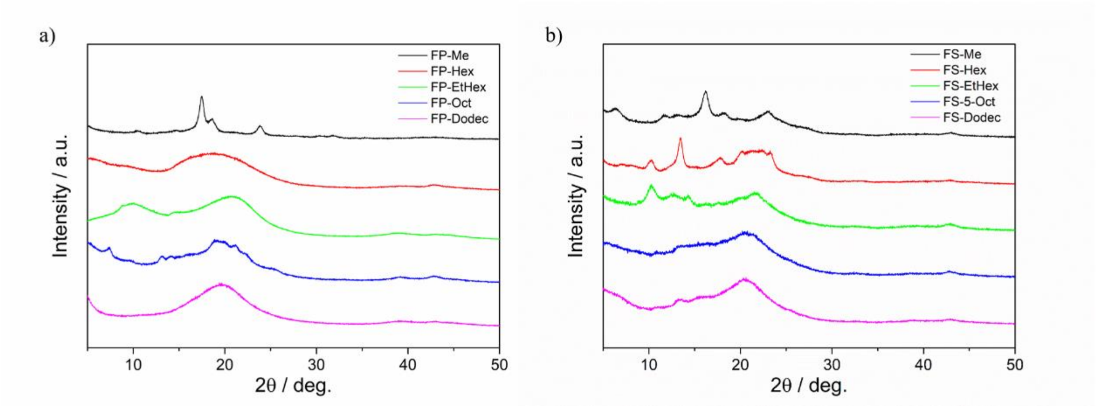

Figure 2.19. PXRD patterns of **a) FP** and **b) FS** polymer series.

Contact angle measurements were again performed on polymer films (**Table 2.4**). As with **P8-s** and **P9-s**, an increase in contact angle is generally observed with increasing alkyl side-chain length, for example from 89 ± 1° for **FS-Hex** to 98.6 ± 0.4° for **FS-Dodec**.

Table 2.4. Contact angle measurements of polymers with droplets of H_2O (300 µL).

	Polymer backbone	**Side-chains**				
		Me[i]	**Hex**[ii]	**EtHex**[ii]	**Oct**[ii]	**Dodec**[ii]
Contact Angle (H_2O) / °	**FP**	94 ± 8	92.8 ± 0.6	94.7 ± 0.3	101.4 ± 0.6	99.4 ± 0.5
	FS	77 ± 3	89 ± 1	85.4 ± 0.6	89.3 ± 0.4	98.6 ± 0.4

[i] Measured for pressed pellets of the polymers.
[ii] Measured for films of the polymers drop-cast from chloroform solution on glass.

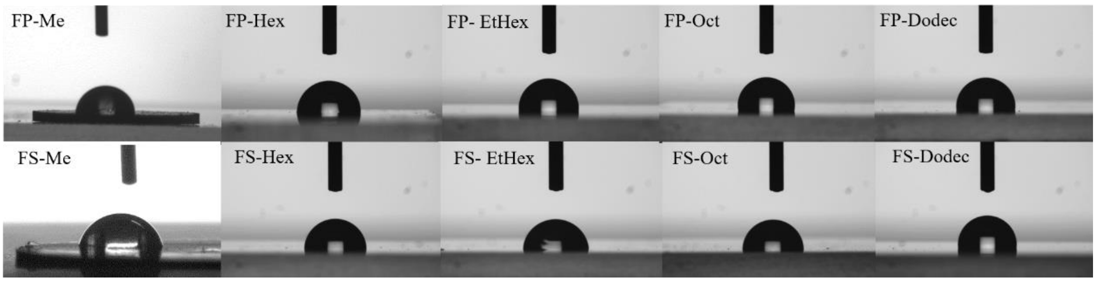

Figure 2.20. Images of water droplets used for contact angles measurements on cast films of all polymers apart from **FP-Me** and **FS-M**e which were measured as pellets.

Particle size distributions of **FS-Hex, FS-Oct** and **FS-Dodec** were measured by static light scattering (SLS) in water and the water/methanol/TEA mixture used for photocatalysis experiments (**Figure 2.21**, **Table 2.5**). The Sauter mean diameter, *D*[3,2], accounts for the higher active surface area of smaller particles and is therefore of particular relevance for photocatalytic applications.[33] In water, the Sauter mean diameters of the polymers seems to increase with increasing alkyl side-chain length (**FS-Hex** = 18.9 µm, **FS-Oct** = 45.4 µm, **FS-Dodec** = 79.5 µm). All polymers formed smaller particles in water/methanol/TEA mixtures and larger particles were again observed for polymers with longer side-chains (**FS-Hex** = 4.3 µm, **FS-Oct** = 6.0 µm, **FS-5-Dodec** = 10.6 µm). The morphologies of the polymer particles was found to be similar from scanning electron microscopy (SEM) images (**Figure 2.22**).

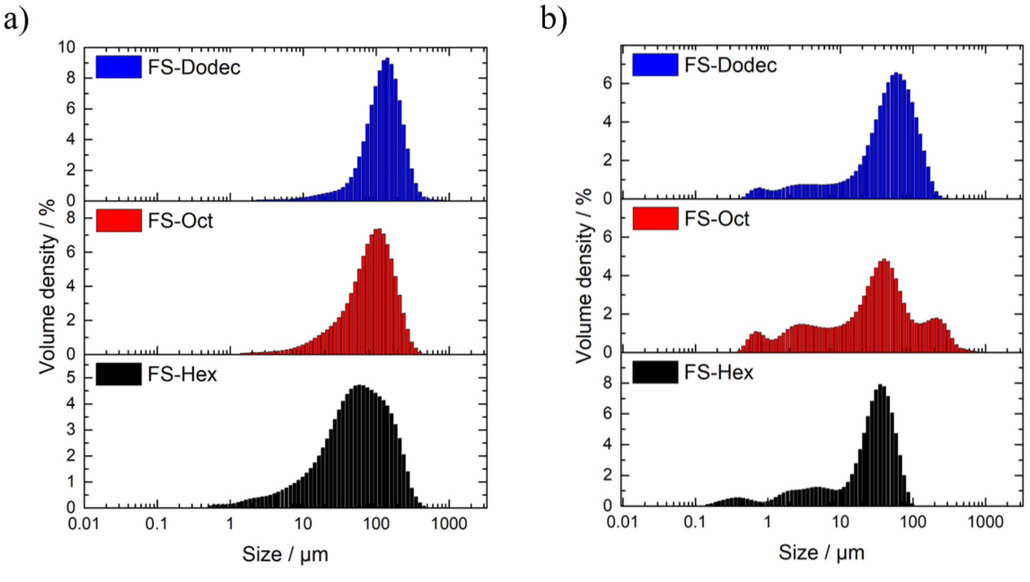

Figure 2.21. Particle size distributions of **FS-Hex**, **FS-Oct** and **FS-Dodec** obtained from static light scattering measurements in **a)** water and **b)** water/methanol/TEA (1:1:1).

Table 2.5. Particle sizes of **FS-Hex**, **FS-Oct** and **FS-Dodec** by SLS measurements.

Medium	Polymer	D_x50^{i} / µm	$D[4,3]^{ii}$ / µm	$D[3,2]^{iii}$ / µm
Water	**FS-Hex**	58.4	82.7	18.9
	FS-Oct	92.9	106	45.4
	FS-Dodec	135	149	79.5
Water/Methanol/TEA	**FS-Hex**	29.7	30.9	4.3
	FS-Oct	33.3	63.1	6.0
	FS-Dodec	51.4	59.6	10.6

[i] 50th Percentile of particle size volume distribution

[ii] Volume mean diameter

[iii] Surface area mean diameter (Sauter mean diameter).

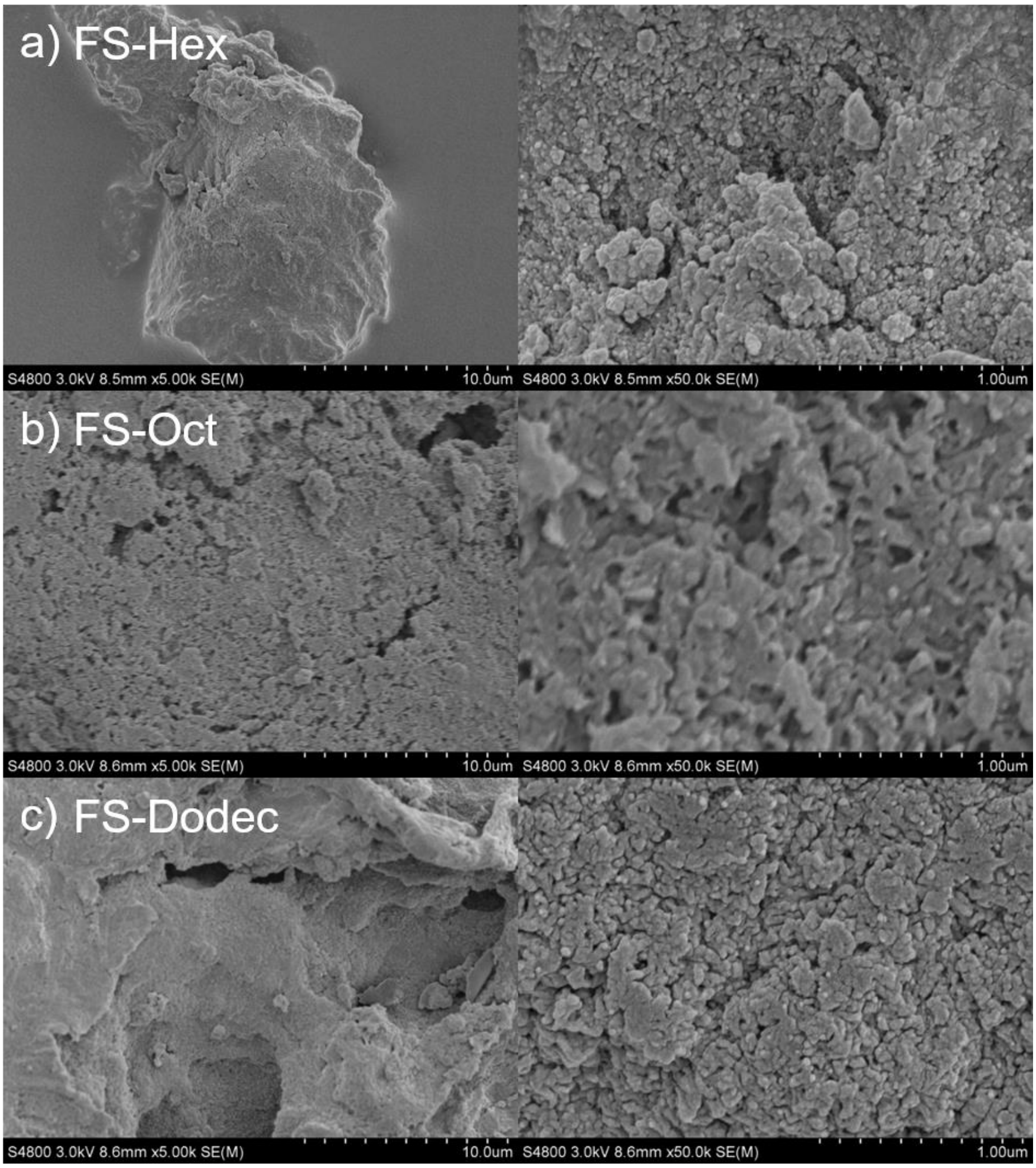

Figure 2.22. SEM images of **a) FS-Hex**, **b) FS-Oct** and **c) FS-Dodec** particles at the specified magnifications.

The photocatalytic performance of these polymers was measured under visible light irradiation. The **FP** series all exhibited poor HERs (<10 µmol g^{-1} h^{-1}) in these conditions. This may be in part due to the hydrophobicity of these polymers as the polymers appear to disperse poorly in the water/methanol/TEA mixture. No relationship between HER and alkyl side-chain is discernible with such low performances. However, the **FS** series all exhibit notably higher HERs. Generally, side-chains do not drastically inhibit the photocatalytic performance of these polymers. In fact, the solution-processable **FS-Hex** actually has a higher HER than insoluble **FS-Me**. Decreased photocatalytic activity is apparent with increasing side-chain length (**FS-Hex** > **FS-Oct** > **FS-Dodec)**, although not as noticeably when rates are normalised to the molecular weight of the repeating unit (**Table 2.6**). Interestingly, **FS-EtHex** has the lowest photocatalytic performance of the **FS** polymers studied here.

Table 2.6. Hydrogen evolution performance of all alkylated **FP** and **FS** polymers in suspension.[c]

Polymer	**HER[i]** **λ > 420 nm / µmol g^{-1} h^{-1}**	**HER[ii]** **λ > 420 nm / µmol $mmol^{-1}$ h^{-1}**
FP-Me[1]	8.3 ± 0.2	2.3 ± 0.1
FP-Hex	0	0
FP-EtHex	4.3 ± 0.2	2.0 ± 0.1
FP-Oct	5.2 ± 0.3	2.4 ± 0.1
FP-Dodec	6 ± 1	4 ± 1
FS-Me[34]	840 ± 20	340 ± 10
FS-Hex	1370 ± 20	750 ± 20
FS-EtHex	535 ± 3	323 ± 2
FS-Oct	680 ± 7	410 ± 20
FS-Dodec	577 ± 5	413 ± 4

[i] Rate normalised per gram of polymer.
[ii] Rate normalised to the molecular weight of each polymer's repeating unit.

---

[c] Reaction conditions: 25 mg of the polymer was suspended in 22.5 mL of a water/methanol/TEA solution (1:1:1), irradiated by 300 W Xe light source fitted with a λ > 420 nm band pass filter.

These results offer further evidence that solution-processable polymers can have high photocatalytic activities. **FS-Hex** has the highest HER of the polymers reported here, some twenty times higher than our previous best-performing soluble polymer photocatalyst **P8-s**. Once again though, although the yield of **FS-Hex** (50%) is higher than **P8-s** (9%), a significant amount of insoluble product is also obtained in the polymerisation of **FS-Hex**. Increased yields of soluble polymer can be obtained through the use of longer dodecyl side-chains. However, this increased yield appears to come at the expense of photocatalytic performance, which declines with increasing side-chain length. Contact angle measurements and SLS results suggest this could relate to reduced dispersibility of polymers in the aqueous mixture used for photocatalysis as the inherent hydrophobicity of these conjugated polymers is exacerbated by the incorporation of longer alkyl side-chains. Strategies to increase the wettability of solubilised polymer photocatalysts, such as introducing more hydrophilic side-chains, should be employed to further investigate this hypothesis.

2.3.2. Oligo(ethylene glycol) Side-Chains

2.3.2.1. Introduction

As discussed previously, wettability is recognised as an important factor in determining photocatalytic performance.[27,35] One potential method of improving the wettability of solution-processable polymer photocatalysts is through the use of oligo(ethylene glycol) (OEG) side-chains. The interesting properties of OEG chains, such as good stability, low toxicity, and biocompatibility, means they have been utilised in a wide range of chemical, biological and medical applications.[36,37]

Recently the concept of utilising OEG side-chains in conjugated polymers for electronic applications has been studied more extensively.[38–40] Replacing alkyl side-chains with OEG units can have a significant impact on the electronic properties of conjugated polymers. For instance, the closer π-π stacking enabled by OEG side-chains can result in higher hole mobilities, red-shifted absorption spectra and narrower band gaps.[9]

A key characteristic of OEG side-chains is their greater hydrophilicity in comparison to alkyl side-chains,[9,40–42] which is expected to aid photocatalytic performance in the aqueous environments used here. However, a study in which the alkyl/OEG content was systematically varied found an increase in OEG content to significantly reduce electron mobility which may inhibit photocatalytic activity.[43] By comparing OEG-substituted polymers with polymers containing alkyl side-chains of comparable length, the impact of OEG side-chains on photocatalytic performance will now be studied.

2.3.2.2. Comparing OEG- and Alkyl-Substituted Polymers

FP and **FS** polymers with tri(ethylene glycol) (TEG) side-chains, **FP-TEG** and **FS-TEG**, will be compared to the previously discussed alkylated polymers **FP-Hex**, **FP-Oct**, **FS-Hex** and **FS-Oct** (**Figure 2.23**).[d] The TEG-substituted dibromofluorene monomer was synthesised using a literature procedure (**Figure 2.64**)[36] and used to synthesise polymers **FP-TEG** and **FS-TEG** in analogous Suzuki-Miyaura polycondensations to those used for alkylated polymers. **FS-TEG** was obtained in higher yield than **FP-TEG** (74% *vs.* 19%), with no insoluble fraction obtained for **FS-TEG**. FT-IR transmission spectra show the expected functional groups to be present in the polymers (**Figure 2.24a**). **FS-Oct** and **FS-TEG** both display strong absorbance at 1350-1300 cm^{-1} confirming the presence of the dibenzo[*b,d*]thiophene sulfone (DBTS) moiety while the TEG-substituted polymers absorb strongly at 1150-1085 cm^{-1} which corresponds to the aliphatic ether stretching frequency. ^{1}H NMR spectroscopy in chloroform-*d* was also performed to confirm the polymer structures (**Figure 2.24b**) with differences in aromatic proton signals between the phenylene and DBTS-containing polymers clearly observed. The spectra of **FP-TEG** and **FS-TEG** contain more shifted aliphatic proton signals characteristic of OEG side-chains.

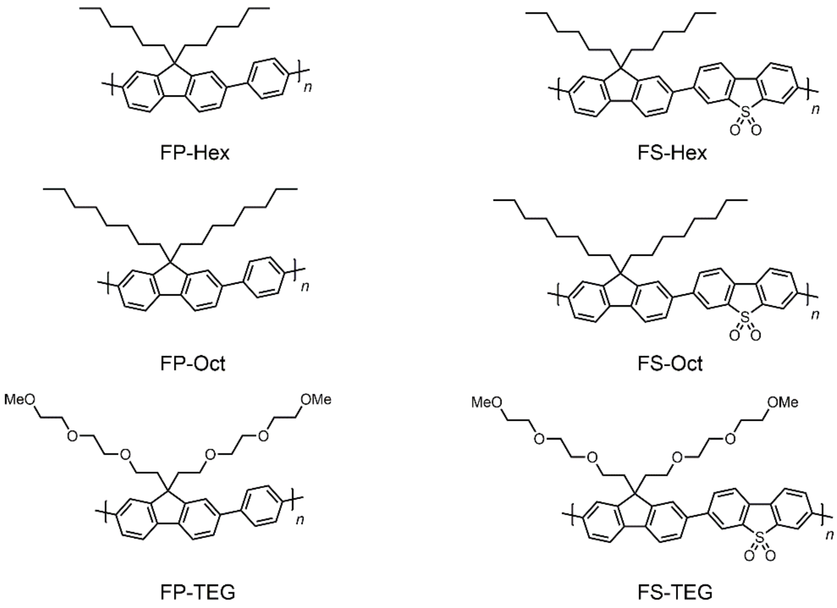

FP-Hex

FS-Hex

FP-Oct

FS-Oct

FP-TEG

FS-TEG

Figure 2.23. Structure of **FP-R** and **FS-R** polymers where R is the alkyl or OEG side-chain being varied as shown

---

[d] The effect of varying OEG side-chain length will be discussed in **Chapter 2.3.2.3**.

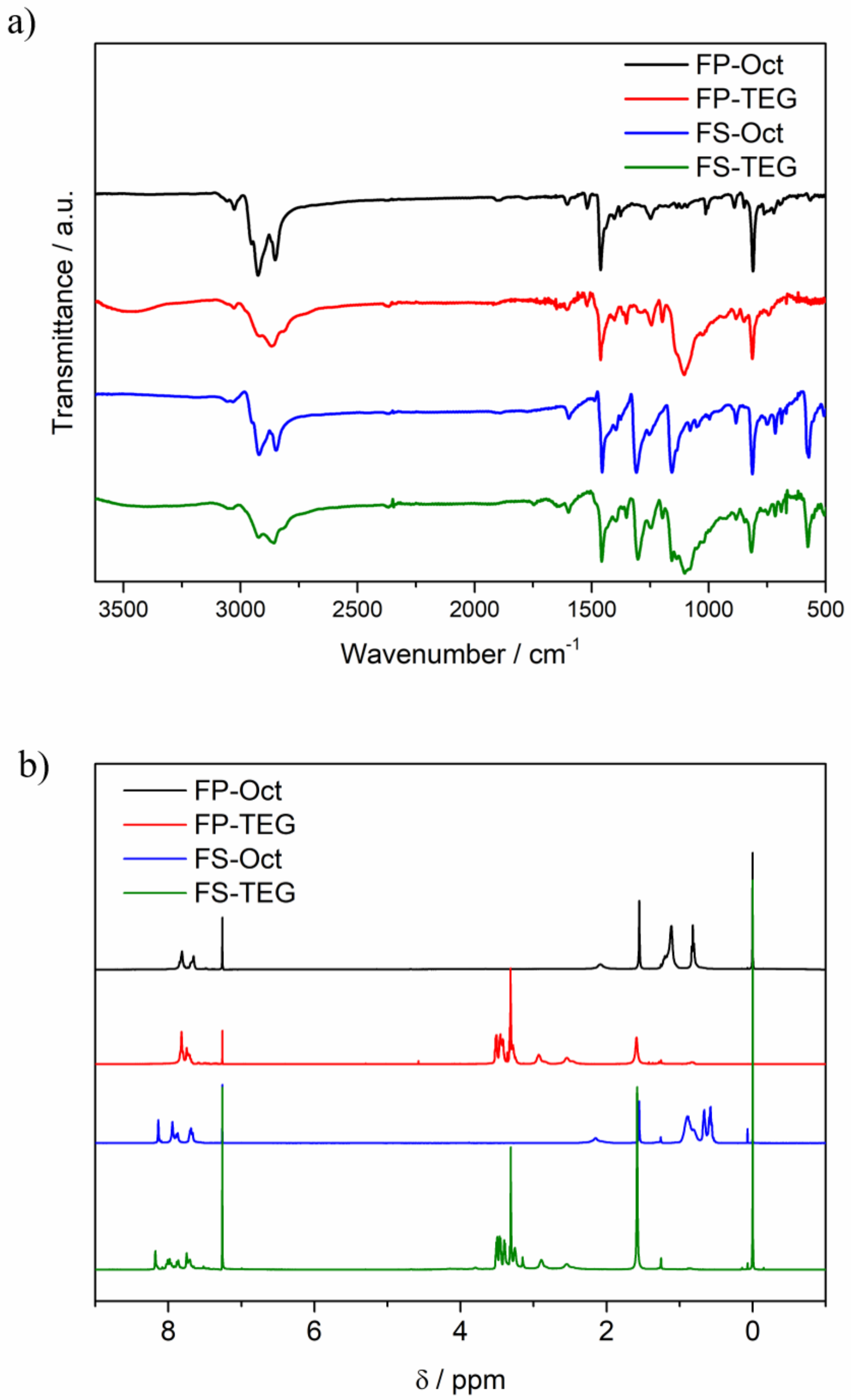

Figure 2.24. a) Transmission FT-IR spectra of **FP-Oct**, **FP-TEG**, **FS-Oct** and **FS-TEG** as KBr pellets **b)** ^{1}H NMR spectra of **FP-Oct**, **FP-TEG**, **FS-Oct** and **FS-TEG** in $CDCl_3$. Peaks of residual impurities correspond to chloroform (7.26 ppm) and water (1.56 ppm).

The molecular weights of **FP-TEG** and **FS-TEG** are lower than octyl-substituted polymers (M_w = 12,300 and 8700 g mol^{-1} compared to 27,300 and 25,400 g mol^{-1} respectively). TGA showed lower onsets of thermal degradation for OEG-substituted polymers (**FP-TEG**: T_d = 249 ºC, **FS-TEG**: T_d = 280 ºC. **Figure 2.25**) but these temperatures are still suitable for photocatalytic applications.

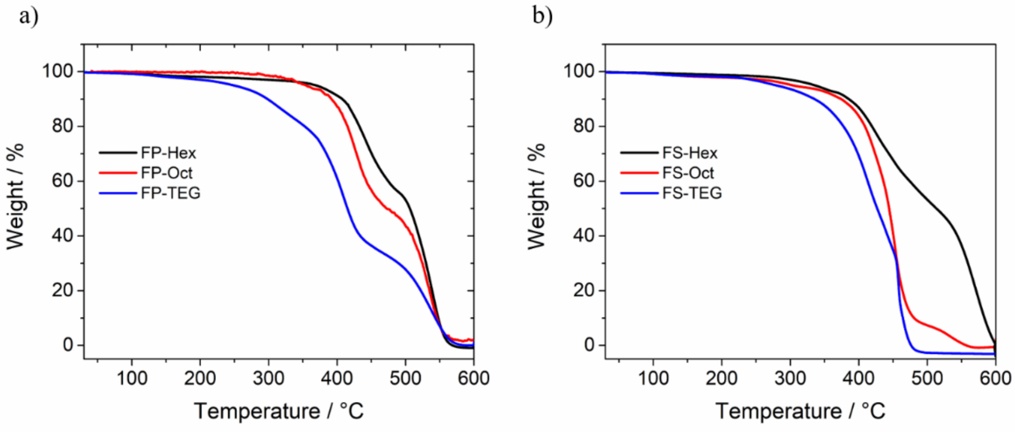

Figure 2.25. TGA traces of **a) FP-Hex**, **FP-Oct** and **FP-TEG** and **b) FS-Hex**, **FS-Oct** and **FS-TEG** in air at a heating rate of 10 °C min^{-1}.

The nature of the side-chain does not appear to significantly alter the absorption and emission profiles of these polymers in solution (**Figure 2.27** and **Figure 2.28a** and **b**). The molar extinction coefficients are also similar; **FP-TEG** has an extinction coefficient between those of **FP-Hex** and **FP-Oct** ($\varepsilon = 3.8 \times 10^5$ m^2 mol^{-1} *vs.* 3.3 and 4.2×10^5 m^2 mol^{-1} respectively) while **FS-TEG**'s is marginally higher than its alkylated analogues ($\varepsilon = 5.6 \times 10^5$ m^2 mol^{-1} *vs.* 4.5 and 5.3×10^5 m^2 mol^{-1} for **FS-Hex** and **FS-Oct**). Thin films of **FP-TEG** and **FS-TEG** are slightly red-shifted relative to their alkylated counterparts (**Figure 2.27c** and **Figure 2.28c**) as expected from previous studies.[44] **FS-TEG** powder has a notably red-shifted absorption onset relative to powders of alkylated **FS** polymers (**Figure 2.28e**).

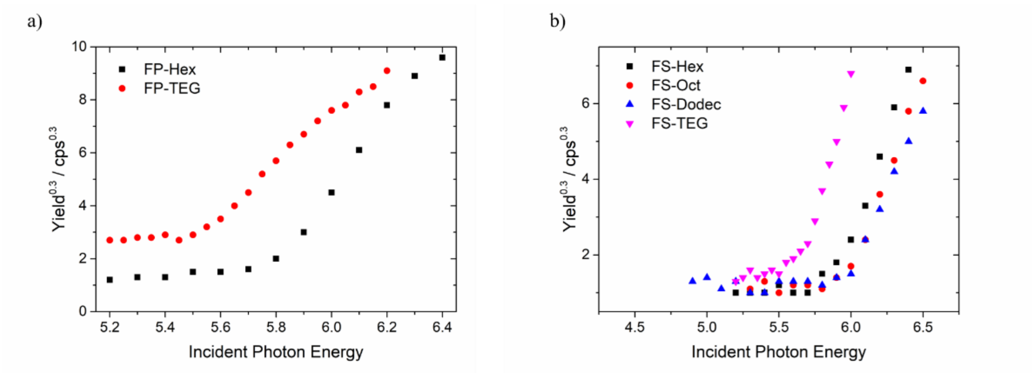

Figure 2.26. PESA traces of **a) FP** polymers and **b) FS** polymers.

Photoelectron spectroscopy in air (PESA), performed on films of the polymers, was used to determine the ionisation potentials (IPs) of these polymers (**Table 2.7**, **Figures 2.26** and **2.49**). The IP values of **FP-TEG** and **FS-TEG** (+ 1.09 and 1.24 eV *vs*. SHE) are both shifted to less deep values, relative to vacuum, than their alkylated analogues (**FP-Hex** and **FS-Hex** = + 1.33 and 1.37 eV *vs*. SHE). This actually reduces the driving force for TEA oxidation and, subsequently, overall proton reduction. Therefore, although a narrowing of the band gap in TEG-substituted polymers may contribute to improved harvesting of visible light, their shallower IPs are less favourable for hydrogen evolution in the conditions used here.

Table 2.7. Workfunction and ionisation potential *vs*. SHE of **FP-Hex**, **FP-TEG**, **FS-Hex** and **FS-TEG** obtained from PESA measurements.

Polymer	**Workfunction / eV**	**IP vs. SHE / eV**
FP-Hex	5.77	+ 1.33
FP-TEG	5.53	+ 1.09
FS-Hex	5.81	+ 1.37
FS-Oct	5.96	+ 1.52
FS-Dodec	5.97	+ 1.53
FS-TEG	5.68	+ 1.24

The emissive properties of the polymers are also influenced by the nature of the side-chain. An emissive g-band is more apparent in the PL spectra of both a thin film of and, more prominently, powdered **FS-TEG** in comparison to its alkylated analogues (**Figure 2.28d** and **f**), further suggesting a difference in packing behaviour. The g-band is also evident in the PL spectrum of a film of **FP-TEG** (**Figure 2.27c**), more so than in the spectrum of powdered **FP-TEG** (**Figure 2.27e**). These results suggest a difference in packing behaviour which could influence charge transport in these materials.[45]

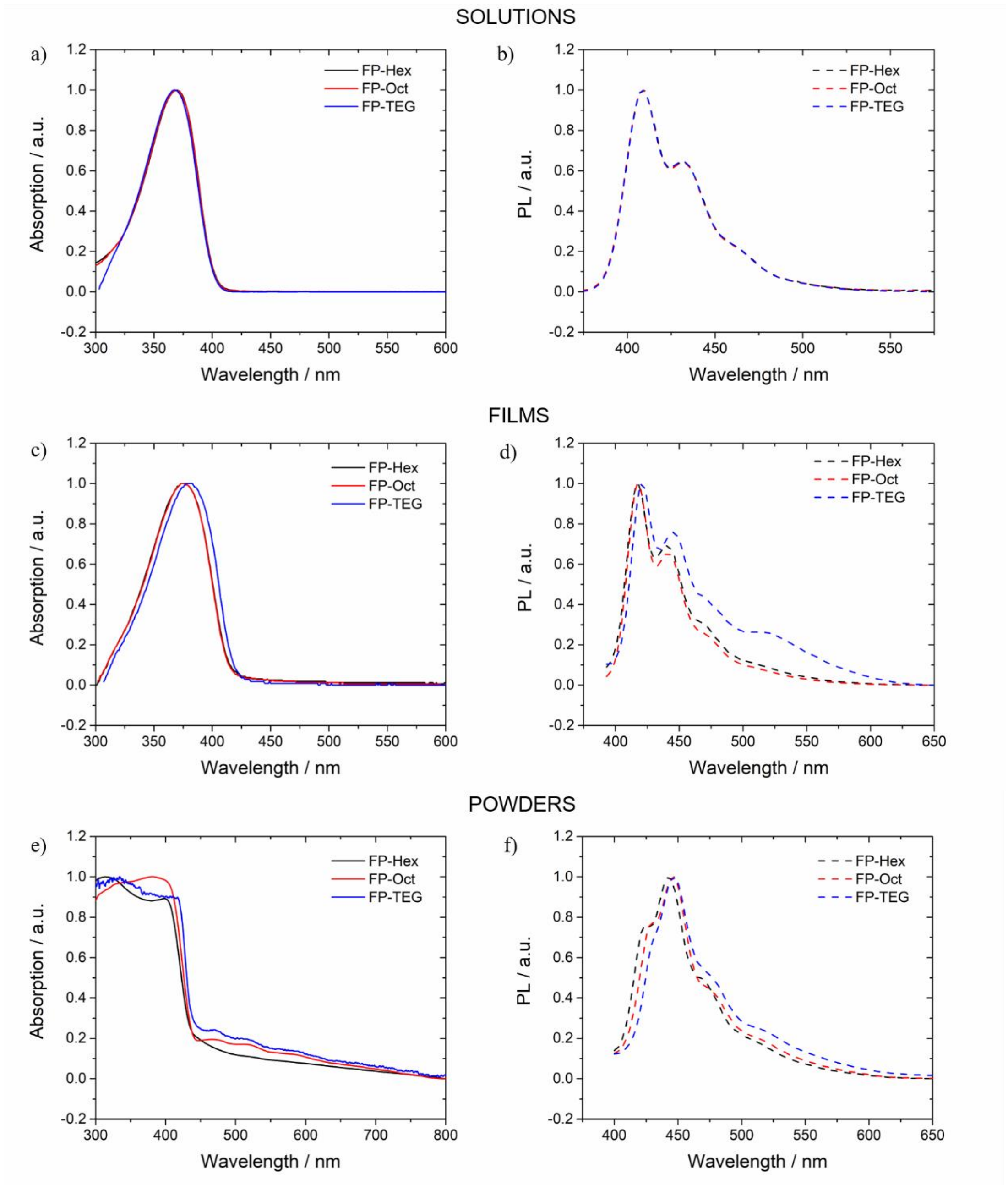

Figure 2.27. Normalised UV-vis and PL spectra of **FP-Hex**, **FP-Oct** and **FP-TEG** dissolved in chloroform (**a** and **b**), cast as spin-coated films from chloroform on glass substrates (**c** and **d**) and as powders (**e** and **f**).

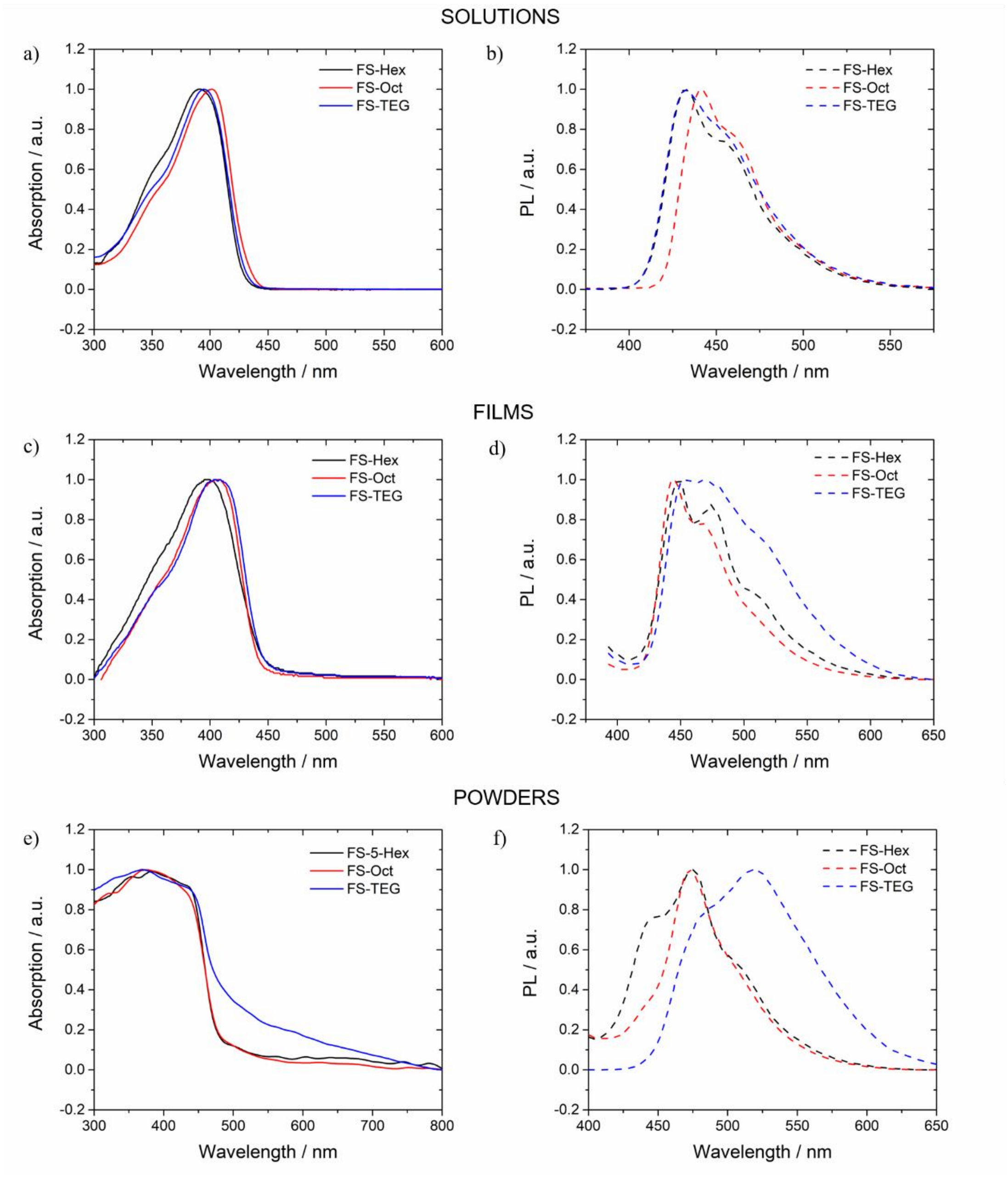

Figure 2.28. Normalised UV-vis and PL spectra of **FS-Hex**, **FS-Oct** and **FS-TEG** dissolved in chloroform (**a** and **b**), cast as spin-coated films from chloroform on glass substrates (**c** and **d**) and as powders (**e** and **f**).

The photocatalytic performances of TEG-substituted polymers are notably higher than their alkylated equivalents (**Table 2.8**). The HER of **FP-TEG** (306 μmol g^{-1} h^{-1}) was over 30 times higher than the virtually inactive alkylated **FP** polymers (HER < 10 μmol g^{-1} h^{-1}). Moreover, **FS-TEG** has a HER more than double that of **FS-Hex** (2900 ± 100 vs. 1370 ± 20 μmol g^{-1} h^{-1}). Incorporation of TEG chains therefore seems to significantly enhance the photocatalytic performance of these polymers.

Table 2.8. Selected properties and photocatalytic HERs of hexyl-, octyl- and TEG-substituted **FP** and **FS** polymers.

Polymer	**M_n / g mol^{-1}**	**M_w / g mol^{-1}**	**Đ**	**Optical gap / eV**	**ε / 10^5 m^2 mol^{-1}**	**CA (H_2O) / °**	**HER / μmol g^{-1} h^{-1}**	**HER / μmol mmol^{-1} h^{-1}**
FP-Hex	18,200	43,200	4.4	2.97	3.3	92.8 ± 0.6	0	0
FP-Oct	16,300	57,900	3.6	2.98	4.2	101.4 ± 0.6	5.2 ± 0.3	2.4 ± 0.1
FP-TEG	8200	12,300	1.5	2.94	3.8	73 ± 1	306 ± 6	163 ± 3
FS-Hex	3800	8200	2.2	2.80	4.5	89 ± 1	1370 ± 20	750 ± 20
FS-Oct	14,900	25,400	1.7	2.83	5.3	89.3 ± 0.4	680 ± 7	410 ± 20
FS-TEG	8700	11,500	1.4	2.79	5.6	69.6 ± 0.3	2900 ± 100	1,980 ± 70

The EQE of hydrogen evolution by **FS-TEG** was measured at specific wavelengths using an LED light source (**Figure 2.29b**). Good agreement with the absorption spectrum of **FS-TEG** was observed thus confirming the photocatalytic nature of hydrogen evolution. An EQE of 10.0 ± 0.5% at 420 nm, comparable to the DBTS homopolymer (**P10** = 11.6 ± 0.5% at 420 nm).[35] The long-term performance of **FS-TEG** was demonstrated over 90 hours, with over 2.1 mmol of hydrogen evolved (**Figure 2.29a**). Hydrogen evolution was also observed by dispersions of **FS-TEG** in other scavenger systems, although the water/methanol/TEA (1:1:1) mixture enabled the highest performance (**Figure 2.71**).

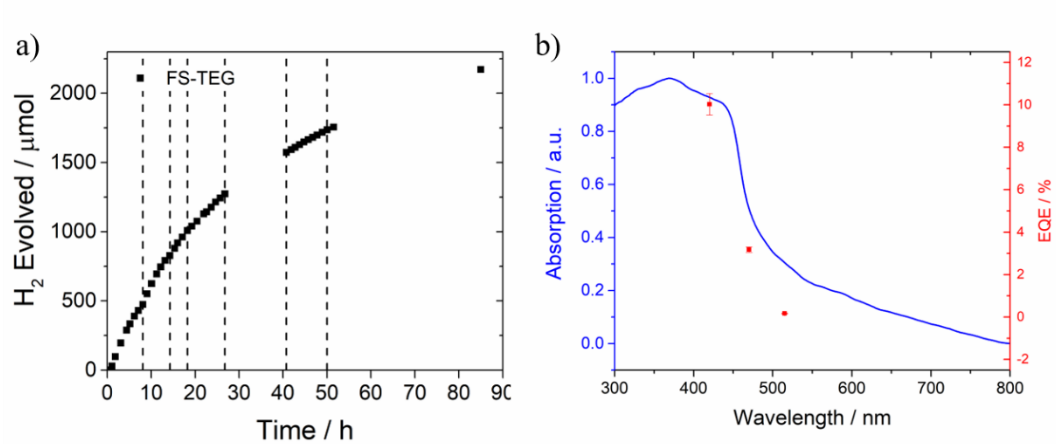

Figure 2.29. **a)** Hydrogen evolution of **FS-TEG** (25 mg) from a water/methanol/TEA mixture under visible light irradiation over a 90 hour period with intermittent degassing (dashed lines). b) UV-vis absorption spectrum (blue trace) and EQE of hydrogen evolution (red points) of **FS-TEG.**

The difference in performance between alkyl- and TEG-substituted polymers cannot be easily explained by the findings of the characterisation performed thus far. For example, it is unlikely that the improved HER is due to the slight red-shifts observed in the absorption spectra alone. A number of further experiments were therefore conducted in an effort to rationalise the improved performance of TEG-substituted polymers.

As discussed previously, the greater hydrophilicity of the TEG side-chains might be expected to enhance performance. Molecular dynamic (MD) simulations are an effective tool for modelling the behaviour of solvated polymers in aqueous mixtures.[35,46] MD simulations were performed on oligomers of **FS-Oct** and **FS-TEG** in the water/methanol/TEA (1:1:1) mixture used in photocatalysis experiments. A more polar environment around the polymer has been shown to increase the driving force for charge transfer to TEA.[35] According to these simulations, the presence of TEG side-chains results in a higher water content in the local environment of the polymer whereas **FS-Oct** is preferentially surrounded by TEA molecules, thus creating a less polar environment (**Figure 2.30a**). The difference in behaviour can be seen more clearly in a water/TEA (1:1) mixture, in which **FS-Oct** is completely surrounded by TEA while **FS-TEG** sits at the water/TEA interface (**Figure 2.30b**). Quantitative representations of the environments around the polymer are given in (**Table 2.9**).

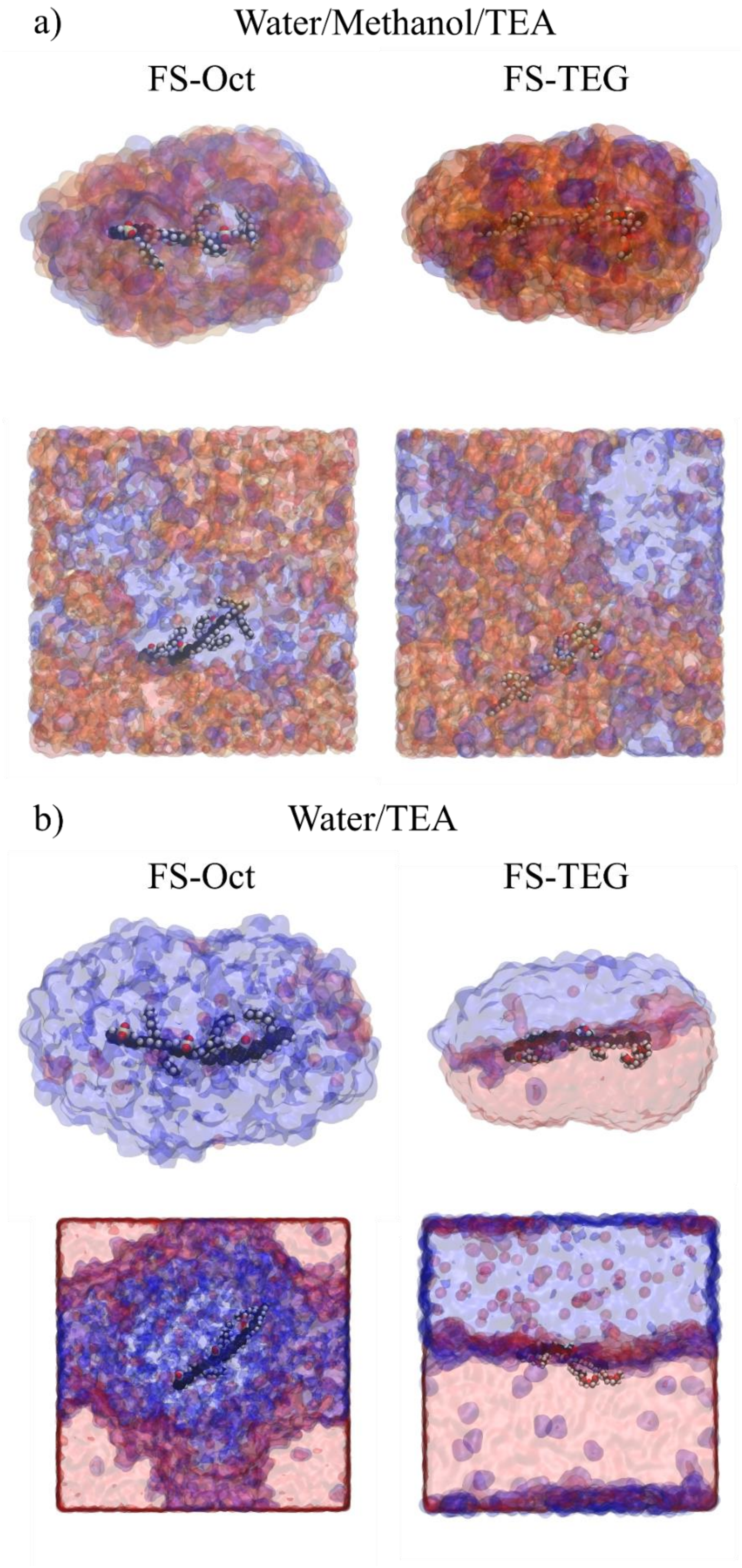

Figure 2.30. Snapshots of atomistic MD simulations of oligomers of **FS-Oct** and **FS-TEG** in **a)** water/methanol/TEA (1:1:1) and **b)** water/TEA (1:1). Blue areas are used to represent TEA, pink areas are water and orange areas are methanol.

Table 2.9. Composition of the aqueous mixtures surrounding **FS-Oct** and **FS-TEG** according to MD simulations.

Aqueous mixture	**Component**	**Vol. % 2 nm from polymer**[i]	
		FS-Oct	**FS-TEG**
Water/methanol/TEA	H_2O	24	36
	TEA	48	27
	Methanol	27	36
Water/TEA	H_2O	1	40
	TEA	98	59

[i] Percentage volume of the aqueous mixture at a distance of 2 mm from the oligomer chains used to represent the polymers in these simulations

Contact angle measurements on polymer films (**Figure 2.31**) confirm the TEG-substituted polymers to be significantly more hydrophilic. **FP-TEG** exhibits a much lower contact angle with water (72 ± 1˚) than both **FP-Hex** (92.8 ± 0.6°) and **FP-Oct** (101.4 ± 0.6°). Similarly, **FS-TEG** has a significantly reduced contact angle with water compared to **FS-Hex** and **FS-Oct** (69.6 ± 0.3˚ *vs* 89 ± 1° and 89.3 ± 0.4°). The TEG side-chains seem to enhance the wettability of these materials considerably compared to their alkylated counterparts as expected from the MD simulations.

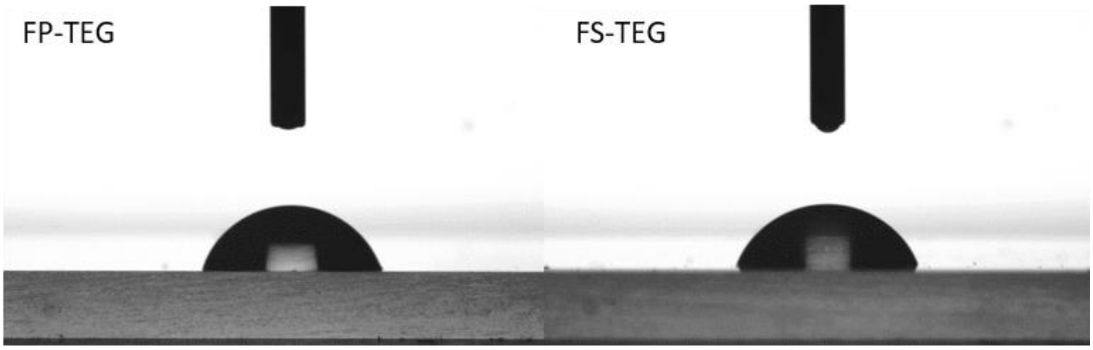

Figure 2.31. Images of water droplets on cast films of **FP-TEG** and **FS-TEG** used for contact angle measurements.

These polymers are non-porous to nitrogen with Brunauer–Emmett–Teller (BET) surface areas of 46 and 6 m^2 g^{-1} for **FS-Hex** and **FS-TEG**, respectively, which are both notably lower than **FS-Me** (114 m^2 g^{-1}, **Figure 2.32a**).[27] However, dynamic water vapour sorption (DVS) measurements showed a notably higher uptake of water for **FS-TEG** than **FS-Hex** across all relative pressures (**Figure 2.32b**). The type-III water uptake isotherm of **FS-TEG** is indicative of swelling of the polymer in an aqueous environment.[47]

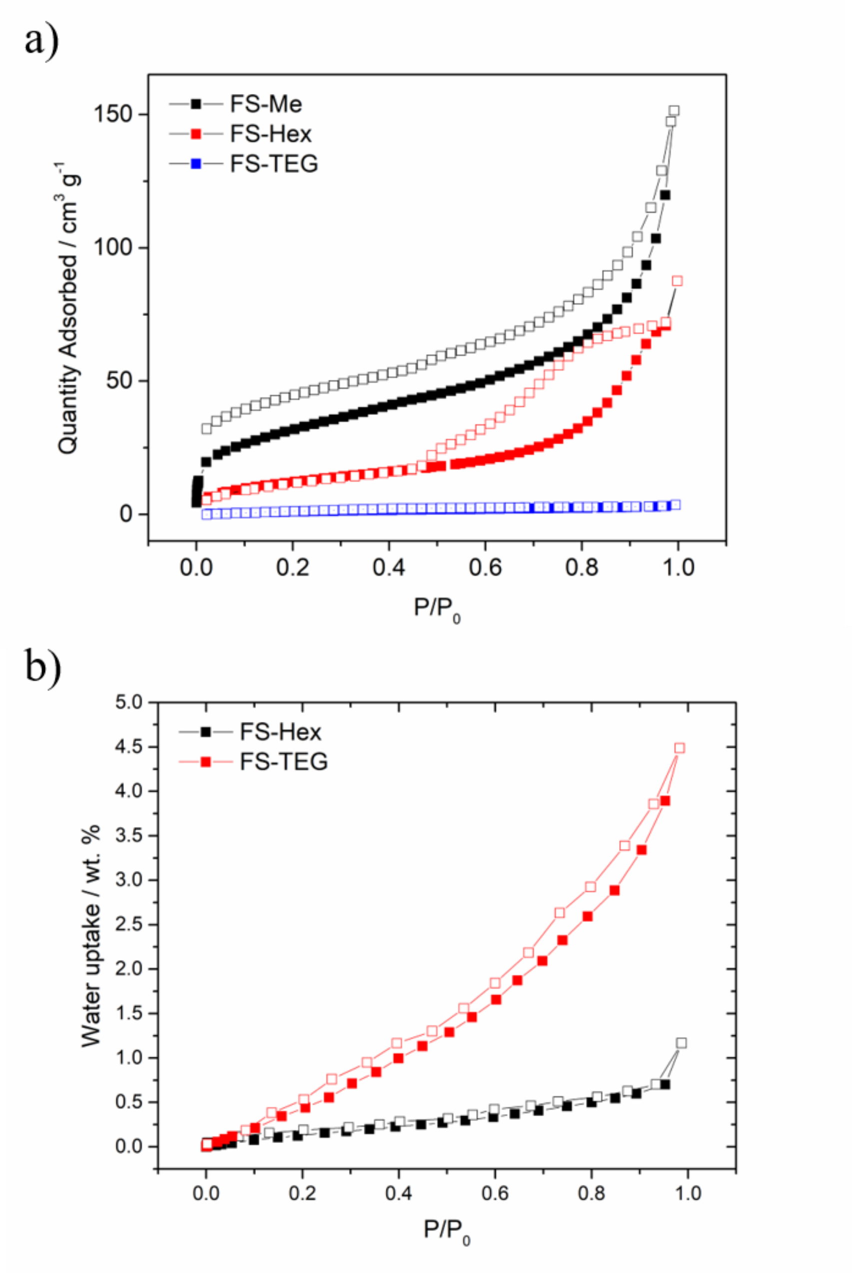

Figure 2.32. **a)** Nitrogen sorption isotherms for **FS-Me**, **FS-Hex** and **FS-TEG** measured at 77.3 K up to 1 bar (desorption curves shown as open symbols). **b)** Water vapour isotherms of **FS-Hex** and **FS-TEG** at 293.15 K up to 23 mbar.

The swelling behavior of **FS-TEG** was further investigated by atomic force microscopy (AFM) and quartz crystal microbalance gravimetry (QCM). **FS-TEG** and **FS-Hex** films were in turn measured in ambient conditions and in the presence of TEA and water. Both polymers were found to negatively swell by approximately 20% in the presence of TEA, suggesting that permeation of TEA is not significantly impacted by the nature of the side-chains (**Figure 2.33a** and **b**). However, **FS-TEG** was found to swell by 37% when exposed to water while **FS-Hex** exhibits negligible swelling. QCM measurements support this observation, indicating that the swelling of an **FS-TEG** film upon exposure to water vapour was four times that of an equivalent **FS-Hex** film (**Figure 2.33c** and **d**). These results suggest a profound difference in wetting behavior of polymers as a consequence of the presence of these different side-chains, as seen in previous investigations.[43]

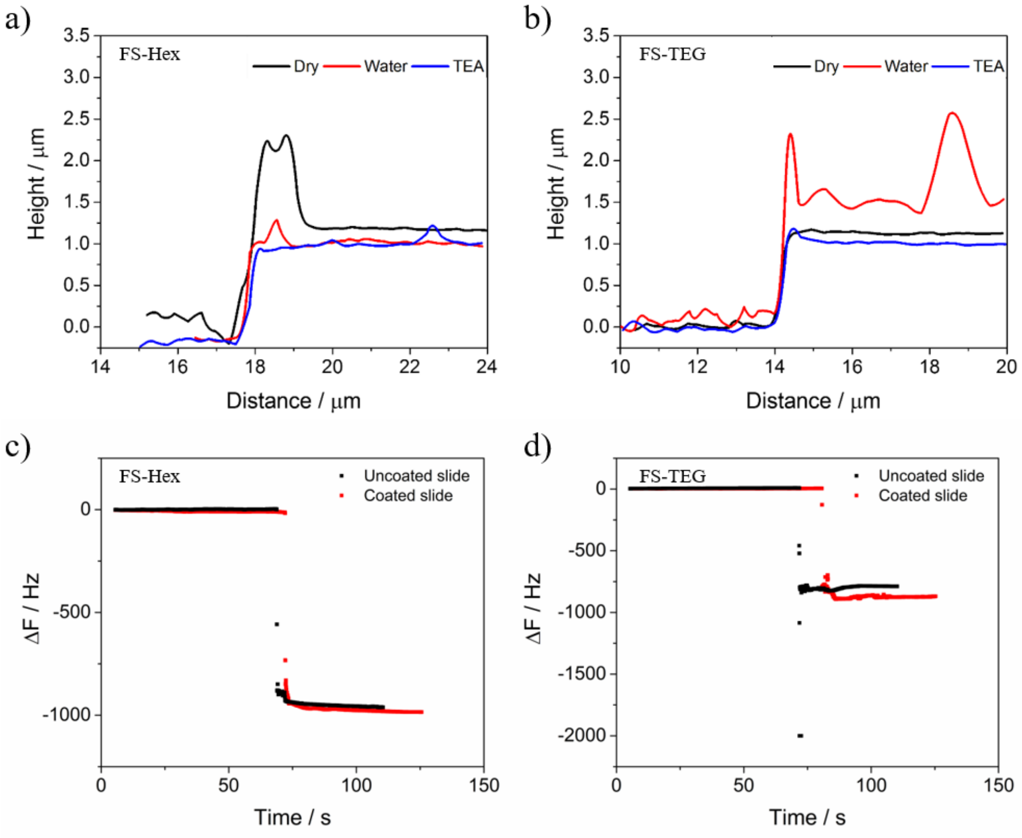

Figure 2.33. AFM profiles of films of **a) FS-Hex** and **b) FS-TEG** in dry conditions and in the presence of different liquids. QCM data showing the frequency of the bare crystal and crystal coated with **c) FS-Hex** and **d) FS-TEG**. Initial frequencies are obtained in air before a step change takes place upon submersion in water.

Increased hydrophilicity might be expected to result in reduced particle sizes in dispersions, which could account for the enhanced performance of TEG-substituted polymers. However, SLS measurements suggest that particle sizes of these polymers are not significantly different to comparable alkylated polymers (**Figure 2.34**, **Table 2.10**). **FS-TEG** particles appear to be larger than **FS-Hex** particles in both water (*D*[3,2] = 25.7 *vs.* 18.9 µm) and the water/methanol/TEA mixture used for photocatalysis (*D*[3,2] = 16.2 *vs.* 4.3 µm). The swelling behaviour of **FS-TEG** may explain this increased particle size. Regardless, reduced particle size does not appear to account for the high activity of **FS-TEG**.

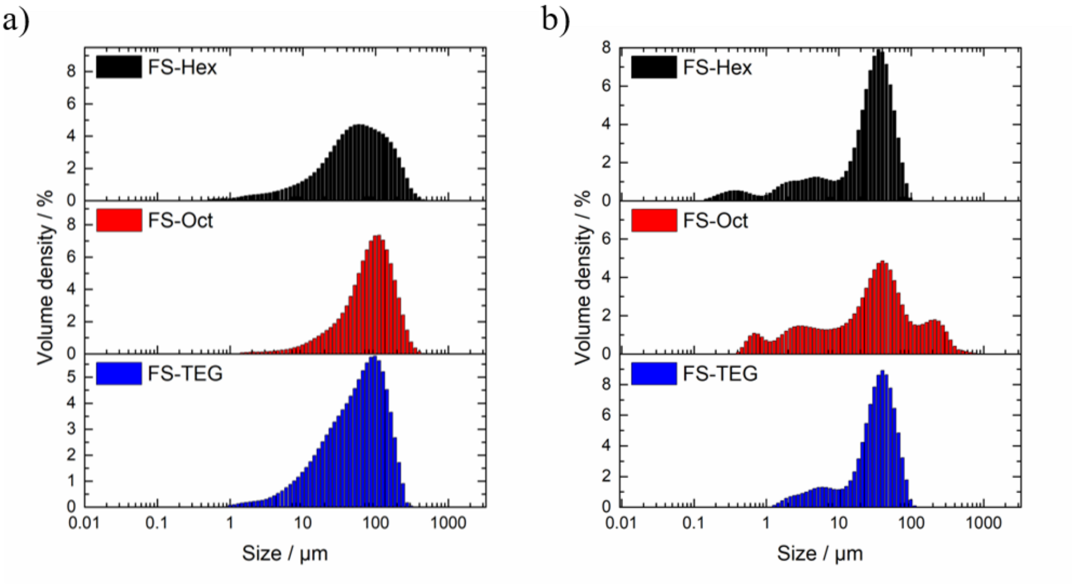

Figure 2.34. Particle size distributions of **FS-Hex**, **FS-Oct** and **FS-TEG** obtained from SLS measurements in **a)** water and **b)** water/methanol/TEA (1:1:1).

Table 2.10. Particle sizes of **FS-Hex**, **FS-Oct** and **FS-TEG** from SLS measurements.

Medium	**Polymer**	**D_x50**\ / µm	***D*[4,3]**[ii] / µm	***D*[3,2]**[iii] / µm
Water	**FS-Hex**	58.4	82.7	18.9
	FS-Oct	92.9	106	45.4
	FS-TEG	61.8	75.3	25.7
Water/MeOH/TEA	**FS-Hex**	29.7	30.9	4.3
	FS-Oct	33.3	63.1	6
	FS-TEG	35.8	37.3	16.2

[i] 50th Percentile of particle size volume distribution

[ii] Volume mean diameter

[iii] Surface area mean diameter (Sauter mean diameter).

Transient absorption spectroscopy (TAS) was used to gain greater insight into the photophysics of these polymers and to further probe how increased hydrophilicity may lead to enhanced photocatalytic activity. The nature of species formed upon initial photoexcititation in water/methanol/TEA mixtures were first established using femtosecond-TAS (fs-TAS). Three key features are evident in the fs-TAS spectra of both polymers (λ_{exc} = 360 nm); two positive peaks, one around 600 nm and another which extends to wavelengths above 750 nm, and a negative feature in the region of 470-500 nm (**Figure 2.35a** and **b**). The 750 nm peak is due to absorption of the exciton while the negative feature can be attributed to photoluminescence from the excitonic state, as has previously been observed in similar polyfluorenes.[48]

The feature centred around 600 nm decays much slower than the excitonic features, as shown by the deconvoluted kinetics of this species (**Figure 2.35c**). A significant proportion of this feature remains for both polymers 6 ns after excitation, at which point the excitonic absorption has decayed to virtually zero. This feature is not seen when the polymers are dispersed in a water/methanol mixture (**Figure 2.35d** and **e**) and is therefore assigned, as with **P8-s** previously, to the formation of an electron polaron. This is in good agreement with previous work, in which a similar positive feature (λ_{max} = 630 nm) in the spectrum of a dibenzo[*b*,*d*]thiophene sulfone homopolymer was also attributed to a polymer anion.[35]

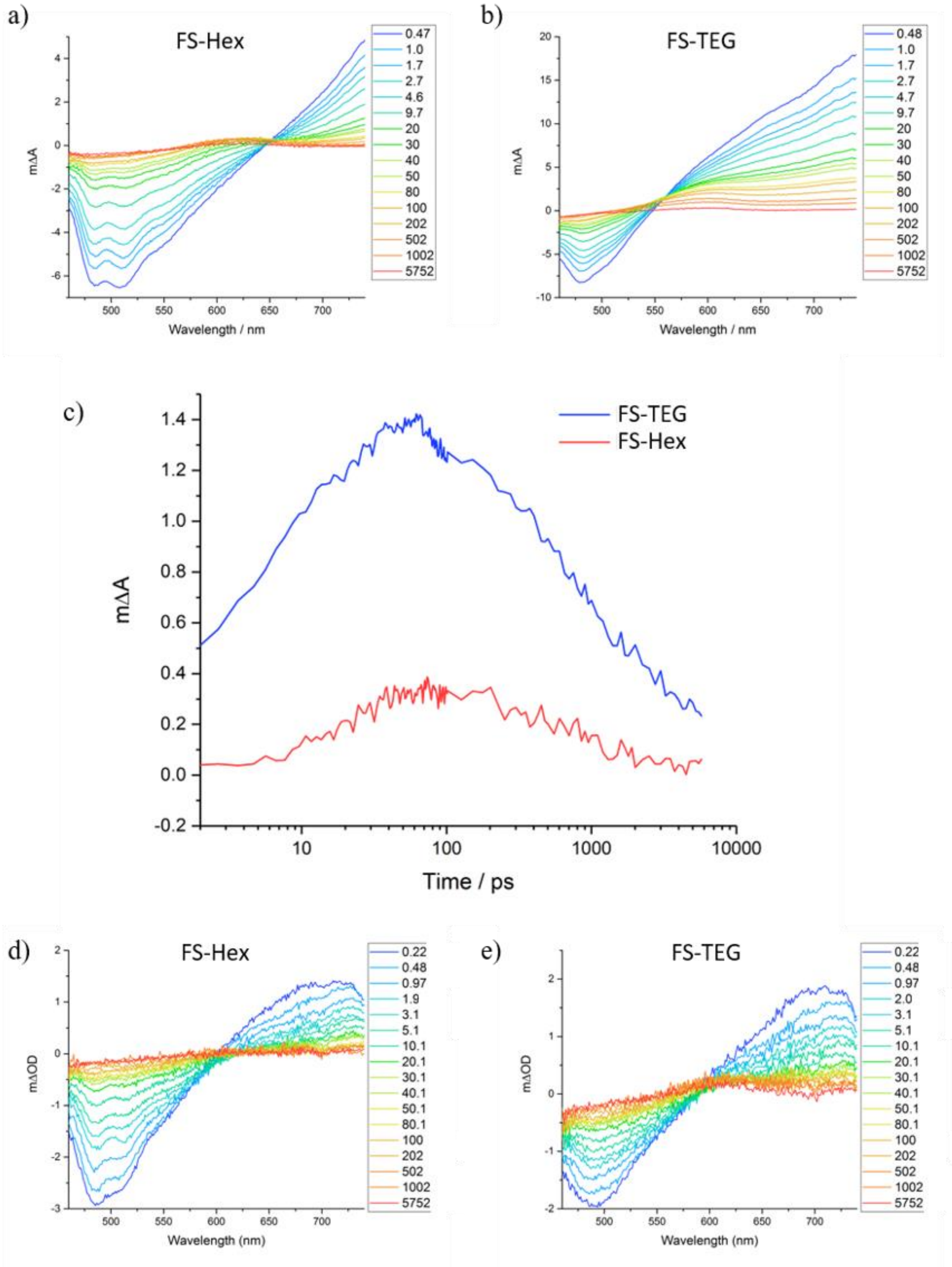

Figure 2.35. fs-TAS spectra of **a) FS-Hex** and **b) FS-TEG** dispersed in water/methanol/TEA (0.2 mg mL^{-1}) at the specified times (ms) after excitation. **c)** Deconvoluted fs-TAS kinetics of the peak at 600 nm. fs-TAS spectra of **d) FS-Hex** and **e) FS-TEG** dispersion in water/methanol (0.2 mg mL^{-1}) at the specified times (ms) after excitation. All spectra obtained using fluences of 87 µJ cm^{-2}.

Microsecond-TAS (µs-TAS) was performed to analyse the difference in longer-lived excited state species, on the timescale at which proton reduction is expected to occur. µs-TAS spectra of **FS-Hex** (**Figure 2.36a**) and **FS-TEG** (**Figure 2.36b**) dispersed in water/methanol/TEA mixtures both have the same 600 nm polaronic absorption peak as seen in fs-TAS. As with fs-TAS, µs-TAS performed on dispersions in a water/methanol mixture showed no absorption features (**Figure 2.36c** and **d**).

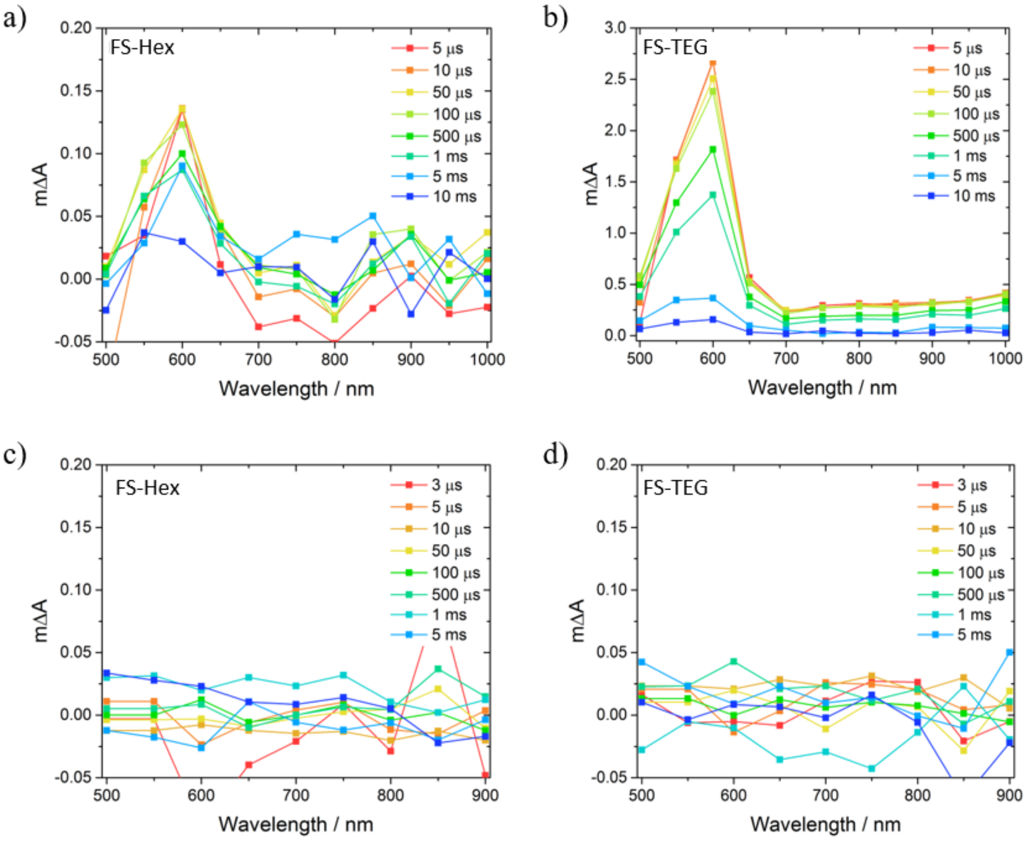

Figure 2.36. **a)** µs-TAS spectra of **a) FS-Hex** and **b) FS-TEG** dispersed in water/methanol/TEA and water/methanol (c and **d)** at the specified times after excitation (0.2 mg mL^{-1}, excitation fluence of 1.5 mJ cm^{-2}, λ_{exc} = 420 nm).

The assignment of the electron polaron was corroborated by spectroelectrochemical (SEC) measurements of an **FS-TEG** film. In SEC measurements an electrical potential was applied and the steady state absorption spectrum of the reduced polymer was monitored *in situ*. When a negative bias greater than -1.7 V is applied to the film, a single absorption peak (λ_{max} = 585 nm) grows into the absorption spectrum (**Figure 2.37**). The strong similarity between the reduced polymer's absorption spectrum and the spectra measured by TAS gives confidence in the assignment of the 600 nm TAS feature as the electron polaron.

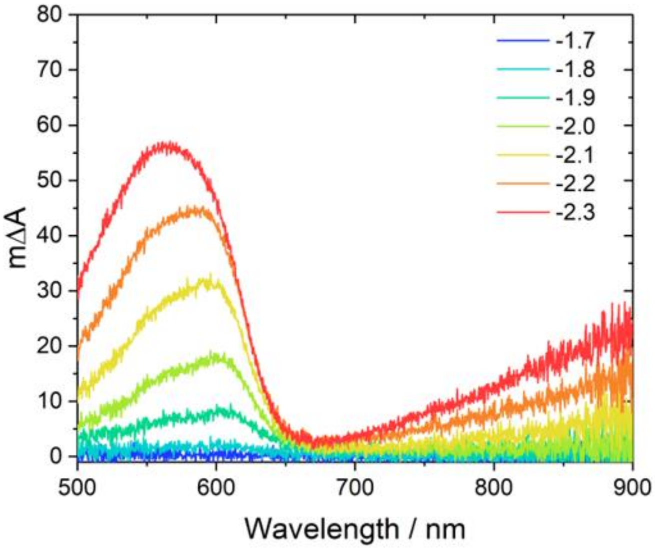

Figure 2.37. Difference in absorption of an **FS-TEG** film in acetonitrile and tetrabutylammonium hexafluorophosphate under negative bias (of specified voltage) and the spectrum of a film at open circuit.

Although the same spectral features are present regardless of the nature of the side-chain, the TAS experiments reveal key differences between **FS-TEG** and **FS-Hex**. When dispersions of the same concentration (0.02 mg mL^{-1}) are illuminated under identical conditions, the amplitude of the electron polaron signal initially formed by **FS-TEG** is significantly higher than **FS-Hex** (**Figure 2.38a**). This indicates that the number of photogenerated electrons strongly influences the photocatalytic performance of these materials.

The polymers also differ in terms of charge carrier lifetimes. When the exciton density of **FS-TEG** in the sample is identical to **FS-Hex** (achieved by using a lower fluence for **FS-TEG** than **FS-Hex**) the exciton lifetime is substantially longer in **FS-TEG** (**Figure 2.38b**). The deconvoluted spectrum shows that photogenerated electrons in **FS-TEG** also decay notably slower than those in **FS-Hex** (**Figure 2.38c**). In the fs-TAS experiments, electrons appear to decay at a similar rate in **FS-Hex** and **FS-TEG** (**Figure 2.35a** and **b)**. However, as the electron densities in both materials reduce beyond the timescales of the fs-TAS measurements, the electrons decay at a slower rate in **FS-TEG** than **FS-Hex**. This improvement in charge carrier lifetime may be due to the greater water content surrounding **FS-TEG** creating a more polar environment that stabilises the polaronic state.

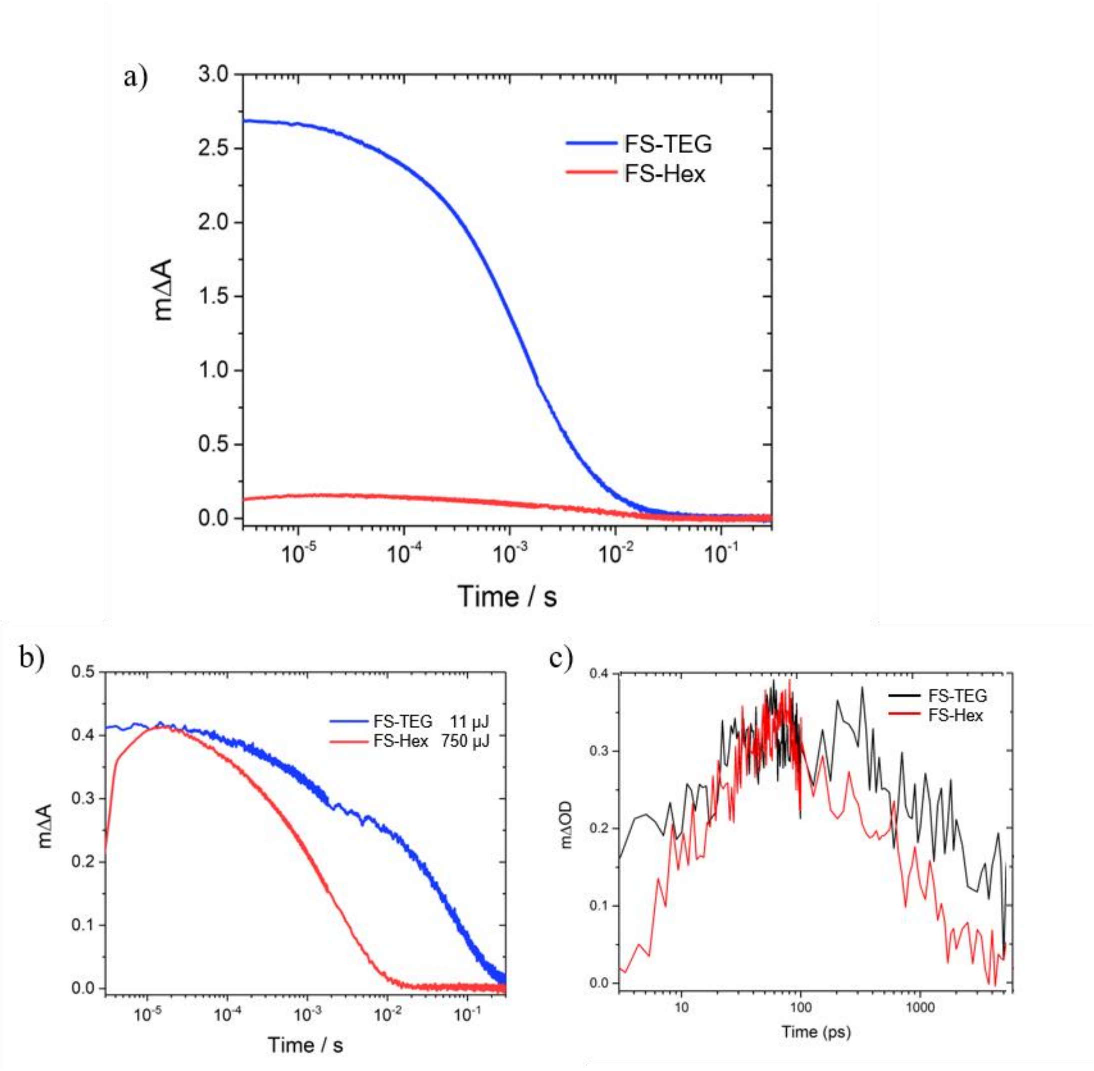

Figure 2.38. **a)** μs-TAS kinetics of the feature at 600 nm for 0.02 mg mL^{-1} dispersions of **FS-Hex** and **FS-TEG** in water/methanol/TEA, excitation fluence of 1.5 mJ cm^{-2}. **b)** Comparison of kinetics when **FS-Hex** and **FS-TEG** dispersions in water/methanol/TEA are excited at different fluences in order to achieve equivalent maximum exciton densities. **FS-Hex** was excited at 0.02 mJ cm^{-2} (11μJ) and **FS-TEG** was excited at 1.5 mJ cm^{-2} (750 μJ). **c)** Comparison of deconvoluted electron kinetics, probed at 600 nm.

Other factors besides increased wettability may also contribute to the improved performance of TEG-substituted polymers. It has been reported that the reduced number of CH_2–CH_2 steric interactions in OEG side-chains reduces the energy barrier to rotation of these chains and enables closer π-π stacking than in equivalent alkylated polymers.[49,50] In these studies, closer packing was inferred from shifted peak maxima in grazing incidence x-ray diffraction (GIXRD) patterns. GIXRD was attempted on films spin-coated on silicon wafers to determine if this is the case in the polymers reported here. However, the poor crystallinity of these polymers gave rise to low signals that could not be accurately resolved. While the broad peaks of PXRD patterns should be analysed with caution, peak maxima do appear to be shifted to higher values for TEG-substituted polymers, possibly indicating closer stacking ($2\theta_{\mathbf{FP\text{-}Oct}}$ = 18.9°, $2\theta_{\mathbf{FP\text{-}TEG}}$ = 20.3°, $2\theta_{\mathbf{FS\text{-}Oct}}$ = 20.2°, $2\theta_{\mathbf{FS\text{-}TEG}}$ = 21.4°) (**Figure 2.39**). However, 2-ethylhexyl side-chains appeared to induce even closer stacking ($2\theta_{\mathbf{FP\text{-}EtHex}}$ = 20.6 °, $2\theta_{\mathbf{FS\text{-}EtHex}}$ = 21.8 °, **Figure 2.19**). **FS-EtHex** has the lowest HER of all **FS** polymers studied here, implying that inter-chain stacking distances may not be critical to photocatalytic performance.

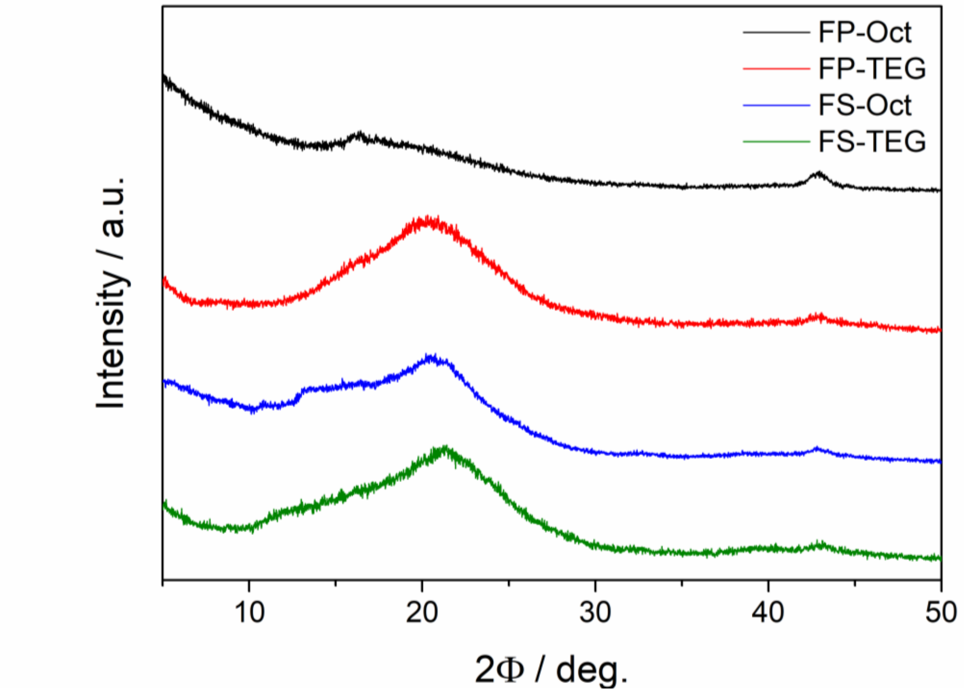

Figure 2.39. PXRD patterns of **FP-Oct**, **FP-TEG**, **FS-Oct** and **FS-TEG**.

To summarise, TEG-substituted polymers have notably higher HERs than equivalent alkylated polymers. The factors affecting photocatalytic performance are characteristically inter-related and difficult to isolate. However, increased photocatalytic performance appears to correlate with greater interaction of the TEG side-chains with water. The ability of TEG-substituted polymers to attract water, as suggested by MD simulations, seems to generate an environment more favourable for charge transfer which stabilises charge carriers and increases their lifetimes. The apparent ability of TEG-substituted polymers to swell in the presence of water may also enhance performance by increasing the interface with water. The optimum length of OEG side-chains will now be studied to see if HERs can be further enhanced.

2.3.2.3. Modifying OEG Side-chain Length

FS polymers with di(ethylene glycol) (**FS-DEG**) and tetra(ethylene glycol) (**FS-TeEG**) side-chains were compared to the previously discussed **FS-TEG**. Monomers were synthesised using the same literature procedure[36] as the TEG-substituted monomer before Suzuki-Miyaura polycondensations were, once again, performed using identical conditions. NMR spectra indicate the presence of the different side-chains in the chloroform-soluble fractions of the polymers (**Figure 2.41**).

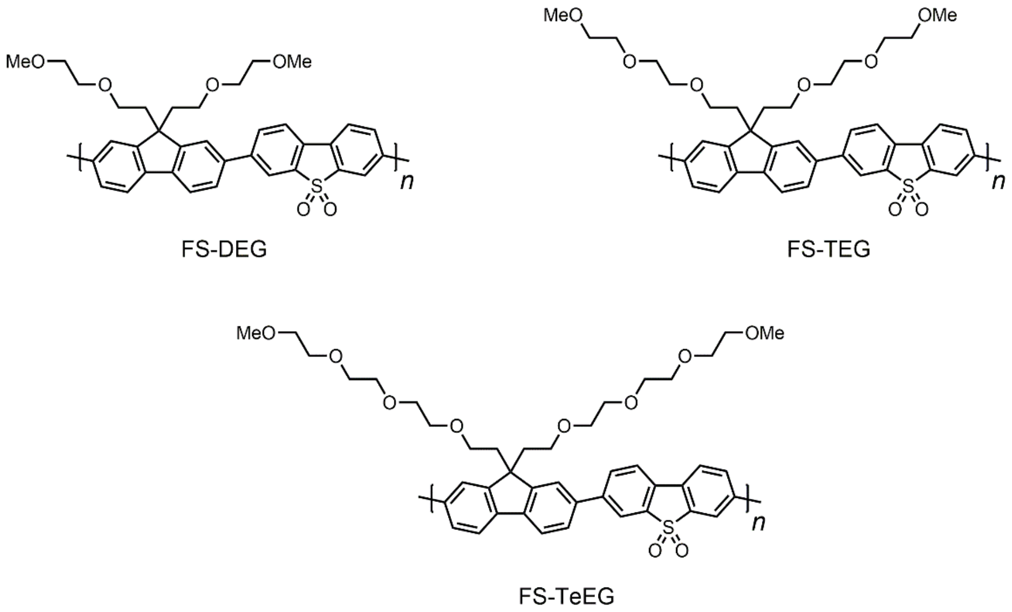

Figure 2.40. Structure of **FS-DEG**, **FS-TEG** and **FS-TeEG** polymers.

GPC results suggest increased OEG side-chain length enables higher molecular weights (**Table 2.11**), presumably as a result of greater solubility in the reaction mixture. PXRD patterns suggest that the polymers are similarly amorphous (**Figure 2.42a**) with no apparent relationship between stacking distances and OEG side-chain length according to the position of the peak maxima ($2\theta_{\textbf{FS-TEG}} < 2\theta_{\textbf{FS-DEG}} < 2\theta_{\textbf{FS-TeEG}}$). TGA also shows the polymers to have similar T_d (**Figure 2.42b**) while, as expected, contact angles with water reduce with increasing OEG side-chain length (**Figure 2.42c**).

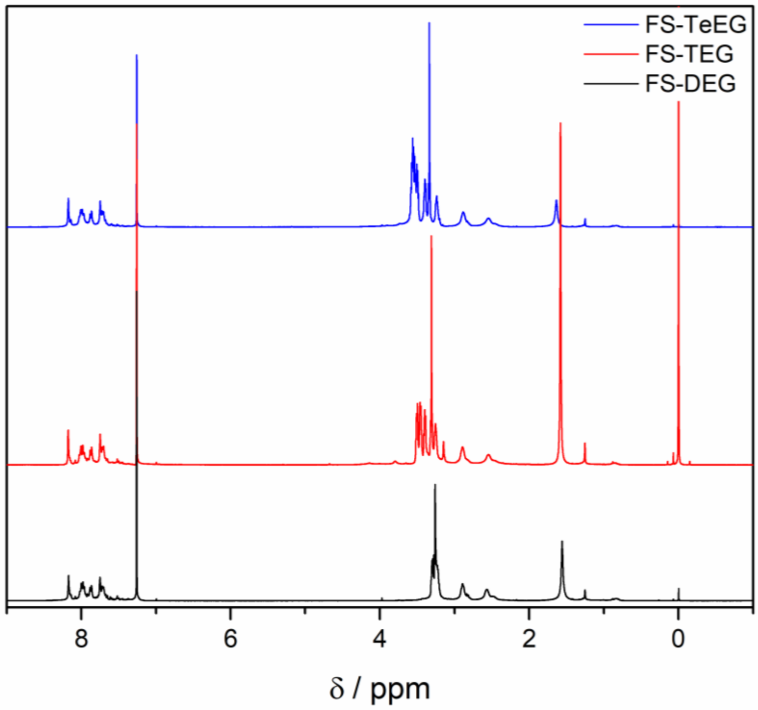

Figure 2.41. ^{1}H NMR spectra of **FS-DEG**, **FS-TEG** and **FS-TeEG** in $CDCl_3$. Peaks of residual impurities correspond to chloroform (7.26 ppm), water (1.56 ppm) and grease (1.26, 0.86 ppm).

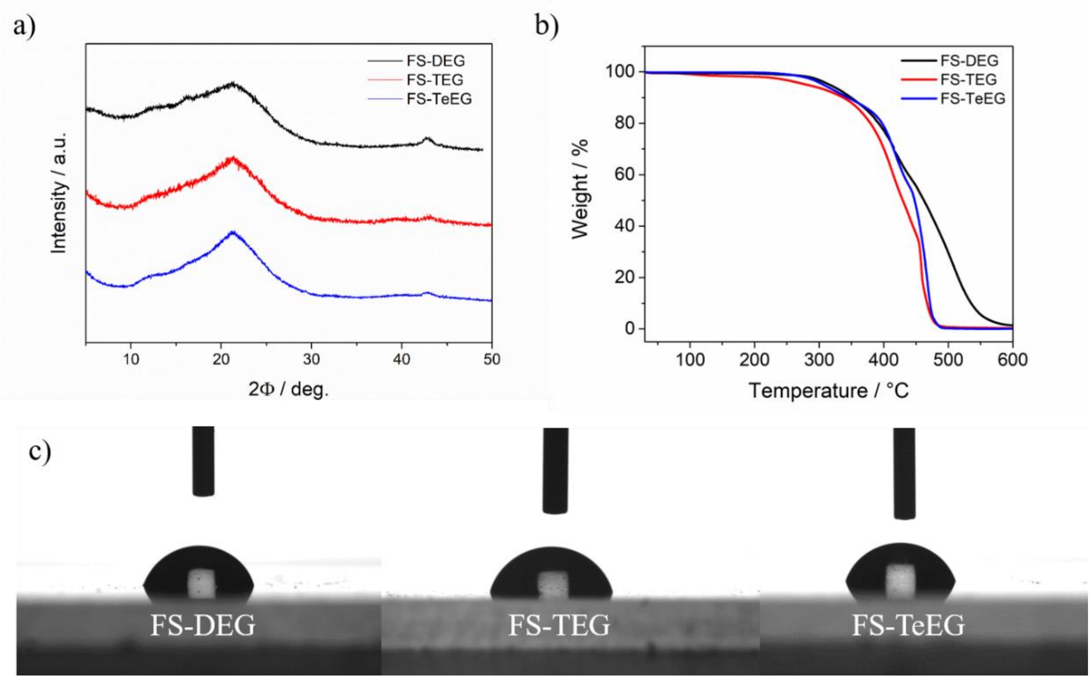

Figure 2.42 a) PXRD patterns, **b)** TGA traces in air at a heating rate of 10 °C min^{-1} and **c)** Images of water droplets on the surface of glass slides with drop-cast films of **FS-DEG**, **FS-TEG** and **FS-TeEG**.

Molar extinction coefficients of the polymers seem to increase with increased side-chain length (**Table 2.11**). This may be due to the higher molecular weights of polymers with longer side-chains, although a weaker correlation between molecular weight and extinction coefficient was previously observed in the two series of alkylated polymers. Polymers display near identical absorption and emission spectra in solution (**Figure 2.43a** and **b**). Films display a marginally red-shifted absorption profile with increasing OEG side-chain length and **FS-TeEG** has a slightly broadened emission spectrum (**Figure 2.43c** and **d**).

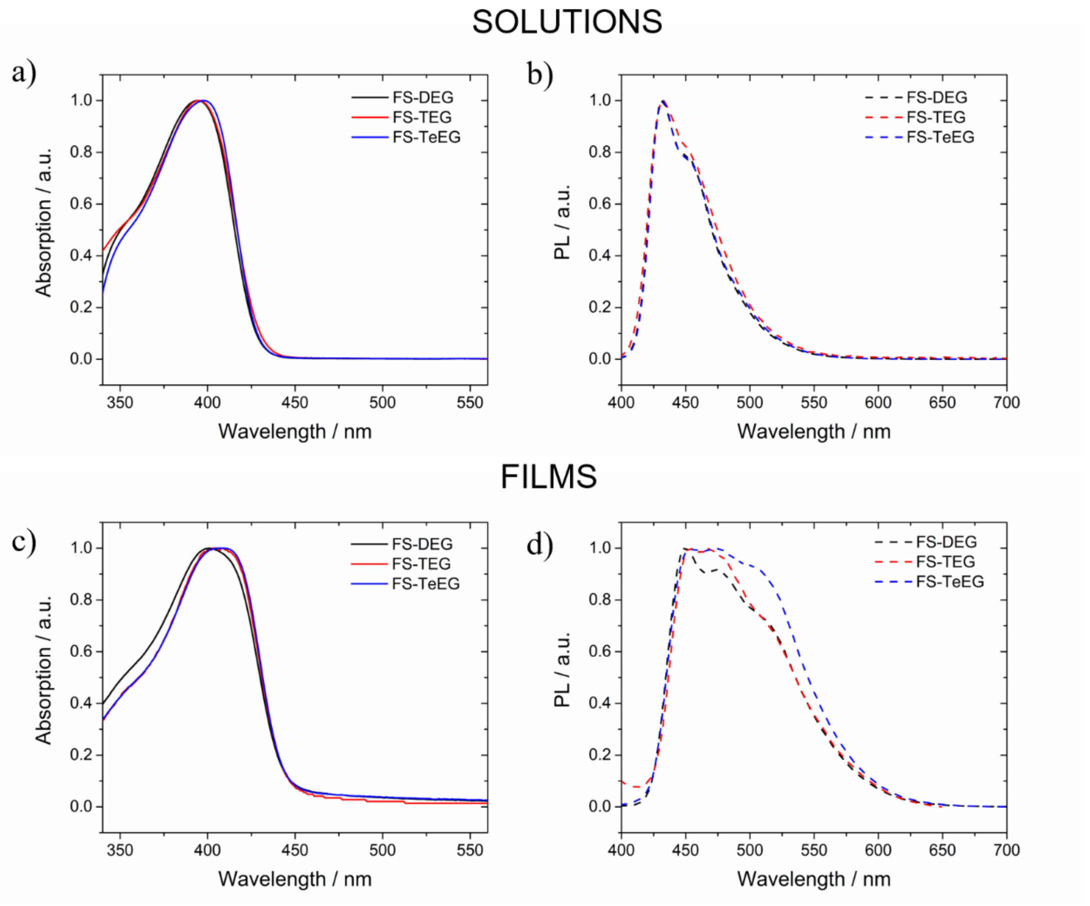

Figure 2.43. Normalised UV-vis and PL spectra of **FS-DEG**, **FS-TEG** and **FS-TeEG** dissolved in chloroform (**a** and **b**) and cast as spin-coated films from chloroform on glass substrates (**c** and **d**).

Table 2.11. Selected properties and photocatalytic HERs of **FS-DEG**, **FS-TEG** and **FS-TeEG**.

Polymer	**M_n / g mol^{-1}**	**M_w / g mol^{-1}**	**Đ**	**Optical gap / eV**	**ε / 10^5 m^2 mol^{-1}**	**CA (H_2O) / °**	**HER[i] / µmol g^{-1} h^{-1}**	**HER[i] / µmol mmol^{-1} h^{-1}**
FS-DEG	3500	5200	1.49	2.791	4.7	73.9 ± 0.7	2100 ± 80	1,220 ± 50
FS-TEG	6400	8700	1.35	2.792	5.6	69.6 ± 0.3	2900 ± 100	1,980 ± 70
FS-TeEG	7600	13,500	1.78	2.793	7.9	67.2 ± 0.7	626 ± 9	475 ± 7

[i] HERs of polymers (25 mg) measured in water/methanol/TEA (22.5 mL) under visible light irradiation using a 300 W Xe light source.

TEG units appear to be the optimum length of OEG side-chain for enhancing photocatalytic performance within this series of polymers (**Table 2.11**, **Figure 2.44**). The HER of **FS-DEG** is somewhat lower than **FS-TEG** (2100 ± 80 *vs.* 2900 ± 100 µmol g^{-1} h^{-1}), possibly because of its lower extinction coefficient, lower molecular weight or, more likely, reduced hydrophilicity of the shorter DEG side-chains. However, the HER of **FS-TeEG** is significantly lower than both **FS-DEG** and **FS-TEG,** some four times lower than **FS-TEG** when normalised to the mass of the repeating unit (475 ± 7 *vs.* 1980 ± 70 µmol mmol^{-1} h^{-1}). This drop-off in performance with the addition of a single ethylene glycol unit into the side-chains—despite the seemingly preferential properties including increased molecular weight, molar extinction coefficient and hydrophilicity—is striking. It is possible that the longer side-chains may inhibit charge transport between polymer chains or interfere with the mechanism of photocatalysis by shrouding the polymer backbone. Alternatively, longer TeEG side-chains may be ‘too’ hydrophilic, with the low TEA content inhibiting the rate of proton reduction. Performing MD simulations on these polymers with different OEG side-chains would be useful to investigate this further.

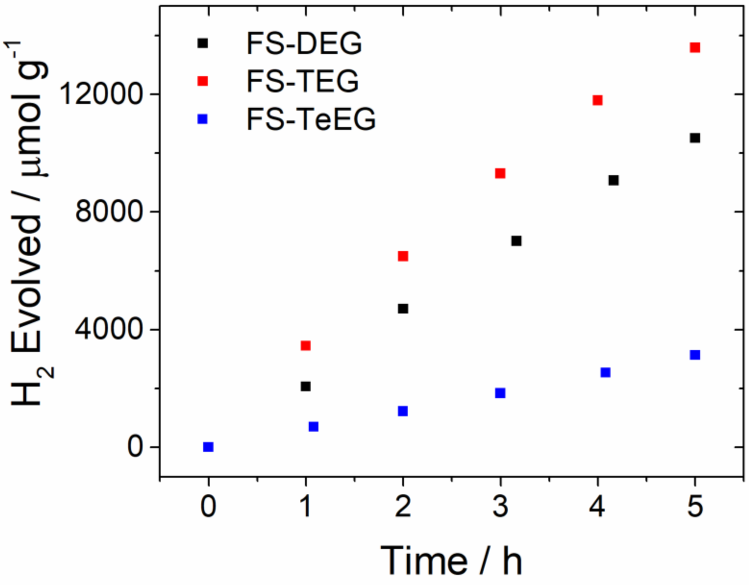

Figure 2.44. Hydrogen evolution runs of **FS-DEG**, **FS-TEG** and **FS-TeEG** (25 mg) in water/methanol/TEA (1:1:1, 22.5 mL) under visible light irradiation. Amount of hydrogen evolved normalised to the mass of photocatalyst present.

In conclusion, TEG side-chains appear to represent the optimum length of OEG side-chain for achieving high hydrogen evolution rates in these polymers. Modifying the OEG side-chain length was shown to markedly affect photocatalytic performance. These results further underline the significant influence that side-chain modification can have on photocatalytic activity. So far, little consideration has been given to the polymer backbone in these polymers, the modification of which has been shown to radically effect the photocatalytic performance of linear polymers in a multitude of studies.[1,51,52]

2.4. Backbone Variation in Solution-Processable Polymer Photocatalysts

2.4.1. Comonomer Variation

2.4.1.1. Incorporation of Dibenzo[*b,d*]thiophene Sulfone

The backbones of conjugated polymers are inherently insoluble in common organic solvents. As previously discussed, solubilising side-chains can be readily attached to the fluorene moiety at the 9-position. Poly(9,9-di-*n*-octylfluorenyl-2,7-diyl) (PFO) is considered a benchmark solution-processable conjugated polymer and was therefore selected as the starting point for this work.[23] The HER of PFO under visible light irradiation was, however, found to be negligible. It was anticipated that the systematic incorporation of the dibenzo[*b,d*]thiophene sulfone (DBTS) unit into the backbone of an alkylated polyfluorene polymer could enhance activity.

The DBTS unit has been identified as being well suited for photocatalytic hydrogen evolution from water.[1,35,53] The large static dipole moment of the DBTS unit (5.7 D) attracts water molecules which orientate themselves to form a shell around the sulfone group, thus making electron transfer from the sacrificial electron donor more thermodynamically favourable.[35] The incorporation of DBTS will of course influence a host of other properties including optical properties and charge transport.[25] Incorporation of DBTS into fluorene oligomers and polymers has been found to enhance charge transfer between chains, lower the LUMO energy level and improve electron mobility in materials that are intrinsically more suited to hole transport.[54–56]

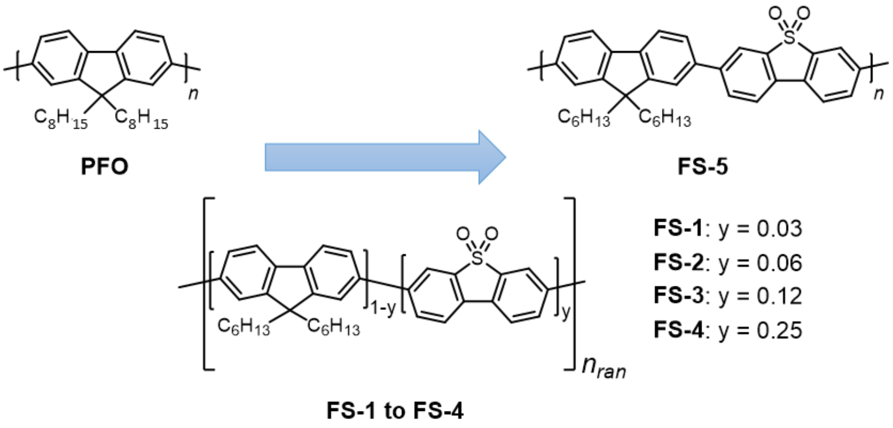

Figure 2.45. Structure of **PFO** and the **FS-1** to **FS-5** series of polymers where the content of dibenzo[*b,d*]thiophene sulfone is increasing as shown.

The DBTS content was varied in a series of fluorene-dibenzo[*b,d*]thiophene sulfone (**FS**) polymers by changing the composition of the monomer feed (**Figure 2.45**). The dibrominated monomer composition was changed from 5% 3,7-dibromodibenzo[*b*,*d*]thiophene 5,5-dioxide and 95% 2,7-dibromo-9,9-di-*n*-hexyl-9*H*-fluorene for **FS-1** up to 100% 3,7-dibromodibenzo[*b*,*d*]thiophene 5,5-dioxide for **FS-5**.[e] This resulted in the series of polymers **FS-1** to **FS-5** with DBTS contents of 3, 6, 12, 25 and 50% respectively, randomly distributed through the polymers (**Figure 2.45**). **FS-1** to **FS-4** were obtained in high yield although the high DBTS content in **FS-5** meant it was not fully soluble and a significant amount of insoluble material (40% yield) was also obtained. Once again, only the chloroform-soluble fraction will be compared to the other polymers in this series.

As anticipated, incorporation of DBTS significantly enhances photocatalytic performance (**Table 2.12**). This seems to correlate with a reduced contact angle with water and also a narrowing of the band gap. Interestingly, there is no clear correlation between the light-absorbing ability of these polymers and DBTS content within this series. The absorption onset shifts approximately 20 nm from **PFO** to **FS-5**) enabling greater harvesting of visible light. This is more prominent in films (**Figure 2.46c**) but a red-shift is also evident in solution (**Figure 2.46a**).

A change in the emissive band of polymers with increased DBTS content is also observed in solution (**Figure 2.46b**). This has previously been observed in a similar study and attributed to the formation of an intramolecular charge transfer state in the chloroform solvent.[57] A similar broadening is apparent in the emission spectra of films (**Figure 2.46d**) across the series along with a red-shift concurrent with the absorption spectra.

---

[e] NB. **FS-5** = **FS-Hex**, previously discussed in **Chapter 2.3.1.2**.

Table 2.12. Selected properties and photocatalytic HERs of **PFO**, **FS-1**, **FS-2**, **FS-3**, **FS-4** and **FS-5**.

Polymer	**DBTS content / mol.%**	**M_n / g mol^{-1}**	**M_w / g mol^{-1}**	**Đ**	**Optical gap / eV**	**ε / 10^5 m^2 mol^{-1}**	**CA (H_2O) / °**	**HER[i] / µmol g^{-1} h^{-1}**
PFO	0	44,600	144,000	3.2	3.00	3.0	99 ± 2	0
FS-1	2.5	14,800	51,700	3.5	3.00	6.8	98 ± 1	5
FS-2	6.25	16,800	74,500	4.4	2.98	5.3	96 ± 1	18
FS-3	12.5	18,900	97,800	5.2	2.95	5.7	93 ± 1	15
FS-4	25	11,100	50,900	4.6	2.92	4.3	86 ± 8	238
FS-5	50	3800	8200	2.2	2.80	3.7	88 ± 1	1370 ± 20

[i] HERs of polymers (25 mg) measured in water/methanol/TEA (22.5 mL) under visible light irradiation using a 300 W Xe light source.

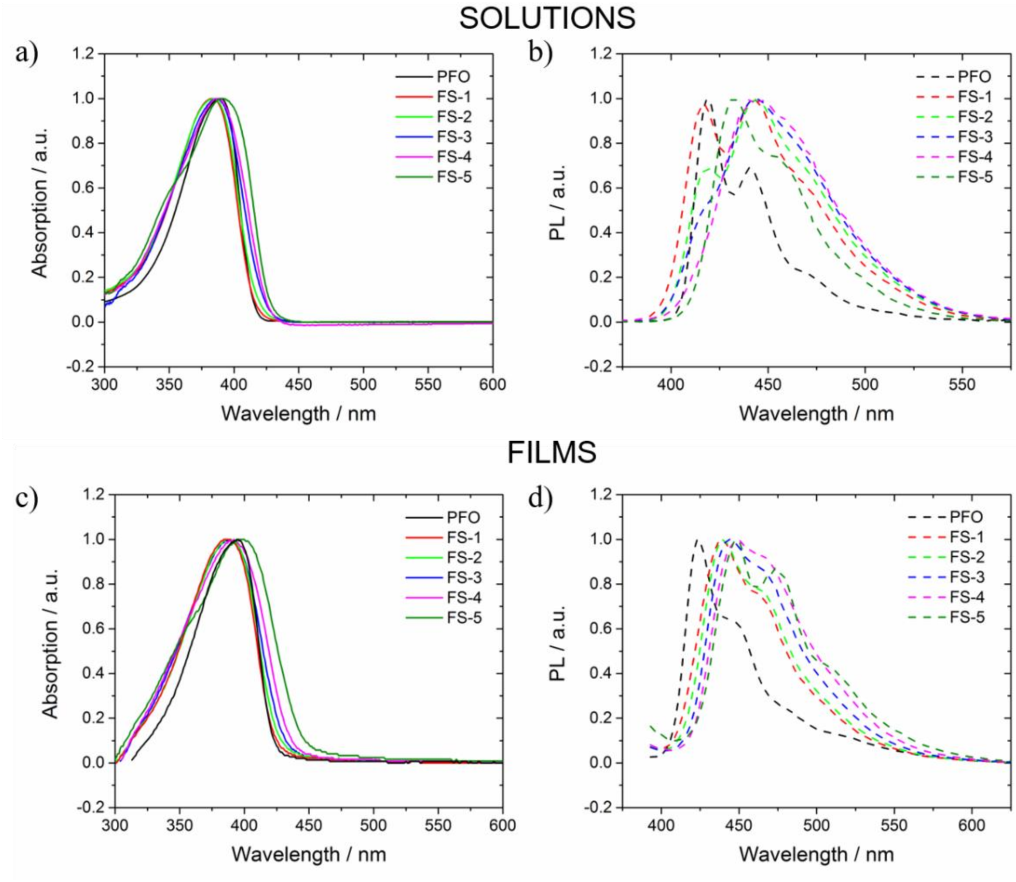

Figure 2.46. Normalised UV-vis and PL spectra of **PFO, FS-1, FS-2, FS-3, FS-4 and FS-5** dissolved in chloroform (**a** and **b**) and cast as spin-coated films from chloroform on glass substrates (**c** and **d**).

The band positions must also be considered in conjunction with absorption onsets. Whereas side-chain variation does not significantly alter the potentials, changing the backbone structure is likely to appreciably influence the electronic structure and, therefore, the driving force for hydrogen evolution. Computational predictions of the potentials of these polymers were made using time-dependent density functional theory ((TD)-DFT)), a quantum mechanical method commonly used to predict the band structure of conjugated polymers.[58–61]

The ionisation potential (IP) represents the energetic cost of removing an electron from the top of the polymer's valence band. Conversely, the electron affinity (EA) of the ground-state photocatalyst is the energy released by addition of an electron to the bottom of the conduction band. IP* and EA* represent the ionisation potential and electron affinity of the excited-state of the polymer, which must also be considered. The length of the alkyl side-chain is not expected to significantly affect the potentials and side-chains were therefore defined as methyl groups in all calculations to ensure computational tractability.

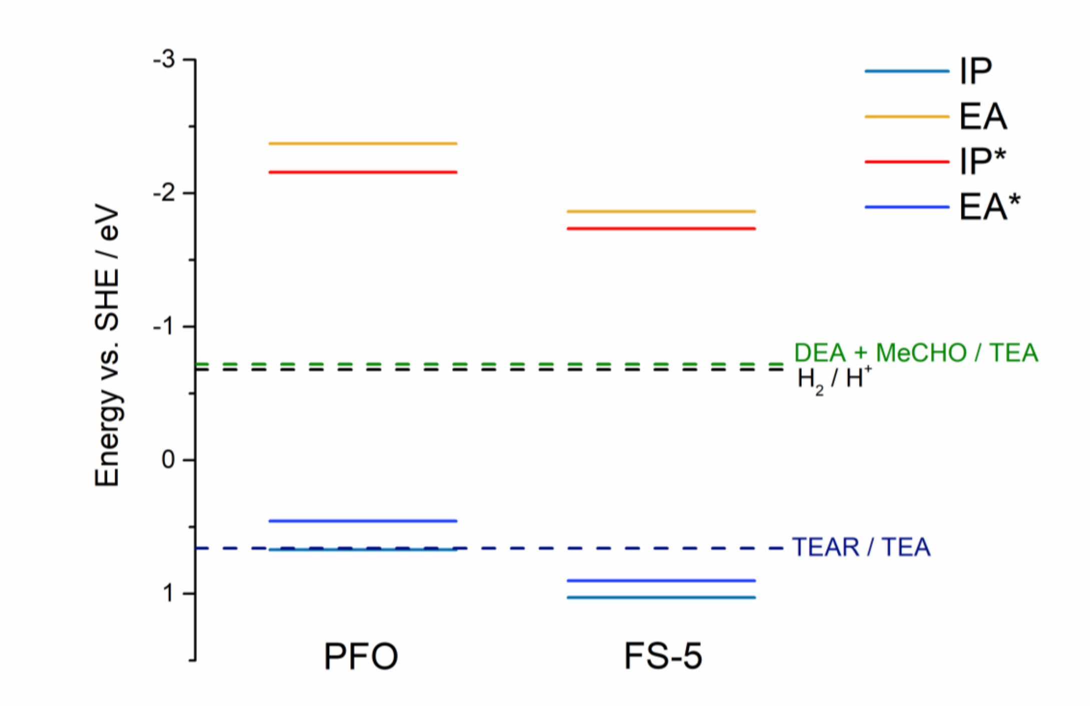

Figure 2.47. Calculated potentials of PFO and FS-5 polymers in water using (TD)-DFT vs. SHE. Predicted IP, EA, IP* and EA* potentials were calculated using a relative dielectric permittivity of 80.1 (aqueous environment). Solution potentials have been taken from previous work.[53]

(TD)-DFT calculations performed on methyl-substituted fluorene and fluorene-sulfone polymers (analogous to **PFO** and **FS-5**) resulted in the potentials shown in **Figure 2.47**. The calculated potentials, when compared to the half-reactions for proton reduction and oxidation of TEA to its radical form (TEAR) at pH 11.5 (the expected pH of a TEA solution), suggests that both polymers should have a sizeable driving force for the proton reduction half-reaction. However, the IP of **PFO** is only marginally deeper than the potential for TEA oxidation to its radical TEAR so has a weak driving force for this reaction. By contrast, the deeper (more positive) IP of **FS-5** is able to drive the reaction more strongly. These calculations suggest, therefore, that incorporation of the DBTS unit may also enhance HERs by lowering the potentials of charge carriers in these polymers increase driving force for hydrogen evolution.

μs-TAS was performed on the polymers in the photocatalysis suspensions. The same long-lived absorption around 600 nm is observed as in the spectrum of **FS-TEG** discussed previously (**Figure 2.48a)**. The amplitude of this signal appears to correlate strongly with the DBTS content of these polymers with an increased number of electrons generated upon excitation of polymers with higher DBTS content (**Figure 2.48b**). This is again expected to stem from the superior stability of the excited state in the water-rich environment instigated by the presence of sulfone moieties.[35] The polymers were excited at a wavelength at which absorption is similarly strong in all polymers. These results, therefore, suggest that it is factors relating to the greater hydrophilicty of the DBTS unit, rather than the red-shifted absorption onset, which are chiefly responsible for the increased performance of **FS-5**.

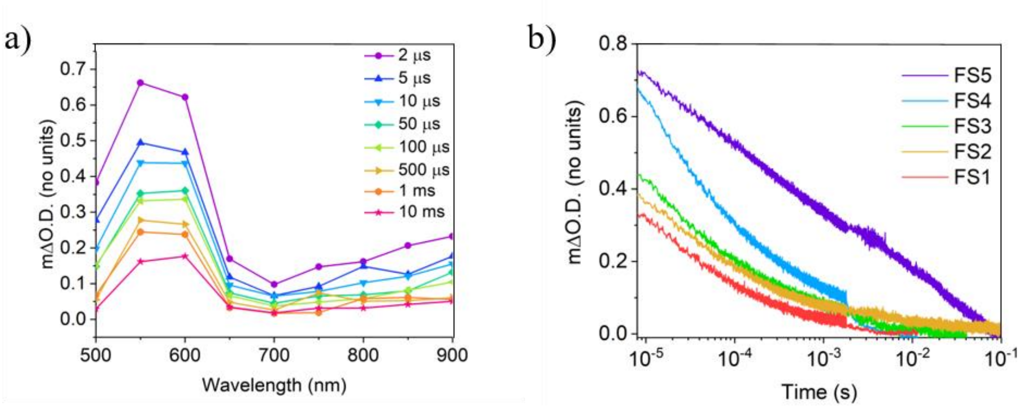

Figure 2.48. **a)** μs-TAS spectra of **FS-5** in water/methanol/TEA at the specified times after excitation and **b)** μs-TAS kinetics of the feature at 600 nm for 0.02 mg mL^{-1} dispersions of **FS-1, FS-2, FS-3, FS-4** and **FS-5** in water/methanol/TEA.

2.4.1.2. Comparison of Dibenzo[*b*,*d*]thiophene Sulfone and Phenylene in Solution-Processable Polymer Photocatalysts

The two series of fluorene-phenylene (**FP**) and fluorene-dibenzo[*b*,*d*]thiophene sulfone (**FS**) polymers were presented in **Chapter 2.3.1.2** with focus on the impact of side-chain variation on properties and photocatalytic performance within each series. This section will instead discuss how the variation in backbone structure accounts for the significant discrepancy in performance between the two series. The **FP** series have significantly lower HERs than equivalent members of the **FS** series (**Table 2.6**). The improved activity of the **FS** polymers can again be rationalised in terms of the polarity of the DBTS unit attracting water molecules and thus creating a more favourable environment for charge transfer. The absence of a static dipole moment in phenylene means the **FP** series are significantly less hydrophilic.[35] The lower contact angles of the **FS** series with water appear to support this conclusion (**FS-R** < **FP-R** in all cases, **Table 2.4**).

The band structures of these polymers are also notably affected by the variation in backbone structure. The potentials of the polymers and their excited states were again calculated using (TD)-DFT for both the case of dry polymer films and polymer films immersed in water (**Figure 2.49**).

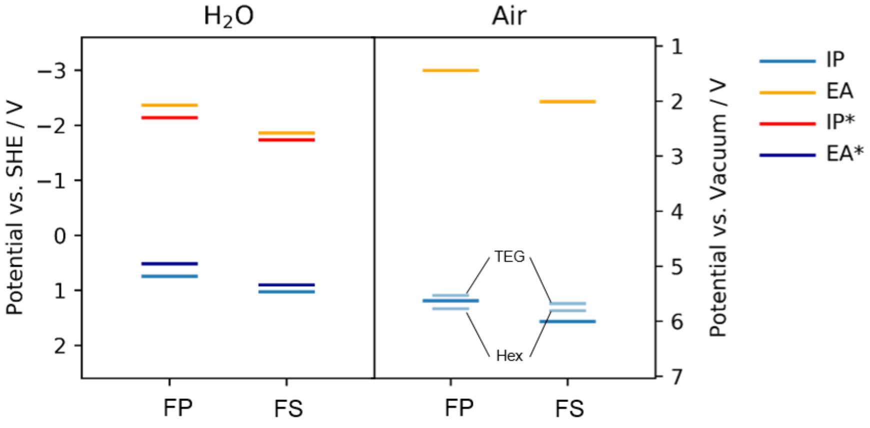

Figure 2.49. Predicted and measured potentials of the charge carriers and excitons in **FP** and **FS** polymer in the presence (left) and absence of water (right). Predicted IP/EA/IP*/EA* potentials (long lines) have been calculated using (TD)-DFT using relative dielectric permittivity values of 2 (organic environment) and 80.1 (aqueous environment). Experimental IP potentials (short lines) have been measured using PESA and are shown for FP-TEG and FS-TEG, labelled as TEG, and for **FP-Hex** and **FS-Hex**, labelled as Hex.[53]

The IP and EA values predicted for **FP-Me** and **FS-Me** in water show the same ordering as in the absence of water but the band gap is narrowed, as observed previously.[58] As in **Chapter 2.4.1.1**, both polymers exhibit a strong driving force for proton reduction. However, as with PFO, the IP of **FP-Me** is too shallow to forcibly drive TEA oxidation, whereas **FS-Me** has a slight driving force for this reaction. These calculated potentials were verified experimentally. The absorption spectra onsets of both films and solutions of the **FS** series (**Figure 2.18a** and **c**) are red-shifted in relation to the **FP** series (**Figure 2.17a** and **c**) as predicted by (TD)-DFT calculations. Band positions could also be obtained experimentally as IPs of dry films in a vacuum were measured using photoelectron spectroscopy in air (PESA). The measured IP values are similar to those predicted computationally. These results corroborate the findings of (TD)-DFT calculations and suggest that reduced driving force for overall proton reduction by **FP** polymers in sacrificial conditions could also explain their reduced photocatalytic performance.

The physical properties of the two series also differ, albeit more subtly. The different backbones of **FP** and **FS** polymers also influences their relative solubilities in chloroform. The presence of two octyl side-chains enables complete solubility of **FP-Oct** which was obtained in high yield (72%) whereas an insoluble higher molecular weight fraction was also obtained for **FS-Oct**, leading to a lower yield of soluble material (37%). TGA shows analogous members of the two series have similar T_d although degradation is less stepwise for **FS** polymers. Degradation takes place rapidly upon heating from 400 to 500 °C suggesting the DBTS unit is less thermally stable than phenylene but is still suitable for photocatalysis (**Figure 2.16**). As previously discussed, although most polymers in both series can be considered amorphous, **FS** polymers with shorter side-chains have a degree of crystallinity (**Figure 2.19**). The morphologies of polymers in the two series are also visibly different. Particles of **FP** polymers formed after precipitation in methanol have a spongier texture (**Figure 2.50**), presumably due to the apolar nature of **FP** polymers influencing how they ‘crash out’ in methanol. Larger particle sizes of the more hydrophobic **FP** polymers may also affect their photocatalytic performance, although this was not measured in this study.

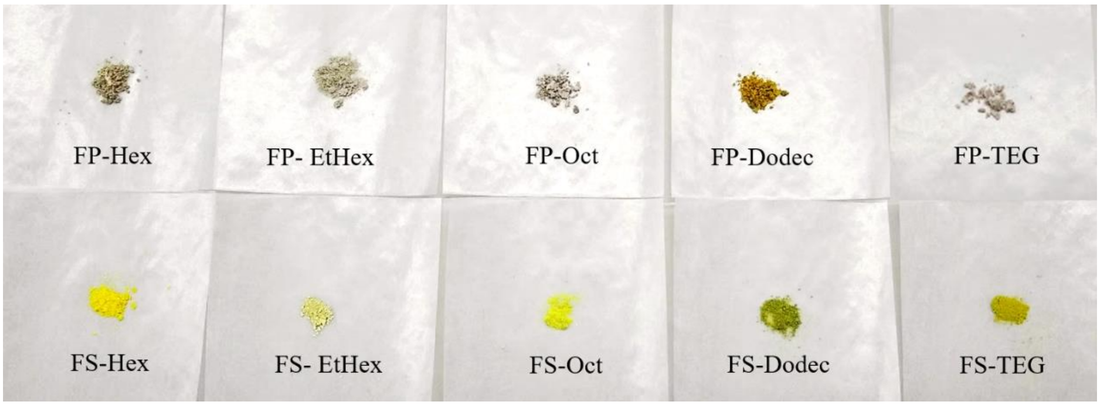

Figure 2.50. Image of the **FP** and **FS** series of polymers as powders.

2.4.1.3. Summary

The results in this section clearly recommend the incorporation of DBTS units into solution-processable polymer photocatalysts. Although they limit solubility in organic solvents, DBTS units are of central importance in achieving good activity in the soluble polyfluorene structures reported here. The greater hydrophilicity of DBTS appears to be key, along with the shift of charge carrier potentials to deeper levels leading to an improved driving force for proton reduction. A narrowing of the band gap may also contribute to the increased performance under visible light.

2.4.2. Modification of the Bridgehead Atom

Varying the bridgehead atom has been found to profoundly alter the electronic properties of polyfluorenes and polythiophenes.[62,63] The presence of silicon atoms in the polymer backbone may improve charge transport; polymers with silole units have been shown to have higher electron affinity and greater electron mobility than their fluorene-containing counterparts.[64] The high stability of the silole anion may also be beneficial for hydrogen evolution.[65]

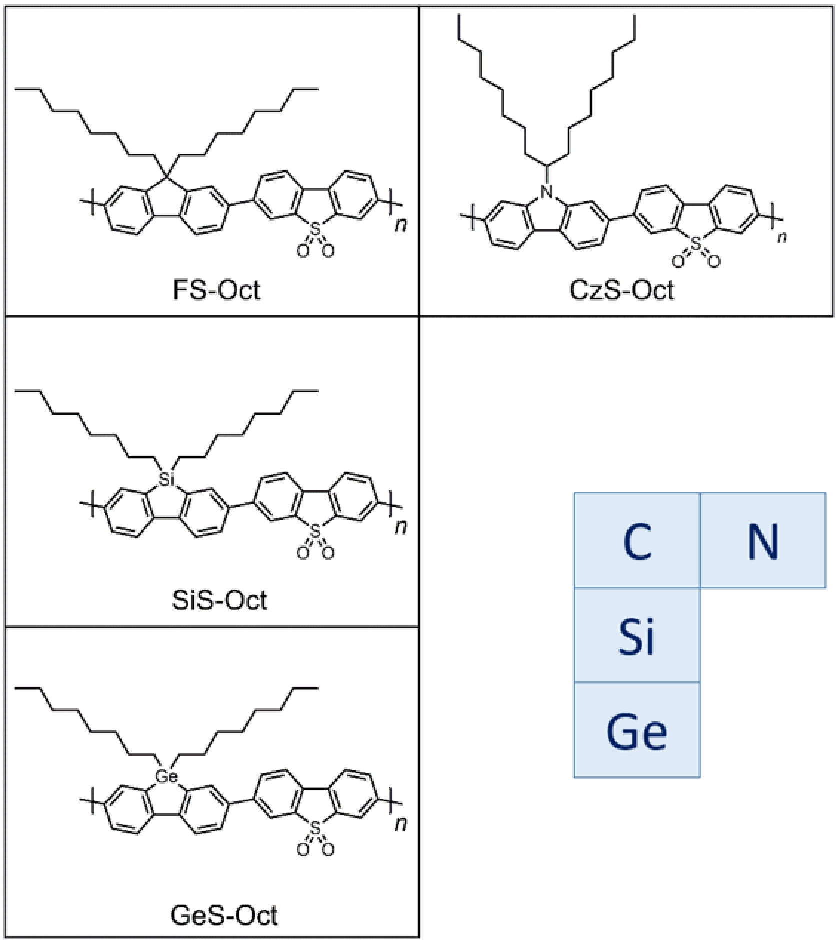

Figure 2.51. Chemical structures of **FS-Oct**, **SiS-Oct**, **GeS-Oct** and **CzS-Oct** and an image of the bridgehead atoms being varied and their relative positions in the periodic table.

The bridgehead atom was varied between the first three tetravalent Group 4 elements, carbon, silicon and germanium. Previously discussed **FS-Oct** was compared to the dibenzosilole-DBTS polymer (**SiS-Oct**) and germafluorene-DBTS polymer (**GeS-Oct**) (**Figure 2.51**). These polymers were also compared to the carbazole-DBTS polymer (**CzS-Oct**) with nitrogen at the bridgehead position. The trivalency of nitrogen means a single heptadecan-9-yl side-chain, effectively equivalent to two octyl side-chains, was used in this case. The silole and carbazole monomers were commercially available while the germafluorene was synthesised in house using a procedure adapted from literature.[66] These 2,7-dibromo-9-heterofluorene monomers can be synthesised via intramolecular coupling following lithiation of a diiodo-substituted intermediate (**Chapter 2.8.1**).[67]

FS-Oct and **SiS-Oct** have similar optical gaps although the absorption profile is broadened into the UV region (**Figure 2.52a**). The broadened spectra of silole-containing polymers has been observed previously[45,68] although this should not enhance photocatalytic rates in the visible light conditions employed here. A notable blue shift in absorption and PL is observed upon changing the heteroatom from Si to Ge while **CzS-Oct** possesses similar absorption and emission profiles to **FS-Oct**. The same trends are generally observed in films of these polymers (**Figure 2.52c** and **d**).

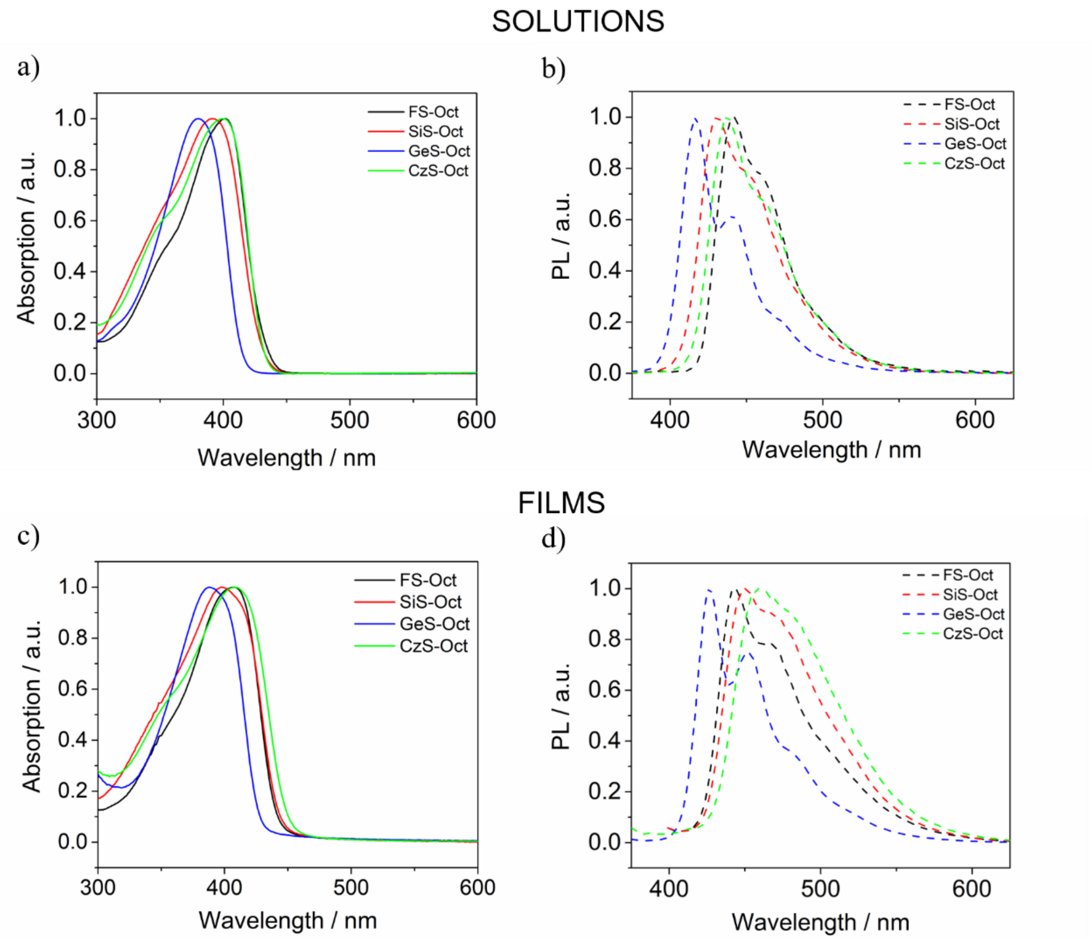

Figure 2.52. Normalised UV-vis and PL spectra of **FS-Oct**, **SiS-Oct**, **GeS-Oct** and **CzS-Oct** dissolved in chloroform (**a** and **b**) and cast as spin-coated films from chloroform on glass substrates (**c** and **d**).

All of the polymers appear to be relatively amorphous (**Figure 2.53a**). However, a peak at 2θ = 3.9° is evident in the pattern of **SiS-Oct**, not present in the case of **FS-Oct**, that is thought to correspond to lateral stacking of polymer chains.[69] This peak becomes even more pronounced in **GeS-Oct** and moves to shorter stacking distance (2θ = 4.5°). The spectrum of **CzS-Oct** is analogous to that of **FS-Oct**. These results therefore seem to suggest more regioregular interchain stacking with increasing atomic mass of the bridgehead heteroatom. Contact angle measurements with water show that **FS-Oct** (92 ± 2°) is more hydrophobic than **GeS-Oct** (89 ± 1°) but less hydrophobic than **SiS-Oct** (95 ± 2°), implying there is no strong correlation between the bridgehead atoms and hydrophilicity.

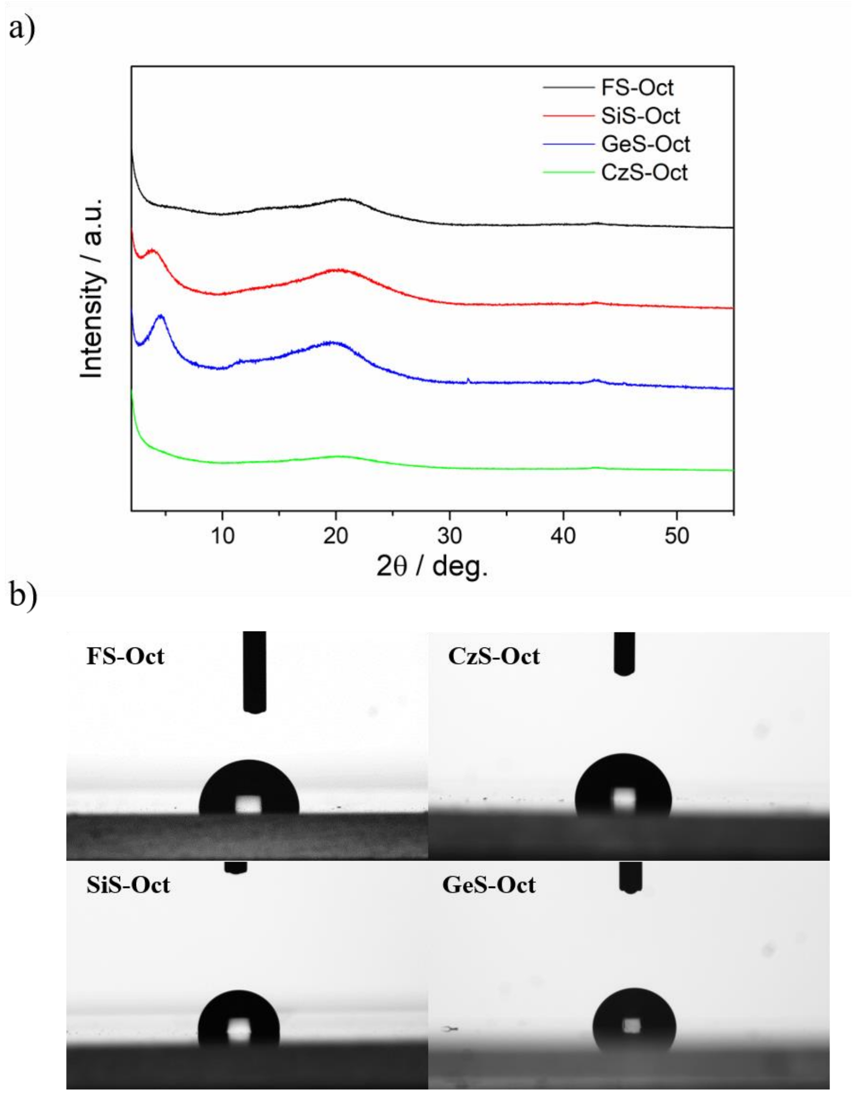

Figure 2.53. **a)** PXRD patterns of **FS-Oct**, **SiS-Oct**, **GeS-Oct** and **CzS-Oct** and **b)** contact angles of these polymers with water.

Table 2.13. Selected properties and photocatalytic HERs of **FS-Oct**, **SiS-Oct**, **GeS-Oct** and **CzS-Oct**.

Polymer	**Bridge-head atom**	**M_n / g mol^{-1}**	**M_w / g mol^{-1}**	**Đ**	**ε / 10^5 m^2 mol^{-1}**	**Optical gap / eV**	**CA (H_2O) / °**	**HER[i] / µmol g^{-1} h^{-1}**
FS-Oct	C	18,900	31,900	1.69	5.0	2.88	92 ± 2	680 ± 7
SiS-Oct	Si	5900	14,000	2.36	3.8	2.87	95 ± 1	1520 ± 30
GeS-Oct	Ge	7900	16,900	2.14	5.6	2.97	89 ± 1	0.70 ± 0.08
CzS-Oct	N	4800	7800	1.64	4.7	2.83	89 ± 1	670 ± 30

[i] HERs of polymers (25 mg) measured in water/methanol/TEA (22.5 mL) under visible light irradiation using a 300 W Xe light source.

The photocatalytic activities of these polymers vary considerably (**Figure 2.54**, **Table 2.13**). The HER of **SiS-Oct** is more than double that of **FS-Oct** (1520 ± 30 compared to 680 ± 7 µmol g^{-1} h^{-1}) whereas **GeS-Oct** is virtually inactive (0.70 ± 0.08 µmol g^{-1} h^{-1}). The HER of **CzS-Oct** (670 ± 30 µmol g^{-1} h^{-1}) is very similar to that of **FS-Oct**. This is consistent with a previous investigation which observed similar HERs in unsubstituted linear fluorene and carbazole-containing polymers.[1]

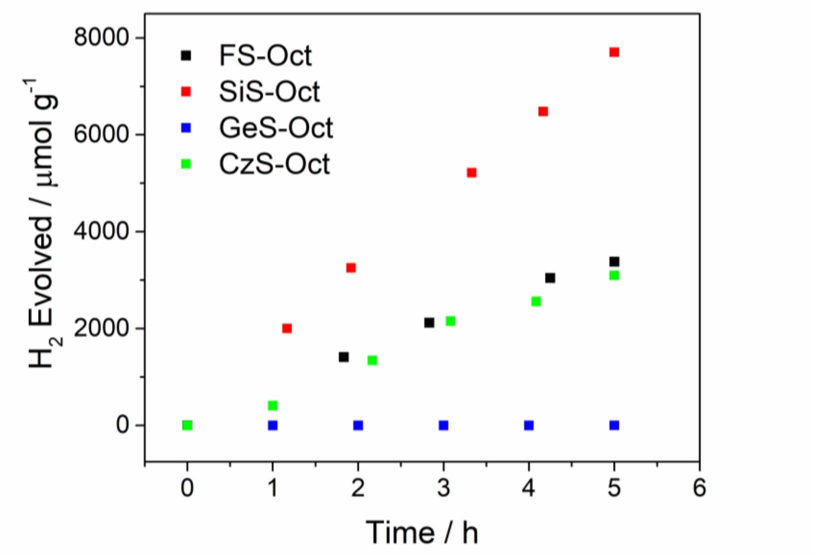

Figure 2.54. Hydrogen evolution runs of **FS-Oct**, **SiS-Oct**, **GeS-Oct** and **CzS-Oct** (25 mg) in water/methanol/TEA (1:1:1, 22.5 mL) under visible light irradiation. Amount of hydrogen evolved normalised to the mass of photocatalyst present.

Changing the heteroatom in fluorenes clearly has a major influence on photocatalytic performance, with significant variation seen in the HERs of the polymers studied here. However, the reasons behind this variation are not immediately clear as changing the bridging atom seems to have minimal effect on the physical properties studied here. In fact, the most active polymer has the seemingly least desirable attributes; **SiS-Oct** seems to be more hydrophobic and has a lower molecular weight and molar extinction coefficient than **FS-Oct** but has a notably higher HER. The reasons may lie in the packing behaviour of these polymers and the inter-chain stacking observed in the PXRD pattern of **SiS-Oct**. The stability of the silole anion, outlined previously,[65] may also improve photocatalytic performance by extending the excited state lifetime of the polymer.

By these explanations, **GeS-Oct** might be expected to have even higher performance than **SiS-Oct**. However, **GeS-Oct** is, in fact, over 2000 times less active. The blue-shifted absorption spectrum may partially account for the low activity of **GeS-Oct** although some activity would be expected as the absorption spectrum of a film of the polymer extends slightly into the visible region. Regardless, according to this study, incorporating silicon atoms into the polymer backbone appears to be an effective method of enhancing photocatalytic activity although further studies observing this trend in multiple polymer series are needed to confirm this.

2.5. The Influence of Residual Palladium on the Photocatalytic Performance of Polymer Photocatalysts

2.5.1. Background

Polycondensation reactions, as used in this study and throughout the field, require the use of heavy metal catalysts. The use of these catalysts inevitably leads to the presence of residual heavy metal particles in the polymer photocatalysts. The influence of these residues on photocatalytic performance has been relatively unexplored, although some attempts have been made to study their influence in polymers for electronic applications, particularly organic photovoltaic (OPV) devices.[70–72] The presence of heavy metals in polymers at amounts as low as 0.01 wt.% has been described as “fatal” to the performance of these devices.[18] These residues have been found to act as traps for charge carriers, thus preventing the extraction of charges that is essential for device performance.[71] Of course, the requirements of polymers for photocatalytic hydrogen evolution are different and the presence of these traps could enhance rather than inhibit performance by acting as active sites for proton reduction.[14] In fact, metals such as platinum and ruthenium are often added as co-catalysts post-synthesis like in inorganic materials discussed previously.[14]

Generally, the performance of photocatalysts improves with the addition of heavy metal co-catalysts up to a point. An upper threshold has been shown in a number of systems[73,74] above which the addition of co-catalysts has a detrimental effect, presumably by blocking the incident light from reaching the photocatalysts’ surface.[20] However, the existence of a lower threshold, below which photocatalytic performance reduces, has been less explored primarily because of the difficulty of removing these heavy metal particles using conventional purification methods.[70] This is particularly true for the network polymers commonly used in photocatalysis for which attempts to remove palladium by treating with solutions of EDTA or acid have proved unsuccesful.[18] Observations about the potential influence of heavy metal residues on the photocatalytic activity of these insoluble network materials have therefore been tentative, often limited to attempts to correlate photocatalytic performance with residual metal content across a range of polymers with a number of uncontrolled variables.[7]

However, the influence of residual metals in polymer photocatalysts has recently been the subject of increased attention. The ratio of the palladium catalyst to the monomers was varied during the preparation of conjugated polymer networks.[18] Photocatalytic activity was found to increase with increasing Pd up to 0.46 wt. % Pd at which point a plateau was reached. However, as previously suggested,[12] the possible influence of varying the amount of catalyst amount on other properties such as molecular weight was not considered. This was presumably in part due to the limited characterisation that can be performed on these insoluble networks.

In a recent landmark study by Kosco *et al.*, residual palladium was removed using methods enabled by the solubility of an alkyl-substituted conjugated polymer photocatalyst.[12,75] Poly(9,9-dioctylfluorene-alt-benzothiadiazole) (F8BT) was purified using GPC and by washing the polymer with a previously reported Pd-chelating molecule, sodium diethyldithiocarbamate (Na(detc)).[76] Using these methods in conjunction reduced Pd content to <1 ppm , which rendered the polymer inactive for hydrogen evolution. The threshold at which the activity of F8BT was maximised was found to be around 250 ppm (0.025 wt. %), much lower than suggested by the previous study on network polymers (0.46 wt. %).[18] Good agreement with this threshold was observed when Pd was added back into the polymer with <1 ppm Pd. The observed threshold, when coupled with TAS experiments, suggested Pd particles act as active sites for photocatalysis and that, at low metal concentrations, the availability of these active sites is rate-limiting. Although the exact mechanisms at play are still not fully known, a growing consensus is building that residual heavy metals play a critical role in photocatalytic reactions. The influence of residual palladium from the Suzuki-Miyaura polycondensations used in the present work will therefore now be considered.

2.5.2. Palladium Levels in Soluble and Insoluble Fractions

As previously discussed, in some instances the solubilising side-chains were insufficient to achieve full solubility and higher molecular weight, insoluble fractions of the polymer were also obtained. It is possible that extraction of the soluble fractions in chloroform removes residual Pd and a comparison of activities of the soluble and insoluble fractions is therefore worthwhile.

In the initial study of **P8-s** and **P8-i** in **Chapter 2.2**, the difference in Pd content, measured using inductively coupled plasma optical emission spectrometry (ICP-OES), was notable (**P8-s** = 200 ppm, **P8-i** = 5000 ppm). The insoluble fraction was found to have higher photocatalytic activity which may be in part be due to the higher Pd content. Of course, the soluble and insoluble polymers must also differ in terms of other properties, most notably molecular weight, which is expected to account for the difference in solubility of the two fractions.

A similar difference in Pd content was observed in the two fractions of **FS-Hex** according to inductively coupled plasma mass spectrometry (ICP-MS) (**Table 2.14**). However, in the case the insoluble fraction was found to have a notably lower activity than the soluble fraction (770 ± 10 vs. 1370 ± 20 µmol g^{-1} h^{-1}). The reasons for this reversal in trend from the **P8** polymers are unclear but these results suggest that activity does not simply scale with palladium content within a polymer. The difficulty in disentangling Pd content and factors such as molecular weight necessitates the need for an investigation in which Pd is varied systematically within a single polymer sample.

Table 2.14. Molecular weight, Pd content and HER of soluble and insoluble fractions of **P8** and **FS-Hex**.

Polymer	Fraction	M_n / g mol^{-1}	M_w / g mol^{-1}	Đ	Pd / ppm	HER / µmol g^{-1} h^{-1}
P8	Soluble	1500	2100	1.4	200[i]	72 ± 1
	Insoluble	n/a	n/a	n/a	5000[i]	124 ± 1
FS-Hex	Soluble	3800	8200	2.16	290 ± 10[ii]	1370 ± 20
	Insoluble	n/a	n/a	n/a	1990 ± 60[ii]	770 ± 10

Palladium content obtained from [i] ICP-OES [ii] ICP-MS.

2.5.3. Systematic Variation of Palladium Content in Soluble Polymers

The solubility of the polymer photocatalysts in this thesis enables Pd removal by washing a solution of the polymer in chloroform with an aqueous solution of Na(detc), as discussed previously.[12] First, the levels of residual Pd were determined in a series of polymers to find suitable candidates in which to vary Pd content. Amounts of residual Pd were found to vary significantly within the **FS** series of polymers. No correlation between Pd content and HER is evident in this series (**Figure 2.55**) although substantial levels of Pd are present in some polymers, not least the best-performing photocatalyst **FS-TEG** (3050 ± 60 ppm).

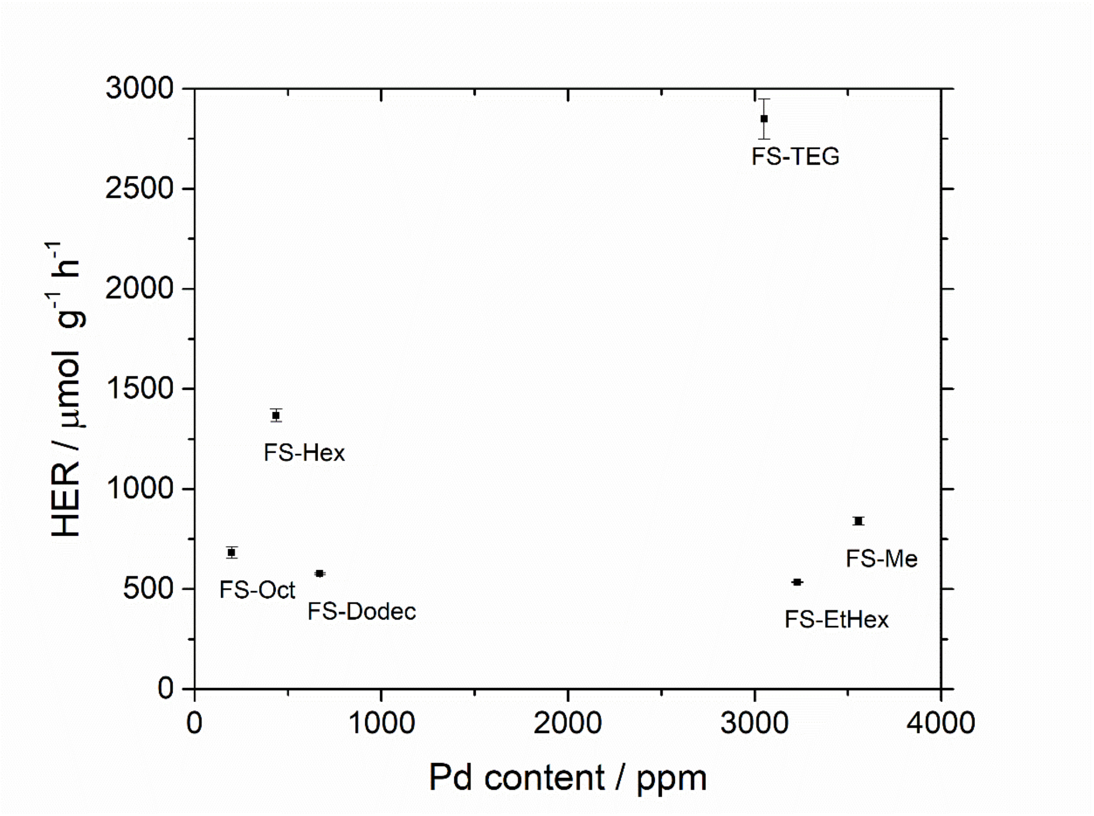

Figure 2.55. Plot of HER against Pd content for the **FS** series of polymers. Photocatalysis conditions: Polymer (25 mg) in water/methanol/TEA (1:1:1, 22.5 mL) under visible light irradiation using a 300 W Xe light source.

Pd content was varied in **FS-TEG** to ensure that its high activity cannot be solely attributed to its high Pd content. Similar Pd levels were observed across multiple batches of **FS-TEG** (3050 ± 60, 2400 ± 50 and 2530 ± 60 ppm), all with HERs in the range of 2900 ± 100 µmol g^{-1} h^{-1}. The batch with highest Pd content (3050 ± 60 ppm) was selected for variation. Two samples of this polymer batch were purified separately (Purifications 1 and 2) to ensure reproducibility, with the polymer washed with Na(detc) twice in each purification (Washes 1 and 2, **Figure 2.56**). In both cases, one wash was found to be sufficient to remove over 95% of residual Pd. However, the washing procedure was not able to remove Pd completely, with Pd content above 20 ppm observed after two washes in each case. Chromatography therefore appears to be necessary for the complete Pd removal (< 1 ppm) observed previously.[12]

Figure 2.56. Images of **FS-TEG** as-synthesised and after removal of Pd by one and two washes with Na(detc) (Purification 1).

Generally, removal of Pd was found to reduce photocatalytic performance (**Table 2.15**). In Purification 1 this trend was particularly apparent, with HER clearly reducing with subsequent washes (**Figure 2.57**). Pd was added back into the washed polymer with the lowest Pd content (20 ± 1 ppm) to a level (254 ± 8 ppm) similar to the threshold observed in a previous study.[12] Photocatalytic activity was found to recover with the addition of Pd back into the polymer, almost to the level of the as-synthesised **FS-TEG** (2800 ± 30 *vs* 2900 ± 100 µmol g^{-1} h^{-1}). These results therefore appear to be consistent with a threshold of around 250 ppm, as previously observed in similar materials.[12]

Table 2.15. Pd content and HER of **FS-TEG** and **FS-Hex** after removal and addition of Pd.

Polymer	**Treatment**		**Pd / ppm**	**HER[i] / µmol g^{-1} h^{-1}**
FS-TEG	As-synthesised		3050 ± 60	2900 ± 100
	Purification 1	Wash 1	47 ± 4	1750 ± 40
		Wash 2	30.2 ± 0.4	1000 ± 100
	Purification 2	Wash 1	143 ± 4	1870 ± 10
		Wash 2	20 ± 1	1880 ± 30
		Wash 2 + Pd	254 ± 8	2800 ± 30
FS-Hex	As-synthesised		290 ± 10	1370 ± 30
	As-synthesised + Pd		1110 ± 20	1850 ± 20

[i] HERs of polymers (25 mg) measured in water/methanol/TEA (22.5 mL) under visible light irradiation using a 300 W Xe light source.

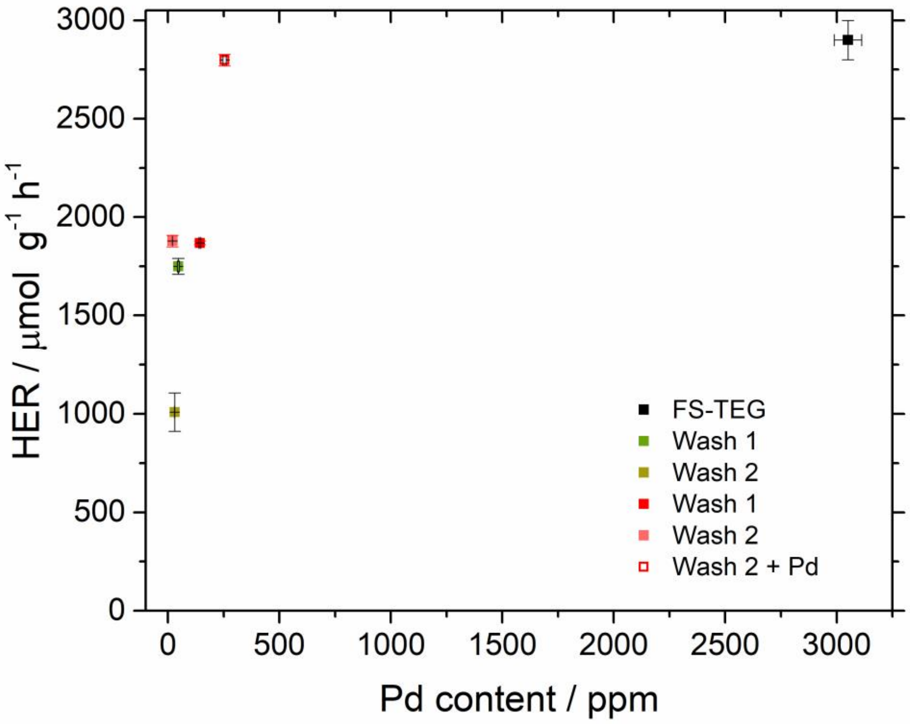

Figure 2.57. Correlation between HER and Pd content in **FS-TEG**. Green symbols are from Purification 1 while red symbols are Purification 2. The hollow red symbol is the polymer with Pd added back in. Photocatalysis conditions: polymer (25 mg) in water/methanol/TEA (1:1:1, 22.5 mL) under illumination from a 300 W Xe light source ($\lambda > 420$ nm)

Pd was also added into a polymer with a lower as-synthesised Pd content to see if photocatalytic activity could be enhanced. As-synthesised **FS-Hex** has a Pd content of 290 ± 10 ppm, similar to the threshold observed in **FS-TEG**. Addition of Pd up to 1110 ± 20 ppm somewhat unexpectedly increased HER by 35% (**Table 2.15**). This suggests the Pd content at which performance saturates may be slightly higher in this material. Further experiments are necessary to fully determine the Pd-dependence of this and other polymers in this series.

2.5.4. Summary

This section highlights the importance of considering residual heavy metal content when studying photocatalytic materials. Extraction of polymers into chloroform appears to remove Pd relative to insoluble counterparts while, as in previous studies, no correlation between Pd content and HER within a series of polymers was observed. This confirms that Pd content alone does not determine the photocatalytic activity of the polymers discussed in this study.

The findings of this section appear to confirm the dependence of photocatalytic reactions on the presence of residual metals although only small amounts of Pd (approximately 250 ppm) were required to maximise HER in **FS-TEG**. However, the increase in performance of **FS-Hex** after addition of Pd suggests that the threshold may vary from polymer to polymer and that not all as-synthesised polymers have Pd contents above this threshold. The as-synthesised Pd content may therefore affect photocatalytic performance in some cases.

More comprehensive studies are required in which Pd content is systematically varied in a range of polymers to fully observe the dependence of photocatalytic activities on the Pd content of these materials. Factors such as particle size should also be more carefully controlled as this will have an effect on the distribution of Pd. The influence of particle size could be negated, as in previous studies, with the formation of nanoparticles[12] or alternatively with the formation of photocatalytic films, which will be discussed more fully in **Chapter 3**.

2.6. The Effect of Molecular Weight on the Photocatalytic Performance of Polymer Photocatalysts

2.6.1. Background

Molecular weight is regarded as an important property in polymer electronics.[77] Increased molecular weights in linear conjugated polymers have been shown to result in materials with advantageous properties, such as increased light absorption,[78] that might be expected to aid photocatalysis. However, the relationship between molecular weight and photocatalytic performance of polymer photocatalysts has not been widely studied, which must again be put down to the insolubility of most photocatalysts reported to date. The molecular weights of insoluble materials can be determined using techniques such as Matrix-Assisted Laser Desorption/Ionization Resolution Time-of-Flight Mass Spectrometry (MALDI-TOF MS). However, determining the molecular weight of high molecular weight polymer samples with any accuracy is notoriously challenging.[79,80] Branched phenyl triazine oligomers were characterised using this technique and shown to have higher photocatalytic activity than the equivalent extended covalent triazine framework (CTF).[81] This was rationalised by a narrowing of the band gap resulting in reduced driving force for proton reduction. However, the exact molecular weight of the CTF polymer was not discernible due to the difficulty of performing MALDI-TOF on this material. The facile determination of molecular weights of soluble polymers by gel permeation chromatography (GPC) should enable a more thorough investigation in the polymers studied here.

2.6.2. Observing Variations in the Molecular Weight in Soluble Polymer Photocatalysts

The relationship between molecular weight and photocatalytic activity in the **FS** series of polymers was investigated. Attempting to correlate molecular weight and photocatalytic performance within a series must be done with great caution due to the multitude of other varying properties. **FS** polymers with higher molecular weights seem to have lower photocatalytic performance (**Figure 2.58**). However, this is likely to be a correlative rather than causative relationship as this can be interpreted as longer side-chains enabling the attainment of higher molecular weights but also acting to screen the polymers from water and reduce the polarity of the surrounding environment in photocatalysis experiments, thus decreasing performance. In other words, the hydrophilicity of polymers with shorter alkyl or OEG side-chains appears to have greater influence on HERs than their diminished molecular weights. An investigation in which the molecular weight is varied within a single polymer sample is necessary to probe the effect of varying molecular weight in greater detail.

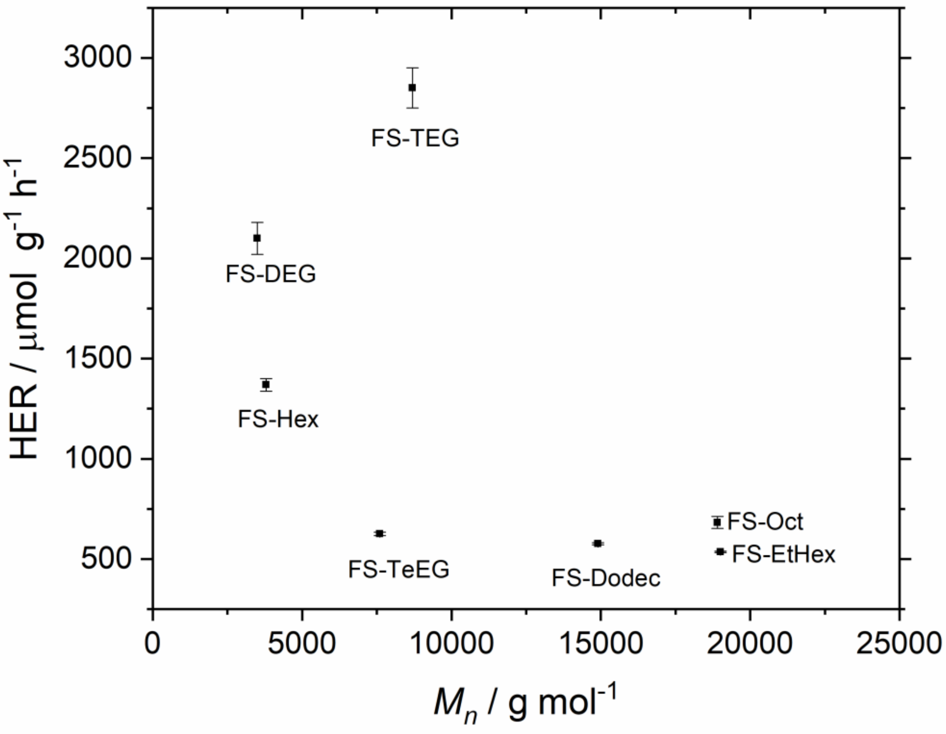

Figure 2.58. Plot of HER against number-average molecular weight (M_n) for the **FS** series of polymers. Photocatalysis conditions: polymer (25 mg) in water/methanol/TEA (1:1:1, 22.5 mL) under illumination from a 300 W Xe light source (λ > 420 nm).

2.6.3. Varying the Molecular Weight of FS-Dodec

Soluble and insoluble fractions of the same polymer, such as **P8-s** and **P8-i**, are expected to have different molecular weights. However, as previously discussed, determining the molecular weight of the insoluble fraction is extremely challenging. Moreover, these fractions have been shown to differ in other ways such as Pd content (**Chapter 2.5.2**). For these reasons, a qualitative comparison of soluble and insoluble fractions is not expected to be particularly useful and molecular weight should be varied in a fully soluble polymer. **FS-Dodec** was selected due to its high yield, high molecular weight and reasonable photocatalytic activity offering scope for systematic variation.

The molecular weight of soluble polymers can be varied by controlling the degree of polymerisation either by changing the monomer feed ratio or reaction duration[82] or with the use of an end capper.[83] The introduction of an end-capper into the Suzuki-Miyaura polycondensation of **FS-Dodec** resulted in greater yields of polymer fractions that were soluble in acetone, and ethyl acetate, which were expected to be of lower molecular weight. Different fractions of **FS-Dodec** with different solubilities—**FS-Dodec-a** (acetone-soluble), **FS-Dodec-e** (ethyl acetate-soluble) and **FS-Dodec-c** (chloroform-soluble)—were collected and compared to previously reported **FS-Dodec**, synthesised in the absence of any end-capper.

GPC results confirmed the samples differ in terms of molecular weight (**Table 2.16**). The molecular weights increased in the fractions obtained from subsequent Soxhlet extractions (**FS-Dodec-a** < **FS-Dodec-e** < **FS-Dodec-c)**. The well-resolved GPC traces of **FS-Dodec-a** and **FS-Dodec-e** appear to be oligomeric in character (**Figure 2.59**) while chloroform-soluble **FS-Dodec-c** has a broader single peak similar to previously synthesised **FS-Dodec**. However, the molecular weight of the end-capped chloroform-soluble **FS-Dodec-c** fraction (9000 g mol^{-1}) was lower than the original **FS-Dodec** sample (14,900 g mol^{-1}). The polymers were found to consist of approximately 2, 5, 13 and 21 co-monomer repeating units for **FS-Dodec-a**, **FS-Dodec-e**, **FS-Dodec-c** and **FS-Dodec** respectively, giving a suitably broad range of chain lengths for this investigation.

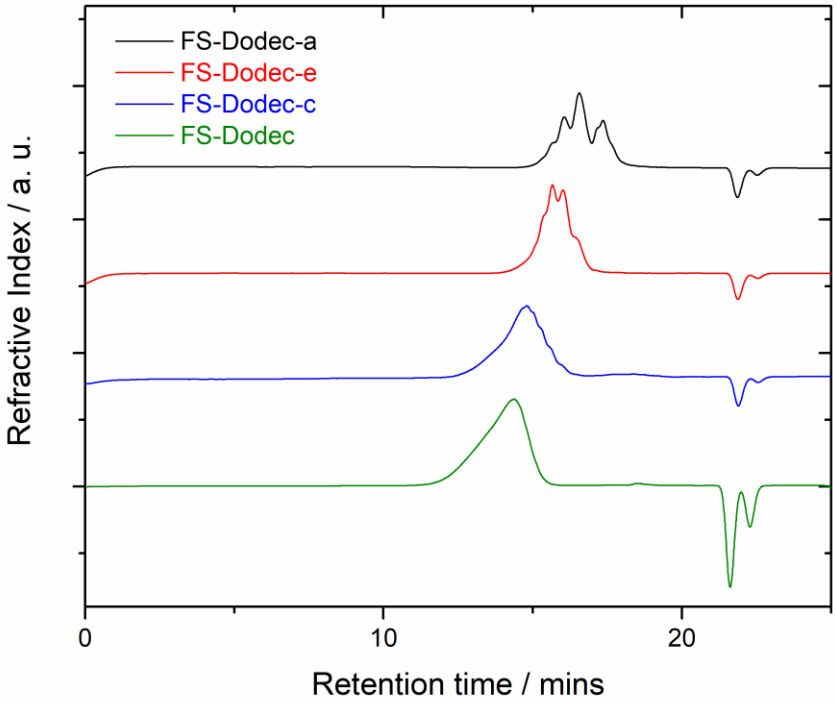

Figure 2.59. GPC traces of **FS-Dodec-a**, **FS-Dodec-e**, **FS-Dodec-c** and **FS-Dodec**, measured in chloroform

Though it is hard to distinguish between the phenyl end-capper and fluorene end groups, the presence of a variety of aromatic signals in the ^{1}H NMR spectra of **FS-Dodec-a** and **FS-Dodec-e** confirm their oligomeric nature (**Figure 2.60**). **FS-Dodec-c** has a near-identical spectra to **FS-Dodec** with fewer, more well-defined aromatic signals typical of polymers with longer chain lengths. The polymer appears to become more amorphous with increasing chain length (**Figure 2.61**). The PXRD pattern of **FS-Dodec-a** has sharp peaks at 2θ = 25.8° and 2θ = 29.8° while both **FS-Dodec-a** and **FS-Dodec-e** exhibit a strong diffraction peak at 2θ = 4.5°. In **FS-Dodec** and **FS-Dodec-c**, this latter peak is diminished and the broad peak with a maximum around 2θ = 20.6° predominates.

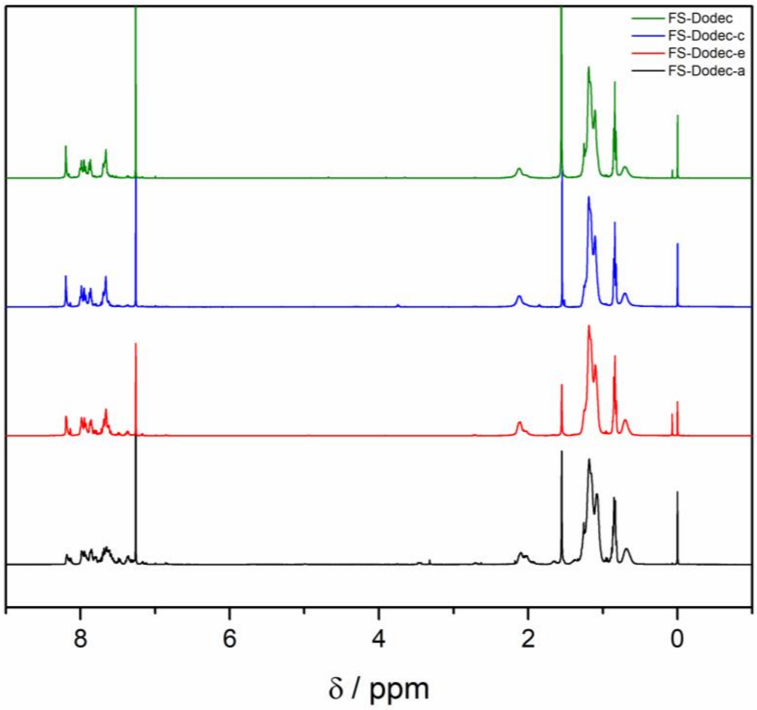

Figure 2.60. ^{1}H NMR spectra of **FS-Dodec-a**, **FS-Dodec-e**, **FS-Dodec-c** and **FS-Dodec** in $CDCl_3$.

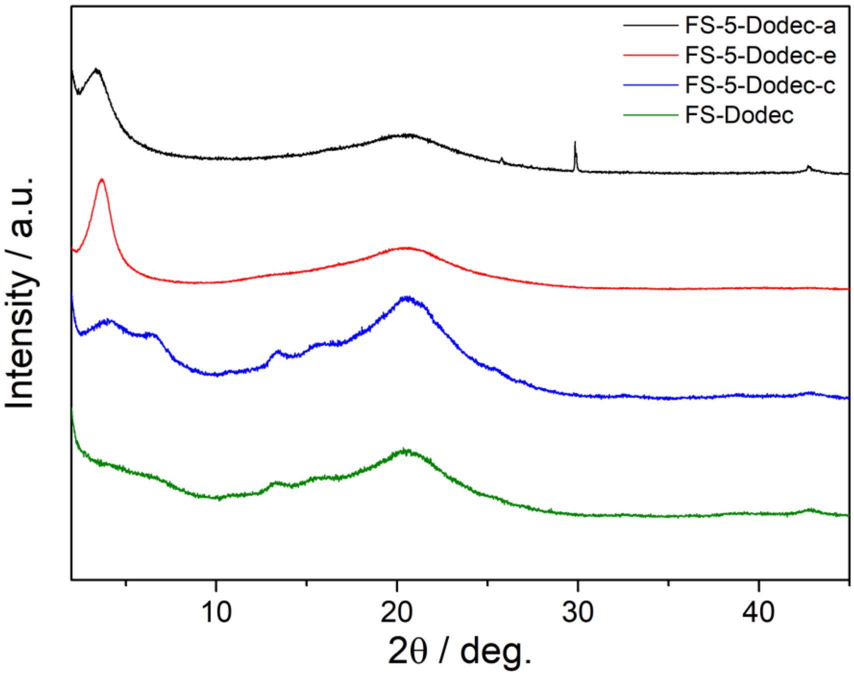

Figure 2.61. PXRD patterns of **FS-Dodec-a**, **FS-Dodec-e**, **FS-Dodec-c** and **FS-Dodec**.

It is well known that increasing conjugation length leads to a narrowing of the band gap of conjugated polymers[84] and a red shift of the absorption spectra was indeed observed with increasing molecular weight in **FS-Dodec** polymers (**Figure 2.62a**). **FS-Dodec-c** has a similar absorption profile to **FS-Dodec** suggesting that no narrowing of the band gap occurs at molecular weights above that of **FS-Dodec-c**. This is consistent with the GPC data, which showed that only **FS-Dodec-c** and **FS-Dodec** have chain lengths longer than the effective conjugation length of polyfluorene materials (approximately 12 monomeric repeating units).[30] The absorption spectra of **FS-Dodec-a** and **FS-Dodec-e** show no evidence of formation of a more ordered, linear arrangement of chains, known as a β-phase, as previously seen in polyfluorene oligomers.[85] The PL spectra show reduced emission from the shoulder peak (λ_{em} = 467 nm) with a narrowing of the band gap (**Figure 2.62b**).

Table 2.16. Selected properties and photocatalytic performances of **FS-Dodec-a**, **FS-Dodec-e**, **FS-Dodec-c** and **FS-Dodec**.

Sample	**M_n / g mol^{-1}**	**M_w / g mol^{-1}**	**Đ**	**HER / µmol g^{-1} h^{-1}**
FS-Dodec-a	1500	2300	1.5	1.84 ± 0.01
FS-Dodec-e	3400	4300	1.3	194 ± 7
FS-Dodec-c	9000	14,400	1.6	612 ± 4
FS-Dodec	14,900	25,500	1.7	577 ± 5

[i] HERs of polymers (25 mg) measured in water/methanol/TEA (22.5 mL) under visible light irradiation using a 300 W Xe light source.

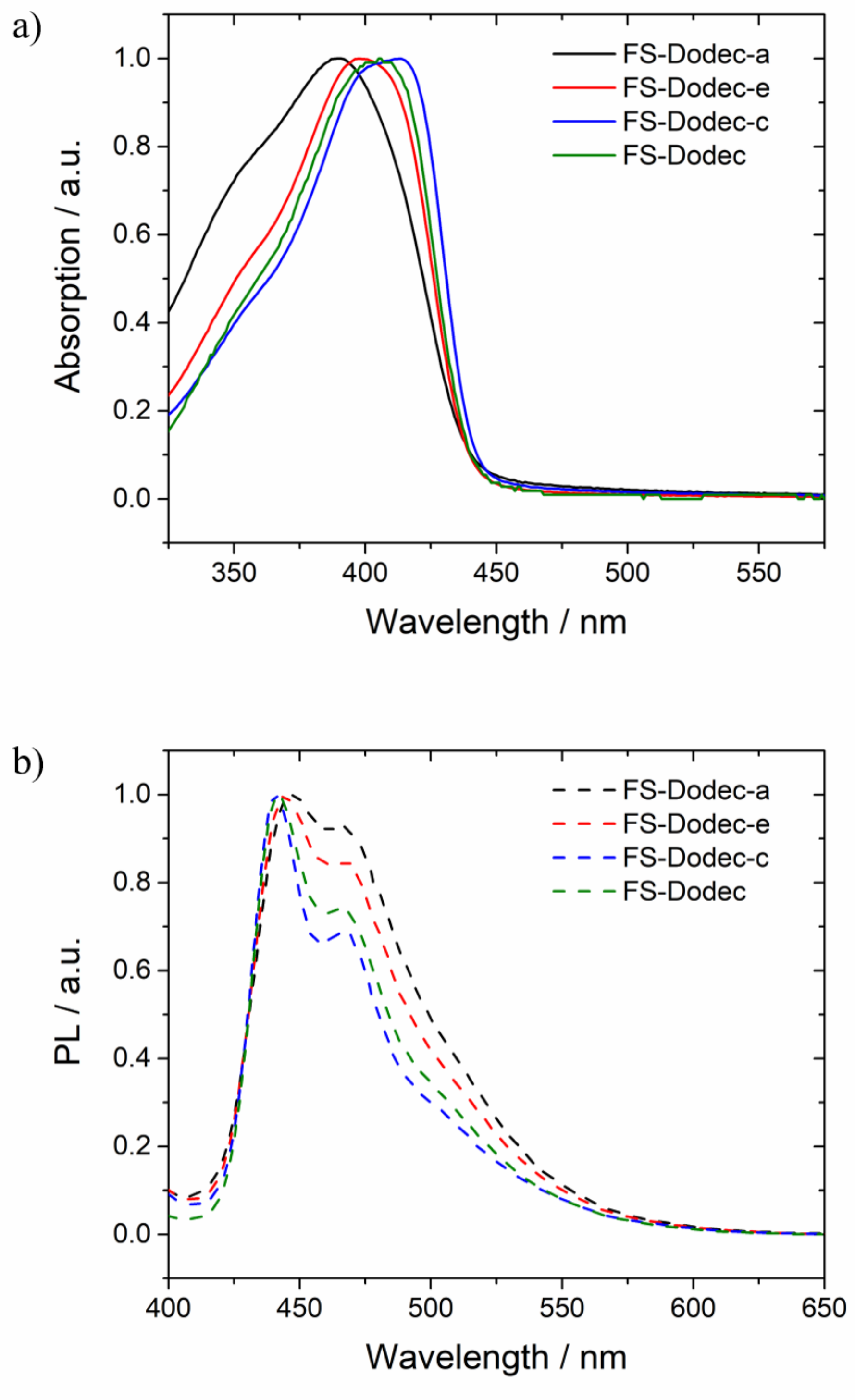

Figure 2.62. Normalised **a)** UV-vis and **b)** PL spectra of **FS-Dodec-a**, **FS-Dodec-e** and **FS-Dodec-c** as spin-coated films (λ_{exc} = 360 nm).

The HERs of the polymers were measured over a 5 hour period. Photocatalytic performance seems to increase with increasing molecular weight up to **FS-Dodec-c** which has a marginally higher HER than **FS-Dodec** (**Table 2.16**). These results appear to be consistent with an increase in photocatlytic performance with increasing molecular weight up to the effective conjugation length, at which point performance saturates. The extremely low activity of **FS-Dodec-a** is striking given its apparent similarity in optical properties with **FS-Dodec** and underlines the importance of conjugation length in determining photocatalytic performance.

2.6.4. Summary

This investigation was intended to address the shortage of studies investigating how the molecular weight of polymer photocatalysts affects their properties and performances. Analogous solution-processable polymers with varying chain lengths were prepared and tested for hydrogen evolution. The molecular weight of the polymer was varied by introduction of an end-capping molecule into the polymerisation mixture and subsequent extraction of the polymer using a range of solvents.

Photocatalytic performance was found to increase with increased molecular weight before a plateau was reached, seemingly corresponding with the effective conjugation length of the polymer. This investigation was far from comprehensive and some factors which are also likely to vary within these polymers, such as residual Pd levels and extinction coefficients, were not considered. Nevertheless, the study demonstrates how the molecular weights of solution-processable polymer photocatalysts can be easily varied and how this can be used to optimise the performance of these materials.

2.7. Summary of Solution-Processable Polymer Photocatalysts

A host of solution-processable polymer photocatalysts were prepared and characterised, making use of a variety of techniques enabled by the solubility of these materials. The key finding in this chapter is that photocatalytic activities are not necessarily reduced by the introduction of solubility and can, in some cases, actually be enhanced by the addition of solubilising side-chains.

A common theme in this chapter is the importance of wettability of polymer photocatalysts in determining their performance. Incorporation of the DBTS into polymer backbones was found to be beneficial for this reason, supporting the findings of previous investigations.[1,35,53] However, the choice of side-chain was found to have an equally significant effect on photocatalytic performance. When HERs are plotted against the contact angles of the FS series with water, a strong correlation is observed (**Figure 2.63**). Long alkyl side-chains impair photocatalytic activity in the polymers studied here whereas shorter alkyl side-chains do not inhibit performance but can result in polymers of limited solubility, such as **FS-Hex**.

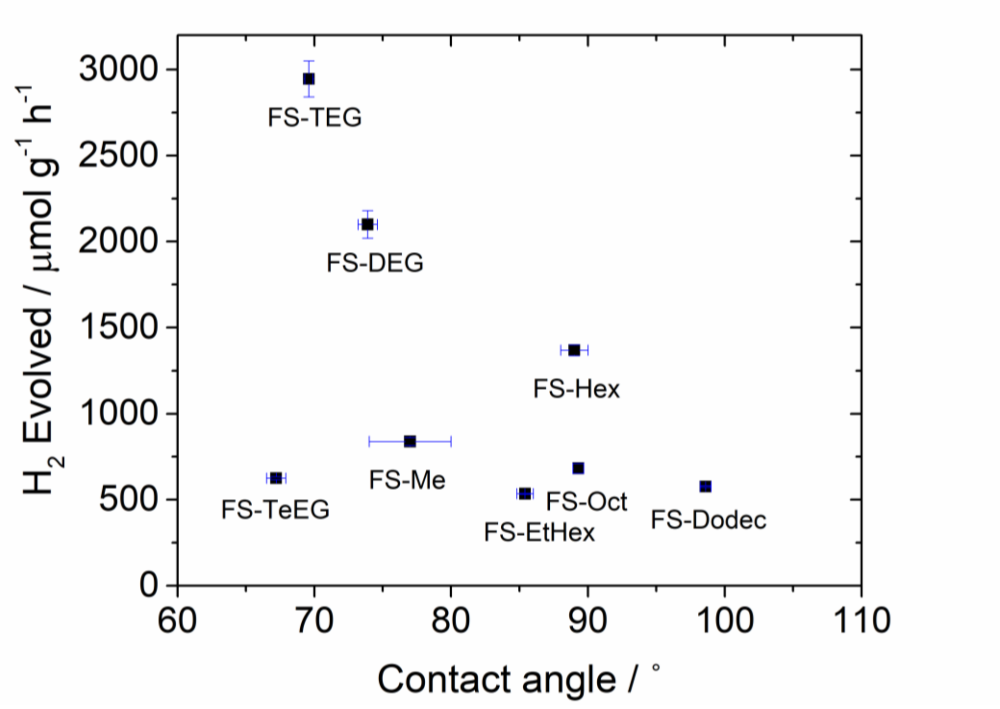

Figure 2.63. Plot of HER against contact angles of the **FS** series of polymers. Photocatalysis conditions: Polymer (25 mg) in water/methanol/TEA (1:1:1, 22.5 mL) under illumination from a 300 W Xe light source (λ > 420 nm). Contact angles with films reported in all cases except **FS-Me**, in which case a pellet was used.

Oligo(ethylene glycol) side-chains hold great promise as they are able to both promote solubility in organic solvents and improve the photocatalytic performance of polymer photocatalysts. MD simulations and charge carrier dynamics of excited state species support the conclusion that the hydrophilicity of OEG side-chains accounts for their rate-enhancing effect. QCM and AFM results also indicate the ability of OEG-substituted polymers to swell in aqueous conditions unlike equivalent alkylated polymers. An EQE of 10.0 ± 0.5% at 420 nm was achieved in the best-performing soluble polymer, **FS-TEG**, which is amongst the highest reported in the field of polymer photocatalysis to date. During the completion of this thesis, another study was published which also found OEG side-chains to enhance the photocatalytic performance of polymers,[50] further advocating their inclusion in future photocatalytic polymers.

Other factors were also found to influence photocatalytic performance. Molecular weight was found to affect HERs dramatically in polymers shorter than the effective conjugation length, with the shortest oligomers found to be virtually inactive. Further evidence was found that photocatalytic activity is dependent on the presence of small amounts of residual Pd. Modification of the bridgehead atoms of polyfluorenes also appears to strongly affect performance although the reasons for this remain unclear.

Expansion of the library of solubilised photocatalysts is required to study structure-property-activity relationships in these materials in greater detail. However, it is also important to consider how these solubilised photocatalysts might be processed in future photocatalytic set-ups. The focus of this thesis will now shift to how these polymers could be processed into forms that are more suited to application.

2.8. Experimental Methods

2.8.1. Monomer Synthesis

2,7-Dibromo-9,9-bis[2-[2-(2-methoxyethoxy)ethoxy]ethyl]-9*H*-fluorene

A previously reported literature procedure was used for the preparation of this monomer.[36] 1-Bromo-2-(2-(2-methoxyethoxy)ethoxy)ethane (6.16 g, 27.2 mmol) and 2,7-dibromofluorene (4.00 g, 12.36 mmol) were used as starting materials. The title compound was obtained as a white powder (3.9028g, 51%). ^{1}H NMR (400 MHz, $CDCl_3$, δ): 7.38-7.47 (m, 6H; ArH), 3.40-3.48 (m, 8H; CH_2), 3.30-3.34 (m, 4H; CH_2), 3.27 (s, 6H; CH_2), 3.12-3.16 (m, 4H; CH_2), 2.71 (t, J = 8.0 Hz, 4H; CH_2), 2.26 (t, J = 8.0 Hz, 4H; CH_2).

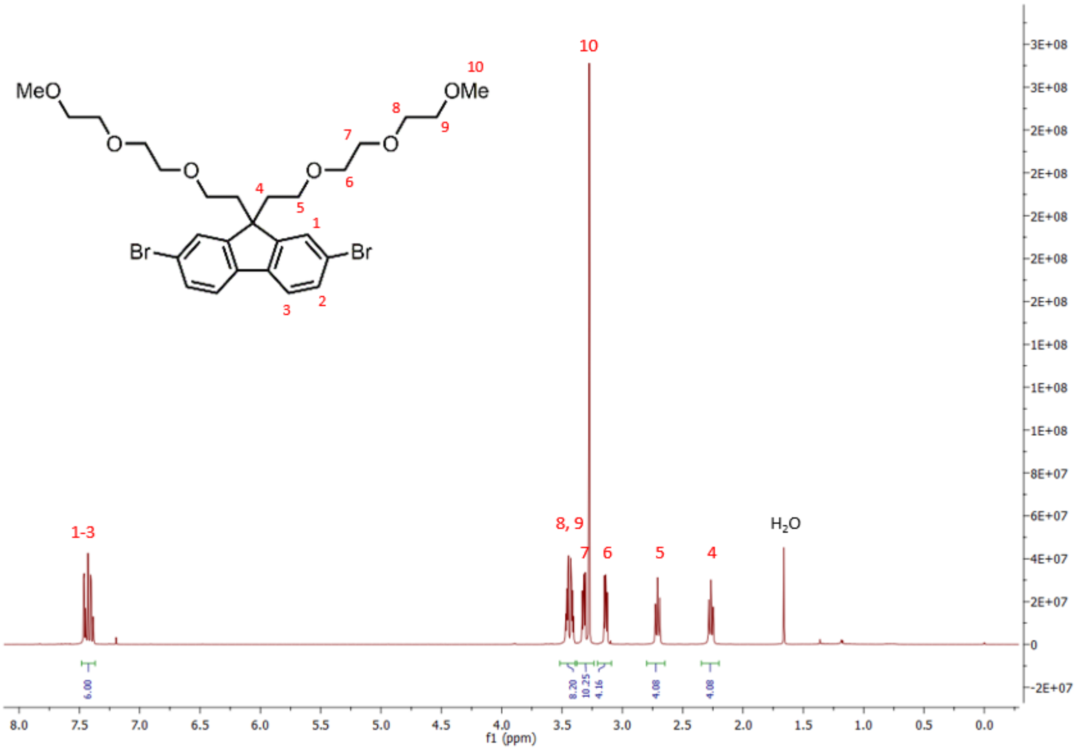

Figure 2.64. ^{1}H NMR spectrum of 2,7-dibromo-9,9-bis[2-[2-(2-methoxyethoxy)ethoxy]ethyl]-9*H*-fluorene in $CDCl_3$.

2,7-Dibromo-9,9-bis[2-(2-methoxyethoxy)ethyl]-9*H*-fluorene

A solution of 1-Bromo-2-(2-methoxyethoxy)ethane (2.489 g, 13.6 mmol), 2,7-dibromofluorene (2.00 g, 6.18 mmol) and potassium iodide (33.8 mg, 0.136 mmol) in dimethylsulfoxide (20 mL) was degassed under vacuum and cooled to 0 °C. Potassium hydroxide (1.14 g, 20.4 mmol) was added and the solution was allowed to heat back up to room temperature and was stirred at this temperature for 16 hours. The reaction mixture was then poured into 50 mL of water. The solvents were removed by evaporation under reduced pressure and the crude residue was dissolved in dichloromethane (100 mL). This solution was washed with water (3 ×100 mL) and brine (100 mL) and the organic layer was removed under reduced pressure. The crude product was purified by silica column chromatography, eluting with ethyl acetate/petroleum ether (2:3) and then ethyl acetate. The title compound was further treated to remove any monoalkyl defects by stirring at room temperature for 15 minutes with potassium *t*-butoxide (755 mg, 6.18 mmol) in tetrahydrofuran (100 mL). The solution was then filtered through neutral alumina, which was then washed with tetrahydrofuran (150 mL). The solvent was removed under reduced pressure to afford the title compound (1.578 g, 22%). ^{1}H NMR (400 MHz, $CDCl_3$, δ): 7.44-7.56 (m, 6H; ArH), 3.28-3.31 (overlapped peaks, 10H; CH_2 and CH_3), 3.17-3.20 (m, 4H; CH_2), 2.78 (t, J = 8.0 Hz, 4H; CH_2), 2.36 (t, J = 8.0 Hz, 4H; CH_2).

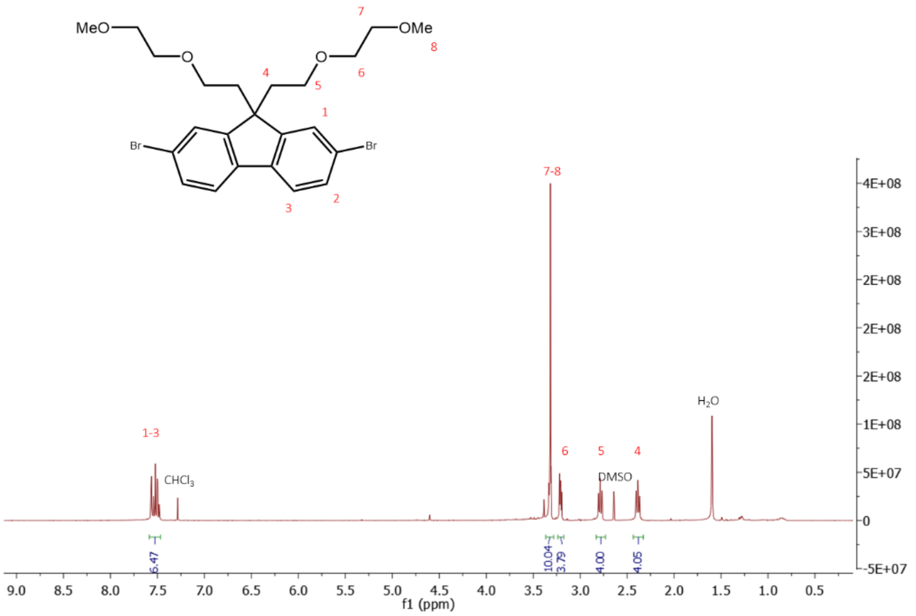

Figure 2.65. ^{1}H NMR spectrum of 2,7-Dibromo-9,9-bis[2-(2-methoxyethoxy)ethyl]-9*H*-fluorene in $CDCl_3$

2,7-Dibromo-9,9-bis[2-[2-(2-(2-methoxyethoxy)ethoxy)ethoxy]ethyl]-9*H*-fluorene

The previous procedure was repeated using triethylene glycol 2-bromoethyl methyl ether (3.688 g, 13.6 mmol) rather than 1-bromo-2-(2-methoxyethoxy)ethane. The title compound was obtained as a white powder (2.1078g, 22%). ^{1}H NMR (400 MHz, $CDCl_3$, δ): 7.43-7.54 (m, 6H; ArH), 3.49-3.61 (m, 16H; CH_2), 3.35-3.39 (m, 4H; CH_2), 3.35 (s, 6H; CH_2), 3.16-3.20 (m, 4H; CH_2), 2.76 (t, J = 8.0 Hz, 4H; CH_2), 2.30 (t, J = 8.0 Hz, 4H; CH_2).

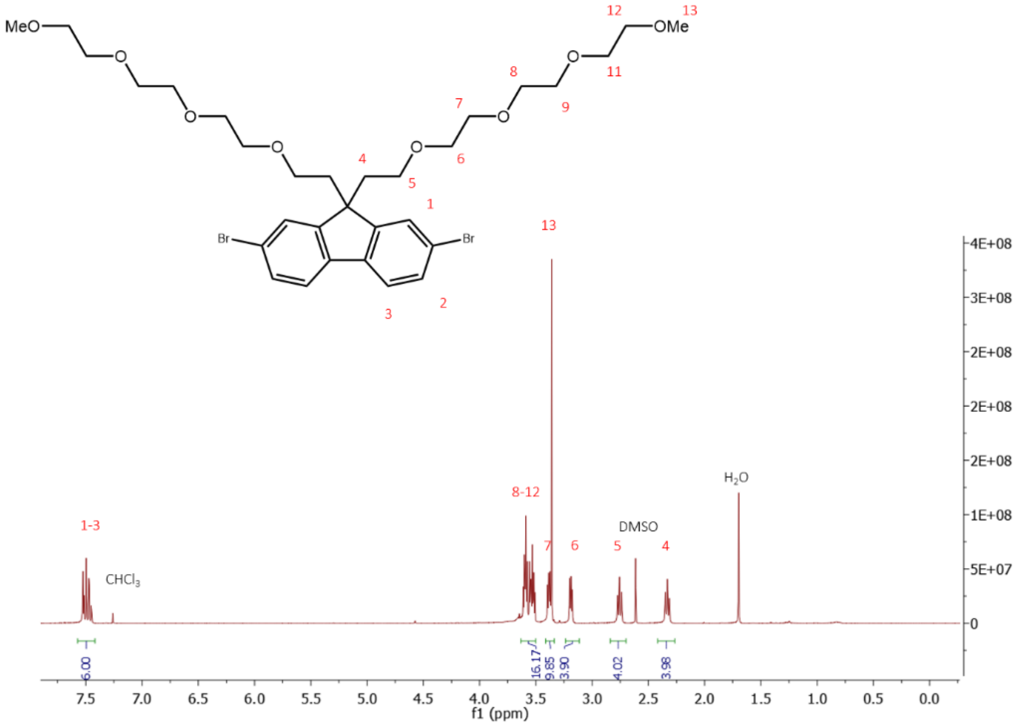

Figure 2.66. ^{1}H NMR spectrum of 2,7-dibromo-9,9-bis[2-[2-(2-(2-methoxyethoxy)ethoxy)ethoxy]ethyl]-9*H*-fluorene in $CDCl_3$.

3,7-dibromo-5,5-dioctyl-5*H*-Dibenzo[*b*,*d*]germole

4,4‘-Dibromo-2,2‘-diiodobiphenyl was first synthesised using a literature procedure.[86] *n*-Butyllithium (1.6 mL, 3.64 mmol, 2.28 M in hexane) was added to a solution of 4,4‘-Dibromo-2,2‘-diiodobiphenyl (1.00g, 1.78 mmol) in dry THF (20 mL) at -78 °C under nitrogen atmosphere for 1 h. The mixture was stirred for a further 1 h at -78 °C, then di-n-octylgermanium dichloride (7.02 mg, 1.86 mmol) was added and the mixture was brought up to room temperature and stirred overnight. The reaction was quenched with distilled water. The organic layer was washed with brine (100 mL), dried with anhydrous Na_2SO_4, and evaporated. The crude product was then purified by column chromatography with hexane as the eluent and by high-pressure liquid chromatography with methanol as the eluent. Compound 5 was obtained as colourless crystals (0.657 g, 60%). ^{1}H NMR (400 MHz, $CDCl_3$, δ): 7.67 (m, 4H; ArH), 7.51 (dd, J=4.0 Hz, 2H; ArH), 1.41 (m, 4H; CH_2), 1.17-1.30 (m, 24H; CH_3), 0.86 (t, J=8.0 Hz 6H; CH_3).

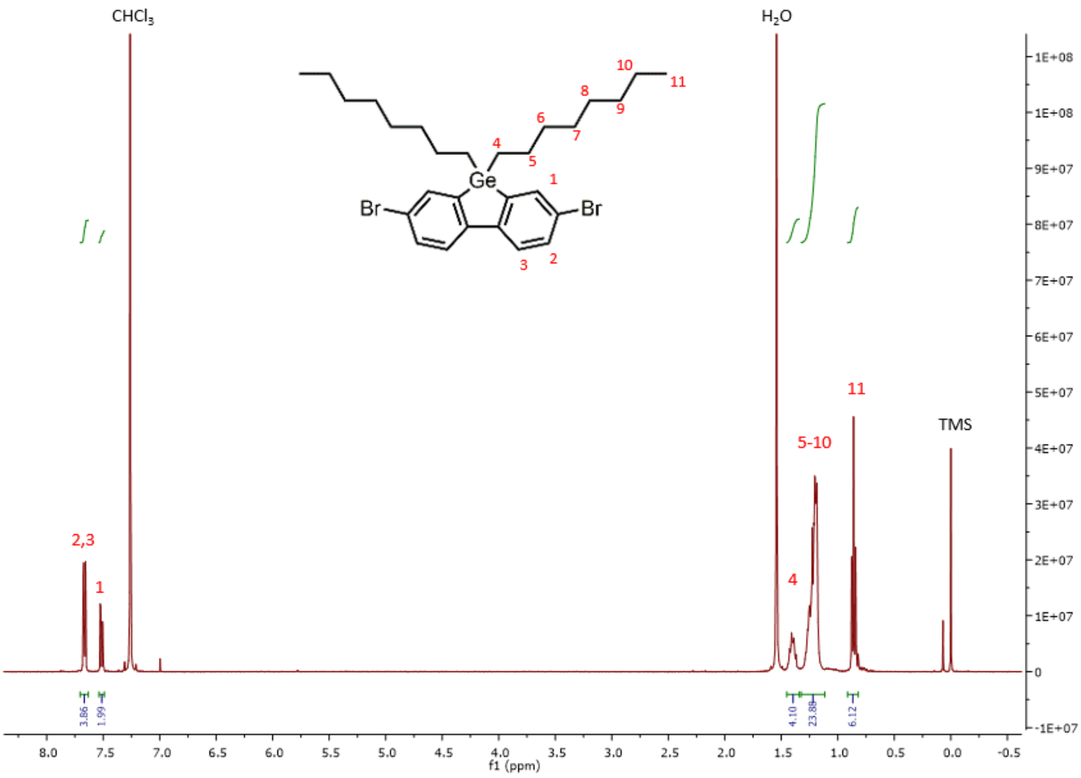

Figure 2.67. ^{1}H-NMR spectrum of 3,7-dibromo-5,5-dioctyl-5*H*-Dibenzo[*b*,*d*]germole in $CDCl_3$.

2.8.2. Polymerisations

All monomers and reagents were obtained from Sigma Aldrich unless the synthesis was stated previously or the source is stated. [Pd(PPh_3)$_4$] was obtained from Strem Chemicals Ltd. (99%). 3,7-dibromodibenzo[*b*,*d*]thiophene 5,-dioxide and dibenzo[*b*,*d*]thiophene sulfone diboronic acid bis(pinacol) ester were obtained from Manchester Organics. 3,7-Dibromo-9,9-dioctyldibenzosilole (3) was obtained from abcr (95% purity). 9-(heptadecan-9-yl)-2,7-bis(4,4,5,5-tetramethyl-1,3,2-dioxaborolan-2-yl)-9H-carbazole was obtained from Ossila (>97%). 2,7-Dibromo-9-(2-ethylhexyl)-9*H*-carbazole,[3] 2,7-Dibromo-9-(*n*-hexadecyl)-9*H*-carbazole[3] and 2,7-Dibromo-9,9-bis[2-[2-(2-methoxyethoxy)ethoxy]ethyl]-9H-fluorene[36] were synthesised using previously reported procedures.

General Procedure: A flask was charged with the monomers, toluene, Starks' catalyst, and an aqueous solution of Na_2CO_3. The mixture was degassed by bubbling with N_2 for 30 minutes, before [Pd(PPh_3)$_4$] was added, and heated. The mixtures were evaporated to dryness and washed with water. The crude polymer was then further purified by Soxhlet extraction with methanol, acetone, and ethyl acetate. The high molecular weight fraction of the polymer was recovered by Soxhlet extraction with chloroform. The chloroform was removed and the polymer redissolved in a minimal amount of chloroform, precipitated into a large excess of methanol, filtered off and dried under reduced pressure. Note: For all polymers the yields were calculated ignoring the presence of end functional groups whose nature is unclear.

P8-s and P8-i: 2,7-Dibromo-9-(2-ethylhexyl)-9*H*-carbazole (1.749 g, 4.0 mmol), 1,4-benzenediboronic acid bis(pinacol) ester (1.323 g, 4.0 mmol), [Pd(PPh_3)$_4$] (93.4 mg, 0.08 mmol), toluene (70 mL) and aqueous Na_2CO_3 (2.0 M, 30 mL) were used in this reaction. After work-up and Soxhlet extraction with chloroform, the soluble product (**P8-s**) was obtained as a yellow-brown powder (0.124 g, 9%) and the insoluble product (**P8-i**) was obtained as a dark green-brown powder (1.194 g, 84%). Anal. Calcd for **P8-s** $(C_{26}H_{27}N)_n$ and **P8-i** $(C_{26}H_{27}N)_n$: C, 88.34; H, 7.70; N, 3.51%; Pd, 0.02%; Found for **P8-s** $(C_{26}H_{27}N)_n$: C, 83.71, H 7.32, N, 3.51%, and **P8-i** $(C_{26}H_{27}N)_n$: C, 78.79; H, 6.85%; N, 3.44%; Pd 0.50%

P9-s and P9-i: 2,7-Dibromo-9-(*n*-hexadecyl)-9*H*-carbazole (1.0992 g, 2.0 mmol), 1,4-benzenediboronic acid bis(pinacol) ester (0.6600 g, 2.0 mmol), [Pd(PPh_3)$_4$] (46.2 mg, 0.04 mmol), toluene (35 mL) and aqueous Na_2CO_3 (2.0 M, 15 mL) were used in this reaction. After work-up and Soxhlet extraction with chloroform, the soluble product (**P9-s**) was obtained as a yellow-brown powder (0.0976 g, 10%) and the insoluble product (**P9-i**) was obtained as a dark green-brown powder (0.3216 g, 35%). Anal. Calcd for **P9-s** $(C_{34}H_{43}N)_n$ and

P9-i $(C_{34}H_{43}N)_n$: C, 87.69; H, 9.31; N, 3.01%; Found for **P9-s** $(C_{34}H_{43}N)_n$: C, 86.44, H 9.07, N, 2.66%, and **P9-i** $(C_{34}H_{43}N)_n$: C, 85.01; H, 9.00%; N, 2.68%

FP-Hex: 1,4-Benzenediboronic acid bis(pinacol) ester (660 mg, 2.0 mmol), 2,7-dibromo-9,9-di-*n*-Hexyl-9*H*-fluorene (985 mg, 2.0 mmol), toluene (35 mL), Na_2CO_3 (15 mL, 2 M), Starks' catalyst (2 drops), and $[Pd(PPh_3)_4]$ (35 mg) were used in this reaction. After 2 days at 110 °C the reaction was worked up as described above giving the product as a grey solid in 47% yield (0.384 g) Anal. Calcd for **FP-Hex** $(C_{31}H_{36})_n$: C, 91.12; H, 8.88%. Found: C, 89.27; H, 8.75; Pd, 0.48%. ^{1}H NMR (400 MHz, $CDCl_3$) δ 7.93-7.53 (10 H, m), 2.09 (4 H, s, br), 1.11 (12 H, m), 0.79 (10 H, m).

FP-EtHex: 1,4-Benzenediboronic acid bis(pinacol) ester (660 mg, 2.0 mmol), 2,7-dibromo-9,9-bis(2-ethylhexyl)fluorene (1100 mg, 2.0 mmol), toluene (35 mL), Na_2CO_3 (15 mL, 2 M), Starks' catalyst (2 drops), and $[Pd(PPh_3)_4]$ (35 mg) were used in this reaction. After 2 days at 110 °C the reaction was worked up as described above giving the product as a grey solid in 90% yield (837 mg). Anal. Calcd for **FP-EtHex** $(C_{35}H_{44})_n$: C, 90.46; H, 9.54%. Found: C, 89.16; H, 9.41; Pd, 0.38%. ^{1}H NMR (400 MHz, $CDCl_3$) δ 7.92-7.60 (10 H, m), 2.12 (4 H, s, br), 0.89 (18 H, m), 0.71-0.62 (6 H, m), 0.62-0.53 (6 H, m) .

FP-Oct: 1,4-Benzenediboronic acid bis(pinacol) ester (660 mg, 2.0 mmol), 2,7-dibromo-9,9-di-*n*-octyl-9*H*-fluorene (1100 mg, 2.0 mmol), toluene (35 mL), Na_2CO_3 (15 mL, 2 M), Starks' catalyst (2 drops), and $[Pd(PPh_3)_4]$ (35 mg) were used in this reaction. After 2 days at 110 °C the reaction was worked up as described above giving the product as a grey solid in 72% yield (0.669 g). Anal. Calcd for **FP-Oct** $(C_{35}H_{44})_n$: C, 90.46; H, 9.54%. Found: C, 89.15; H, 9.44; Pd, 0.44%. ^{1}H NMR (400MHz, $CDCl_3$) δ 7.7-7.91 (6 H, m), 7.61-7.73 (4 H, m) 2.09 (4 H, s, br), 1.01-1.26 (20 H, m), 0.7-0.85 (10 H, m).

FP-Dodec: 1,4-Dibromobenzene (472 mg, 2.0 mmol), 9,9-Di-*n*-dodecyl-9*H*-fluorene-2,7-diyl-diboronic acid (1.18 g, 2.0 mmol), toluene (35 mL), Na_2CO_3 (15 mL, 2 M), Starks' catalyst (2 drops), and $[Pd(PPh_3)_4]$ (35 mg) were used in this reaction. After 2 days at 110 °C the reaction was worked up as described above giving the product as a grey solid in 57% yield (0.642 g). Anal. Calcd for **FP-Dodec** $(C_{43}H_{60})_n$: C, 89.52; H, 10.48%. Found: C, 87.43; H, 10.28; Pd, 0.43%. ^{1}H NMR (400MHz, $CDCl_3$) δ 7.66-7.86 (6 H, m), 7.60-7.72 (4 H, m) 2.08 (4 H, s, br), 1.03-1.34 (40 H, m), 0.85 (6 H, t, J = 5.3 Hz).

FS-Hex: 9,9-Di-*n*-Hexylfluorene-2,7-diboronic acid (844 mg, 2.0 mmol), 3,7-dibromodibenzo[*b*,*d*]thiophene 5,-dioxide (748 mg, 2.0 mmol), toluene (35 mL), Na_2CO_3 (15 mL, 2 M), Starks' catalyst (2 drops), and $[Pd(PPh_3)_4]$ (35 mg) were used in this reaction. After 2 days at 110 °C the reaction was worked up as described above giving the product as a green-yellow solid in 50% yield (550 mg). Anal. Calcd for **FS-Hex** $(C_{37}H_{38}O_2S)_n$: C, 81.28;

H, 7.01; S, 5.86%. Found: C, 79.14; H, 6.86; S, 5.76; Pd, 0.04%. ^{1}H NMR (400MHz, $CDCl_3$) δ 8.14 (2 H, s),7.81-8.00 (6 H, m) 7.63-7.73 (4 H, m), 1.93-2.25 (4 H, m), 1.01-1.20 (12 H, m), 0.60-0.83 (10 H, m). Note: An insoluble fraction was also obtained in 40% yield (439 mg).

FS-EtHex: 9,9-Di(2-ethylHexyl)fluorene-2,7-diboronic acid bis(1,3-propanediol) ester (2 mL, 0.5 M solution in toluen**e)**, 3,7-dibromodibenzo[*b*,*d*]thiophene 5,-dioxide (374 mg, 2.0 mmol), toluene (17.5 mL), Na_2CO_3 (7.5 mL, 2 M), Starks' catalyst (2 drops), and [$Pd(PPh_3)_4$] (17.5 mg) were used in this reaction. After 2 days at 110 °C the reaction was worked up as described above giving the product as a green solid in 63% yield (382 mg). Anal. Calcd for **FS-EtHex** $(C_{41}H_{46}O_2S)_n$: C, 81.68; H, 7.69; S, 5.32%. Found: C, 81.18; H, 7.79; S, 5.12; Pd, 0.32%. ^{1}H NMR (400 MHz, $CDCl_3$) 8.14 (2 H, s),7.81-8.00 (6 H, m) 7.63-7.73 (4 H, m), 2.12 (4 H, s, br), 0.73-1.01 (18 H, m), 0.50-0.72 (12 H, m).

FS-Oct: 2,2'-(9,9-Di-*n*-octyl-9*H*-fluorene-2,7-diyl-bis(4,4,5,-tetramethyl-1,3,2-dioxaborolane) 643 mg, 1.0 mmol), 3,7-dibromodibenzo[*b*,*d*]thiophene 5,-dioxide (374 mg, 1.0 mmol), toluene (17.5 mL), Na_2CO_3 (7.5 mL, 2 M), Starks' catalyst (2 drops), and [$Pd(PPh_3)_4$] (17.5 mg) were used in this reaction. After 2 days at 110 °C the reaction was worked up as described above giving the product as a green solid in 37% yield (248 mg). Anal. Calcd for **FS-Oct** $(C_{41}H_{46}O_2S)_n$: C, 81.68; H, 7.69; S, 5.32%. Found: C, 81.30; H, 7.70; S, 5.31; Pd content, 0.02%. ^{1}H NMR (400 MHz, $CDCl_3$) δ 8.19 (2 H, s),7.83-8.04 (6 H, m) 7.61-7.72 (4 H, m), 2.12 (4 H, s, br), 1.01-1.30 (20 H, m), 0.7-0.85 (10 H, m).

FS-Dodec: 9,9-Di-*n*-dodecyl-9*H*-fluorene-2,7-diyl-diboronic acid (591 mg, 1.0 mmol), 3,7-dibromodibenzo[*b*,*d*]thiophene 5,-dioxide (374 mg, 1.0 mmol), toluene (17.5 mL), Na_2CO_3 (7.5 mL, 2 M), Starks' catalyst (2 drops), and [$Pd(PPh_3)_4$] (17.5 mg) were used in this reaction. After 2 days at 110 °C the reaction was worked up as described above giving the product as a dark green solid in 79% yield (561 mg). Anal. Calcd for **FS-Dodec** $(C_{49}H_{62}O_2S)_n$: C, 81.91; H, 8.74; S, 4.48%. Found: C, 81.97; H, 8.88; S, 4.29; Pd, 0.07%. ^{1}H NMR (400MHz, $CDCl_3$) 8.19 (2 H, s),7.83-8.03 (6 H, m) 7.61-7.72 (4 H, m), 2.12 (4 H, s, br), 1.03-1.32 (40 H, m), 0.84 (6 H, t, *J* = 6.2 Hz).

FP-TEG: 2,7-Dibromo-9,9-bis[2-[2-(2-methoxyethoxy)ethoxy]ethyl]-9*H*-fluorene (0.650 g, 1.1 mmol), 1,4-benzenediboronic acid bis(pinacol) ester (0.355 g, 1.1 mmol), [$Pd(PPh_3)_4$] (26.5 mg, 0.02 mmol), toluene (20 mL) and aqueous Na_2CO_3 (2.0 M, 7 mL) were used in this reaction. After work-up and Soxhlet extraction with chloroform, the soluble product was obtained as a grey-brown powder (0.096 g, 17%). Anal. Calcd for **FP-TEG** $(C_{33}H_{40}O_6)_n$: C, 74.41; H, 7.57%. Found: C, 71.78; H, 7.29; Pd, 0.43%. ^{1}H NMR (400 MHz, $CDCl_3$) δ 7.66-7.88 (10 H, m) 3.37-3.56 (16 H, m), 3.31 (10 H, t, *J* = 9.3 Hz), 2.93 (4 H, s, br), 2.54 (4 H, s, br).

FS-TEG: 2,7-Dibromo-9,9-bis[2-[2-(2-methoxyethoxy)ethoxy]ethyl]-9*H*-fluorene (0.6164 g, 1.0 mmol), dibenzo[*b*,*d*]thiophene sulfone diboronic acid bis(pinacol) ester (0.4682 g, 1.0 mmol), [Pd(PPh$_3$)$_4$] (17.5 mg, 0.02 mmol), toluene (17.5 mL) and aqueous Na_2CO_3 (2.0 M, 7.5 mL) were used in this reaction. After work-up and Soxhlet extraction with chloroform, the soluble product was obtained as a dark green powder (0.483 g, 74%). Anal. Calcd for **FS-TEG** $(C_{39}H_{42}O_8S)_n$: C, 69.83; H, 6.31; S, 4.78%; Found: C, 68.47; H, 6.19; S, 4.64; Pd, 0.30%. ^{1}H NMR (400MHz, $CDCl_3$) δ 8.18 (2 H, s),7.81-8.06 (6 H, m) 7.64-7.79 (4 H, m), 3.11-3.53 (26 H, overlapped peaks), 2.89 (4 H, s, br), 2.55 (4 H, s, br).

FS-DEG: 2,7-Dibromo-9,9-bis[2-(2-methoxyethoxy)ethyl]-9*H*-fluorene (0.5285 g, 1.0 mmol), dibenzo[*b*,*d*]thiophene sulfone diboronic acid bis(pinacol) ester (0.4682 g, 1.0 mmol), [Pd(PPh$_3$)$_4$] (17.5 mg, 0.02 mmol), toluene (17.5 mL) and aqueous Na_2CO_3 (2.0 M, 7.5 mL) were used in this reaction. After work-up and Soxhlet extraction with chloroform, the soluble product was obtained as a dark green powder (0.294 g, 50%). ^{1}H NMR (400MHz, $CDCl_3$) δ 8.15 (2 H, s),7.80-8.00 (6 H, m) 7.64-7.76 (4 H, m), 3.18-3.44 (18 H, overlapped peaks), 2.90 (4 H, s, br), 2.55 (4 H, s, br).

FS-TeEG: 2,7-Dibromo-9,9-bis[2-[2-(2-(2-methoxyethoxy)ethoxy)ethoxy]ethyl]-9*H*-fluorene (0.5416 g, 0.77 mmol), dibenzo[*b*,*d*]thiophene sulfone diboronic acid bis(pinacol) ester (0.3602 g, 0.77 mmol), [Pd(PPh$_3$)$_4$] (13.7 mg, 0.016 mmol), toluene (13.5 mL) and aqueous Na_2CO_3 (2.0 M, 5.8 mL) were used in this reaction. After work-up and Soxhlet extraction with chloroform, the soluble product was obtained as a dark green powder (0.188 g, 25%). ^{1}H NMR (400MHz, $CDCl_3$) δ 8.18 (2 H, s),7.81-8.06 (6 H, m) 7.63-8.06 (6 H, m), 3.47-3.61 (18 H, m), 3.44 (6 H, t), 3.35 (6 H, t) 3.23 (4H, s, br), 2.89 (4 H, s, br), 2.56 (4 H, s, br).

PFO was synthesised according to a previously reported procedure**.**[87] Anal. Calcd for **PFO** $(C_{25}H_{32})_n$: C, 90.30; H, 9.70%. Found: C, 89.34; H, 10.45%. ^{1}H NMR (400MHz, $CDCl_3$) δ 7.84 (2 H, s),7.75-7.62 (4 H, m) 7.63-8.06 (6 H, m), 2.12 (4 H, s, br), 1.01-1.30 (20 H, m), 0.7-0.85 (10 H, m).

FS-1: 9,9-Di-*n*-hexylfluorene-2,7-diboronic acid (844 mg, 2.0 mmol), 2,7-dibromo-9,9-di-*n*-hexyl-9*H*-fluorene (923 mg, 1.9 mmol), 3,7-dibromodibenzo[*b*,*d*]thiophene 5,5-dioxide (47 mg, 0.1 mmol), toluene (35 mL), Na_2CO_3 (15 mL, 2 M), Starks' catalyst (2 drops), and [Pd(PPh$_3$)$_4$] (35 mg) were used in this reaction. After 2 days at 110 °C the reaction was worked up as described above giving the product as a grey-green solid in 78% yield (1.03 g). Anal. Calcd for **FS-1** $(C_{2170}H_{3122}O_6S_3)_n$: C, 88.64; H, 10.70; S, 0.33%. Found: C, 88.54; H, 9.52%.

FS-2: 9,9-Di-*n*-hexylfluorene-2,7-diboronic acid (844 mg, 2.0 mmol), 2,7-dibromo-9,9-di-*n*-hexyl-9*H*-fluorene (862 mg, 1.75 mmol), 3,7-dibromodibenzo[*b*,*d*]thiophene 5,5-dioxide

(94 mg, 0.25 mmol), toluene (35 mL), Na_2CO_3 (15 mL, 2 M), Starks' catalyst (2 drops), and [$Pd(PPh_3)_4$] (35 mg) were used in this reaction. After 2 days at 110 °C the reaction was worked up as described above giving the product as a green-grey solid in 86% yield (1.12 g). Anal. Calcd for **FS-2** $(C_{1070}H_{1522}O_6S_3)_n$: C, 88.16; H, 10.52; S, 0.66%. Found: C, 87.93; H, 9.33%.

FS-3: 9,9-Di-*n*-hexylfluorene-2,7-diboronic acid (844 mg, 2.0 mmol), 2,7-dibromo-9,9-di-*n*-hexyl-9*H*-fluorene (738 mg, 1.5 mmol), 3,7-dibromodibenzo[*b*,*d*]thiophene 5,5-dioxide (187 mg, 0.5 mmol), toluene (35 mL), Na_2CO_3 (15 mL, 2 M), Starks' catalyst (2 drops), and [$Pd(PPh_3)_4$] (35 mg) were used in this reaction. After 2 days at 110 °C the reaction was worked up as described above giving the product as a yellow solid in 70% yield (0.895 g). Anal. Calcd for **FS-3** $(C_{1070}H_{1522}O_6S_3)_n$: C, 88.16; H, 10.52; S, 0.66%. Found: C, 87.93; H, 9.33%.

FS-4: 9,9-Di-*n*-hexylfluorene-2,7-diboronic acid (844 mg, 2.0 mmol), 2,7-dibromo-9,9-di-*n*-hexyl-9*H*-fluorene (492 mg, 1.0 mmol), 3,7-dibromodibenzo[*b*,*d*]thiophene 5,5-dioxide (374 mg, 1.0 mmol), toluene (35 mL), Na_2CO_3 (15 mL, 2 M), Starks' catalyst (2 drops), and [$Pd(PPh_3)_4$] (35 mg) were used in this reaction. After 2 days at 110 °C the reaction was worked up as described above giving the product as a pale green solid in 84% yield (1.01 g). Anal. Calcd for **FS-4** $(C_{87}H_{102}O_2S)_n$: C, 86.22; H, 8.48; S, 2.65%. Found: C, 84.45; H, 8.40;

SiS-Oct: 3,7-Dibromo-5,5-dioctyl-5*H*-dibenzo[*b*,*d*]silole (565 mg, 1.0 mmol) 3,7-dibenzo[*b*,*d*]thiophene 5,5-dioxide diboronic acid bis(pinacol) ester (468 mg, 1.0 mmol) toluene (17.5 mL), Na_2CO_3 (7.5 mL, 2 M), Starks' catalyst (2 drops), and [$Pd(PPh_3)_4$] (17.5 mg) were used in this reaction. After 2 days at 110 °C the reaction was worked up as described above giving the product as a yellow-green solid in 55% yield (343 mg). Anal. Calcd for **SiS-Oct** $(C_{40}H_{46}O_2SSi)_n$: C, 77.62; H, 7.49; S, 5.18%. Found: C, 76.51; H, 7.53; S, 4.93%. Pd content: 0.084%.

GeS-Oct: 3,7-dibromo-5,5-dimethyl-5*H*-Dibenzo[*b*,*d*]germole (85 mg, 0.14 mmol) 3,7-dibenzo[*b*,*d*]thiophene 5,5-dioxide diboronic acid bis(pinacol) ester (65 mg, 0.14 mmol) toluene (7 mL), Na_2CO_3 (3 mL, 2 M), Starks' catalyst (1 drop), and [$Pd(PPh_3)_4$] (2.4 mg) were used in this reaction. After 2 days at 110 °C the reaction was worked up as described above giving the product as a grey solid in 68% yield (62 mg). Anal. Calcd for **GeS-Oct** $(C_{40}H_{46}O_2SGe)_n$: C, 72.41; H, 6.99; S, 4.83%. Found: C, 76.69 %; H, 9.21%. Pd content: 0.17%. ^{1}H NMR (400 MHz, $CDCl_3$) δ 8.00 (2 H, **d)**, 7.94 (4 H, s) 7.57-7.85 (6 H, overlapped peaks) 7.61-7.72 (4 H, m), 2.10 (4 H, s, br), 1.54 (6 H, s, br), 1.05-1.40 (20 H, m), 0.7-0.85 (10 H, m).

CzS-Oct: 9-(heptadecan-9-yl)-2,7-bis(4,4,5,5-tetramethyl-1,3,2-dioxaborolan-2-yl)-9H-carbazole (658 mg, 1.0 mmol), 3,7-dibromodibenzo[*b*,*d*]thiophene 5,5-dioxide (374 mg, 1.0 mmol), toluene (17.5 mL), Na_2CO_3 (7.5 mL, 2 M), Starks' catalyst (2 drops), and [$Pd(PPh_3)_4$] (17.5 mg) were used in this reaction. After 2 days at 110 °C the reaction was worked up as described above giving the product as a yellow-green solid in 25% yield (153 mg). Anal. Calcd for **CzS-Oct** $(C_{41}H_{47}NO_2S)_n$: C, 79.70; H, 7.67; N, 2.27; S, 5.19%. Found: C, 76.56; H, 7.41%; N, 2.27 %; S, 4.92%. Pd content: 0.10%. ^{1}H NMR (400 MHz, $CDCl_3$) δ 8.10-8.31 (4 H, m), 7.65-8.07 (4 H, m), 7.46-7.60 (4 H, m), 4.75 (1 H, s), 2.39 (2 H, s, br), 2.09 (2 H, s, br), 1.05-1.38 (24 H, overlapped peaks), 0.75-0.85, 6 H, m).

2.8.3. Characterisation Methods

Solution ^{1}H NMR spectra were recorded at 400.13 MHz using a Bruker Avance 400 NMR spectrometer. Single detection gel permeation chromatography (GPC) was performed using an Agilent 1260 Infinity II GPC/SEC system, two PLgel 5 µm MIXED-D columns and a PLgel 5 µm guard column), with samples detected by refractive index (RI). A mobile phase of chloroform was used with a flow-rate of 1 mL min^{-1} at 40 ˚C. GPC data was analyzed using Agilent software and Agilent EasiCal PS-2 standards were used. Thermogravimetric analysis was performed on a Hitachi High-Tech EXSTAR6000 instrument by heating samples at 10 °C min^{-1} under air in open aluminium pans to 600 °C. PXRD measurements were performed on a Panalytical Empyrean diffractometer, with a Cu X-ray source (λ = 1.5418 Å, Cu-Kα), used in high throughput transmission mode with a Kα focusing mirror and PIXcel 3D detector.

UV-Vis absorption spectra of the polymers were recorded on a Shimadzu UV-2550 UV-vis spectrometer by measuring the transmittance of films and solutions or the reflectance of powders in the solid state. The fluorescence spectra of the polymer powders were measured with a Shimadzu RF-5301PC fluorescence spectrometer at room temperature.Contact angle measurements were performed using a Krüss DSA100 instrument on films of all soluble polymers drop-cast from chloroform onto glass microscope slides and a pellet of insoluble **FS-Me** and **FP-Me**. The Laplace-Young method was used to calculate contact angles of 5 µL droplets of water over the course of eleven frames taken over ten seconds at three different positions on the cast films.

Nitrogen sorption isotherms were measured using Micromeritics 2420 volumetric adsorption analyser. Surface areas were calculated in 3 the relative pressure (P/P0) range from 0.01 to 0.10 of the adsorption branch. Water vapour isotherms were determined at 293 K using an IGA gravimetric adsorption apparatus (Hiden Isochema, U.K.) with anti-condensation system, which was carried out in an ultrahigh vacuum system equipped with a diaphragm and turbo pumps.

Static light scattering measurements were performed on a Malvern Mastersizer 3000 Particle Sizer, polymers were dispersed in water and water/methanol/triethylamine (1:1:1) mixtures by sonication for 40 minutes. The resultant suspensions were injected into a stirred Hydro SV quartz cell, containing more of the requisite medium to give a laser obscuration of 5 – 10%. Particle sizes were fitted according to Mie theory, using the Malvern 'General Purpose' analysis model, for non-spherical particles with fine powder mode turned on. A polymer refractive index of 1.59, polymer absorbance of 0.1 and solvent refractive indices of 1.330 and 1.353 were used for fitting for the respective media. Imaging of the polymer morphology was performed on a Hitachi S4800 Cold Field Emission SEM, with secondary electron, backscatter and transmission detectors and an acceleration voltage of 3.0 kV. Photoelectron spectroscopy in air (PESA) measurements were recorded using a Riken Keiki PESA spectrometer (Model AC-2) with a power number of 0.33. Samples for PESA were prepared on glass substrates.

AFM Profilometry. All AFM images were taken on an Asylum Research Cypher-ES instrument. Dry thickness measurements were taken by imaging across a razor blade scratch in tapping mode using 75 kHz HQ:NSC18/Pt tips (MikroMasch). Swollen measurements were then taken by depositing 100 µl of solvent (Milli-Q water or TEA) onto the sample and imaging the same area of the film in contact mode using ContGB-G tips (BudgetSensors). Quartz Crystal Microbalance (QCM). QCM measurements were performed using a QCM200 (Stanford Research Systems) on 5 MHz gold-coated AT quartz crystals. Prior to polymer deposition, each crystal's steady-state frequency was measured in both air and water. After spin coating the polymer, the new steady-state frequency in both air and water was recorded. Signals were recorded using a potentiostat (MetroOhm Autolab PGSTAT204).

Transient absorption spectroscopy: Microsecond[35] and femtosecond[88] transient absorption spectroscopy (TAS) were performed in transmission mode using in-house setups described previously. Dispersions of each polymer in different liquid environments were excited using 420 nm light, matching the cut-off wavelength used in hydrogen evolution experiments. Ground state transmission spectra for all TAS samples, used for absorption normalisation, were taken using an Agilent Cary 60 UV-vis spectrophotometer and converted to absorption data using a cuvette of the appropriate solvent as a reference.

Microsecond TAS samples were made at a concentration of 0.02 mg mL^{-1} in 10 mm quartz cuvettes (Hellma Analytics). Unless otherwise stated, these were excited at a fluence of 1.5 mJ cm^{-2} with kinetic traces taken over an average of 500 individual excitation pulses generated at a frequency of 1.0 Hz. Femtosecond TAS samples were made at a concentration of 0.2 mg mL^{-1} in 2 mm quartz cuvettes (Hellma Analytics). Transient transmission spectra were probed in the visible spectrum by adjusting the referenced setup such that the amplifier output was focussed into a Ti:sapphire crystal which produces a continuum in the 460-740 nm range. Unless otherwise stated, the excitation fluence was 87 µJ cm^{-2}. Transmission spectra were averaged over a minimum of 8 sequential measurements depending on the size of the optical response. Group velocity dispersion was corrected using the software Surface Xplorer 4.2 (Ultrafast Systems).

2.8.4. Photocatalysis Experiments

Water for the hydrogen evolution experiments was purified using an ELGA LabWater system with a Purelab Option S filtration and ion exchange column without further pH level adjustment. For powder samples, a quartz flask was charged with the polymer powder (25 mg), water (7.5 mL), methanol (7.5 mL) and triethylamine (7.5 mL)—unless stated otherwise—and sealed with a septum. The resultant suspensions were ultrasonicated until the photocatalyst was well dispersed before degassing by N_2 bubbling for 30 minutes. All reaction mixtures were then illuminated with a 300 W Newport Xe light-source (Model: 6258, Ozone free) for the time specified using appropriate filters (**Figure 2.68**). NIR light was absorbed by circulating water through a fused silica window.

Gas samples were taken with a gas-tight syringe and run on a Bruker 450-GC gas chromatograph equipped with a Molecular Sieve 13X 60-80 mesh 1.5 m × ⅛” × 2 mm ss column at 50 °C with an argon flow of 40.0 mL min^{-1}. Hydrogen was detected with a thermal conductivity detector referencing against standard gas with a known concentration of hydrogen. Hydrogen dissolved in the reaction mixture was not measured and the pressure increase generated by the evolved hydrogen was neglected in the calculations. The rates were determined from a linear regression fit once a consistent rate of increase of hydrogen evolution was observed and the error is given as the standard deviation of the amount of hydrogen evolved. No hydrogen evolution was observed for a mixture of water/methanol/triethylamine under λ >295 nm illumination in absence of a photocatalyst.

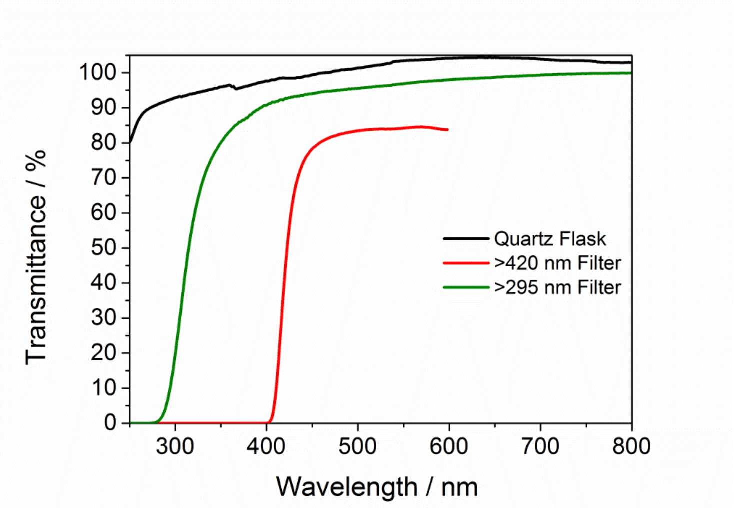

Figure 2.68. Transmittance spectra of the quartz flask, $\lambda > 295$ nm, and $\lambda > 420$ nm filter used in this chapter.

High throughput hydrogen evolution experiments: The Agilent Technologies vials (crimp top, headspace, clear with graduation marks and write-on spot, flat bottom, 10 mL, 23 × 46 mm) were charged with approximately 5 mg of polymer powders and transferred to the Chemspeed Sweigher for liquid transfer. The mass of polymer in each vial was noted. Degassed scavenger solutions were loaded in the robot and water from an ELGA water purification system was degassed with nitrogen and connected to the setup. The system was closed and flushed with nitrogen from the house supply for 6 hours. The automatic setup dispenses the requisite amount of liquids and seals the vials with Agilent Technologies caps (crimp, headspace, with septum, 20 mm, silver aluminum cap with safety feature, moulded PTFE/butyl septum). The total volume of the reaction mixture was 5.0 ± 0.1 mL in each vial. The sealed vials were transferred to an ultrasonic bath for 10 minutes to disperse the polymers in the scavenger solutions. The vials were illuminated with an Oriel Solar Simulator 94123A with an output of 1.00 sun on a Stuart Scientific Gyro rocker SRT9 for 130 minutes (classification IEC 60904-9 2007 spectral match A, uniformity classification A, temporal stability A, 1600 W Xenon light source, 25 × 25 cm output beam, Air mass 1.5G filter, 350-1000 nm). After photocatalysis, the amount of evolved hydrogen was measured on an Agilent Technologies GC 7890B connected to an Agilent Technologies headspace sampler 7697A.

External quantum efficiency: EQE was measured using a $\lambda = 420$ nm LED controlled by an IsoTech IPS303DD power supply. For the experiments polymer (12 mg) was suspended in water, triethylamine, methanol (1:1:1 volume mixture, 8 mL). An area of 8 cm^2 was illuminated and the light intensity was measured with a ThorLabs S120VC photodiode power sensor controlled by a ThorLabs PM100D Power and Energy Meter Console. The external quantum efficiencies were estimated using the following equation:

$$\text{EQE \%} = 2 \times \frac{\text{moles of hydrogen evolved}}{\text{moles of incident photons}} \times 100\ \%$$

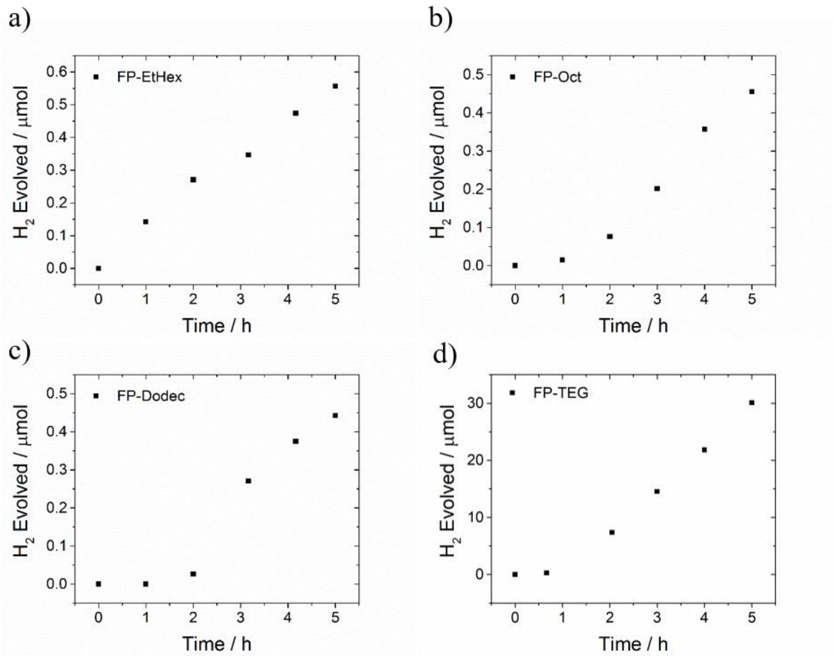

Figure 2.69. Hydrogen evolved from dispersions of the **FP** series of polymers (25 mg) in water/methanol/TEA (1:1:1) under visible light irradiation using a 300 W Xe light source.

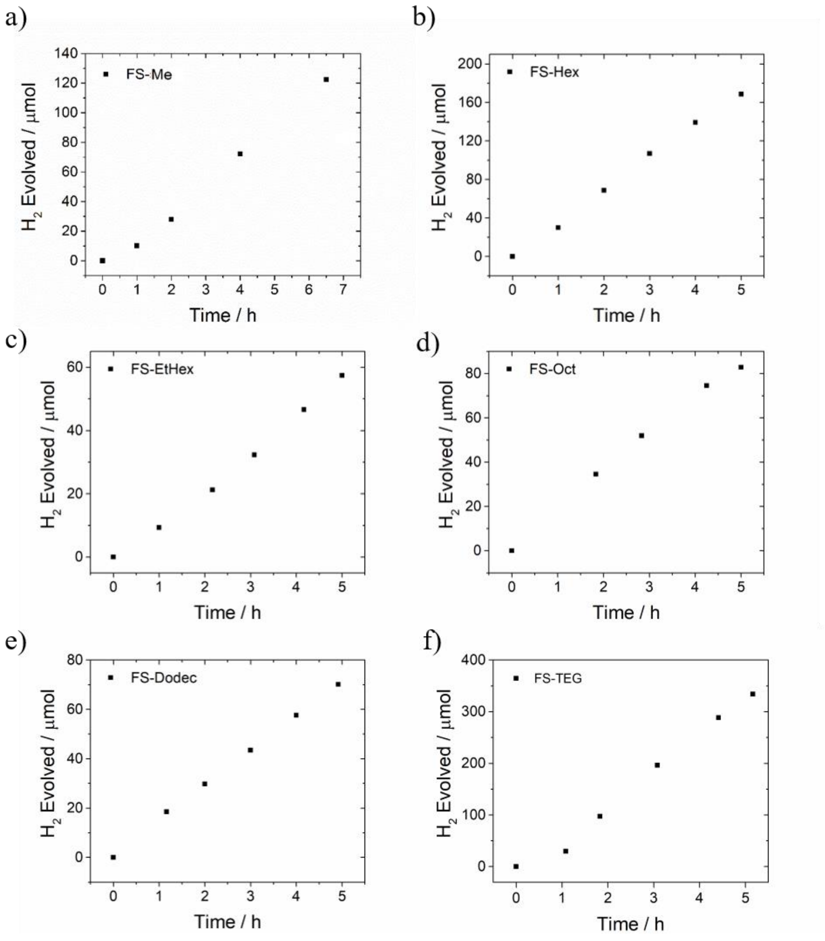

Figure 2.70. Hydrogen evolved from dispersions of the **FS** series of polymers (25 mg) in water/methanol/TEA (1:1:1) under visible light irradiation using a 300 W Xe light source.

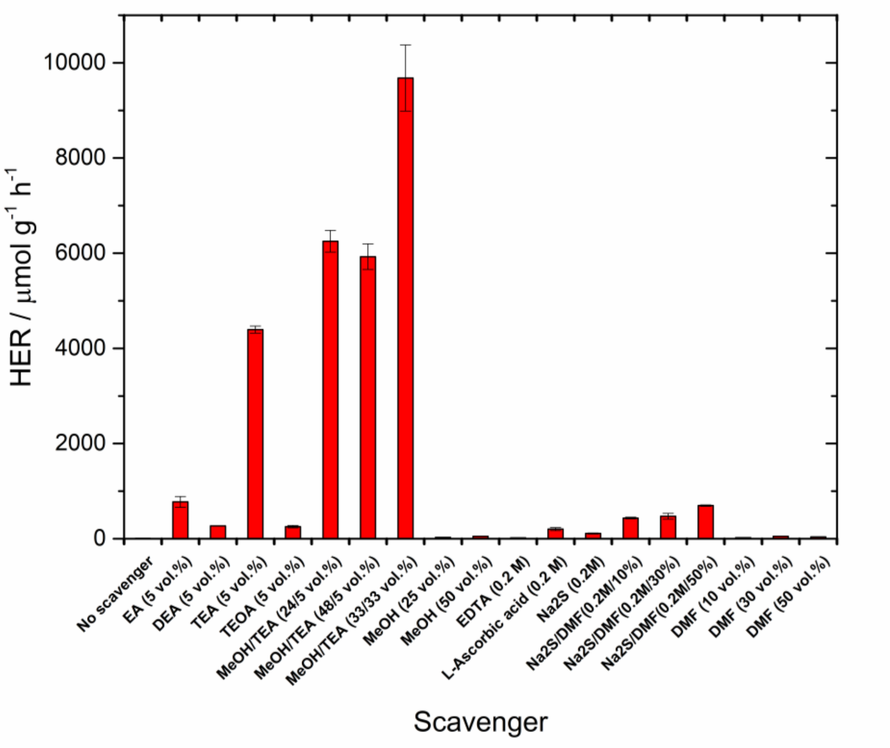

Figure 2.71. Hydrogen evolution rates of **FS-TEG** (5 mg) in the presence of various sacrificial donors under irradiation by a solar simulator (AM1.5G, 1 Sun).

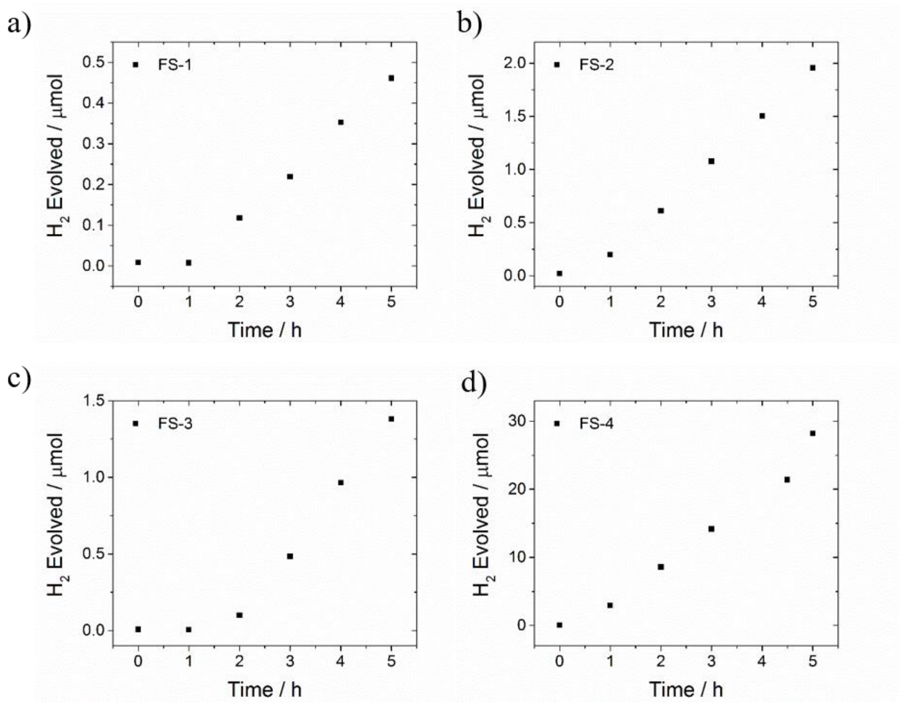

Figure 2.72. Hydrogen evolved from dispersions of **FS-1-4** (25 mg) in water/methanol/TEA (1:1:1) under visible light irradiation using a 300 W Xe light source.

2.8.5. Computational Methods

Molecular Dynamics Simulations: Molecular dynamics simulations were performed using the same methodology outlined in previous work.[35] OPLS forcefields were used for the solvents and an OPLS-based forcefield was used for polymers. The forcefield uses the previously used forcefield with the bridging groups replaced by the side-chains. Simulations used short oligomers with an equivalent length of six flourene units (trimers of **FS** polymers and tetramers of **FP** polymers) as a model for the polymers. Oligomers were simulated in a water/TEA (1:1) mixture as well as the reaction medium of water/methanol/TEA (1:1:1). Radial distribution functions (RDFs) were calculated in order to calculate the volume occupied by each solvent as a function of distance from the oligomer backbone.

(TD)-DFT: The ionisation potential and electron affinity associated with the charge carriers (IP/EA) and excitons (IP*/EA*) in **FP** and **FS** polymers were calculated using a previously reported approach[58] based around (time-dependent) density functional theory ((TD-)DFT) calculations. These □(TD-)DFT calculations used the B3LYP density functional,[89–91] the DZP basis-set[92] and the COSMO solvation model[93] to describe the environment of the polymer. The absorption onset of the polymers was calculated using the same set-up, except that while for the calculation of the exciton potentials the Tamm-Dancoff approximation[94] is made this approximation is omitted here. All (TD-)DFT calculations were performed using Turbomole 7.1.[95,96]

Table 2.17. (TD-)B3LYP predicted optoelectronic properties of oligomers of **FP** and **FS** polymers. Potentials are reported vs the standard hydrogen electrode (SHE, -4.44 V).

Series	Structure	ε[a]	R	IP / V	EA / V	IP* / V	EA* / V	S0 -> S1 / eV	f
FP	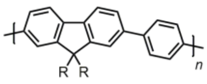	80.10	CH_3	0.7425	-2.3637	-2.1358	0.5147	3.1552	4.1895
		4.81	CH_3	-	-	-	-	3.1509	4.1870
		2.38	CH_3	1.1280	-2.9214	-1.7672	-0.0262	3.1998	4.0129
		2.00	CH_3	1.1865	-2.9973	-	-	-	-
FS	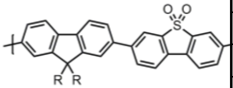	80.10	CH_3	1.0280	-1.8612	-1.7345	0.9013	2.9055	3.4579
		4.81	CH_3	-	-	-	-	2.9099	3.5084
		2.38	CH_3	1.4999	-2.3680	-1.2548	0.3867	2.9510	3.2760
		2.00	CH_3	1.5650	-2.4303	-	-	-	-

[a] Relative permittivities used in COSMO implicit solvent model for Turbomole calculations. Relative permittivities correspond to water, chloroform, triethylamine and expected constant of polymer material.

2.8.6. Varying Palladium Content (Chapter 2.5.3)

Purification 1: FS-TEG (150 mg) was dissolved in chloroform (50 mL) and washed with an aqueous solution of Na(detc) (602 mg in 60 mL) followed by water (5 ×40 mL). The washed polymer was then obtained following evaporation of chloroform (110 mg). The washed polymer (75 mg) was then dissolved in chloroform (25 mL) and washed again with Na(detc) (0.3 g in 30 mL). The twice-washed polymer was then dried and collected (40.6 mg).

Purification 2: FS-TEG (150 mg) was dissolved in chloroform (50 mL) and washed with an aqueous solution of Na(detc) (602 mg in 60 mL) followed by water (5 ×40 mL). The washed polymer was then obtained following evaporation of chloroform (110 mg). The washed polymer (75 mg) was then dissolved in chloroform (25 mL) and washed again with Na(detc) (0.3 g in 30 mL). The twice-washed polymer was then dried and collected (70.7 mg).

For the addition of Pd back into washed **FS-TEG**, a 1 mL aliquot of tris(dibenzylideneacetone)dipalladium(0) (3.2 mg) dissolved in chloroform (100 mL) was added to the washed polymer dissolved in chloroform (30 mg in 60 mL) befrore evaporation of chloroform to obtain the polymer with added Pd (26.5 mg).

For the addition of Pd to **FS-Hex**, a 12 mL aliquot of tris(dibenzylideneacetone)dipalladium(0) (3.2 mg) dissolved in chloroform (100 mL) was added to the polymer dissolved in chloroform (39.2 mg in 60 mL) befrore evaporation of chloroform to obtain the polymer with added Pd (37.0 mg).

2.8.7. Varying the Molecular Weight of FS-Dodec (Chapter 2.6.3)

The polymerisation of **FS-Dodec** reported in **Chapter 2.8.2** was repeated with the addition of bromobenzene (Sigma Aldrich, 99%, 1.85 mmol). The different molecular weight fractions were obtained by collecting the solutions resulting from Soxhlet extractions of the crude polymer with acetone (**FS-Dodec-a**, 0.1199 g, 17%), ethyl acetate (**FS-Dodec-e**, 0.1250 g, 17%) and chloroform (**FS-Dodec-c**, 0.2325 g, 33%).

2.9. References

1 R. S. Sprick, B. Bonillo, R. Clowes, P. Guiglion, N. J. Brownbill, B. J. Slater, F. Blanc, M. A. Zwijnenburg, D. J. Adams and A. I. Cooper, *Angew. Chemie - Int. Ed.*, 2016, **55**, 1792–1796.

2 J. Mei and Z. Bao, *Chem. Mater.*, 2014, **26**, 604–615.

3 F. Dierschke, A. C. Grimsdale and K. Müllen, *Synthesis (Stuttg).*, 2003, **16**, 2470–2472.

4 A. B. Koren, M. D. Curtis, A. H. Francis and J. W. Kampf, *J. Am. Chem. Soc.*, 2003, **125**, 5040–5050.

5 K. B. Woody, R. Nambiar, G. L. Brizius and D. M. Collard, *Macromolecules*, 2009, **42**, 8102–8111.

6 R. S. Sprick, M. Hoyos, M. S. Wrackmeyer, A. V. Sheridan Parry, I. M. Grace, C. Lambert, O. Navarro and M. L. Turner, *J. Mater. Chem. C*, 2014, **2**, 6520–6528.

7 R. S. Sprick, J.-X. Jiang, B. Bonillo, S. Ren, T. Ratvijitvech, P. Guiglion, M. A. Zwijnenburg, D. J. Adams and A. I. Cooper, *J. Am. Chem. Soc.*, 2015, **137**, 3265–3270.

8 P. Blondin, J. Bouchard, S. Beaupré, M. Belletête, G. Durocher and M. Leclerc, *Macromolecules*, 2000, **33**, 5874–5879.

9 B. Meng, H. Song, X. Chen, Z. Xie, J. Liu and L. Wang, *Macromolecules*, 2015, **48**, 4357–4363.

10 L. Marin, H. Penxten, S. Van Mierloo, R. Carleer, L. Lutsen, D. Vanderzande and W. Maes, *J. Polym. Sci. Part A Polym. Chem.*, 2013, **51**, 4912–4922.

11 P. Verstappen, J. Kesters, L. D'Olieslaeger, J. Drijkoningen, I. Cardinaletti, T. Vangerven, B. J. Bruijnaers, R. E. M. Willems, J. D'Haen, J. V. Manca, L. Lutsen, D. J. M. Vanderzande and W. Maes, *Macromolecules*, 2015, **48**, 3873–3882.

12 J. Kosco, M. Sachs, R. Godin, M. Kirkus, L. Francas, M. Bidwell, M. Qureshi, D. Anjum, J. R. Durrant and I. McCulloch, *Adv. Energy Mater.*, 2018, **8**, 1802181.

13 J. Mackison, F. W., R. S. Stricoff, and L. J. Partridge, *Occupational Health Guidelines for Chemical Hazards.*, NIOSH/OSHA, 81-123. 1981.

14 V. S. Vyas, V. W. Lau and B. V Lotsch, *Chem. Mater.*, 2016, **28**, 5191–5204.

15 X. Zhang, J. Xiao, M. Hou, Y. Xiang and H. Chen, *Appl. Catal. B Environ.*, 2018, **224**, 871–876.

16 Z. Jiang, Z. Zhang, W. Shangguan, M. A. Isaacs, L. J. Durndell, C. M. A. Parlett and A. F. Lee, *Catal. Sci. Technol.*, 2016, **6**, 81–88.

17 J. Liu, Y. Zhang, L. Lu, G. Wu and W. Chen, *Chem. Commun.*, 2012, **48**, 8826–8828.

18 L. Li, Z. Cai, Q. Wu, W. Y. Lo, N. Zhang, L. X. Chen and L. Yu, *J. Am. Chem. Soc.*, 2016, **138**, 7681–7686.

19 C. B. Meier, R. S. Sprick, A. Monti, P. Guiglion, J.-S. M. Lee, M. A. Zwijnenburg and A. I. Cooper, *Polymer (Guildf).*, 2017, **126**, 283–290.

20 T. Sreethawong and S. Yoshikawa, *Int. J. Hydrogen Energy*, 2006, **31**, 786–796.

21 C. Huang, M. M. Sartin, M. Cozzuol, N. Siegel, S. Barlow, J. W. Perry and S. R. Marder, *J. Phys. Chem. A*, 2012, **116**, 4305–4317.

22 J. Rawson, P. J. Angiolillo and M. J. Therien, *Proc. Natl. Acad. Sci.*, 2015, **112**, 13779–13783.

23 M. Leclerc, *J. Polym. Sci. Part A Polym. Chem.*, 2001, **39**, 2867–2873.

24 B. U. Scherf and E. J. W. List, *Adv. Mater.*, 2002, **14**, 477–487.

25 L. H. Xie, C. R. Yin, W. Y. Lai, Q. L. Fan and W. Huang, *Prog. Polym. Sci.*, 2012, **37**, 1192–1264.

26 X. Guo, M. Baumgarten and K. Müllen, *Prog. Polym. Sci.*, 2013, **38**, 1832–1908.

27 R. Sebastian Sprick, Y. Bai, A. A. Y Guilbert, M. Zbiri, C. M. Aitchison, L. Wilbraham, Y. Yan, D. J. Woods, M. A. Zwijnenburg and A. I. Cooper, *Chem. Mater.*, 2018, **31**, 305–313.

28 B. Hohl, L. Bertschi, X. Zhang, A. D. Schlüter and J. Sakamoto, *Macromolecules*, 2012, **45**, 5418–5426.

29 J. Sakamoto, M. Rehahn and A. D. Schlüter, *Suzuki Polycondensation: A Powerful Tool for Polyarylene Synthesis*, John Wiley & Sons, 2010.

30 U. Scherf and D. Neher, *Advances in Polymer Science: Polyfluorenes*, Springer-Verlag Berlin Heidelberg, 2008.

31 W Brütting, *Physics of Organic Semiconductors*, John Wiley & Sons, 2006.

32 T. Nakamura, D. K. Sharma, S. Hirata and M. Vacha, *J. Phys. Chem. C*, 2018, **122**, 8137–8146.

33 J. Sauter, *Determining size of drops in fuel mixture of internal combustion engines*, VDI-Verlag, 1926.

34 R. Sebastian Sprick, Y. Bai, A. A. Y Guilbert, M. Zbiri, C. M. Aitchison, L. Wilbraham, Y. Yan, D. J. Woods, M. A. Zwijnenburg and A. I. Cooper, *Chem. Mater.*, 2018, **31**, 305–313.

35 M. Sachs, R. S. Sprick, D. Pearce, S. A. J. Hillman, A. Monti, A. A. Y. Guilbert, N. J. Brownbill, S. Dimitrov, X. Shi, F. Blanc, M. A. Zwijnenburg, J. Nelson, J. R. Durrant and A. I. Cooper, *Nat. Commun.*, 2018, **9**, 4968.

36 J. M. Behrendt, Y. Wang, H. Willcock, L. Wall, M. C. McCairn, R. K. O'Reilly and M. L. Turner, *Polym. Chem.*, 2013, **4**, 1333–1336.

37 J. P. Youngblood, L. Andruzzi, C. K. Ober, A. Hexemer, E. J. Kramer, J. a Callow, J. A. Finlay and M. E. Callow, *Biofouling*, 2003, **19**, 91–98.

38 S. Sax, N. Rugen-Penkalla, A. Neuhold, S. Schuh, E. Zojer, E. J. W. List and K. Müllen, *Adv. Mater.*, 2010, **22**, 2087–2091.

39 C. Kanimozhi, N. Yaacobi-gross, K. W. Chou, A. Amassian, T. D. Anthopoulos and S. Patil, *J. Am. Chem. Soc.*, 2012, **134**, 16532−16535.

40 M. Shao, Y. He, K. Hong, C. M. Rouleau, D. B. Geohegan and K. Xiao, *Polym. Chem.*, 2013, **4**, 5270–5274.

41 L. Zhou, X. Bao, Q. Liu, J. Yu, Y. Chen, R. Yang and M. Sun, *J. Appl. Polym. Sci.*, 2014, **131**, 40478.

42 L. Zhang, H. Zeng and Q. Liu, *J. Phys. Chem. C*, 2012, **116**, 17554–17562.

43 A. Giovannitti, I. P. Maria, D. Hanifi, M. J. Donahue, D. Bryant, K. J. Barth, B. E. Makdah, A. Savva, D. Moia, M. Zetek, P. R. F. Barnes, O. G. Reid, S. Inal, G. Rumbles, G. G. Malliaras, J. Nelson, J. Rivnay and I. McCulloch, *Chem. Mater.*, 2018, **30**, 2945–2953.

44 A. Armin, D. M. Stoltzfus, J. E. Donaghey, A. J. Clulow, R. C. R. Nagiri, P. L. Burn, I. R. Gentle and P. Meredith, *J. Mater. Chem. C*, 2017, **5**, 3736–3747.

45 L. Bian, E. Zhu, J. Tang, W. Tang and F. Zhang, *Prog. Polym. Sci.*, 2012, **37**, 1292–1331.

46 S. Kajimoto, N. Yoshii, J. Hobley, H. Fukumura and S. Okazaki, *Chem. Phys. Lett.*, 2007, **448**, 70–74.

47 A. Nistor, G. Stiubianu, C. Racles and M. Cazacu, *Rev. Mater. Plast.*, 2011, **48**, 33–37.

48 S. Xu, V. I. Klimov, B. Kraabel, H. Wang and D. W. McBranch, *Phys. Rev. B*, 2001, **64**, 193201.

49 B. Meng, H. Song, X. Chen, Z. Xie, J. Liu and L. Wang, *Macromolecules*, 2015, **48**, 4357–4363.

50 Z. Hu, Z. Wang, X. Zhang, H. Tang, X. Liu, F. Huang and Y. Cao, *iScience*, 2019, **13**, 33–42.

51 C. Yang, B. C. Ma, L. Zhang, S. Lin, S. Ghasimi, K. Landfester, K. A. I. Zhang and X. Wang, *Angew. Chemie - Int. Ed.*, 2016, **55**, 9202–9206.

52 Z. Wang, N. Mao, Y. Zhao, T. Yang, F. Wang and J.-X. Jiang, *Polym. Bull.*, 2019, **76**, 3195–3206.

53 R. S. Sprick, C. M. Aitchison, E. Berardo, L. Turcani, L. Wilbraham, B. M. Alston, K. E. Jelfs, M. A. Zwijnenburg and A. I. Cooper, *J. Mater. Chem. A*, 2018, **6**, 11994–12003.

54 W. Yang, Q. Hou, C. Liu, Y. Niu, J. Huang, R. Yang and Y. Cao, *J. Mater. Chem.*, 2003, **13**, 1351–1355.

55 J. Liu, S. Hu, W. Zhao, O. Zou, W. Luo, W. Yang, J. Peng and Y. Cao, *Macromol. Rapid Commun.*, 2010, **31**, 496–501.

56 S. M. King, R. Matheson, F. B. Dias and A. P. Monkman, *J. Phys. Chem. B*, 2008, **112**, 8010–8016.

57 F. B. Dias, S. King, A. P. Monkman, I. I. Perepichka and A. Maxim, *J. Phys. Chem. B*, 2008, **112**, 6557–6566.

58 P. Guiglion, C. Butchosa and M. A. Zwijnenburg, *J. Mater. Chem. A*, 2014, **2**, 11996.

59 C. Butchosa, P. Guiglion and M. A. Zwijnenburg, *J. Phys. Chem. C*, 2014, **118**, 24833–24842.

60 P. Guiglion, C. Butchosa and M. A. Zwijnenburg, *J. Phys. Chem. C*, 2016, **121**, 1498–1506.

61 P. Guiglion, C. Butchosa and M. A. Zwijnenburg, *Macromol. Chem. Phys.*, 2016, **217**, 344–353.

62 C. Gu, D. Zhu, M. Qiu, L. Han, S. Wen, Y. Li and R. Yang, *New J. Chem.*, 2016, **40**, 7787–7794.

63 B. C. Schroeder, R. S. Ashraf, S. Thomas, A. J. P. White, L. Biniek, C. B. Nielsen, W. Zhang, Z. Huang, P. S. Tuladhar, S. E. Watkins, T. D. Anthopoulos, J. R. Durrant and I. McCulloch, *Chem. Commun.*, 2012, **48**, 7699.

64 F. Wang, J. Luo, K. Yang, J. Chen, F. Huang and Y. Cao, *Macromolecules*, 2005, **38**, 2253–2260.

65 B. Goldfuss, P. Von Ragué Schleyer and F. Hampel, *Organometallics*, 1996, **15**, 1755–1757.

66 N. Allard, R. B. Aïch, D. Gendron, P. L. T. Boudreault, C. Tessier, S. Alem, S. C. Tse, Y. Tao and M. Leclerc, *Macromolecules*, 2010, **43**, 2328–2333.

67 R. F. Chen, Q. L. Fan, C. Zheng and W. Huang, *Org. Lett.*, 2006, **8**, 203–205.

68 P. L. T. Boudreault, A. Michaud and M. Leclerc, *Macromol. Rapid Commun.*, 2007, **28**, 2176–2179.

69 F. Caffy, N. Delbosc, P. Chávez, P. Lévêque, J. Faure-Vincent, J. P. Travers, D. Djurado, J. Pécaut, B. Grévin, N. Lemaitre, N. Leclerc and R. Demadrille, *Polym. Chem.*, 2016, **7**, 4160–4175.

70 F. C. Krebs, R. B. Nyberg and M. Jørgensen, *Chem. Mater.*, 2004, **16**, 1313–1318.

71 M. P. Nikiforov, B. Lai, W. Chen, S. Chen, R. D. Schaller, J. Strzalka, J. Maser and S. B. Darling, *Energy Environ. Sci.*, 2013, **6**, 1513–1520.

72 C. Bracher, H. Yi, N. W. Scarratt, R. Masters, A. J. Pearson, C. Rodenburg, A. Iraqi and D. G. Lidzey, *Org. Electron. physics, Mater. Appl.*, 2015, **27**, 266–273.

73 A. Iwase, H. Kato and A. Kudo, *Appl. Catal. B Environ.*, 2013, **136**–**137**, 89–93.

74 H. Yan, J. Yang, G. Ma, G. Wu, X. Zong, Z. Lei, J. Shi and C. Li, *J. Catal.*, 2009, **266**, 165–168.

75 J. Kosco and I. McCulloch, *ACS Energy Lett.*, 2018, **3**, 2846–2850.

76 K. T. Nielsen, K. Bechgaard and F. C. Krebs, *Macromolecules*, 2005, **38**, 658–659.

77 L. Dou, J. You, Z. Hong, Z. Xu, G. Li, R. A. Street and Y. Yang, *Adv. Mater.*, 2013, **25**, 6642–6671.

78 B. Fan, L. Ying, Z. Wang, B. He, X. F. Jiang, F. Huang and Y. Cao, *Energy Environ. Sci.*, 2017, **10**, 1243–1251.

79 M. Jayakannan, J. L. J. Van Dongen and R. A. J. Janssen, *Macromolecules*, 2001, **34**, 5386–5393.

80 S. Nakamura, T. Fouquet and H. Sato, *J. Am. Soc. Mass Spectrom.*, 2019, **30**, 355–367.

81 K. Schwinghammer, S. Hug, M. B. Mesch, J. Senker and B. V Lotsch, *Energy Environ. Sci.*, 2015, **8**, 3345–3353.

82 S. Hayashi, S. I. Yamamoto and T. Koizumi, *Sci. Rep.*, 2017, **7**, 1078.

83 G. L. Gibson, D. Gao, A. A. Jahnke, J. Sun, A. J. Tilley and D. S. Seferos, *J. Mater. Chem. A*, 2014, **2**, 14468–14480.

84 T. Y. Chu, J. Lu, S. Beaupré, Y. Zhang, J. R. Pouliot, J. Zhou, A. Najari, M. Leclerc and Y. Tao, *Adv. Funct. Mater.*, 2012, **22**, 2345–2351.

85 W. C. Tsoi, A. Charas, A. J. Cadby, G. Khalil, A. M. Adawi, A. Iraqi, B. Hunt, J. Morgado and D. G. Lidzey, *Adv. Funct. Mater.*, 2008, **18**, 600–606.

86 R.-F. Chen, Q.-L. Fan, C. Zheng and W. Huang, *Org. Lett.*, 2006, **8**, 203–205.

87 S. T. Hoffmann, J.-M. Koenen, U. Scherf, I. Bauer, P. Strohriegl, H. Bässler and A. Köhler, *J. Phys. Chem. B*, 2011, **115**, 8417–8423.

88 M. Sachs, E. Pastor, A. Kafizas and J. R. Durrant, *J. Phys. Chem. Lett.*, 2016, **7**, 3742-3746.

89 C. Lee, C. Hill and N. Carolina, *Phys. Rev. B*, , DOI:10.1103/PhysRevB.37.785.

90 A. D. Becke, *J. Chem. Phys.*, 1993, **98**, 1372–1377.

91 P. J. Stephens, F. J. Devlin, C. F. Chabalowski and M. J. Frisch, *J. Phys. Chem.*, 1994, **98**, 11623–11627.

92 A. Schäfer, H. Horn and R. Ahlrichs, *J. Chem. Phys.*, 1992, **97**, 2571–2577.

93 A. Klamt and G. Schüürmann, *J. Chem. Soc., Perkin Trans. 2*, 1993, 799–805.

94 S. Hirata and M. Head-Gordon, *Chem. Phys. Lett.*, 1999, **314**, 291–299.

95 R. Ahlrichs, M. Bär, M. Häser, H. Horn and C. Kölmel, *Chem. Phys. Lett.*, 1989, **162**, 165–169.

96 F. Furche, R. Ahlrichs, C. Hättig, W. Klopper, M. Sierka and F. Weigend, *Wiley Interdiscip. Rev. Comput. Mol. Sci.*, 2014, **4**, 91–100.

Chapter 3

Processing Polymer Photocatalysts

3.1 Contributions to this Chapter

The mesoporous SnO_2 substrate was prepared by Charlotte Smith. AFM and profilometry of films of **FS-TEG** were performed by Sam Hillman. (TD-)FDFT calculations of the potentials of **LS-1** were performed by Dr Linjiang Chen. The scaled-up photoreactor was devised and built with the help of Rob Clowes. SEM images were obtained by Catherine Aitchison. All other work was performed by the thesis author.

3.2 Background

The present chapter will focus on how solution-processable photocatalysts can be processed in order to maximise their performance. The scarcity of literature devoted to these processing considerations is notable but this is perhaps unsurprising when the poor processability of most photocatalysts is considered. Solubility enables polymers to be processed into a variety of forms as demonstrated by their application across a diverse range of fields.[1]

In **Chapter 2**, photocatalytic reactions were performed on powders in suspension, following the convention of the field. Powdered photocatalysts are typically kept in suspension by stirring to prevent sedimentation and resultant loss of photocatalytic activity.[2] Consistency of the photocatalyst form could instead be achieving by casting the photocatalyst on a support substrate instead of stirring.[3] Alternatively, solubility also enables facile preparation of nanoparticles that disperse without the need for stirring and are expected to enhance performance.

3.3 Nanoparticles

3.3.1 Background

Nanoparticles are particles of matter that measure less than one micrometre in at least two dimensions. Their small size and biocompatibility means they are commonly used in biomedical applications including biosensing, bioimaging and drug delivery.[4] In the context of the present work, the formation of nanoparticles could increase hydrogen evolution rates. The particles used to perform photocatalytic experiments in **Chapter 2** are micrometre-sized, even after sonication of the reaction mixture (**Figure 2.21**). Conjugated polymers typically have exciton diffusion lengths in the range of a few nm.[5] It follows that there is a certain amount of 'wasted' material in the centre of the as-formed micron-sized particles and that the preparation of nanoparticles may significantly boost performance.

Nanoparticles have been commonly used for photocatalytic applications, particularly in the case of inorganic materials, which have been fabricated into a wide variety of complex nano-sized composites.[6–8] These nanostructured inorganic photocatalysts have been used to achieve some of the highest STH efficiencies reported in the field to date. Polymer nanoparticles are relatively less well studied for photocatalytic applications. Recently, the use of emulsion polymerisation allowed the preparation of nanoparticles of polymers that are usually insoluble with high performance and good stability.[9]

Alternatively, polymers that are soluble in organic solvents can form nanoparticles using a surfactant-free precipitation method. In this case, thorough characterisation is possible prior to application. Recently, hydrogen-evolving polymer nanoparticles have been reported for the first time.[10–12] These 'polymer dots' (PDots) exhibit high HERs normalised to the mass of polymer but low overall hydrogen production levels and rapid loss of performance. The polymers used to prepare these PDots possess large hydrophobic alkyl chains which are likely to limit activity, as discussed in **Chapter 2.2**. In fact, inactive TEG-substituted polystyrene was used as a surfactant in these studies to increase the dispersibility of PDots. Photocatalytically-active TEG-substituted polymers could instead be used to prepare more efficient polymer nanoparticles. The presence of TEG side-chains has been shown to enable the formation of smaller nanoparticles than alkylated analogues.[13] Nanoparticles will therefore be prepared using the most active solution-processable polymer reported in **Chapter 2**, **FS-TEG**.

3.3.2 Nanoparticle Preparation and Characterisation

Nanoparticles of **FS-TEG** (**FS-TEG** NPs) were prepared by precipitation from THF solutions into water. THF was removed by evaporation and the resultant dispersions filtered to remove large impurities. Dynamic light scattering (DLS) measurements showed the Z-average particle size of the nanoparticles to be 36.1 nm with a polydispersity index (PDI) of 0.337. A similar particle size was observed after three days (Z-average = 30.4 nm, PDI = 0.268) confirming good stability of the nanoparticles in water.

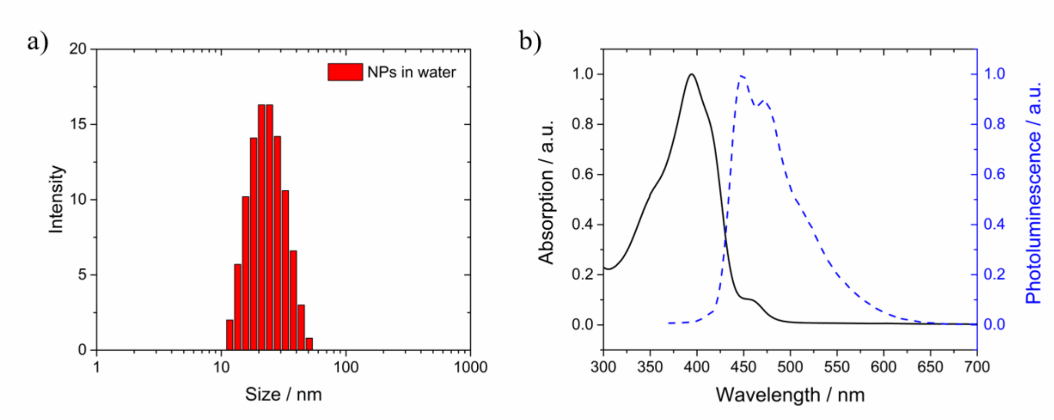

Figure 3.1. a) Particle size distribution of **FS-TEG** nanoparticles obtained from DLS **b)** UV-vis absorption and photoluminescence spectra of **FS-TEG** nanoparticles (λ_{exc} = 360 nm)

The absorption spectrum of **FS-TEG** NPs is similar to **FS-TEG** in solution (**Figure 3.1**) besides the further presence of a shoulder at λ = 470 nm. This shoulder is indicative of the partial formation of a β-phase; a more ordered linear arrangement of polymer chains that is thermodynamically favoured in poor solvents.[14] TEG side-chains have been shown to reduce the formation of a β-phase in comparison to alkylated polymers as a result of improving compatibility with water.[13] The Stokes shift of the PL spectrum underlines the fact that the polymer is mainly in the disordered, glassy phase.[a] However, the fact that **FS-TEG** even partially forms this

---

[a] Almost no Stokes shift is evident for polymers that are predominantly in the β-phase.[90]

more ordered β-phase may be beneficial for hydrogen evolution as the formation of planarised ladder-type structures has been shown to enhance photocatalytic performance.[15]

3.3.3 Photocatalysis Experiments

Photocatalysis experiments were initially performed using TEA as a sacrificial electron donor. A solution of 5 vol. % TEA in water was used to ensure miscibility of the TEA with water. Initial HERs of 11.1 ± 0.2 and 1.2 ± 0.1 mmol g^{-1} h^{-1} were observed under broadband and visible irradiation respectively (**Figure 3.2**). The HER under visible light is actually lower than the as-formed material (2.9 ± 0.1 µmol g^{-1} h^{-1}). This may be as a result of the blue-shifted absorption onset or reduced light absorption due to the particle size being smaller than the irradiation wavelengths. It is also worth noting, however, that this HER was calculated based on the amount of polymer initially used to prepare the nanoparticles and does not account for material lost during filtration. These figures are therefore likely to be an underestimation. However, a significant drop-off in performance is also observed after around only three hours that does not take place in the larger as-formed particles.

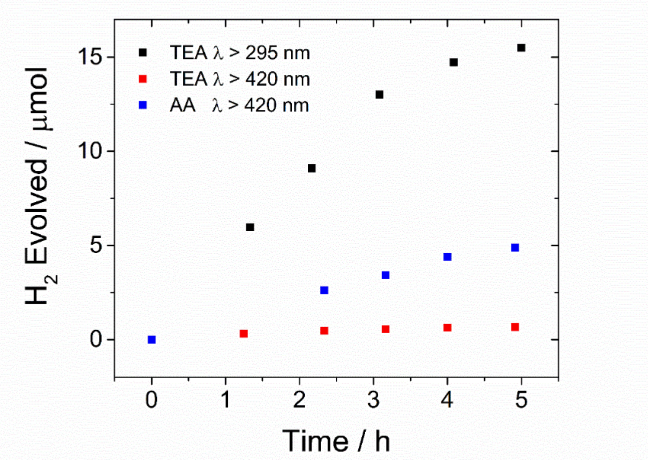

Figure 3.2. Hydrogen evolution of **FS-TEG** NPs over 5 hours using the specified band-pass filters and sacrificial reagents (TEA = 5 vol. % TEA in water, AA = 0.2 M L-ascorbic acid), 300W Xe light source.

The optical properties of the nanoparticles were found to be significantly altered after the photocatalytic runs. The addition of TEA prior to irradiation results in no discernible change in the absorption spectra but increased PL amplitude, which occurs possibly as a result of aggregation.[16] The absorption on-set is significantly blue-shifted particularly after irradiation by a broadband light source (**Figure 3.3a**). The photoluminescence also undergoes a hyperchromic shift and the post-photocatalysis material appears to be more emissive (**Figure 3.3b**).

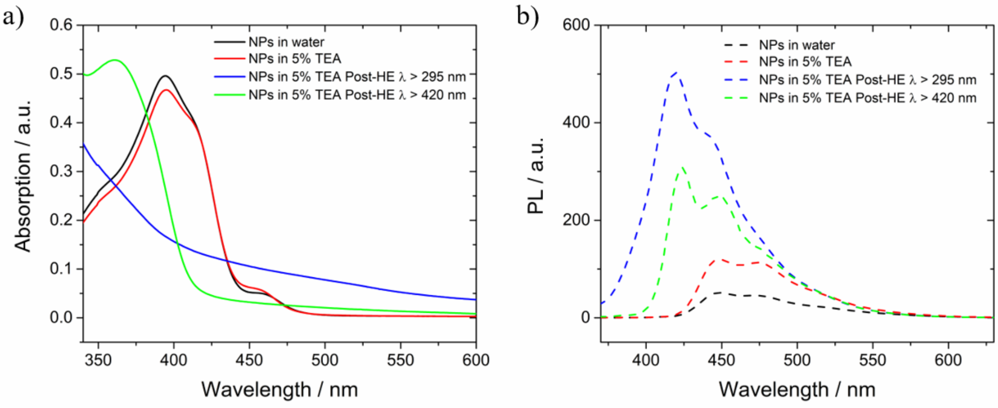

Figure 3.3. a) UV-vis and **b)** PL spectra of **FS-TEG** NPs in water, 5 vol. % TEA, after five hours of irradiation in 5 vol. % TEA by the two light sources specified (λ_{exc} = 360 nm).

The nature of the degradation taking place is somewhat unclear. Oxidation at the 9-position of fluorenes to form fluorenone defects is known.[17–19] However, the formation of fluorenone defects would cause an appearance of a green emissive band. Degradation may instead be taking place as a result of chain scission, which has been shown to result in similar changes in absorption spectra to those observed here.[20] However, further investigation are required to determine the exact nature and mechanism of degradation that is taking place in this case.

Using L-ascorbic acid (0.2 M) instead of TEA resulted in a notably higher HER under visible light irradiation, over twice the rate of the as-formed particles (6.9 ± 0.1 mmol g^{-1} h^{-1}). However, while the initial rate of hydrogen production is high, a drop-off in performance is still observed after approximately three hours (**Figure 3.2**). The UV-vis spectrum is less blue-shifted after five hours of visible light irradiation than in 5 vol. % TEA, although the strength of absorption appears to be reduced (**Figure 3.4a**). An increase in the PL amplitude is, however, again observed following photocatalysis (**Figure 3.4b**).

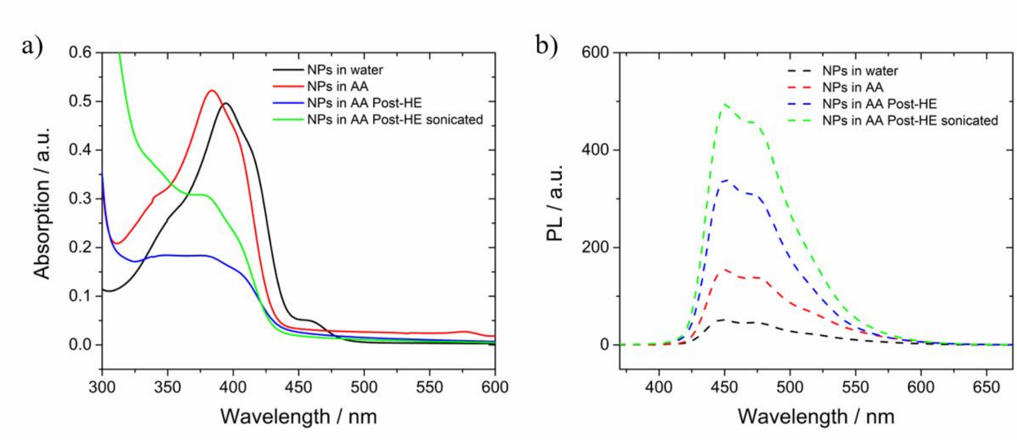

Figure 3.4. a) UV-vis and **b)** PL spectra of **FS-TEG** NPs in water, L-ascorbic acid (0.2 M) (AA), after five hours of irradiation in AA under visible light irradiation and after sonication of the post-photocatalysis suspension (λ_{exc} = 360 nm).

The addition of L-ascorbic acid and subsequent photocatalysis results in aggregation of particles and a significant increase in polydispersity (**Table 3.1**). Sonication of the particles was found to redisperse the nanoparticles to give a similar particle size to before photocatalysis (Z-average = 231 *vs.* 223 nm). An increase in absorption was also observed upon sonication (**Figure 3.4a**). It is therefore possible that the reduction in performance may be due to aggregation of the nanoparticles.

Table 3.1. Z-average particle sizes and polydispersity index (PDI) of **FS-TEG** NPs in water, L-ascorbic acid (0.2 M) (+ AA), after five hours of irradiation in AA under visible light irradiation (Post-HE) and after sonication of the post-photocatalysis suspension (Post-HE + sonication).

NP conditions	Z-Average / nm	PDI
Water	36.1	0.337
+ AA	223	0.372
Post-HE	2040	0.974
Post-HE + sonication	231	0.245

3.3.4 Summary

Nanoparticles were prepared using a simple precipitation method. A significant improvement in activity was observed when using L-ascorbic acid as a sacrificial electron donor relative to the as-formed particles reported previously, without the need for mechanical stirring. Loss of performance may be due to aggregation although it appears that the reduction in particle size may also make these polymers more susceptible to degradation. Solubility also enables the preparation of films cast on supports, which may have advantageous characteristics and potentially greater stability.

3.4 Photocatalysis on Supports

3.4.1 Background

Solution processability also allows polymers to be cast on supporting substrates, which is expected to offer several key advantages in comparison to particulate systems. Energy is of course consumed in the stirring of powders in suspension but also in their collection by centrifugation or filtration.[21] Crucially, in immobilised set-ups these costs and difficulties associated with handling of polymer particles are avoided. Cast polymer films may also be more stable than the nanoparticles discussed in **Chapter 3.3**. The low areal density of solar energy means the scalability of photocatalytic materials is an important consideration, but it is one that is often overlooked.[22] The formation of thin films should enable coverage of large areas with relatively small amounts of photocatalysts. Photocatalytic films can also be tilted for optimum light absorption.[23]

Few examples exist of photochemical hydrogen evolution from immobilised photocatalysts.[b,24,25] Most impressively, photocatalytic panels of Al-doped $SrTiO_3$ capable of overall water splitting have been prepared[26] and recently scaled up to a 1 m^2 scale.[21] Although these studies demonstrate how insoluble materials can be cast onto substrates from dispersions,[24,25,27,28] or prepared using sol-gel processes,[29] soluble linear polymers are expected to form films of greater mechanical strength. The reproducible formation of highly uniform films that can be achieved when casting from solutions is also likely to be advantageous. This precision and homogeneity is evident in the intricate layered OPV devices that have been constructed in recent years.[30] Similarly specialised devices for photocatalysis are envisaged in the long-term but hydrogen evolution from polymer films that are stable in aqueous conditions must first be achieved.

---

[b] Polymers have been cast on electrodes in photoelectrochemical cells[91] although the requirements of materials for this application are of course different.

3.4.2 Mesoporous Substrates

In initial experiments, a film of **P8-s** was prepared by drop-casting from chloroform solution onto a glass slide. However, immersion of films cast on this support in the water/methanol/TEA photocatalysis mixture resulted in complete delamination of the polymer within minutes. Modification of the substrate to enable better adherence of the polymer is clearly required to achieve film stability in these conditions.

Casting materials on mesoporous supports has been shown to reduce delamination.[31,32] The use of a mesoporous substrate may therefore promote adherence of the polymer film to the glass slide in this case. **P8-s** (0.34 mg) was drop-cast from chloroform onto mesoporous SnO_2 on a fluorine-doped tin oxide (FTO) support. This resulted in a **P8-s** layer of 600 ± 100 nm on top of the SnO_2 support, according to profilometry, with additional **P8-s** expected to be penetrating the SnO_2 (**Figure 3.5a**). Irradiation of the film in a water/methanol/TEA mixture with broadband light resulted in the evolution of 0.66 µmol of hydrogen after 5 hours (450 µmol g^{-1} h^{-1}, **Figure 3.5b**). The slide was then removed and the degassed solution was irradiated, again using a broadband filter, to determine if delamination of the polymer had taken place during the initial experiment. The rate of hydrogen evolution was reduced tenfold, suggesting that the vast majority of hydrogen was evolved from the polymer film on the slide and only a small amount of delamination had taken place. No hydrogen was evolved from the SnO_2 film with no **P8-s** under the same irradiation conditions.

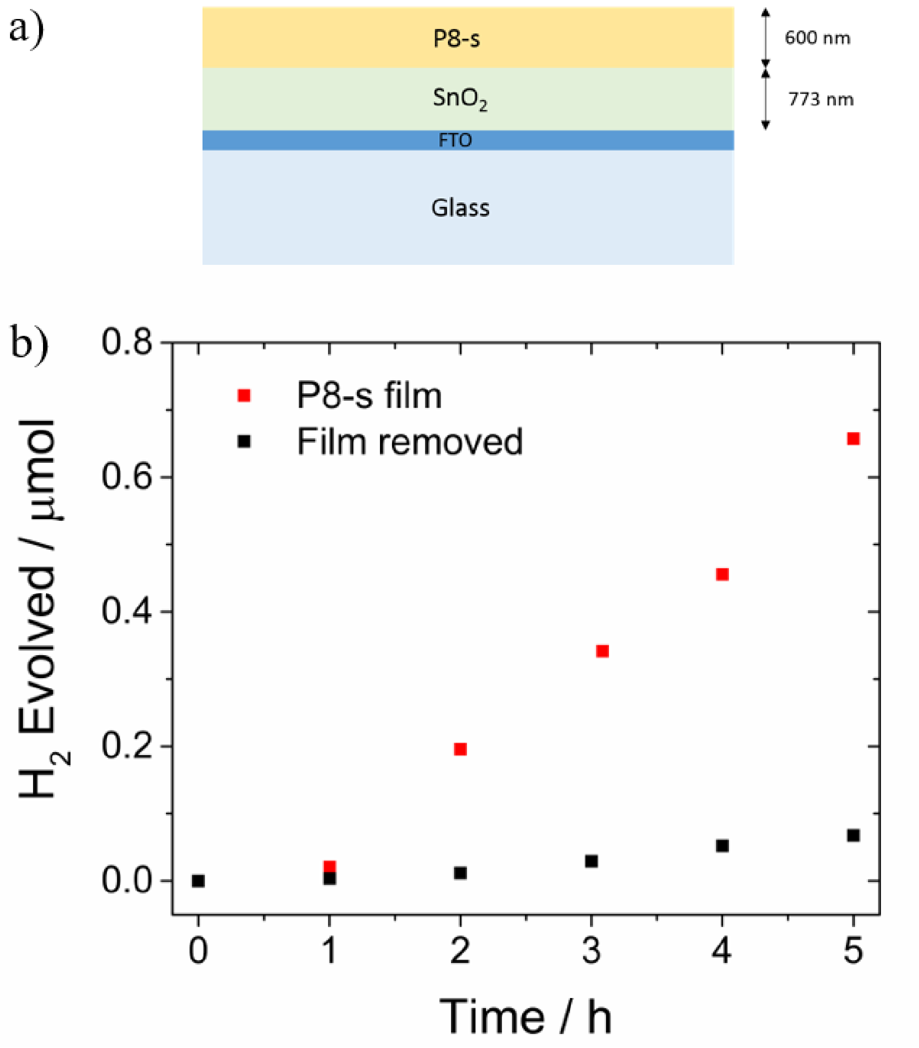

Figure 3.5. a) Illustration of the **P8-s** film cast on a SnO_2/FTO support used for hydrogen evolution experiments with thicknesses obtained from profilometry **b)** Hydrogen evolution of the **P8-s** film cast on a SnO_2-coated slide submerged in water/methanol/TEA mixture under broadband irradiation (red symbols) and residual hydrogen evolution of the solution following removal of the glass slide and degassing (black symbols), using a 300 W Xe light source.

The use of a metal oxide support that requires a complex preparation procedure is not desirable. More importantly, some delamination still occurred from the substrate in the medium used here. Further efforts to develop simpler substrates while eradicating delamination are therefore required.

3.4.3 Roughened Glass Substrates

Surface roughening has been shown to promote adherence of conjugated polymers to silver electrodes.[33] Using a roughened support may have the added benefit of increasing the macroscopic surface area of the cast polymer, thereby enhancing the polymer-water interface in a given irradiated area. **FS-TEG** was used in this investigation rather than **P8-s** to enhance photocatalytic performance. A scavenger solution of 5 vol. % TEA in water was used instead of water/methanol/TEA in the hope that this less organic environment would further improve adherence of the polymer to the glass substrate.

Glass slides were roughened manually using sandpaper and cleaned with water, methanol and acetone before drying. The polymer was then drop-cast onto the roughened slide from chloroform, allowed to dry slowly before being heated at 80 °C to evaporate any remaining chloroform. The polymer-coated roughened slide was then submerged in 5 vol. % TEA and irradiated with visible light. A steady release of hydrogen bubbles from the surface of the photocatalyst was visible to the naked eye (**Figure 3.6a**). Consistent hydrogen evolution was observed, with 44.8 µmol of hydrogen produced after five hours (**Figure 3.6b**). This corresponds to an exceptionally high HER of 64 mmol g^{-1} h^{-1} when normalised to the mass of the cast polymer (0.14 mg). Moreover, in this case negligible hydrogen (< 0.1 µmol) was evolved from the solution after removal of the polymer-coated slide, implying good adhesion of the polymer to the roughened substrate.

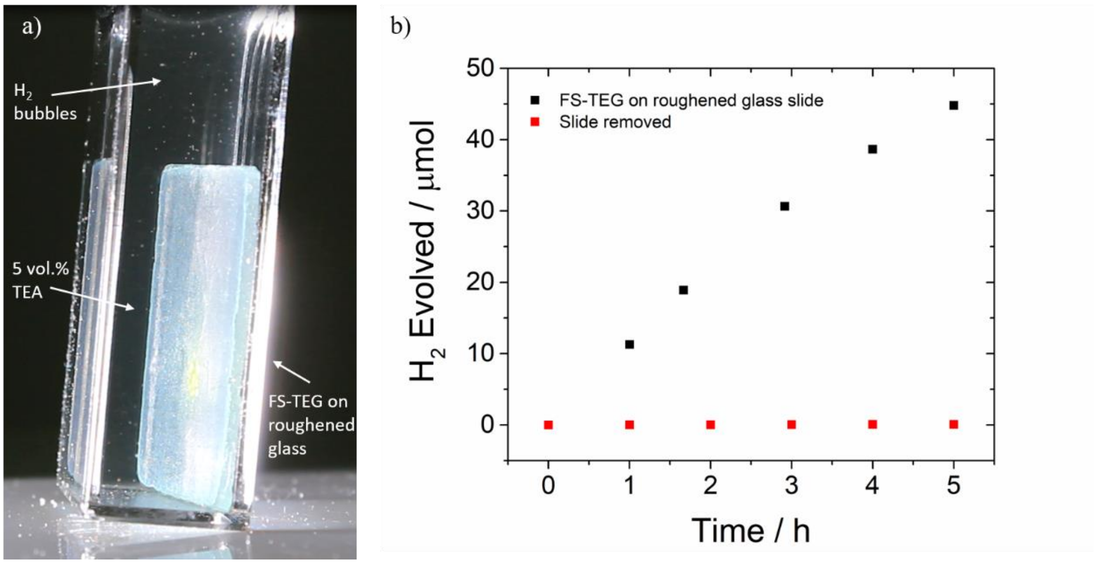

Figure 3.6. a) Image showing evolution of hydrogen bubbles from **FS-TEG** cast on roughened glass substrate submerged in 5 vol. % TEA. **b)** Hydrogen evolution of a **FS-TEG** film cast on roughened glass submerged in 5 vol. % TEA under visible light irradiation (black symbols) and residual hydrogen evolution of the solution containing delaminated polymer following removal of the glass slide and degassing (red symbols), using a 300 W Xe light source.

While roughened glass substrates appear to enable high activities and strong polymer adhesion, they also possess some inherent limitations. Although this surface roughness may enable good polymer adhesion, it may hamper reproducibility. Controlling the thicknesses of thin polymer films cast on roughened substrates is likely to be challenging. Moreover, the opacity of these slides limits the possibility of fabricating layered or stacked devices to further increase performance. Alternative substrates that enable greater control over the film formation process should therefore be considered.

3.4.4 OTS-Functionalised Glass Substrates

Instead of using the mechanical roughening approach employed in **Chapter 3.4.3**, adhesion can also be achieved chemically. Functionalising planar glass surfaces with a hydrophobic coating such as *n*-octadecyltrichlorosilane (OTS) has been used to achieve polymer adhesion in the fabrication of devices such as organic field-effect transistors (OFETs).[34-36] OTS molecules can be viewed as a polar trichlorosilane 'head' and a long, hydrophobic octadecyl 'tail' (**Figure 3.7a**). When spin-coated onto glass from a non-polar solvent, OTS forms a self-assembled monolayer (SAM) with the heads chemically bonded to the surface of the glass slide and the hydrophobic tails pointing away from the glass (**Figure 3.7b**).[37] This creates a robust hydrophobic surface that polymers can bind to *via* van der Waals interactions. It has been shown that depositing polymers on OTS-functionalised glass may actually enhance charge carrier mobilities in comparison to SiO_2 substrates.[35,38]

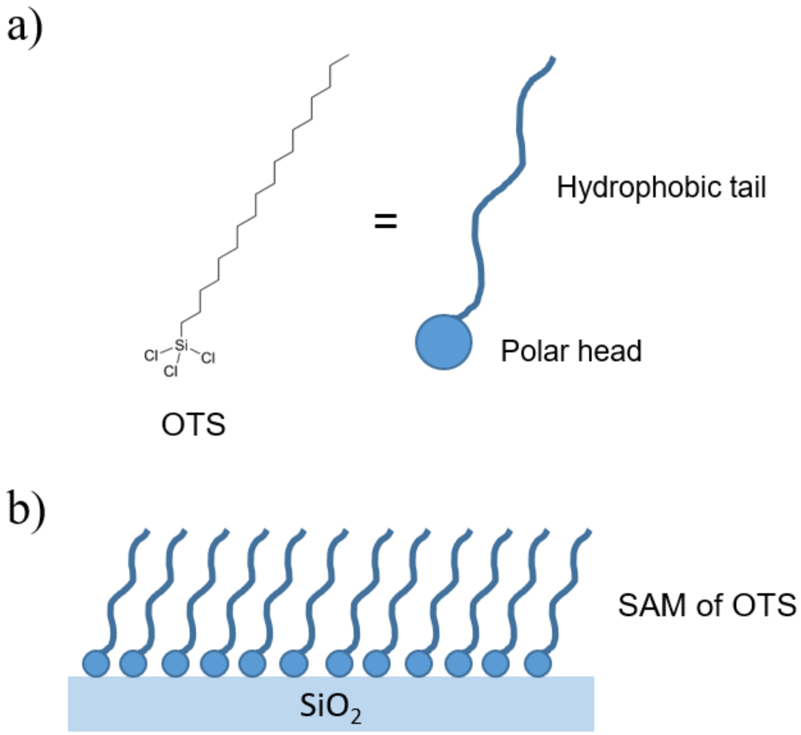

Figure 3.7. **a)** Chemical structure of OTS molecules and an illustrative representation of their 'head and tail' nature. **b)** Schematic representation of the self-assembled monolayer formed when OTS is spin-coated on a glass slide.

Glass slides were functionalised with OTS by spin-coating from 1,1,2-trichloroethylene (TCE) using a literature method.[39] The planarity of the OTS-functionalised substarte lends itself to polymer deposition by spin-coating; a reliable method of polymer deposition commonly used in the fabrication of photovoltaic devices.[40] **FS-TEG** was spin-coated onto the OTS-functionalised slide from chloroform, which appeared to give a homogeneous film (**Figure 3.8a**). The polymer-coated OTS-functionalised slide was then annealed at 80 °C for two hours before photocatalysis experiments were conducted in 5 vol. % TEA solution under visible light irradiation (**Figure 3.8b**).

Bubbles of hydrogen were again visible although, unlike with the roughened substrate, they were not released in a constant stream. The bubbles appear larger than those released from the roughened slide and adhere more strongly to the surface (**Figure 3.8c**). 1.7 μmol of hydrogen was evolved from the polymer after five hours of irradiation (**Figure 3.8d**). No hydrogen was evolved after five hours of irradiation when the slide was removed, confirming excellent adhesion of the polymer to the OTS-functionalised substrate in aqueous conditions. A direct comparison of equivalent films prepared on roughened and OTS-functionalised substrates will be made in **Chapter 3.4.5**.

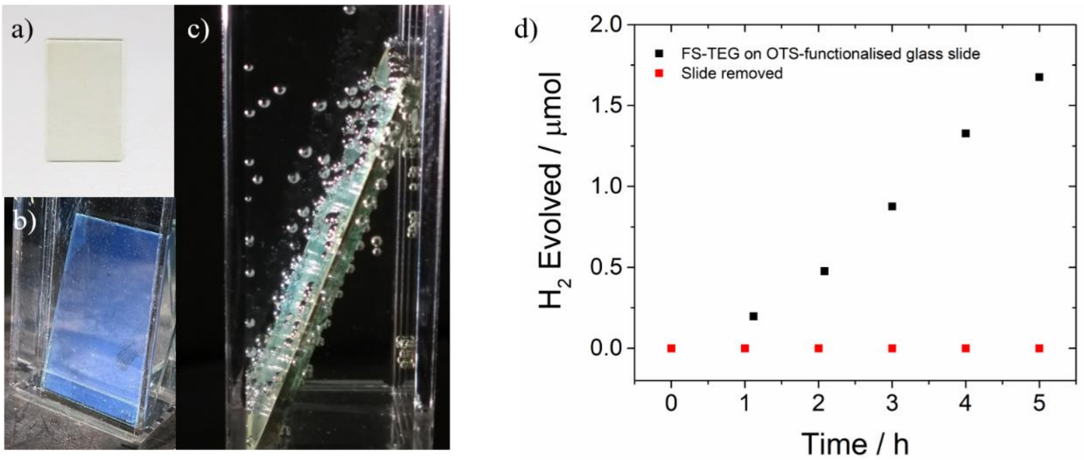

Figure 3.8. a) Image of **FS-TEG** cast on OTS-functionalised glass and **b)** submerged in 5 vol. % TEA **c)** Image showing evolution of hydrogen bubbles from the polymer-coated glass slide. **d)** Hydrogen evolution of an **FS-TEG** film on OTS-functionalised glass submerged in 5 vol. % TEA under visible light irradiation (black symbols) and residual hydrogen evolution of the solution containing delaminated polymer following removal of the glass slide and degassing with nitrogen (red symbols), using a 300 W Xe light source.

3.4.5 Comparison of OTS-Functionalised and Roughened Glass Substrates

The experiments conducted thus far are not comparable due to the difference in deposition methods. In this comparative study, spin-coating was used to deposit the polymer on the two substrates as it gives more homogeneous films than drop-casting.[41] The mass of films deposited by spin-coating are too low to determine accurately so rates were normalised to the illuminated area. This is arguably a more useful metric of measuring photocatalytic performance in the sense that it encourages photocatalysts to be processed into forms that will harness sunlight more efficiently and will therefore be used in this chapter.

FS-TEG was deposited on the two substrates by spin-coating from 10 mg mL^{-1} solutions of the polymer in chloroform. HERs of films cast on OTS-functionalised slides were found to be lower than a film deposited on an unfunctionalised roughened slide (2.0 vs. 2.9 mmol m^{-2} h^{-1}, **Figure 3.9**). This could be due to a higher macroscopic surface area of the polymer when cast on the roughened slide. The rate of nucleation of hydrogen bubbles being affected by the planarity and hydrophobicity of the surface of these OTS-functionalised slides is another possible explanation. Furthermore, although equivalent amounts of polymers were used to prepare the solutions, the actual amounts of polymer on slides may not be equivalent as the spin-coating procedure is likely to be impacted by the nature of the surface.

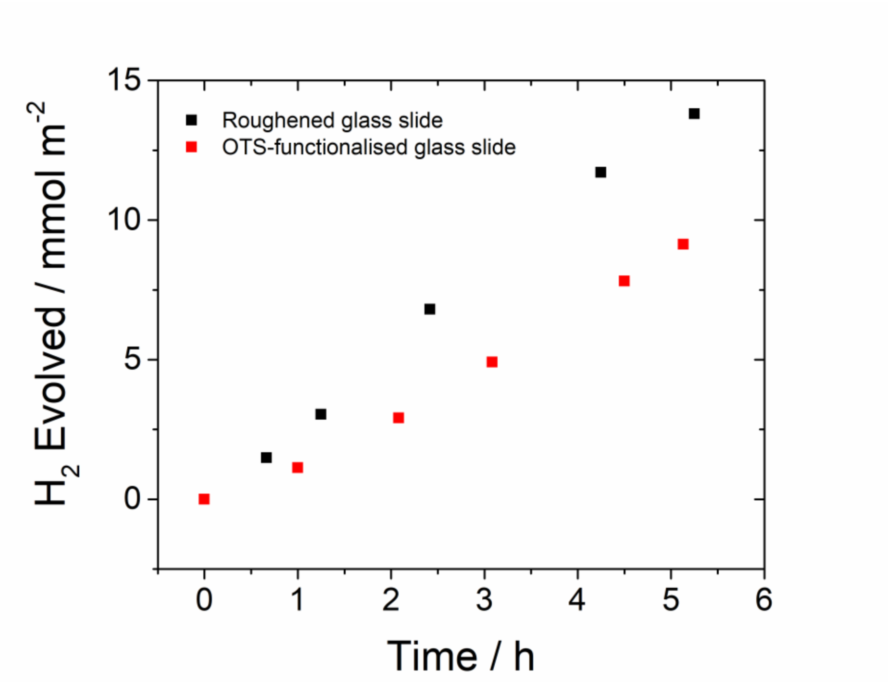

Figure 3.9. Hydrogen evolution of films of **FS-TEG** spin-coated from 10 mg mL^{-1} solutions of chloroform onto a roughened glass slide and an OTS-functionalised slide. Films placed in 5 vol. % TEA mixture under visible light irradiation using a 300 W Xe light source.

Nevertheless, the homogeneity of films cast on OTS-treated glass enables reproducible film formation that could facilitate more detailed studies into the photocatalytic performance of these polymers. For example, the effect of altering important parameters, such as film thickness, on photocatalytic rates could be investigated.

3.4.6 Film Thickness

3.4.6.1 Background

Although its potential importance has been recognised,[42] little consideration has been given to optimisation of film thickness in the few studies on hydrogen evolution from immobilised photocatalytic films and panels.[21,26] The activity of TiO_2 thin films for the photocatalytic degradation of pollutants has however been shown to depend strongly on their thickness.[27,43] Although the precise relationship between film thickness and performance is still the subject of some debate,[44] a general consensus appears to be building that performance increases linearly with thickness due to increased light absorption before plateauing.[44–47] This plateauing may result from the inability of charge carriers to migrate to the surfaces of thicker films. Material in the film beyond this depth may therefore be superfluous, as is expected to be the case in the centre of large particles. Optimum thicknesses appear to depend strongly on the microstructures of the films but are typically in the range of hundreds of nanometres.[44]

The different behaviour of charge carriers in polymer matrices means it is unclear how the thickness of polymer films will affect their photocatalytic performance. Excitons are more strongly bound than in inorganic materials due to the lower relative permittivity of polymers.[48,49] Exciton diffusion lengths generally do not exceed 20 nm in conjugated polymers[50] and are typically below 10 nm for fluorene-based polymers similar to those studied here.[51,52] Therefore, although light absorption of polymer films should increase with increasing film thickness up to the optical pass length (100-200 nm),[5] optimum film thicknesses may be limited to a few nanometres by exciton diffusion lengths. However, the inhomogeneous nature of polymer films means exciton dynamics are difficult to predict and are likely to be affected by a number of factors including the relative degrees of interchain and intrachain exciton transfer.[5]

3.4.6.2 Characterisation of Films with Varied Thicknesses

Film thicknesses were varied by changing the concentration of the solution from which the polymer was spin-coated (1, 3, 5, 10, 15 and 20 mg mL^{-1}, **Figure 3.10a**). Duplicate films were prepared in order to ensure reproducibility. The opacity of films visibly increases with increasing concentration of spin-coated solutions (**Figure 3.10b**).

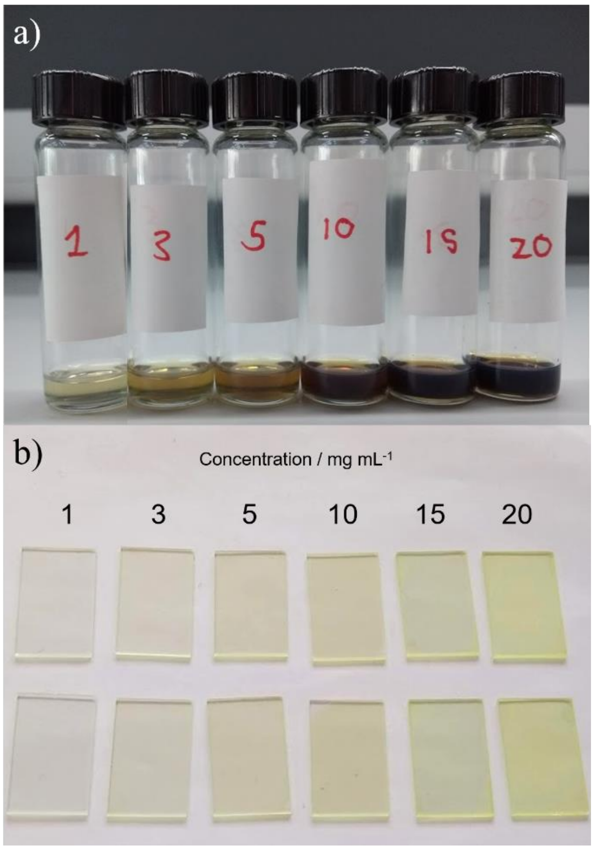

Figure 3.10. **a)** Image of 1, 3, 5, 10, 15 and 20 mg mL^{-1} solutions of **FS-TEG** dissolved in chloroform and **b)** image of duplicated films spin-coated from these solutions.

UV-vis absorption spectra demonstrate the reproducibility of preparing films using this spin-coating method as the absorption maxima of duplicates were found to be within 5% of one another (**Figure 3.11a**). A notable hyperchromic shift in absorption maxima was observed for films cast from solutions of higher concentration (Abs. = 0.09 for a film cast from 1 mg mL^{-1} solution, Abs. = 1.71 for a film cast from 20 mg mL^{-1}). Normalised absorption spectra show a widening and slight blue shift of the absorption profile with increasing film thickness, from λ_{max} = 402 nm for films cast from 1 mg mL^{-1} to λ_{max} = 395 nm for films cast from 20 mg mL^{-1} (**Figure 3.11b**).

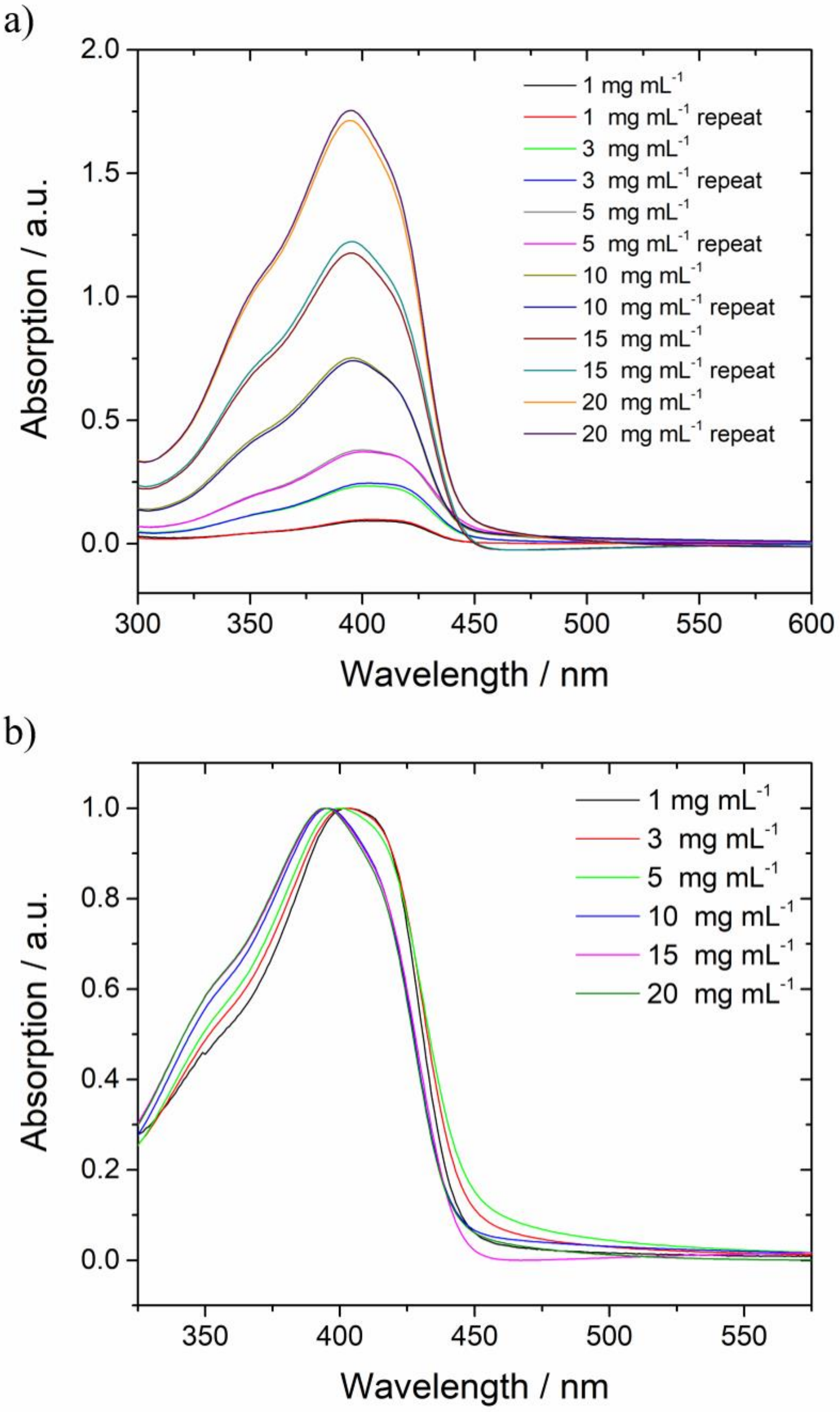

Figure 3.11. a) UV-vis absorption spectra of duplicate films spin-coated from 1, 3, 5, 10, 15 and 20 mg mL^{-1} solutions of **FS-TEG** in chloroform **b)** Normalised absorption spectra of these films.

Thicknesses of thin films were measured using atomic force microscopy (AFM) while profilometry was performed on thicker films. Good agreement between the two methods of thickness measurement was observed in a film of intermediate thickness; a film cast from 10 mg mL^{-1} solution was found to be 81 ± 8 nm thick from AFM and 79 ± 3 nm from profilometry. Film thicknesses ranged from 11.3 ± 0.2 nm to 161 ± 3 nm and appear to increase linearly with concentration of deposited polymer solution as anticipated (**Figure 3.12a**). Films were found to be smooth; the thickest films 161 ± 3 nm has a roughness of just 1.8 ± 0.6 nm according to profilometry. A linear correlation was also observed between film thickness and absorption strength (**Figure 3.12b**), in good agreement with the Beer-Lambert law.

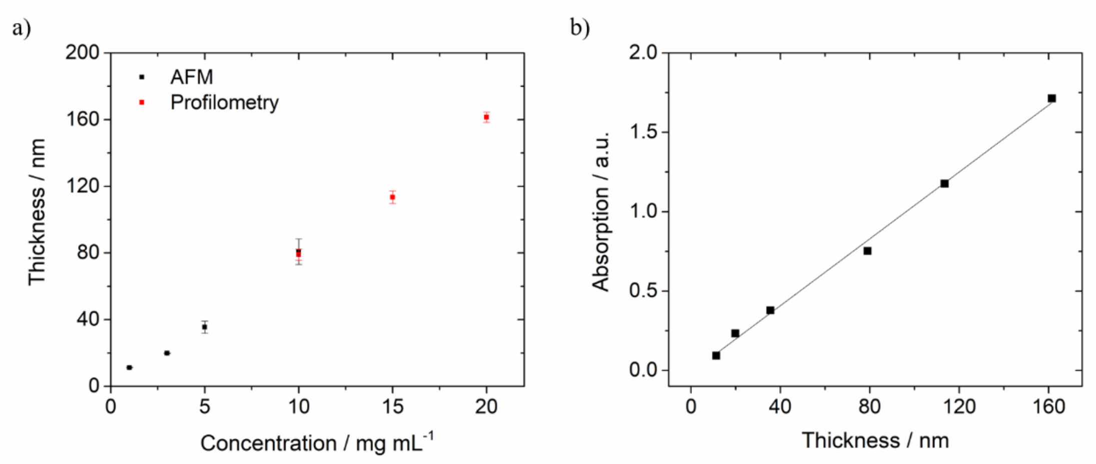

Figure 3.12. **a)** Thicknesses of films of **FS-TEG** spin-coated from various concentrations of solutions of chloroform onto OTS-functionalised glass slides, measured using AFM (black points) and profilometry (red points). **b)** Absorption of **FS-TEG** films plotted against their measured thicknesses with trendline showing the linearity of the relationship.

3.4.6.3 Effect of Altering Film Thickness on Photocatalytic Performance

Hydrogen evolution rates were obtained by irradiating the **FS-TEG** slides in 5 vol. % TEA solutions over a 5 hour period. A linear increase in performance with increasing film thickness from 11.3 ± 0.2 nm up to 79 ± 3 nm was found, before performance appears to level off (**Figure 3.13**). The fact that performance is still increasing at thicknesses significantly above the expected exciton diffusion length of the polymer is possibly further indication of the swellable nature of **FS-TEG** suggested by QCM and water sorption measurements (**Chapter 2.3.2.2**). In other words, **FS-TEG** film performance is not limited by the depth from which excitons can diffuse to the surface but rather the sum of this depth and the depth to which water can penetrate into the film. This is further evidenced by the fact that the thickness above which deviation from linearity is observed (79 ± 3 nm) is similar to that previously observed in TiO_2 (93 ± 1 nm)[29] which is expected to have much longer charge carrier diffusion lengths.

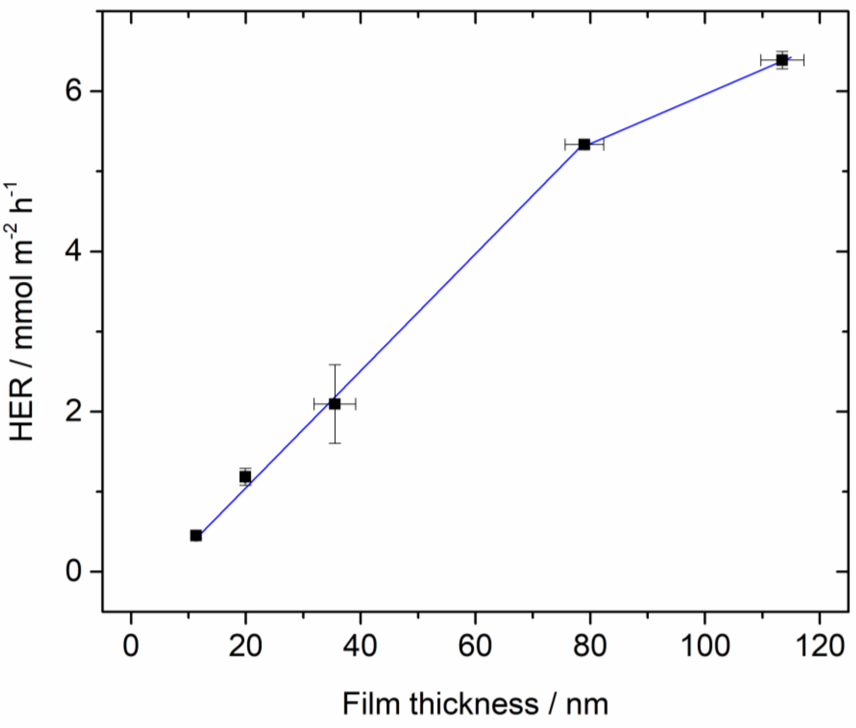

Figure 3.13. Hydrogen evolution rates of films of **FS-TEG** of varying thicknesses on OTS-functionalised glass slides with thicknesses measured by AFM or profilometry. Films placed in 5 vol. % TEA mixture under visible light irradiation using a 300 W Xe light source.

The tailing off of performance is not expected to be due to scattering of light by thicker films as absorption is still increasing linearly at this thicknesses according to the UV-vis spectra (**Figure 3.12b**). Although performance appears to be reaching a plateau, HER is still increasing at a thickness of 113 ± 4 nm. The thickest film (161 ± 3 nm) would have been expected to have a higher HER but delaminated after 20 minutes due to the formation of hydrogen bubbles between the film and slide (**Figure 3.14**). A balance seems to exist between the increased performances of thicker films and reduced mechanical stability.

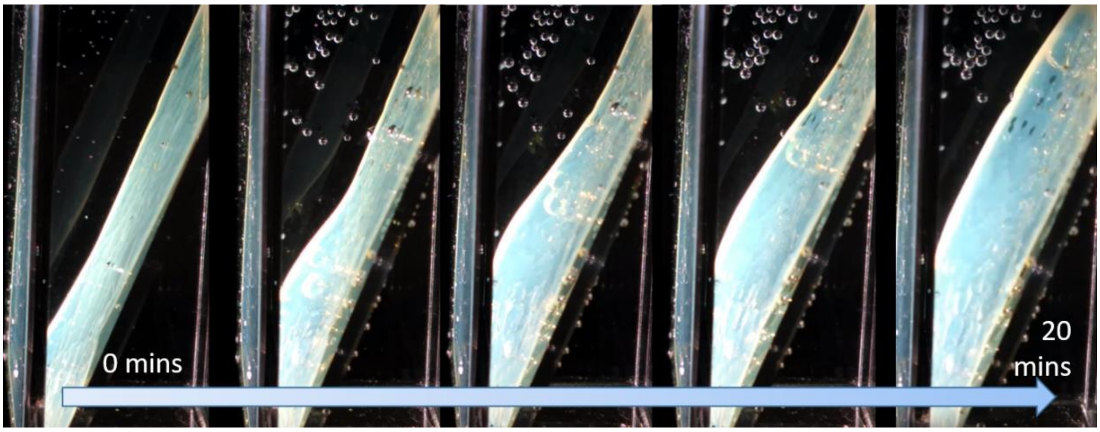

Figure 3.14. Image showing delamination of a 161 ± 5 nm **FS-TEG** film spin-coated on an OTS-functionalised slide in 5 vol. % TEA under visible light irradiation using a 300 W Xe light source.

Table 3.2.Film thicknesses and HERs of **FS-TEG** films spin-cast on OTS-functionalised glass from the specified concentrations of chloroform solutions. HER of films in 5 vol.% TEA under visible light irradiation using a 300 W Xe light source.

Polymer concentration / mg mL^{-1}	**Thickness / nm**		**HER / mmol m^{-2} h^{-1}**
	AFM	Profilometry	
1	11.3 ± 0.2	-	0.45 ± 0.4
3	19.9 ± 0.2	-	1.2 ± 0.1
5	36 ± 4	-	2.1 ± 0.5
10	81 ± 8	79 ± 3	5.3 ± 0.4
15	-	113 ± 4	6.4 ± 0.1
20	-	161 ± 3	(Delaminated)

3.4.6.4 Summary

Spin-coating polymers on OTS-functionalised glass slides enabled the effect of varying film thickness on photocatalytic performance to be studied. Despite the hydrogen evolution reactions taking place at the polymer-liquid interface, a strong dependence on film thickness was observed. HERs were found to increase linearly with film thickness initially before performance appears to reach a plateau. Assuming the amount of polymer deposited increases linearly with film thickness, films of 79 ± 3 nm represents the most efficient use of a given mass of **FS-TEG**.

However, in terms of maximising hydrogen evolution in a given irradiated area, performance is limited by the stability of thicker films rather than their photocatalytic performance. Therefore, stacking slides coated with more stable, thinner films in series may be a useful strategy to further improve performance in a given area.

3.4.7 Stacking Polymer-Coated Glass Slides in Series

Stacking polymer-coated glass slides in parallel is expected to increase the quantity of hydrogen produced per unit area as a result of improved light absorption (**Figure 3.15**). However, improvements in HER may not be as substantial as anticipated due to increased light scattering and so the ability of stacked polymer-coated slides to absorb light must also be carefully considered. An experiment in which up to three slides were stacked in series was performed with **FS-TEG** films of two different thicknesses; 19.9 ± 0.2 nm (referred to as 20 nm from this point forwards) and 79 ± 3 nm (79 nm).

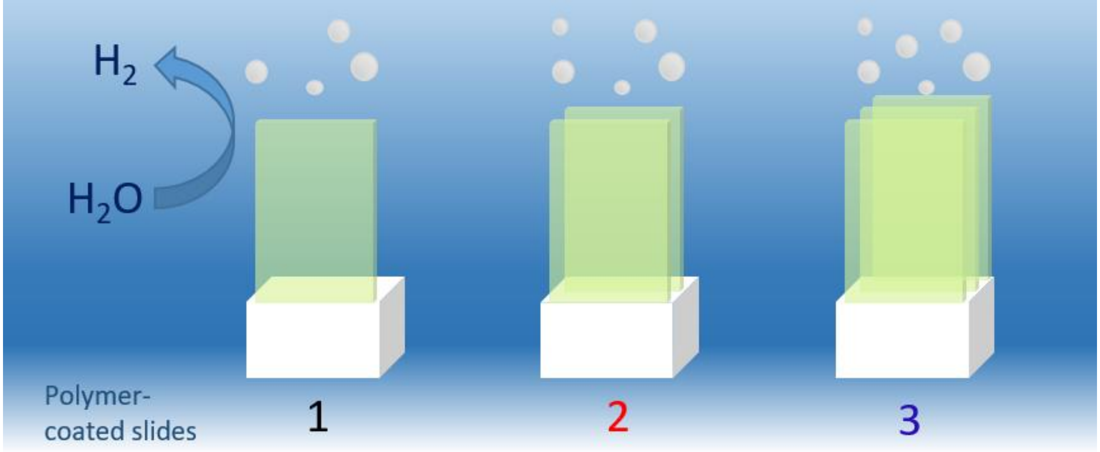

Figure 3.15. Schematic image showing increased hydrogen evolution with the addition of OTS-functionalised slides spin-coated with films of **FS-TEG**.

The transmittance of light through up to three OTS-functionalised glass slides spin-coated with **FS-TEG** was measured by placing the slides vertically in a specifically-produced PTFE rack. Transmittance was found to reduce with the addition of subsequent slides, even when no polymer coating is present. The addition of each uncoated glass slide reduces light transmittance by around 8% presumably due to light scattering. Previously, films of greater thicknesses were found to absorb more light (**Figure 3.11a**). It is observed that stacking three slides coated with 20 nm films in series results in similar transmittance of light as a single slide coated with a 79 nm film as expected. Light absorption was found to increase substantially with the addition of each slide coated with 20 nm films (**Figure 3.16a**) whereas reductions in transmitted light became more incremental in the case of 79 nm films (**Figure 3.16b**). Placing three slides coated with 79 nm films in series was found to reduce transmittance to 0.35% at λ = 420 nm, demonstrating almost complete absorption of light at this wavelength. No further slides were placed in series as it is expected that this would not result in significantly greater light absorption, besides a slight broadening of absorption into the visible region.

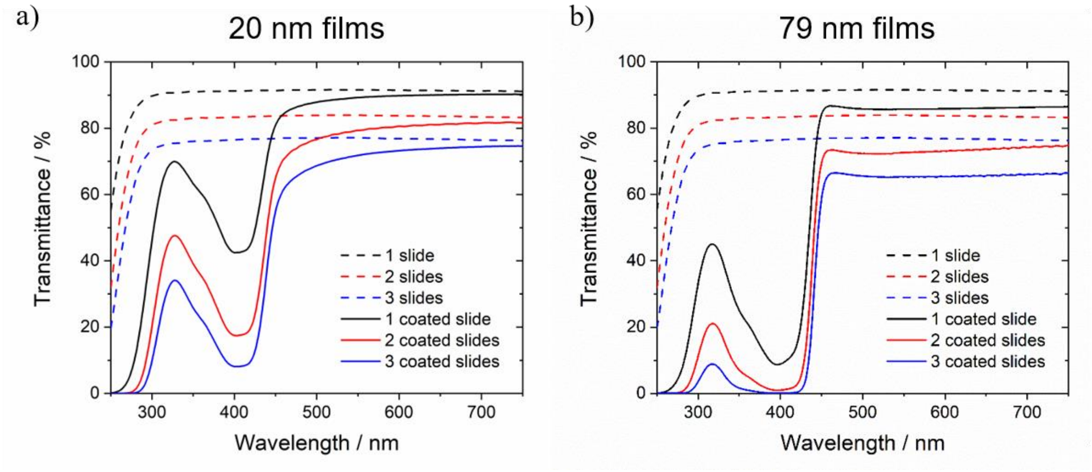

Figure 3.16. Transmittance spectra of up to three OTS-functionalised slides spin-coated with **FS-TEG** films of **a)** 20 nm and **b)** 79 nm thickness placed in series. Spectra of slides without polymer coatings (dashed lines) included for comparison.

Photocatalytic experiments were performed on one, two or three polymer-coated slides stacked in series using a PTFE rack in 5 vol. % TEA. A single slide coated with a 79 nm film evolved hydrogen at a greater rate than three slides coated with 20 nm films in series (4.8 ± 0.2 *vs*. 3.4 ± 0.1 mmol m^{-2} h^{-1}). This was in good agreement with the transmittance spectra and provides further evidence that the photocatalytic performance of polymer films increases linearly to a depth of 79 nm.

Table 3.3. Transmittance at λ = 420 nm and HERs of **FS-TEG** films of specified thicknesses spin-coated on OTS-functionalised glass slides stacked in parallel.

Number of slides	**20 nm films**		**79 nm films**	
	Transmittance / %	**HER / mmol m^{-2} h^{-1}**	**Transmittance / %**	**HER / mmol m^{-2} h^{-1}**
1	45.2	1.2 ± 0.1	14.7	4.8 ± 0.2
2	19.9	2.2 ± 0.2	2.6	8.2 ± 0.4
3	9.8	3.4 ± 0.1	0.35	9.6 ± 0.2

An increase in HER was observed with the addition of subsequent polymer-coated slides in accordance with greater light absorption (**Table 3.3**). **Figure 3.17** shows that the proportionate increase in performance was less pronounced when slides coated with 79 nm films of **FS-TEG** were stacked in series. This is thought to be due to the greater reduction in transmittance of light with each subsequent addition of these thicker polymer films. Therefore, greater hydrogen production in a given area comes at the expense of inefficient use of material and the polymer-coated slides would produce more placed side by side rather than stacked in series. Nevertheless a maximum areal HER of 9.6 ± 0.2 mmol m^{-2} h^{-1} was achieved when three of these slides coated with 79 nm films were stacked in parallel.

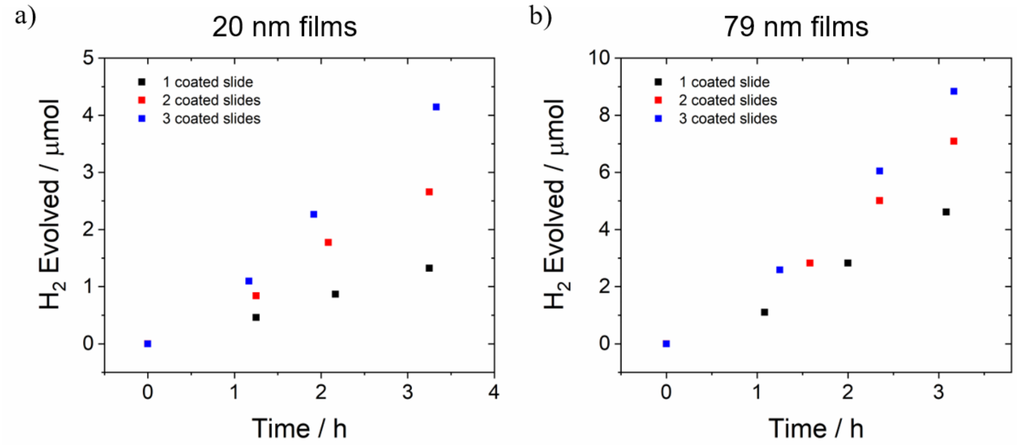

Figure 3.17. Hydrogen evolution of up to three OTS-functionalised slides spin-coated with **FS-TEG** films of a) 20 nm and b) 79 nm thickness placed in series in 5 vol. % TEA mixture under visible light irradiation using a 300 W Xe light source.

3.4.8 Annealing Polymer Films

The properties of polymer films can be dramatically altered by heating them. Thermal annealing can result in structural rearrangements leading to improved charge transport in polymers.[53] In a recent study, optimised annealing led to a doubling of the exciton diffusion length in films of a small molecule.[54] If a similar feat could be achieved in the polymers studied here, significant advancements in photocatalytic performance may be possible.

TGA of **FS-TEG** (**Figure 2.25**) showed the polymer should be stable up to temperatures in excess of 300 °C. Identical **FS-TEG** films were annealed at 150 and 200 °C for two hours. The optical properties of a non-annealed film and a film annealed at 80 °C—the procedure used to evaporate residual chloroform from films so far in this chapter—were also measured for comparison. Annealing at 80 °C does not alter the absorption and emission profiles of **FS-TEG** films besides a slight reduction in the intensity of both (**Figure 3.18**). Annealing films of **FS-TEG** at 200 °C results in further decrease in the intensity of absorption while a big reduction in the intensity of the blue emissive band (λ_{em} ≈ 450 nm) is also observed. Instead the emission profiles of the films annealed at 150 and 200 °C are dominated by a green emission (λ_{em} ≈ 520 nm).

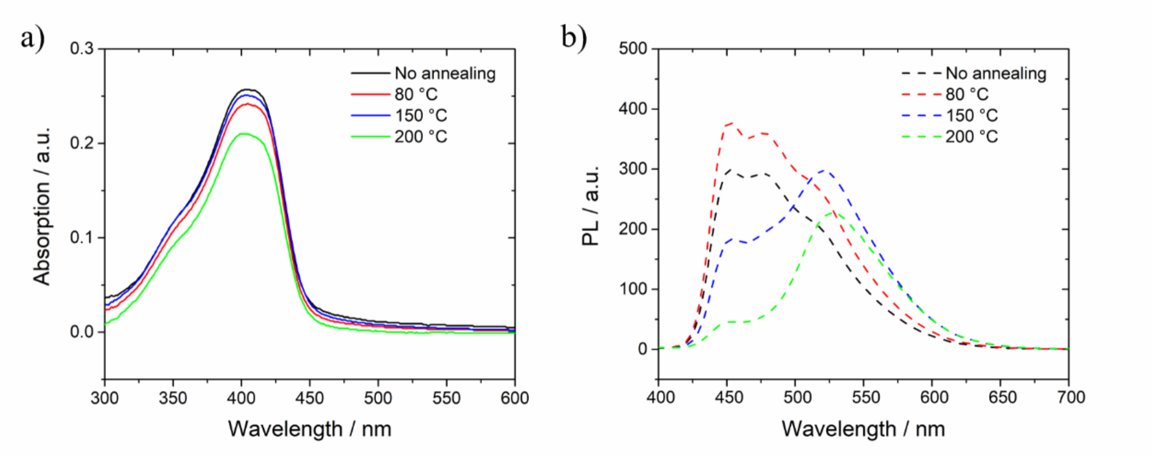

Figure 3.18. a) UV-vis and **b)** PL spectra of **FS-TEG** films spin-coated from 3 mg mL^{-1} chlorform solutions annealed at the specified temperatures for two hours (λ_{exc} = 360 nm).

As previously discussed, this g-band has been assigned to both structural rearrangements[55,56] and the formation of fluorenone defects.[17-19] Further investigations were therefore carried out to probe the nature of the g-band in the emission spectra of the annealed films. If the g-band is present when the film is annealed in the absence of oxygen, it would suggest that a structural rearrangement, rather than oxidation of the fluorene bridgehead, is responsible for appearance of the g-band. The g-band is still evident when the film is annealed under vacuum (**Figure 3.19a**)—albeit to a slightly lesser extent than in the presence of air— suggesting a structural rearrangement of **FS-TEG** is responsible for appearance of the g-band.

Showing reversibility of g-band formation would further support the idea that structural rearrangement is responsible for the change in emissive behaviour. G-band formation has been reversed by quenching polymer films in a bath of dry ice and methanol immediately after annealing.[57] However, no recovery of the blue emission band was observed upon immersion of annealed films in a dry ice/methanol bath (**Figure 3.19b**). A comprehensive explanation of the formation of g-band in the annealed films therefore remains somewhat unclear.

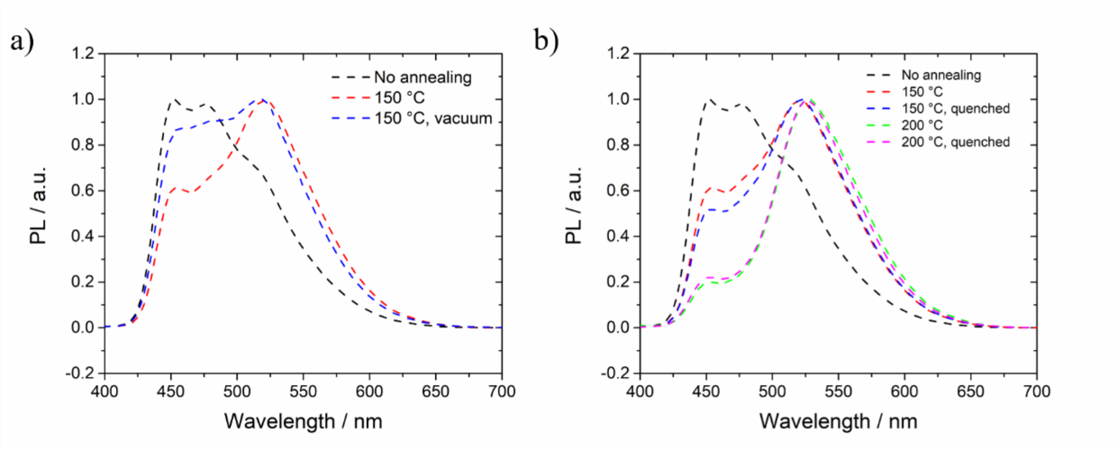

Figure 3.19. a) PL spectra of **FS-TEG** films spin-coated from 3 mg mL^{-1} chloroform solutions annealed at the specified temperatures for two hours in air or in a vacuum **b)** PL spectra of **FS-TEG** films spin-coated from 3 mg mL^{-1} chloroform solutions annealed at the specified temperatures before and after quenching in a dry ice/methanol bath (λ_{exc} = 360 nm in both spectra).

The photocatalytic performance of films was again measured in 5 vol. % TEA. Annealing at 80 °C resulted in a similar HER to a non-annealed film, as expected (**Table 3.4**). Slight reduction in HER was observed in films annealed at higher temperatures. Interestingly, a higher HER was observed for the film annealed at 200 °C than 150 °C. A slightly higher HER was observed in the film annealed under vacuum at 150 °C than in air. Generally though, the effect of annealing films on photocatalytic performance appears to be minimal.

Table 3.4. Initial HERs (0 h < t < 4 h) of **FS-TEG** films annealed at the specified temperatures and in the specified conditions in 5 vol. % TEA under visible light irradiation using a 300 W Xe light source.

Annealing temperature / °C	**Annealing conditions**	**HER / mmol m^{-2} h^{-1}**
None	Air	1.0 ± 0.2
80	Air	1.2 ± 0.1
150	Air	0.7 ± 0.1
	Vacuum	0.80 ± 0.08
200	Air	0.89 ± 0.03

In summary, annealing was not found to enhance the photocatalytic performance of polymer films. In fact a slight reduction in HER was observed when films were annealed at temperatures greater than 80 °C. This seemingly correlated with the appearance of a green emissive band in the PL spectra of films. A structural reorganisation of the polymer seems the most likely explanation for the appearance of this g-band.

3.4.9 Polymer Blends

It is well known that excitons are typically strongly bound in conjugated polymers.[58] The strategy of combining two or more polymer photocatalysts in a 'blend' has therefore been developed to encourage charge separation in OPV devices.[59] In these bulk heterojunctions (BHJs), polymers form inter-connected networks with a large interface between the polymers at which excitons can rapidly dissociate.[60]

Blend formation could similarly enhance photocatalytic performance by encouraging dissociation of the exciton and enhancing charge transfer at the aqueous interface. It has recently been reported that hydrogen evolution rates can be improved by blending polymers in nanomicelles.[61] The formation of films of polymer blends should also enable good interfacial contact between the components and encourage charge separation, like in BHJ solar cells.

FP-TEG and **FS-TEG** were chosen to be components of the blend as they have offset band positions which should enable charge transfer (**Chapter 2.3.1.2**). The '**FP-TEG + FS-TEG**' blend was prepared by spin-coating a 1:1 solution of **FP-TEG** and **FS-TEG** on an OTS-functionalised glass substrate. The absorption spectrum (**Figure 3.20**) shows broad absorption from the polymer blend. The absorption profile of the blend peaks at the absorption maxima of **FS-TEG** presumably as it has a higher molar extinction coefficient than **FP-TEG** (**Chapter 2.2.2.2**).

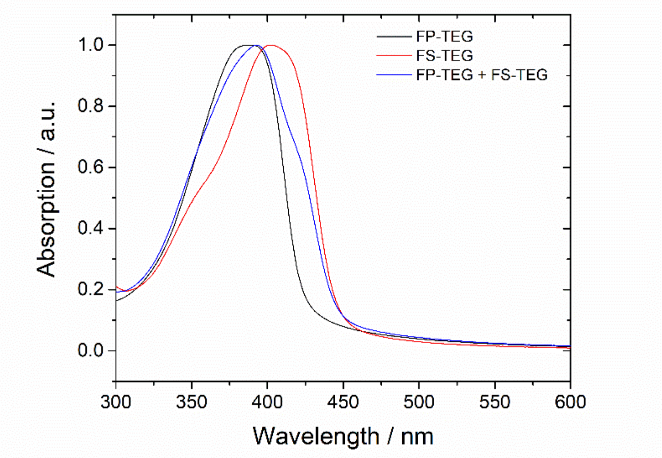

Figure 3.20. a) UV-vis absorption spectrum of films of **FP-TEG**, **FS-TEG** and the **FP-TEG + FS-TEG** blend spin-coated from 3 mg mL^{-1} chlorform solutions.

The HER of the **FP-TEG + FS-TEG** blend was found to be 0.97 ± 0.04 mmol m^{-2} h^{-1}. This is lower than a film of **FS-TEG** (1.2 ± 0.1 mmol m^{-2} h^{-1}) but higher than the HER would be expected to be if it were an average of the two polymers separately (0.67 mmol m^{-2} h^{-1}). This suggests some synergistic effect is taking place although not significant enough to achieve rates in excess of the more active polymer in the blend.

Table 3.5. Initial HERs of films of **FP-TEG, FS-TEG** and the **FP-TEG + FS-TEG** blend in 5 vol. % TEA under visible light irradiation

Polymer	**HER / mmol m^{-2} h^{-1}**
FP-TEG	0.13 ± 0.01
FS-TEG	1.2 ± 0.1
FP-TEG + FS-TEG	0.97 ± 0.04

Although the formation of polymer blends did not significantly increase activity, the suggestion of synergistic behaviour is encouraging. HER enhancements may be possible by optimising the blend morphology just as performance has been improved in BHJ solar cells.[62] This could be done by modifying the film thickness by altering the spin-coating procedure, through the addition of additives[63] or by annealing the blends.[64] Annealing may have a more significant effect on the morphology and photocatalytic performance of blends than the single-component films discussed previously.

3.4.10 Incorporation of Dyes

The performance of polymer films under visible light is restricted by their blue-shifted absorption profiles, as evidenced by wavelength-dependent hydrogen evolution experiments (**Figure 3.21**). Hydrogen evolution rates of **FS-TEG** cast on roughened glass were measured at 50 nm intervals using narrow band-pass filters between λ = 370 nm and λ = 520 nm and compared to **FS-TEG** powder. **FS-TEG** powder showed some activity at wavelengths up to λ = 520 nm (33 ± 2 μmol W^{-1} h^{-1}) while the film was virtually inactive under λ = 470 nm irradiation (5 ± 3 μmol W^{-1} h^{-1}). The wavelength-dependence shown in this experiment also further confirms the photocatalytic nature of the hydrogen evolution reaction involving both powders and films of **FS-TEG**.

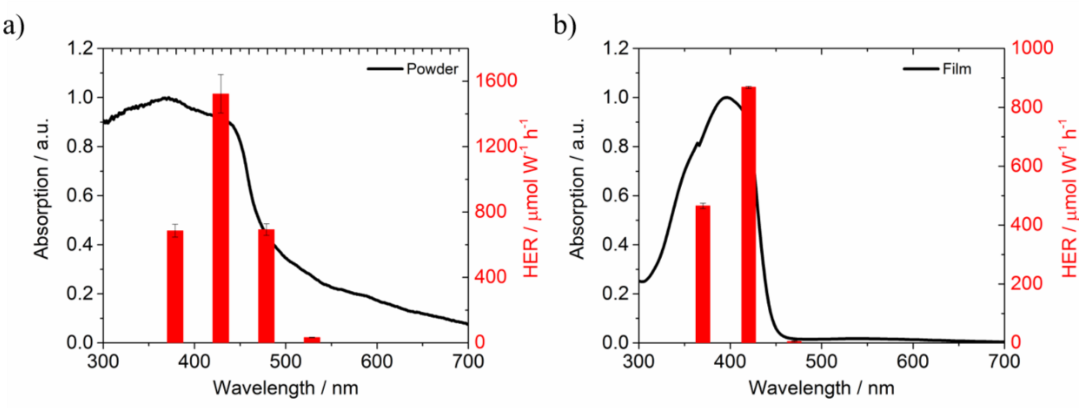

Figure 3.21. Hydrogen evolution rates of **a)** powdered **FS-TEG** and **b)** an **FS-TEG** film drop-cast on roughened glass placed in 5 vol. % TEA/water under λ = 370, 420, 470 and 520 nm irradiation using a 300 W Xe light source, plotted with corresponding UV-vis absorption spectra.

Lack of visible light harvesting therefore appears to be a limitation of polymer films. Visible light accounts for 50% of the solar spectrum and so strategies to enhance performance in this region are required.[65] This light could be harvested through the use of a photosensitiser in a similar vein to dye-sensitised solar cells (DSSCs).[66] Recently, the photocatalytic performance of C_3N_4 has been enhanced with the addition of a xanthene dye.[67] In this investigation, the formation of films of polymer-dye blends should ensure homogeneity and enable efficient energy transfer from the dye to the polymer.

3.4.10.1 High Throughput Screening of Polymer-Dye Blends

A number of inexpensive, commercially-available organic-soluble dyes used industrially for the dying of plastics, were first tested. These have been found to have high photostability and strong light absorption.[68] Anthraquinone-type dyes Solvent Green 28, Solvent Blue 97, Solvent Blue 104 and the thiaxanthene Solvent Yellow 98 were selected (**Figure 3.22a**). The anthraquinone dyes in particular were found to have good absorption in the visible region (**Figure 3.22b**) with Solvent Green 28 absorbing at longer wavelengths (λ_{max} = 686 nm). Solvent Green 28 also has the highest molar extinction coefficient at these visible wavelengths.[69]

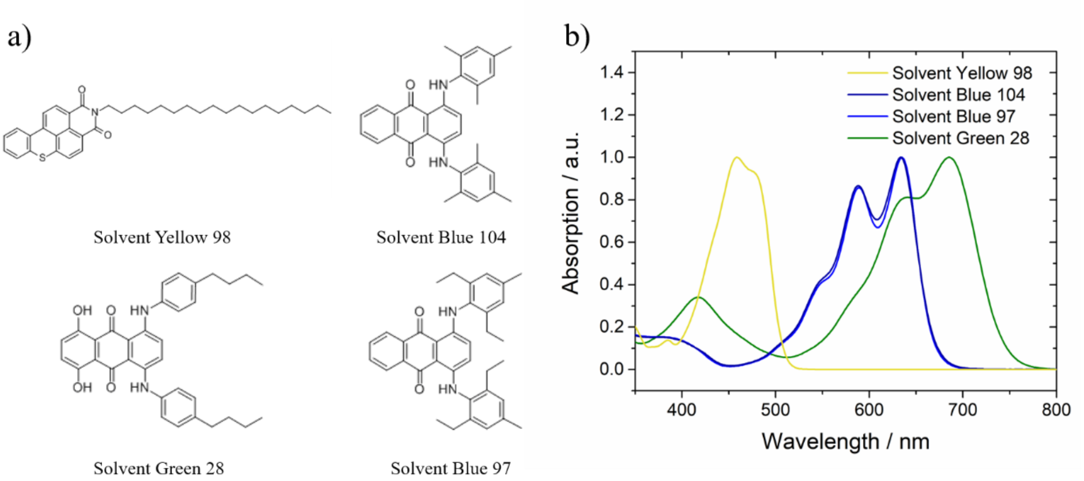

Figure 3.22. a) Chemical structures and **b)** UV-vis absorption spectra of solutions of solvent dyes in chloroform

The dye loading is of critical importance in polymer-dye blends and should be systematically varied to find the optimum loading.[70] The need to modify both the dyes and their loadings means this study lends itself to a high throughput screening (HTS) approach. A HTS workflow was used to rapidly screen different dyes and their loadings (**Figure 3.23**). Dyes were dissolved in chloroform at different concentrations and added to pre-weighed polymer samples. The solvent was then allowed to evaporate which resulted in the formation of polymer-dye films with 0.2, 1, 2 and 5 wt. % dye loadings. Water and TEA were then added to each sample using an automated dispenser before the samples were capped, sonicated to dislodge the films and irradiated using a solar simulator. The amount of hydrogen evolved was then detected using automated gas chromatography (GC).

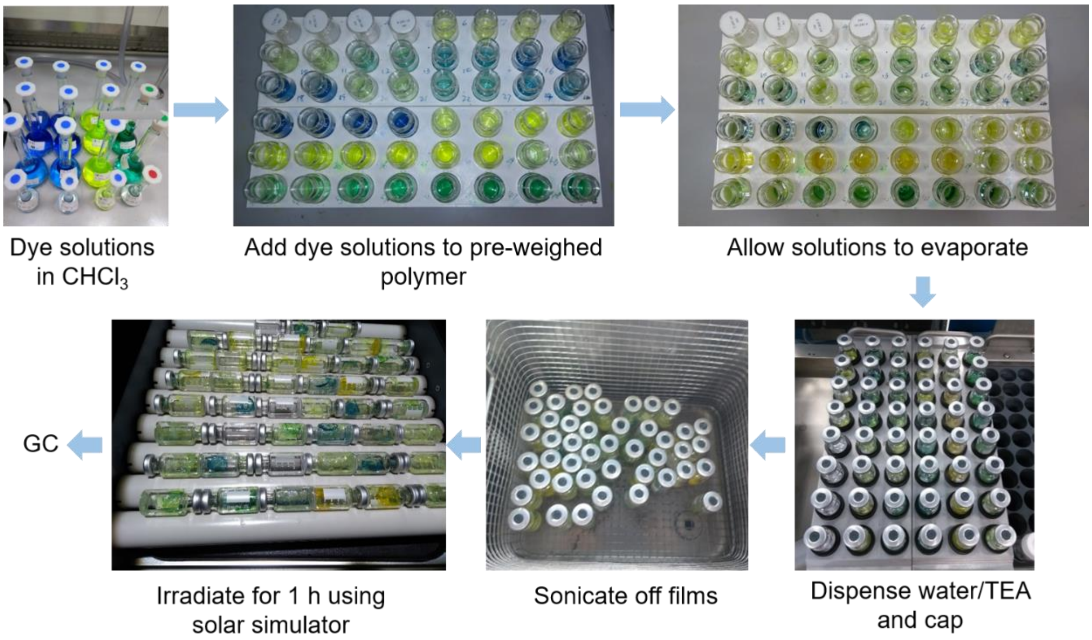

Figure 3.23. Flow diagram of high throughput screening used to study the influence of dyes on photocatalytic performance.

No increases in photocatalytic performance were observed with any of the dyes at the loadings studied here (**Figure 3.24**). Instead, HERs seem to decrease with increasing dye loadings. Solvent Blue 104 and Solvent Yellow 98 appear to reduce HER more than Solvent Blue 97. Interestingly, despite having good visible light absorption, incorporation of Solvent Green 28 at any concentration reduces the activity of **FS-TEG** to below 0.03 mmol g^{-1} h^{-1} (compared to 1.7 ± 0.2 g^{-1} h^{-1} for **FS-TEG** with no added dye).

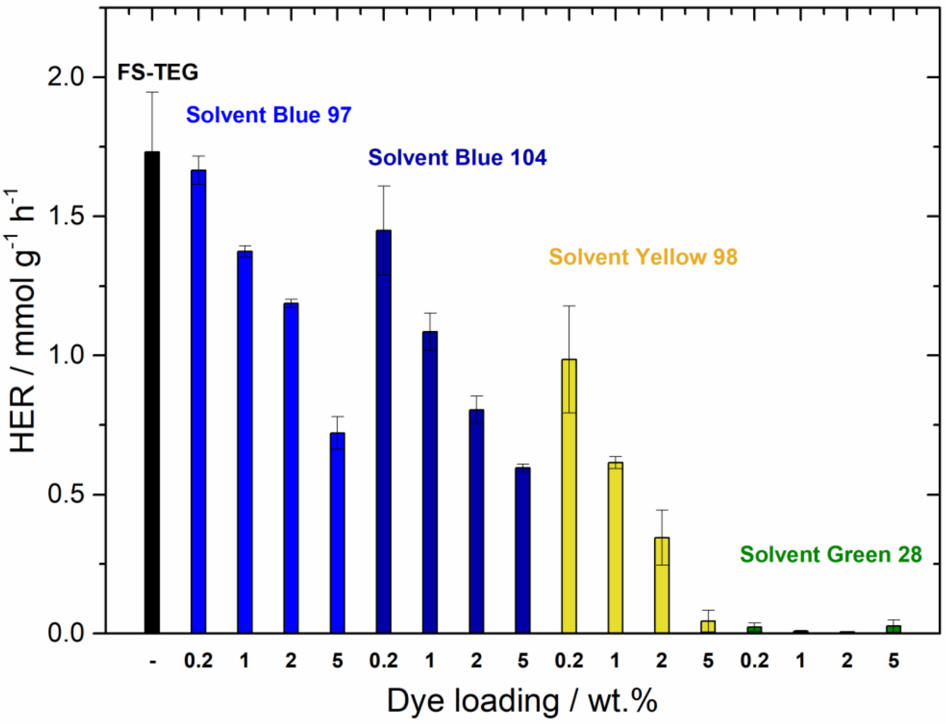

Figure 3.24. HERs of polymer-dye blends after irradiation with a solar simulator (AM1.5G, 1 Sun) for 5 hours.

At high dye loadings, energy trapping has been shown to overcome gains in light absorption.[70] It is possible that the dye loadings studied here are all above the optimum dye loading. Alternatively, the potentials of these dyes may not be suitably aligned for charge transfer from the dye to the polymer. The HTS method used here may also prevent effective charge transfer between the dye and polymer. Dyes and polymers are likely to be deposited at different rates as the chloroform evaporates which may lead to poorly-blended inhomogeneous films. A high concentration of dye on the surface of the films would reduce contact of the polymer with the aqueous medium, which may inhibit activity. Experiments should therefore be performed with lower loadings of dyes in more precisely-controlled spin-coated films with more careful consideration given to the band structure of the dye.

3.4.10.2 Polymer Films Incorporating LS-1 Dye

LS-1 (**Figure 3.25a**) is a sensitiser that has previously been used in DSSC architectures.[71–75] The donor-π-acceptor structure of **LS-1** encourages charge separation in the excited state.[74] **LS-1** is an effective harvester of visible light, with an absorption onset around λ = 630 nm.[71] As previously discussed, the band structure of dyes must be considered. The positions of the potentials of **LS-1** were therefore computationally predicted by (TD-)DFT calculations (**Figure 3.25b**). The calculated potentials appear to be suitable for efficient electron transfer from **LS-1** to **FS-TEG**. Moreover, the calculated optical gap of 2.13 eV confirms that **LS-1** should absorb a significant portion of the visible spectrum.

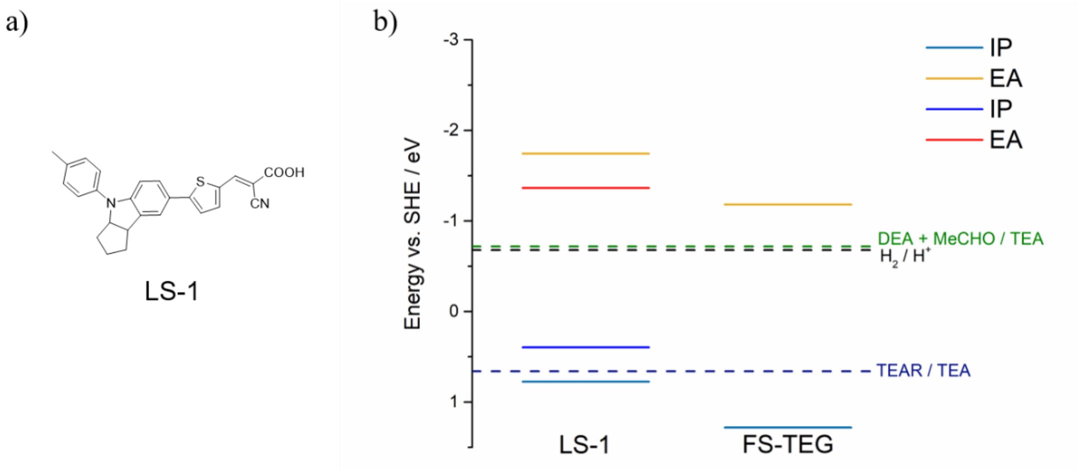

Figure 3.25. a) Structure of **LS-1** and **b)** Potentials of **LS-1** and **FS-TEG**. Potentials of **LS-1** calculated using (TD-)DFT while positions of IP and EA of **FS-TEG** were estimated from PESA and UV-vis absorption onset measurements performed in **Chapter 2**.

Solutions of **FS-TEG** and **LS-1** (0.1, 0.3 and 1.0 wt. %) were prepared and spin-coated on OTS-functionalised glass slides. **LS-1** is not observable in the UV-vis absorption spectra of the resultant films due to the low dye loadings (**Figure 3.26a**). However, the hydrogen evolution rates of films is notably affected by incorporation of **LS-1** (**Figure 3.26b**, **Table 3.6**). Lower loadings resulted in the greatest rate enhancements (0.1 > 0.3 > 1.0 wt. %) with 0.1 wt. % **LS-1** found to increase HER of **FS-TEG** more than threefold. The addition of 1.0 wt. % **LS-1** resulted in no increase in HER.

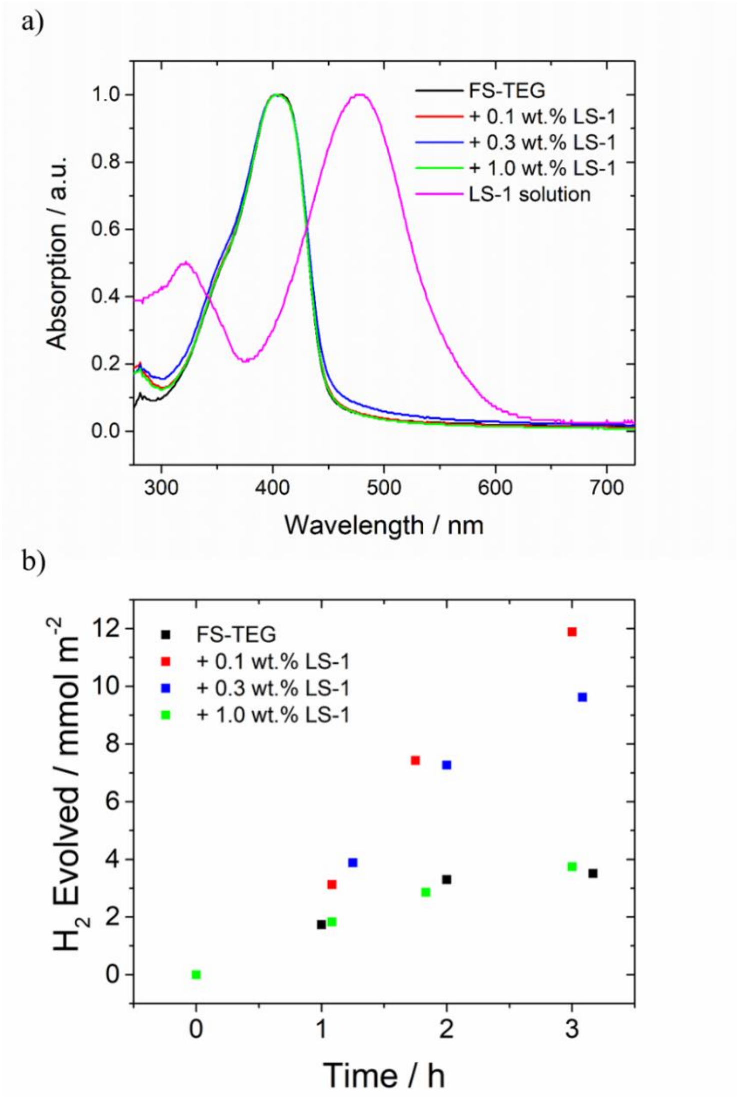

Figure 3.26. **a)** UV-vis absorption spectra of films with specified **LS-1** loadings and **b)** hydrogen evolution runs of these films in 5 vol. % TEA mixture under visible light irradiation by a 300 W Xe light source.

Table 3.6. HERs of films spin-cast on OTS-functionalised glass slides from chloroform solutions (3 mg mL^{-1} of **FS-TEG**) under visible light irradiation by a 300 W Xe light source.

Film	**HER / mmol m^{-2} h^{-1}**
FS-TEG	1.2 ± 0.1
FS-TEG + 0.1 wt. % LS-1	4.4 ± 0.7
FS-TEG + 0.3 wt. % LS-1	3.1 ± 0.6
FS-TEG + 1.0 wt. % LS-1	1.0 ± 0.2

3.4.11 Film Stability

3.4.11.1 Stability of FS-TEG Films

Ensuring the long-term stability of photocatalysts is of critical importance. Powdered photocatalysts were shown to have good stability after irradiation for in excess of 120 hours (**Chapter 2.1.3**) whereas nanoparticles appeared to be more susceptible to degradation (**Chapter 3.1**). So far in **Chapter 3.3**, the HERs reported have been initial rates measured over the course of the first three hours of irradiation. This is because the performances of thin films of **FS-TEG** tail off after irradiation for longer time periods (**Figure 3.27a**).

The reduction in photocatalytic performance is accompanied by changes in the absorption and PL spectra (**Figure 3.27b** and **c**). A blue shift in the absorption is observed as with the nanoparticles studied previously. However, unlike in nanoparticles, the emission of **FS-TEG** films appears to shift to longer wavelengths after photocatalysis. A similar growth of this g-band was seen with thermal annealing (**Chapter 3.4.8**). Again, this observation suggests a structural rearrangement rather than formation of fluorenone defects as a red shift in absorption would be expected with increasing fluorenone content.[76]

Interestingly, solutions of **FS-TEG** made by dissolving pre- and post-photocatalysis films off glass slides were found to have similar spectra (**Figure 3.27d** and **e**). A slight broadening of the absorption spectrum into the UV region is observed in the post-photocatalysis solution although the absorption maximum remains unchanged (**Figure 3.27d**). Moreover, the PL spectrum of the post-photocatalysis film appears to be unaltered (**Figure 3.27e**). Further experiments were conducted to investigate the reason for the drop-off in performance.

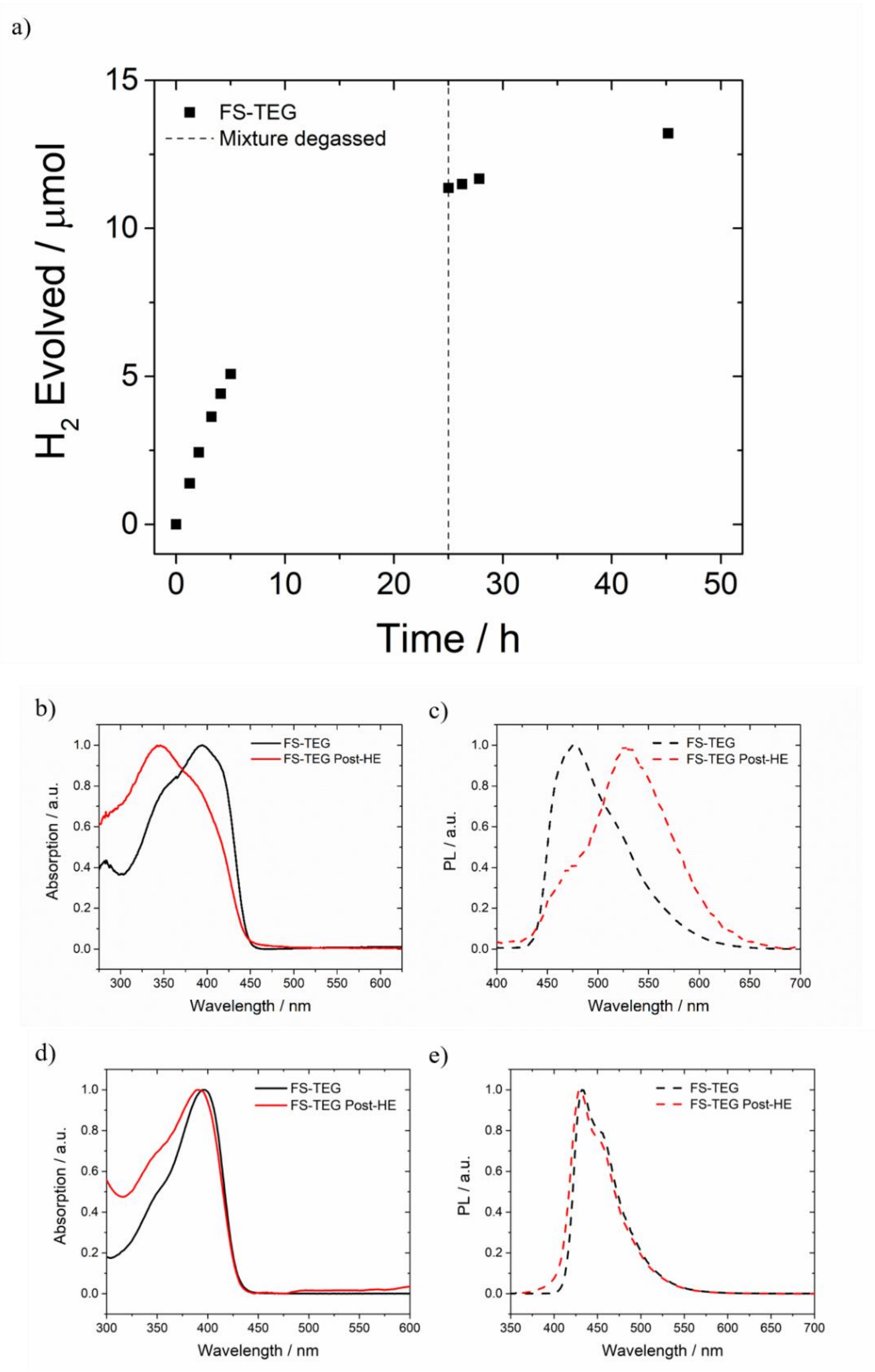

Figure 3.27. a) Hydrogen evolution of an **FS-TEG** film (20 nm) spin-coated on an OTS-functionalised slide. Films placed in 5 vol. % TEA mixture under visible light irradiation. **b)** UV-vis absorption and **c)** PL spectra of the **FS-TEG** film before and after the photocatalysis run (Post-HE). **d)** UV-vis absorption and **e)** PL spectra of equivalent **FS-TEG** films dissolved in chloroform before and after photocatalysis (λ_{exc} = 360 nm).

A film of **FS-TEG** on an OTS-functionalised substrate was placed in the dark in 5 vol. % TEA solution for 22 hours while another was irradiated in atmospheric conditions (not suspended in 5 vol. % TEA) (**Figure 3.28a**). The absorption and PL spectra of the resultant films (**Figure 3. 28b** and **c**) show that the absorption and blue shift occur when films are irradiated in air whereas no changes are evident when the films are placed in suspension in the dark. This study suggests that photobleaching is the cause of these changes in optical properties rather than any chemical degradation that might take place as a result of being placed in the hole-scavenging photocatalytic mixture. Oxidative photobleaching is a common problem among polymers in OPV devices.[77] A number of strategies were thus implemented in an attempt to enhance film stability by improving resistance to photobleaching.

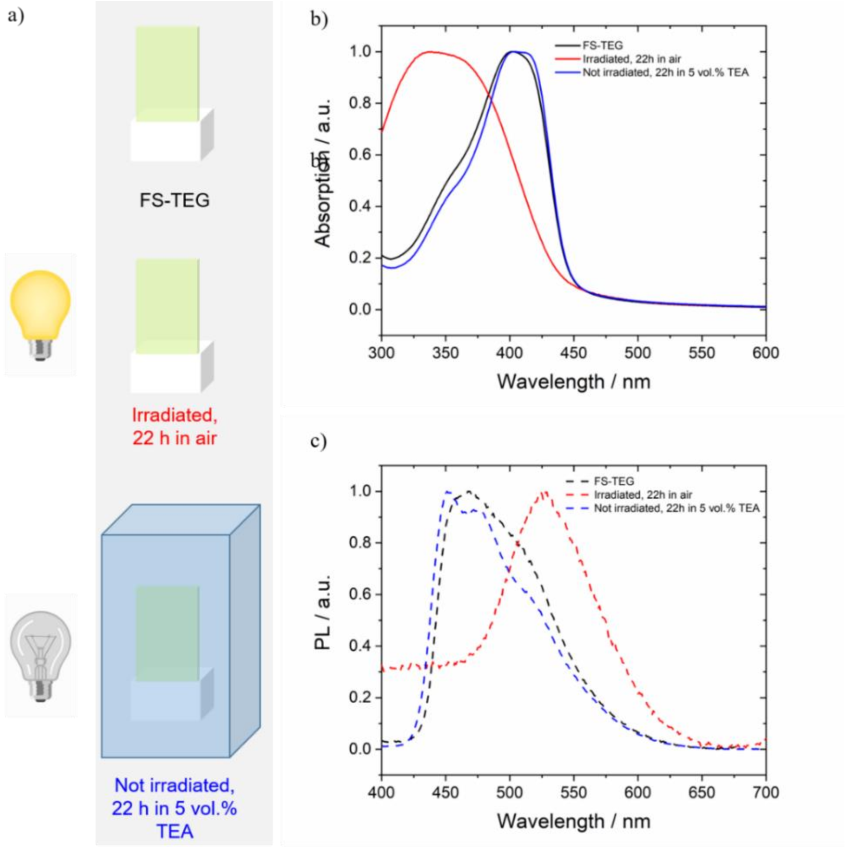

Figure 3.28. a) Images of different conditions **FS-TEG** film (20 nm, spin-coated on an OTS-functionalised slides) were subject to. Films from top to bottom are: as formed, placed in air under visible light irradiation for 22 hours, placed in 5 vol. % TEA mixture in the dark for 22 hours. **b)** UV-vis absorption and **c)** PL spectra of the **FS-TEG** films after being subject to the conditions described (λ_{exc} = 360 nm).

3.4.11.2 Singlet Oxygen Scavengers

Oxygen should not be present at high levels in the hydrogen evolution experiments performed in this thesis as samples are degassed with nitrogen prior to photocatalysis. However, oxygen is difficult to exclude completely and trace amounts may still be responsible for the observed photobleaching. Small molecule additives can be used to prevent photobleaching.[78] For example, nickel (II) dibutyldithiocarbamate ($Ni(dtc)_2$) is a chelating agent that has been shown to improve the stability of polymer films by quenching the singlet oxygen ($^1O_2$) species believed to be responsible for photobleaching.[79]

$Ni(dtc)_2$ (10 wt. %) was incorporated into an **FS-TEG** film by dissolving in the chloroform solution prior to spin-coating. The '**FS-TEG + $Ni(dtc)_2$**' film had a similar initial HER to an **FS-TEG** film with no additive (**Figure 3.29**). After approximately 25 hours, the **FS-TEG + $Ni(dtc)_2$** film exhibited around 20% higher hydrogen evolution. However, a similar rate of drop-off of performance is observed despite the presence of $Ni(dtc)_2$ and it does not appear that performance would greatly exceed 50 hours of usage.

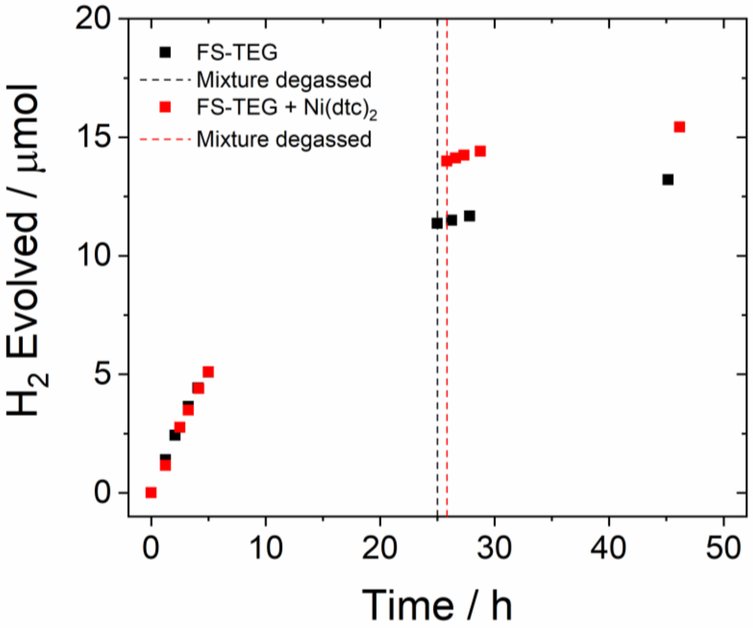

Figure 3.29. a) Hydrogen evolution of **FS-TEG** (black symbols) and **FS-TEG + $Ni(dtc)_2$** (red symbols) spin-coated on OTS-functionalised slides. Films were placed in 5 vol. % TEA mixtures under visible light irradiation with intermittent degassing as shown.

However, the absorption and emission properties do suggest the $Ni(dtc)_2$ has some effect on the optical durability of **FS-TEG** films. The polymer absorption is less blue-shifted after photocatalysis (λ_{max} = 352 nm, **Figure 3.30a**) while the emissive g-band is also less pronounced (λ_{em} = 493 nm, **Figure 3.30b**). The spectrum of a solution of the dissolved-off post-photocatalysis film of **FS-TEG + $Ni(dtc)_2$** is also less broadened than in the absence of $Ni(dtc)_2$ (**Figure 3.30c**). In view of these observations, the fact that the longevity of hydrogen evolution performance is not greatly improved is surprising and suggests that changes in the optical properties may not be the sole reason for the reduction in performance. Nevertheless, these results suggest that the addition of additives such as $Ni(dtc)_2$ is a potentially promising strategy to improve the stability of polymer films and warrants further investigation.

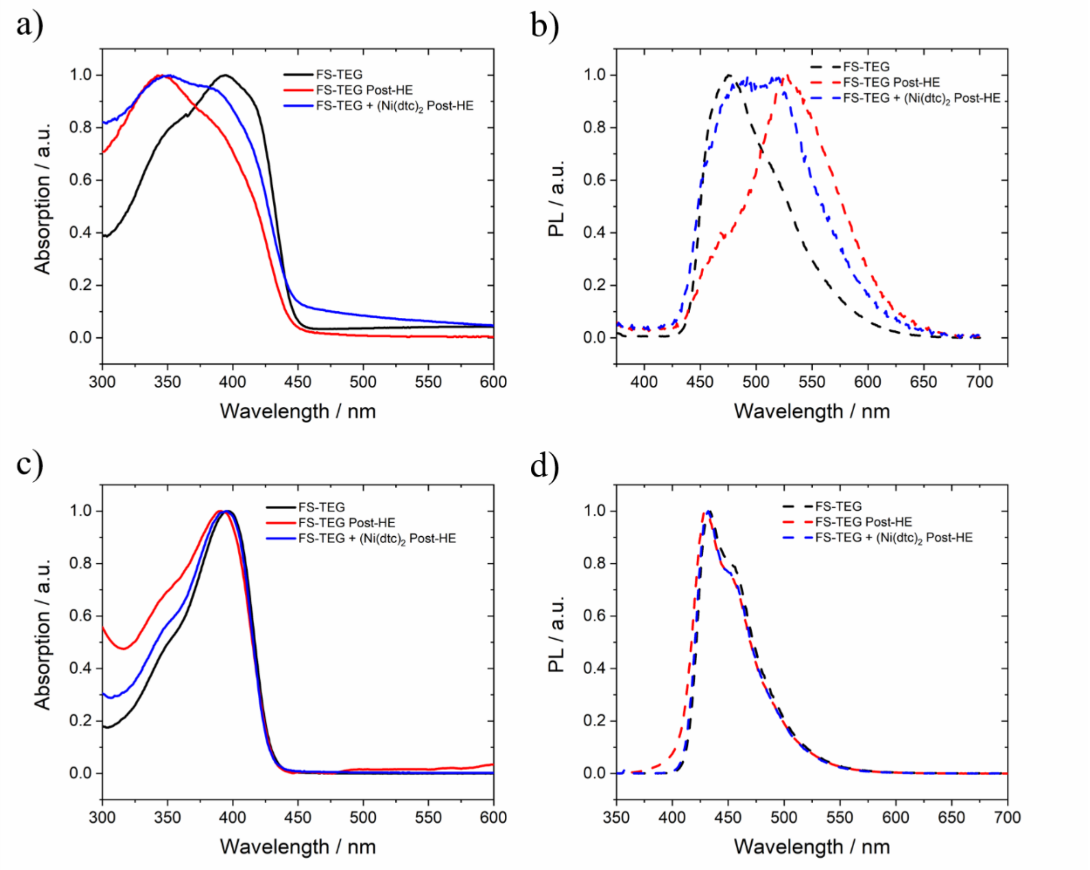

Figure 3.30. a) UV-vis absorption and **b)** PL spectra of the **FS-TEG** and **FS-TEG + $Ni(dtc)_2$** films before and after the 25 hour photocatalysis run (Post-HE). **d)** UV-vis absorption and **e)** PL spectra of the films dissolved in chloroform before or after photocatalysis (λ_{exc} = 360 nm).

3.4.11.3 Stability of Polymers with Modified Bridgehead Atoms

The effect of modifying the bridgehead atom in fluorene-type units was discussed in **Chapter 2.3.2**. A key potential advantage of these polymers that was not addressed is the increased stability of non-carbon bridging atoms. Siloles have been shown to be more stable than fluorenes.[80,81] For instance, the PL spectrum of a polysilole film was unaltered after annealing for 16 hours at 250 °C whereas the equivalent polyfluorene spectrum exhibited the g-band also seen in the spectra of polymers after photocatalysis in this study.[81] The use of alternative bridgehead atoms is therefore anticipated to improve film stability during photocatalysis.

The hydrogen evolution performance of **FS-Oct**, **SiS-Oct**, **GeS-Oct** and **CzS-Oct** was observed in films drop-cast from chloroform on roughened glass slides (**Figure 3.31**). Roughened slides were used in this case to ensure activity was observed in the lower-performing polymers. This does limit the scope of this study as roughened slides are more scattering and optical properties are therefore more difficult to measure. The longevity of photocatalytic performance should still provide useful insights, however.

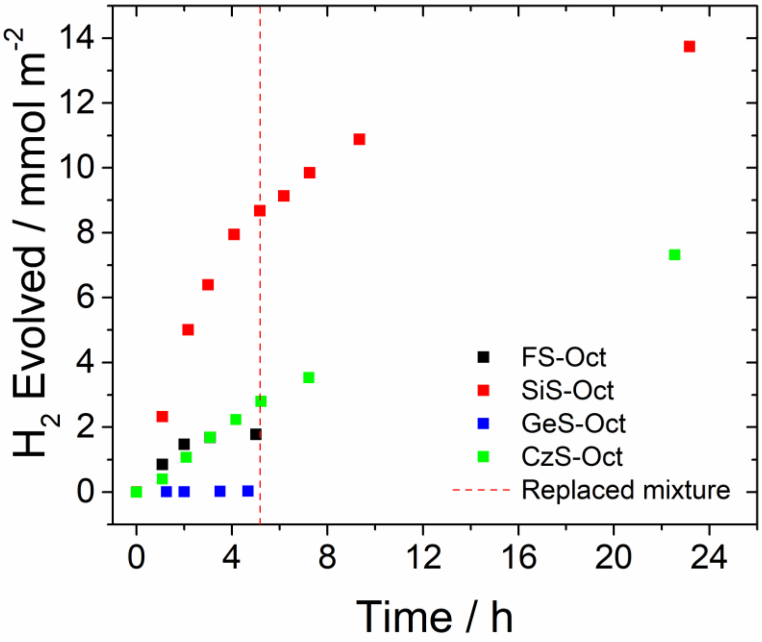

Figure 3.31. Hydrogen evolution runs of **FS-Oct**, **SiS-Oct**, **GeS-Oct** and **CzS-Oct** films drop-cast on roughened glass slides. Films were placed in 5 vol. % TEA mixtures under visible light irradiation with mixtures replaced after approximately 5 hours as shown.

The initial rates of hydrogen evolution reflect the trend seen in powders of these polymers (**SiS-Oct** > **FS-Oct** ≈ **CzS-Oct** > **GeS-Oct**). **SiS-Oct** and particularly **CzS-Oct** display photocatalytic performance after 24 hours whereas the HER of **FS-Oct** levelled off after 5 hours of photocatalysis. The rate of hydrogen production of these materials does drop off over this period but seemingly over longer timescales than **FS-Oct**. The inhomogeneity of drop-cast films means these results should be treated with some caution. However, this limited study indicates improved stability with modification of the bridgehead atom and further endorses the use of carbazole and silole units over equivalent fluorenes.

3.4.11.4 Summary

As with other aspects of photocatalytic hydrogen production from water,[77] it is difficult to fully isolate the factors that influence the stability of polymer photocatalysts. The sometimes contradictory findings of this chapter paint a complex picture that requires more extensive investigations than those undertaken here. However, some interesting observations were made about the durability of these polymer photocatalysts.

Like in other applications that involve light harvesting, photobleaching appears to account, at least partially, for the reduced performance of polymer films over time. Changes in optical properties were found to take place as a result of irradiation rather than participation in the photocatalytic reaction itself. Meanwhile, incorporation of $^1O_2$-chelating $Ni(dtc)_2$ was found to slightly improve long-term film performance.

Attempts to improve polymer stability were hampered by the difficulty in determining the exact nature of any polymer degradation taking place. The observation that silole and carbazole moieties appear to be more stable than fluorene units suggest that oxidation of the bridgehead may contribute to the quicker deterioration of the activity of polyfluorenes. However, the hypothesis that the g-band evident in PL spectra of irradiated films of fluorene-containing polymers is indicative of the formation of fluorenone defects is discredited by the blue-shift in absorption that is concomitantly present.

The fact that the performance of the **FS-TEG + Ni(dtc)$_2$** film tails off despite apparently stable optical spectra points to other possible reasons for poor durability of films that were not explored. The performance of thin films for pollutant degradation has been shown to drop off as a result of adsorption of degradation products.[82] It is possible that degradation of TEA may lead to fouling of the polymer film which may, along with photobleaching, contribute to the depleted activity of polymer films over time.

3.4.12 Glass Fibres

Glass fibres represent an alternative substrate to planar glass slides. These fibrous glass strands are a cheap industrial by-product[83] that are easy to chemically modify and separate from reaction mixtures.[84] These are advantageous properties for use in flow reactors and have therefore been touted as a potentially useful support for heterogeneous catalysts.[84,85] In the context of photocatalysis, depositing on glass fibres should enable a large contact area between the photocatalyst and the aqueous medium.

3.4.12.1 Fabrication and Characterisation of Polymer-Coated Glass Fibres

Glass fibres can be simply coated with solution-processable polymers by adding them to a solution of polymer dissolved in chloroform and evaporating off the solvent (**Figure 3.32a**). Polymer loading can be controlled by altering the concentration of the polymer solution (**Figure 3. 32b**). The optical properties of polymer-coated fibres appear to be similar to **FS-TEG** films (λ_{max} = 309 nm, λ_{em} = 478 nm, **Figure 3. 32c**). SEM images of individual glass fibres confirm the successful deposition of polymers (**Figure 3. 33**).

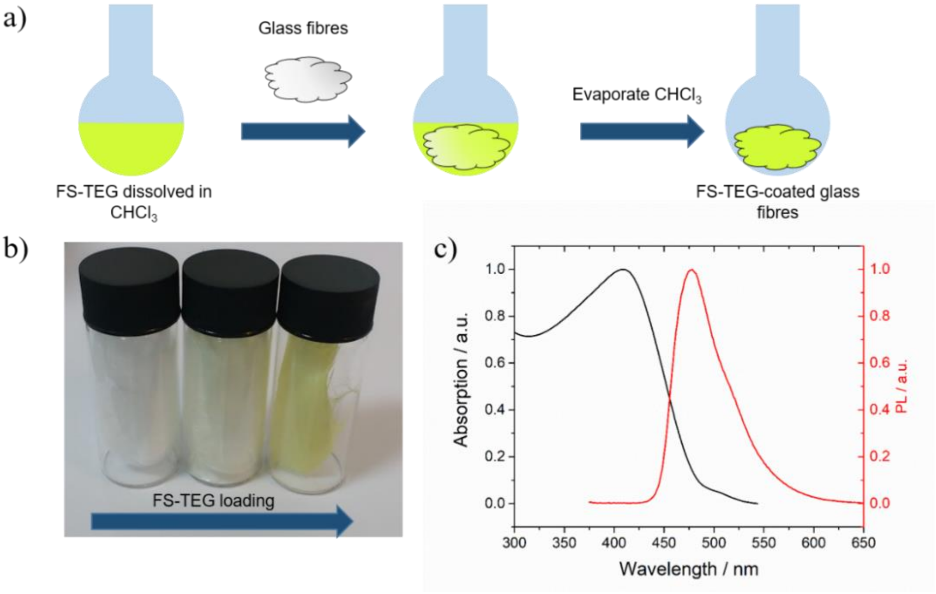

Figure 3.32. a) Schematic illustration of the method of fabrication of **FS-TEG**-coated glass fibres**. b)** Image of glass fibres with different **FS-TEG** loadings **c)** UV-vis absorption and PL spectra of the **FS-TEG**-coated glass fibres (λ_{exc} = 360 nm).

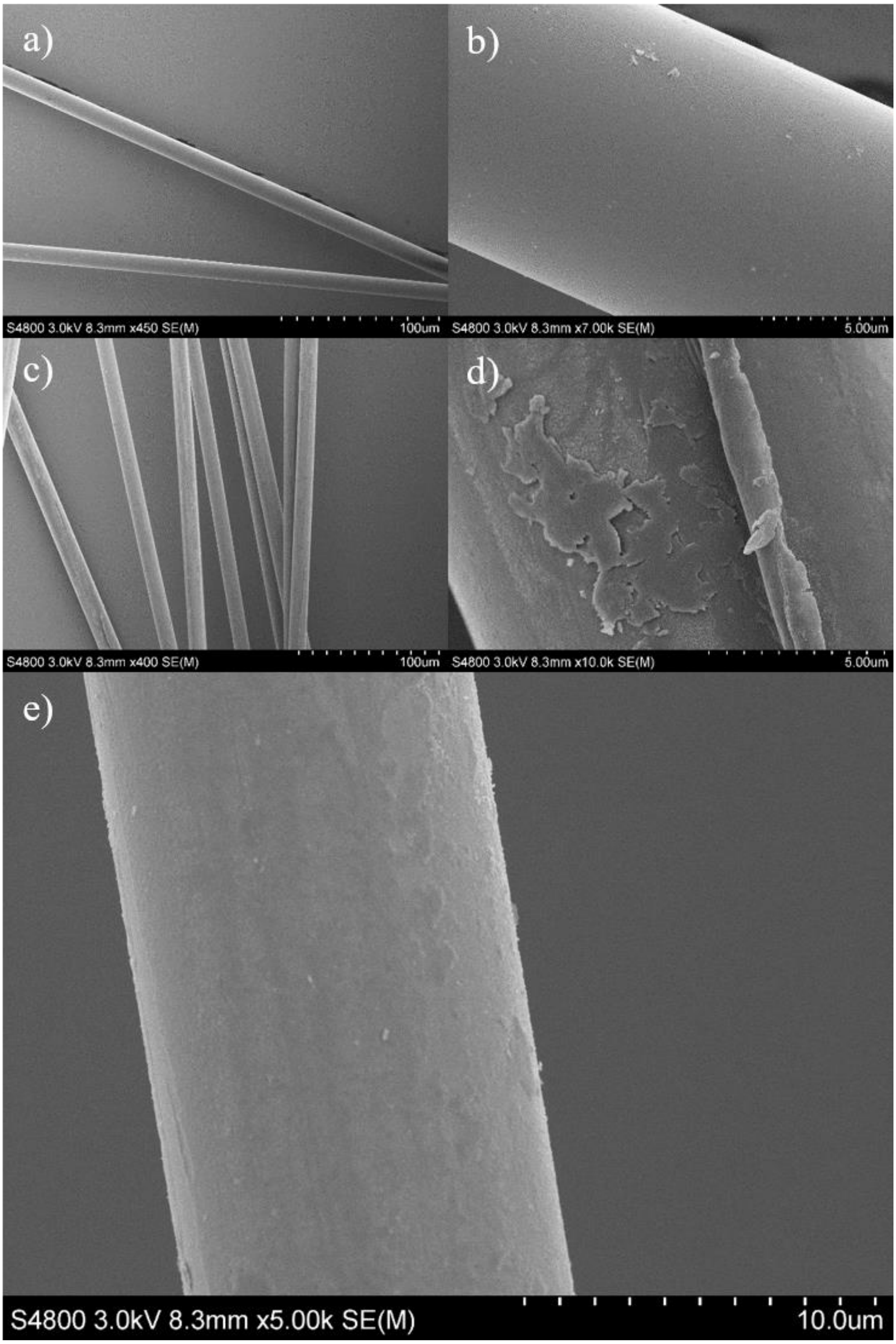

Figure 3.33. SEM images of glass fibres (**a** and **b**) and **FS-TEG**-coated glass fibres (**c**, **d** and **e**) at different magnifications.

3.4.12.2 Photocatalysis Experiments

3.4.12.2.1 Laboratory Experiments

FS-TEG-coated glass fibres (40.8 mg **FS-TEG** on 0.4473 g glass fibres) were placed in 5 vol. % TEA under visible light irradiation for 5 hours giving an initial HER of 30 mmol m^{-2} h^{-1} (**Figure 3.34**). The observed rate is higher than any achieved on planar substrates but 40.8 mg of polymer was used to coat the glass fibres. The mass- and area-normalised rate (750 mmol m^{-2} g^{-1} h^{-1}) is actually lower than that achieved on roughened glass slides.[c] A cuvette with a depth of 1 cm was used for these experiments which was completely filled with the coated glass fibres. A lack of light penetration through the fibres may negate the potentially increased macroscopic surface area of this support. Furthermore, some hydrogen evolution (1.3 mmol m^{-2} h^{-1}, < 5% of the original rate) was observed when the fibres were removed from the solution suggesting some delamination of the polymer from the glass fibres took place during photocatalysis.

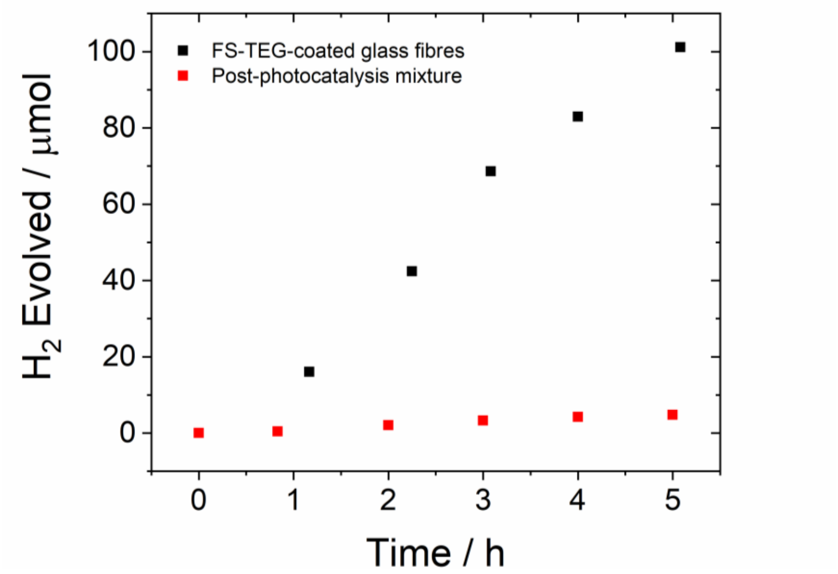

Figure 3.34. Hydrogen evolution of **FS-TEG**-coated glass fibres submerged in 5 vol. % TEA under visible light irradiation (black symbols) and residual hydrogen evolution of the solution containing delaminated polymer following removal of the glass slide and degassing with nitrogen (red symbols). A 300 W Xe light source was used in both cases.

---

[c] A maximum of 3 mg of polymer was spin-coated on roughened glass slides (with some expected to have been lost during spin-coating), giving a normalised rate of 970 mmol m^{-2} g^{-1} h^{-1}

Extended hydrogen evolution runs were performed using cleaned glass fibres. 330 µmol of hydrogen were evolved over 91 hours (**Figure 3.35a**). The HER was highest initially (17.0 ± 0.6 mmol m^{-2} h^{-1}) before the rate of hydrogen evolution slowed. Interestingly, the rate of hydrogen evolution from 20 to 91 hours also appears to be linear (3.38 ± 0.06 mmol m^{-2} h^{-1}), unlike the gradual drop off in performance previously observed in films and powders.

Submerging **FS-TEG**-coated glass fibres in 5 vol. % TEA mixture overnight prior to photocatalysis resulted in a HER similar to the region after 20 hours in the previous plot (3.69 ± 0.07 mmol m^{-2} h^{-1}, **Figure 3.35b**). The initial interaction between fibres and aqueous mixture seemingly leads to a higher rate of hydrogen evolution. Photocatalysis was also carried out using an inorganic scavenger mixture, Na_2S / Na_2SO_3 (0.35/0.25 M), giving a HER that was linear but low (239 ± 3 µmol m^{-2} h^{-1}, **Figure 3.35c**).

The extended hydrogen evolution experiments performed here suggest good long-term stability of polymer-coated glass fibres. The scalability of fabrication of these polymer-coated glass fibres also compares favourably to films, for which scale-up usually requires complex roll-to-roll techniques.[86] This ability to easily cover large areas, coupled with the durability displayed in this chapter, encouraged scaled-up experiments to be carried out using natural sunlight to demonstrate the real-world applicability of this technology.

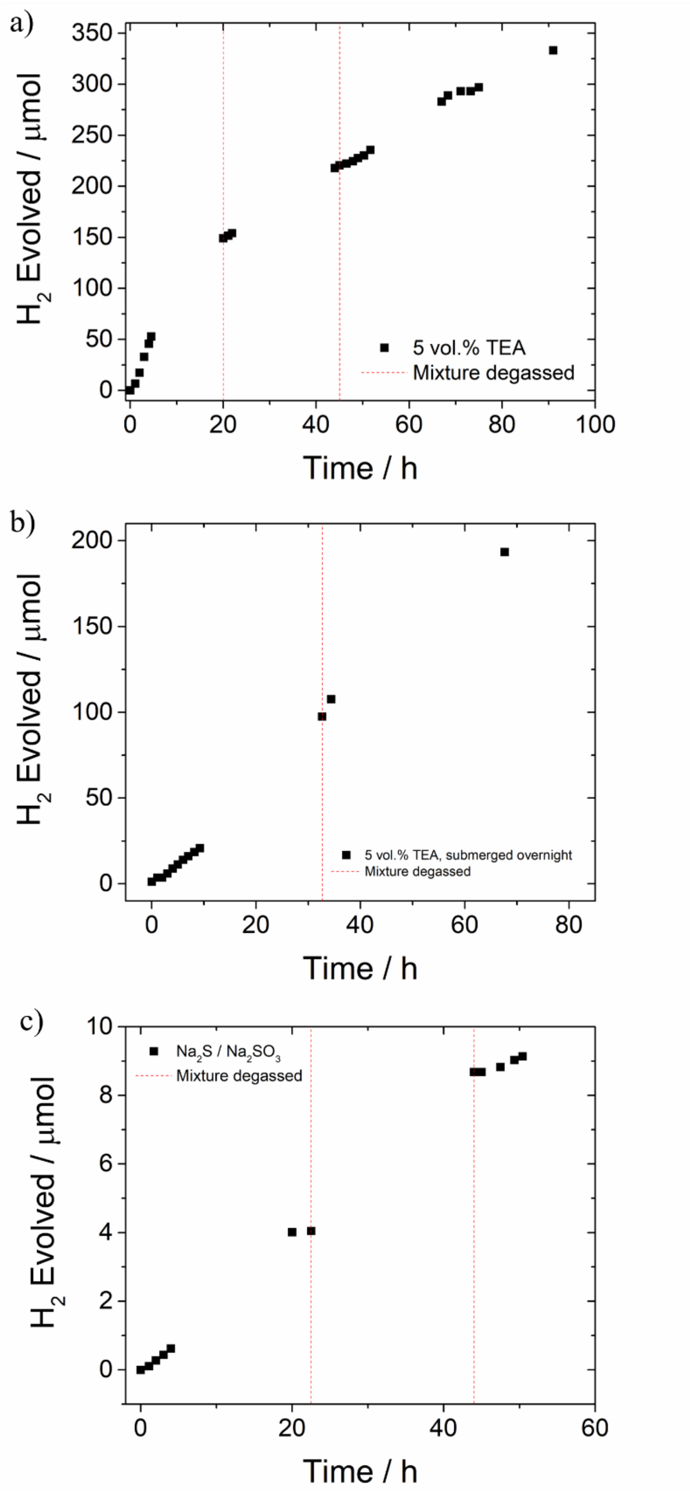

Figure 3.35. a) Hydrogen evolution of **FS-TEG**-coated glass fibres under visible light irradiation using a 300 W Xe light source (black symbols) with intermittent degassing with nitrogen (dashed red lines). The glass fibres were submerged in **a)** 5 vol. % TEA. **b)** 5 vol. %TEA overnight before photocatalysis and **c)** Na_2S / Na_2SO_3 (0.35/0.25 M).

3.4.12.2.2 Scaled-up Photoreactor

The majority of investigations in the field have been conducted on a laboratory scale using artificial light. However, some investigations have focused on achieving scaled-up hydrogen production in more representative environments.[3,21,87,88] Recently, a Cu/TiO_2 catalyst was studied for hydrogen production on a larger scale using waste streams as sacrificial electron donors.[87] Inorganic systems capable of overall water splitting have been produced on a 1 m^2 scale with reasonable stability over 1000 hours of usage under simulated sunlight.[21] Similarly, a newly developed method of co-catalyst loading enabled production of a 1 m^2 C_3N_4 sheet.[3,88] This set-up evolved over 18 L of hydrogen over the course of a month outdoors and represents the only example of representative scaled-up hydrogen production from organic materials to date.

An initial test found hydrogen evolution could be achieved using natural sunlight by placing a small-scale prototype in a window (**Figure 3.36a**). This set-up produced over 140 μmol of hydrogen over the course of a weekend of intermittent sunlight (**Figure 3.36b**).

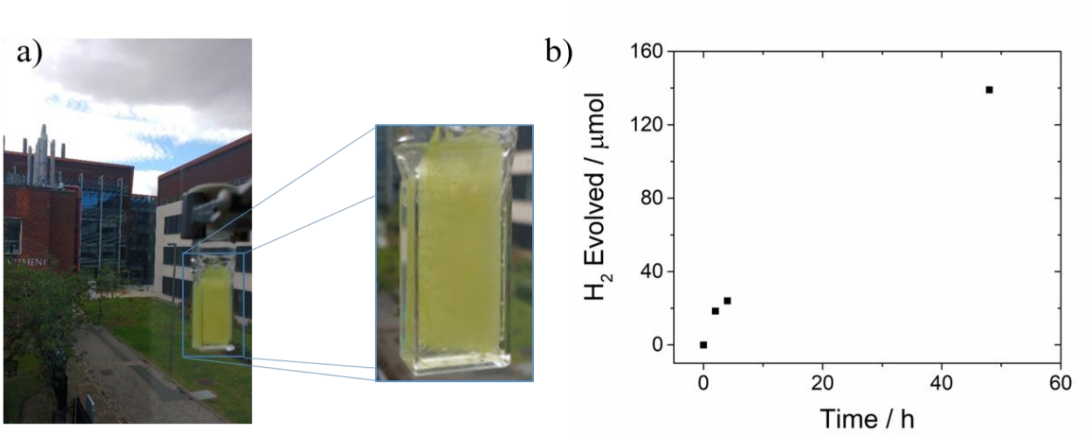

Figure 3.36. a) Image of **FS-TEG**-coated glass fibres submerged in 5 vol. % TEA in the window at the University of Liverpool with zoomed-in image showing hydrogen bubbles formed on the fibres' surface. **b)** Hydrogen evolution of this set-up over the course of 50 hours of a weekend in August 2017.

A scaled-up photoreactor for use under natural light irradiation was subsequently built (**Figure 3.37a**). The photoreactor consists of free-standing polymer-coated glass fibres in a 1 L measuring cylinder filled with 5 vol. % TEA, placed opposite a solar reflector to maximise light harvesting (**Figure 3.37b**). A tube from the top of the cylinder containing polymer-coated glass fibres connected this vessel to an upturned measuring cylinder submerged in water (**Figure 3.37c**), which enabled the amount of hydrogen evolved to be estimated by measuring the volume of water displaced over time.

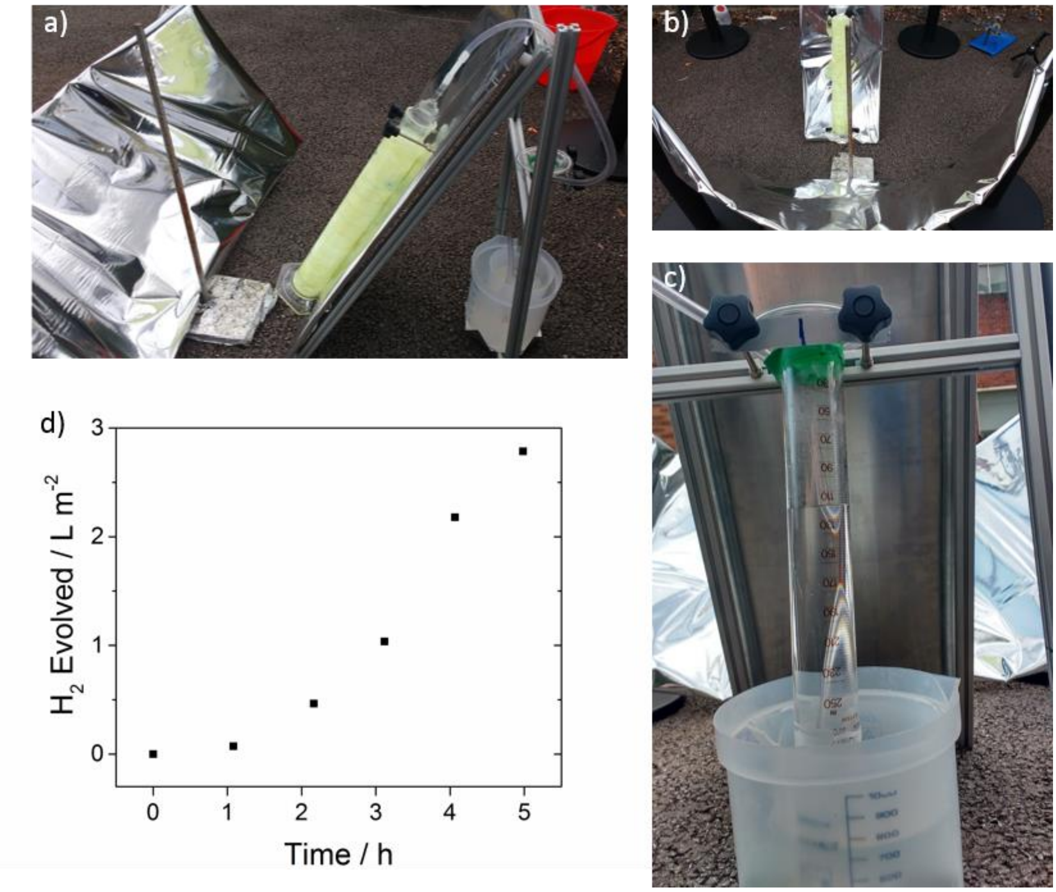

Figure 3.37. **a)** Side-view of photoreactor set-up with reflective panel and **FS-TEG**-coated glass fibres submerged in 5 vol. % TEA connected to a hydrogen collection vessel. **b)** Front view of photoreactor set-up. **c)** Back view of hydrogen collection vessel. **d)** Amount of hydrogen evolved over a 5 hour period on a largely overcast day normalised to the area of glass fibres irradiated.

This set-up enabled 165 mg of polymer to evolve 78 mL of hydrogen over 5 hours on a partially cloudy day at a rate of 0.94 L m^{-2} h^{-1} after an initial induction period (**Figure 3.37d**). This rate is higher than that achieved by the aforementioned C_3N_4 photoreactor (0.1 L m^{-2} h^{-1}) [3] although it should be noted this experiment was conducted over a much shorter timescale. The rate of hydrogen evolution from this set-up is expected to drop off as previously seen in smaller scale experiments. The durability of this photoreactor was therefore studied using a more consistent solar simulator light source.

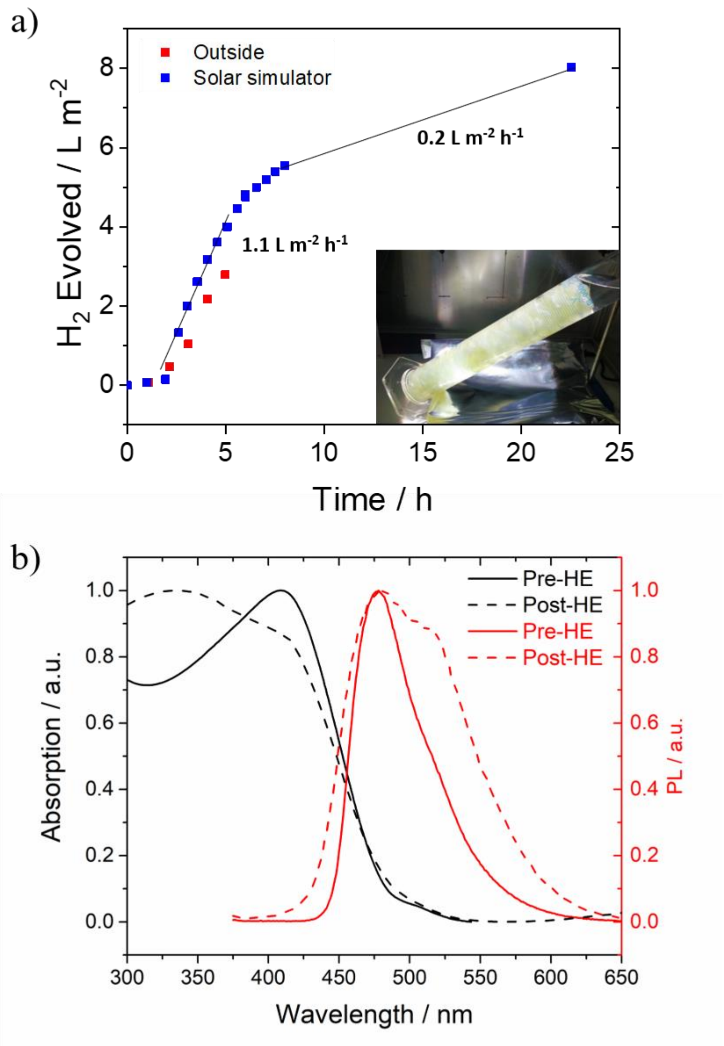

Figure 3.38. a) Hydrogen evolution of **FS-TEG**-coated glass fibres submerged in 5 vol. % TEA outdoors (red symbols) and under irradiation by a solar simulator (AM1.5G, blue symbols). **b)** UV-vis absorption and PL spectra of the **FS-TEG**-coated glass fibres before (Pre-HE) and after (Post-HE) both runs were performed (λ_{exc} = 360 nm).

Hydrogen evolution from the photoreactor under simulated sunlight showed good agreement with the experiment conducted outdoors (**Figure 3.38a**). A slightly higher initial HER was seen in the laboratory experiment (1.11 vs. 0.94 L m^{-2} h^{-1}). As expected, the HER tailed off with extended irradiation times to give a rate of 0.2 L m^{-2} h^{-1}. This was accompanied by blue-shifted absorption and green-shifted emission, as previously seen in **FS-TEG** films (**Figure 3.38b**). The long-term performance of this photoreactor should therefore be improved, possibly using some of the strategies outlined in **Chapter 3.3.4**, although this study constitutes a useful demonstration of the scalability of this processing method.

3.5 Free-Standing Polymer Films

Depositing films on planar substrates inevitably reduces contact of the photocatalyst with the aqueous medium. Processing polymers into free-standing films would avoid these performance losses. A free-standing film of **FS-TEG** was formed during the filtration step following precipitation of the polymer in methanol. **FS-TEG** forms a slurry in this step that, upon drying, forms a film on the filter paper. A portion of this film (10.54 mg) was removed and irradiated by visible light in a 5 vol. % TEA mixture. The free-standing film exhibited remarkable stability in evolving 881 µmol of hydrogen over 141 hours (**Figure 3.39a**). Replacing the 5 vol. % TEA solution was found to completely recover activity (**Figure 3. 39b**).

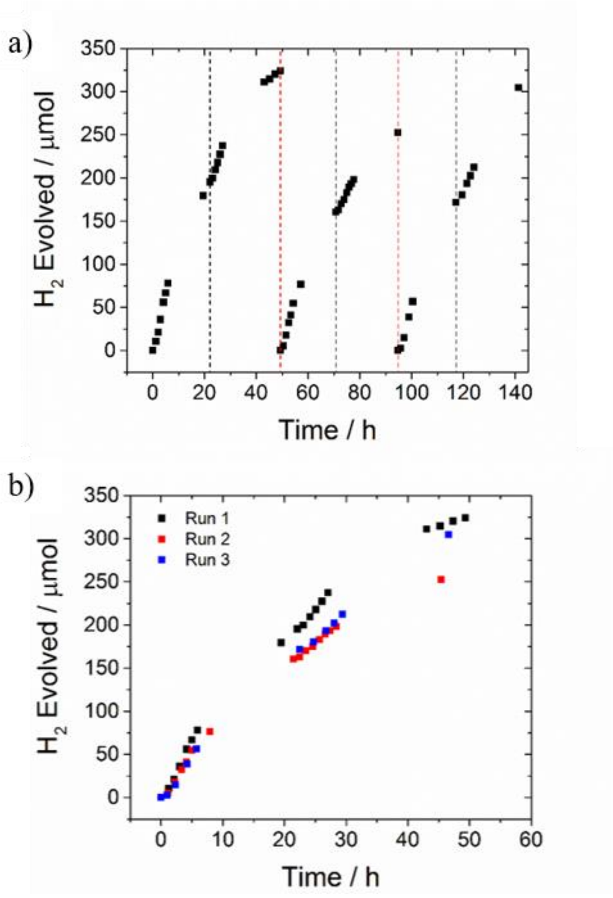

Figure 3.39. a) Hydrogen evolution of free-standing **FS-TEG** film submerged in 5 vol. % TEA under visible light irradiation using a 300 W Xe light source with intermittent degassing with nitrogen (dashed black lines) and replacement of 5 vol. % TEA (dashed red lines). **b)** Direct comparison of amount of hydrogen evolved initially (Run 1) and after the 5 vol. % TEA was replaced for the first (Run 2) and second (Run 3) times.

The free-standing film appeared unchanged after this extended photocatalysis run, with no visible signs of disintegration (**Figure 3.40a**). The absorption on-set does not appear to be dramatically shifted after photocatalysis (**Figure 3.40b**). Furthermore, there was no apparent change in the PL spectrum of the film (λ_{em} = 525 and 527 nm for Pre-HE and Post-HE samples). This thick free-standing film appears to be the most photocatalytically stable form of **FS-TEG** seen in this thesis which, when viewed alongside the poor stability of thin films and nanoparticles, suggests formation of thick films and large particles may be necessary to achieve photocatalytic durability. More precisely-controlled formation of free-standing structures is desirable in future investigations.

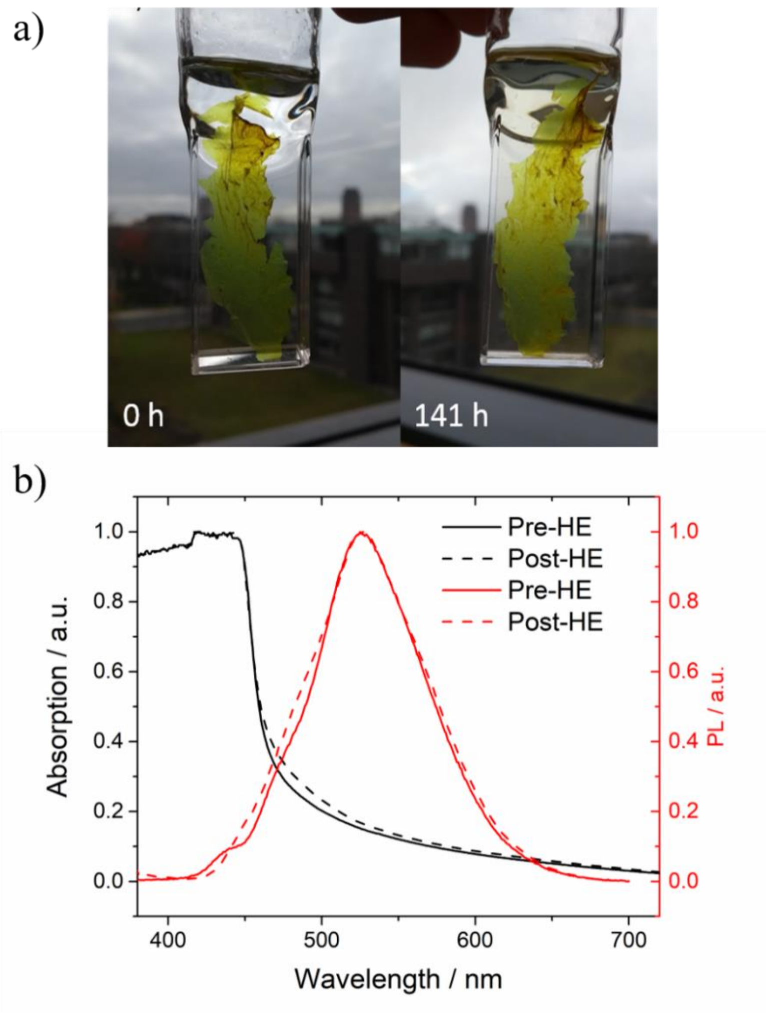

Figure 3.40. a) Hydrogen evolution of free-standing **FS-TEG** film submerged in 5 vol. % before and after the photocatalytic run (141 hours). **b)** UV-vis absorption and PL spectra of the free-standing **FS-TEG** film before (Pre-HE) and after (Post-HE) both runs were performed (λ_{exc} = 360 nm).

3.6 Conclusions

The present chapter attempted to explore the wealth of processing methods enabled by solution-processability and reveals that, when considering processing methods, durability should be considered as well as relative areal performances.

Nanoparticles initially appeared to suffer from aggregation and degradation. Activity and stability were improved with the use of L-ascorbic acid as a hole scavenger, although long-term performance, expected to be an Achilles' heel of nanoparticles, was not extensively studied. Nevertheless, the formation of nanoparticles that are stable in water opens up the possibility of aqueous printing methods. Aqueous printing is considered safer and more sustainable than printing with organic solvents[89] and could enable the fabrication of composite systems with aqueous-compatible inorganic materials.

Immobilised photocatalytic films are gaining some traction within the field.[24,42] Deposition on OTS-functionalised glass slides enabled optimum film thickness to be determined and performance could be boosted by stacking these slides in parallel. However, long-term stability remains a significant obstacle to application of thin films. Processing small amounts of polymer into forms that maximise their performance appears to reduce the longevity of performance of these materials. The loss of activity, seemingly at least partially due to photobleaching, should be more thoroughly addressed in future studies using some of the strategies outlined in **Chapter 3.4.5**. On the other hand, thicker films, both free-standing and immobilised, had high areal performance and displayed good durability. Meanwhile, glass fibres enabled the construction of a technologically simple photoreactor on a larger scale.

Of course, as these polymers are not capable of overall water splitting, a situation where a polymer is cast on a substrate in isolation currently seems unlikely. Instead, composite structures in which a hydrogen-evolving polymer is combined with, for example, an oxygen-evolving metal oxide, may be required. In these circumstances an insoluble component of the composite may become the *de facto* substrate. The ability of these solution-processable polymers to form heterostructures with other photocatalytic materials will therefore be investigated in **Chapter 4**.

3.7 Experimental

The majority of characterisation methods used in this chapter were outlined in **Chapter 2**. When not previously used, equipment and methods used will be outlined in the relevant sections. Photocatalysis experiments were performed using the same equipment in **Chapter 2**. The majority of experiments were performed in quartz cuvettes (10mm × 20mm with a B24 cone, obtained from Starna Scientific), sealed with a septum and containing 8 mL of 5 vol. % TEA in water unless otherwise stated.

3.7.1 Nanoparticles

The nanoparticle preparation procedure was based on a previously reported method.[13] **FS-TEG** (4.96 mg) was dissolved in THF (50 mL) with overnight stirring. 8 mL of the resultant solution was injected rapidly into water (40 mL) with sonication before evaporation of THF (and some water). The solution was made back up to 40 mL with deionised water and filtered through a nylon syringe filter (25 mm, 0.45 µm pore size). Dynamic light scattering measurements were performed on a Malvern Zetasizer Nano Particle Sizer, at 25 °C. Hydrogen evolution experiments were performed using 5 vol. % TEA or L-ascorbic acid.

3.7.2 Deposition on Supports

For film samples, glass substrates (microscope Slides, 26 × 16mm, white glass obtained from G & N Laboratory) were first prepared for polymer deposition using the methods stated below. The quartz cuvette was charged with water containing 5 vol. % TEA (8 mL) before immersion of the polymer-coated slide, sealing with a septum and degassing for 15 minutes. Glass slides were stood in a PTFE support, specially produced by Sensor City, Liverpool, which did not evolve hydrogen on its own. Rates are normalised to the area of polymer irradiated.

3.7.2.1 Mesoporous Substrates

The **P8-s** film was prepared on a fluorine-doped tin oxide (FTO)/SnO_2 support which was prepared as follows. FTO slides were cleaned by sonication in ethanol for 20 minutes, and then allowed to dry at room temperature. A suspension of 20% w/v of SnO_2 nanopowder in 5 M acetic acid in ethanol was prepared by sonication for 20 min. The FTO slides were taped down with Scotch tape (conducting face up), to make a square shaped well for 10 µl of SnO_2 suspension to be deposited evenly across the surface. The SnO_2 film was left to dry at room temperature for 10 min before carefully removing the Scotch tape. The films were then heated in an oven to 350 °C (ramped at 4 °C min^{-1}), and held for 20 min before cooling. Once the film was cooled, silicone was applied around the edges of the exposed face of the slide and left to dry. **P8-s** was subsequently drop-cast from chloroform (1 mg ml^{-1}) on the SnO_2 surface and the resultant film allowed drying to yield a cast film of **P8-s** (0.34 mg). The slide was immersed in a quartz cuvette charged with the water (3 mL), triethylamine (3 mL), methanol (3 mL), and sealed with a septum. The reaction mixture was illuminated with a 300 W Newport Xe light-source and the evolved hydrogen was detected as for the powder suspension measurements. The film thickness was determined using an Ambios Technology XP200 profilometer. The thickness of **P8-s**/SnO_2 on FTO was measured to be 1370 ± 60 nm. The polymer **P8-s** was then removed by dissolving overnight in chloroform before the thickness of the remaining SnO_2 film was obtained by scratching across the surface with a blade three times, and measuring the height relative to these scratches (773 ± 8 nm). This gave an estimated thickness of 600 ± 100 nm for the **P8-s** layer on top of the SnO_2 support, with additional **P8-s** penetrating the SnO_2.

3.7.2.2 Roughened Glass Substrates

Glass slides (Microscope Slides, 26 x 16mm, white glass) were roughened glass substrates were roughened to opacity using sandpaper (P60 grit size) before cleaning by ultrasonication with water, methanol acetone and drying. Polymers were deposited by drop-casting from chloroform solution (3 mg mL^{-1}, 300 µL) unless stated. Wavelength-dependent photocatalysis measurements were performed using $\lambda = 370$, 420, 470 and 520 nm band-pass filters obtained from Edmund Optics.

3.7.2.3 OTS-Functionalised Glass Substrates

Glass slides were functionalised with OTS by spin-coating from 1,1,2-trichloroethylene (TCE) using a literature method.[39] Successful functionalisation was confirmed by observation of large contact angles ($\theta \approx 90°$) of the functionalised slides with water. Polymers were coated onto the OTS-functionalised slide by spin-coating solutions of chloroform (300 µL) of specified concentration at 3000 rpm for 60 s before annealing at 80 °C for two hours, unless stated. Film thicknesses were measured by AFM and Profilometry. All AFM images were taken on an Asylum Research Cypher-ES instrument. Dry thickness measurements were taken by imaging across a razor blade scratch in tapping mode using 75 kHz HQ:NSC18/Pt tips (MikroMasch).

Stacking experiments: The PTFE rack was found not to evolve hydrogen when irradiated under these sacrificial conditions.

Annealing experiments: Annealing was performed in a vacuum oven, with vacuum applied when specified. Quenching in methanol/dry ice baths was performed when specified by submersion of the polymer-coated slides immediately after removal from the oven.

Polymer blends: 300 µL of a 1:1 solution of **FS-TEG** and **FS-TEG** (1.5 mg of each polymer in 1 mL chloroform) was spin-coated on an OTS-functionalised glass substrate.

Incorporation of dyes:

Wavelength-dependent hydrogen evolution experiments: FS-TEG powder (10.2 mg) and an **FS-TEG** film spin-coated from 20 mg mL^{-1} chloroform solution on roughened glass were submerged in 5 vol. % TEA (8 mL) and irradiated with a 300 W Xe light source using various wavelength filters. Rates are normalised to the output of the light when using each filter, taken as an average of three locations on the irradiated sample.

High throughput screening: Organic-soluble dyes were obtained from FastColours LLP. **FS-TEG** (2.5 mg) was accurately weighed into vials. Dye solutions that would result in 5 wt. % of dye relative to the polymer were prepared initially and diluted down to achieve various concentrations (0.2, 1, 2 and 2 wt. %). 500 µL of these solutions were added to the weighed polymers and the solutions were gently heated to fully dissolve the polymer, before being allowed to evaporate overnight. The high throughput screening was then performed in 5 vol. % TEA solutions using the apparatus described in **Chapter 2.8**.

LS-1 incorporation: The potentials asoociated with the ground and excited state of **LS-1** were calculated using a previously outlined (TD-)DFT method.[24] Briefly, the

B3LYP density functional was used, together with the Def2-SVP basis set, using the Gaussian 16 software. S1 optimizations for the calculations of the exciton potentials (i.e., IP* and EA*) used the Tamm–Dancoff approximation as this is more robust than full TD-DFT away from the ground-state geometry. These were compared to the experimentally obtained potentials obtained for **FS-TEG** in **Chapter 2**. **LS-1** was obtained from ECUST. For the film preparation procedure, three 0.5 mL aliquots of **FS-TEG** dissolved in chloroform (6 mg mL^{-1}) were placed in separate vials. Solutions of **LS-1** dissolved in chloroform (0.5 mL) of appropriate concentrations were then added to produce 3 mg mL^{-1} solutions of **FS-TEG** with 0.1, 0.3 and 1.0 wt. % **LS-1** which were then spin-coated on OTS-functionalised glass substrates using the standard procedure.

Stability testing: Stability of FS-TEG films: Extended photocatalytic runs were performed on **FS-TEG** films spin-coated from chloroform (3 mg mL^{-1}, 300 µL). **Singlet oxygen scavengers: FS-TEG** (2.66 mg) and Ni(dtc)$_2$ (0.27 mg) were dissolved in chloroform (0.96 mL). 300 µL of this solution was spin-coated on an OTS-functionalised glass substrate. **Stability of polymers with modified bridgehead atoms:** Films of **FS-Oct**, **SiS-Oct**, **GeS-Oct** and **CzS-Oct** were prepared by drop-casting from chloroform (1 mg mL^{-1}, 300 µL) on roughened glass slides.

3.7.2.4 Glass Fibres

Karl Hecht glass fibres (45 g, obtained from LabUnlimited, textile glass fibres with a nominal diameter of 8 – 50 µm) were used in all experiments.

Laboratory experiments: Glass fibres (0.4473 g) were placed in a solution of **FS-TEG** in chloroform (40.8 mg in 20 mL) and the solution was allowed to evaporate. The polymer-coated glass fibres were then placed in the quartz cuvette and photocatalysis experiments were performed as previously, using enough 5 vol. % TEA solution to cover the polymer-coated fibres. For the extended photocatalysis runs, **FS-TEG** deposited from chloroform (5 mL, 1 mg mL^{-1}) on glass fibres. Equivalent methods were used with the following deviations: **Figure 3.35a**: Glass fibres (0.5260 g) were used that had been etched with piranha solution using a literature procedure.[36] **Figure 3.35b**: Glass fibres (0.7321 g) were coated with **FS-TEG** were placed in 5 vol. % TEA overnight prior to photocatalysis. **Figure 3.35c:** Polymer cast on glass fibres (0.3065 g) as previously although Na_2S / Na_2SO_3 (0.35/0.25 M) was used as the scavenging mixture in this case.

Scaled-up photoreactor: The photoreactor comprised a chamber containing polymer-coated glass wool suspended in 5 vol. % TEA in water which was connected by tubing to an upturned measuring cylinder filled with water to measure the volume of evolved hydrogen. Glass fibres (45 g) were coated with **FS-TEG** (165 mg) by evaporation from chloroform. The polymer-coated glass fibers were then submerged in 950 mL of 5 vol. % TEA in the photoreactor chamber before the set-up was sealed. The volume of evolved hydrogen was measured hourly on a partially cloudy August afternoon in Liverpool, UK. The photoreactor was then placed under a solar simulator for 24 hours before characterisation.

3.7.3 Free-Standing Polymer Films

A free-standing film of **FS-TEG** (10.54 mg) obtained from filtration, as described in **Chapter 3.5**, was tested for hydrogen evolution in the standard conditions.

3.8 References

1 B. A. Miller-Chou and J. L. Koenig, *Prog. Polym. Sci.*, 2003, **28**, 1223–1270.

2 M. Schwarze, D. Stellmach, M. Schröder, K. Kailasam, R. Reske, A. Thomas and R. Schomäcker, *Phys. Chem. Chem. Phys.*, 2013, **15**, 3466.

3 M. Schröder, K. Kailasam, J. Borgmeyer, M. Neumann, A. Thomas, R. Schomäcker and M. Schwarze, *Energy Technol.*, 2015, **3**, 1014–1017.

4 H. A. Khan, M. K. Sakharkar, A. Nayak, U. Kishore and A. Khan, *Nanoparticles for biomedical applications: An overview*, Elsevier Ltd., 2017.

5 Y. Tamai, H. Ohkita, H. Benten and S. Ito, *J. Phys. Chem. Lett.*, 2015, **6**, 3417–3428.

6 J. Li and N. Wu, *Catal. Sci. Technol.*, 2015, **5**, 1360–1384.

7 R. Abe, *J. Photochem. Photobiol. C Photochem. Rev.*, 2010, **11**, 179–209.

8 K. Maeda, K. Teramura, D. Lu, N. Saito, Y. Inoue and K. Domen, *Angew. Chemie - Int. Ed.*, 2006, **45**, 7806–7809.

9 C. M. Aitchison, R. S. Sprick and A. I. Cooper, *J. Mater. Chem. A*, 2019, **7**, 37–39.

10 G. Zhang, Z.-A. Lan, L. Lin, S. Lin and X. Wang, *Chem. Sci.*, 2016, **7**, 3062–3066.

11 P. B. Pati, G. Damas, L. Tian, D. Fernandes, L. Zhang, I. B. Pehlivan, T. Edvinsson, C. M. Araujo and H. Tian, *Energy Environ. Sci.*, 2017, **10**, 1372–1376.

12 A. Liu, C.-W. Tai, K. Holà and H. Tian, *J. Mater. Chem. A*, 2019, **7**, 4797–4803.

13 J. M. Behrendt, Y. Wang, H. Willcock, L. Wall, M. C. McCairn, R. K. O'Reilly and M. L. Turner, *Polym. Chem.*, 2013, **4**, 1333–1336.

14 W. C. Tsoi, A. Charas, A. J. Cadby, G. Khalil, A. M. Adawi, A. Iraqi, B. Hunt, J. Morgado and D. G. Lidzey, *Adv. Funct. Mater.*, 2008, **18**, 600–606.

15 A. Vogel, M. Forster, L. Wilbraham, C. Smith, A. Cowan, M. Zwijnenburg, R. S. S. Sprick and A. Cooper, *Faraday Discuss.*, 2019, **215**, 84–97.

16 B. Muthuraj, S. Mukherjee, C. R. Patra and P. K. Iyer, *ACS Appl. Mater. Interfaces*, 2016, **8**, 32220–32229.

17 B. U. Scherf and E. J. W. List, *Adv. Mater.*, 2002, **14**, 477–487.

18 X. H. Zhou, Y. Zhang, Y. Q. Xie, Y. Cao and J. Pei, *Macromolecules*, 2006, **39**, 3830–3840.

19 Y. C. Sung, A. C. Grimsdale, D. J. Jones, S. E. Watkins and A. B. Holmes, *J. Am. Chem. Soc.*, 2007, **129**, 11910–11911.

20 P. Brenner, L. M. Fleig, X. Liu, A. Welle, S. Bräse and U. Lemmer, *J. Polym. Sci. Part B Polym. Phys.*, 2015, **53**, 1029–1034.

21 Y. Goto, T. Hisatomi, Q. Wang, T. Higashi, K. Ishikiriyama, T. Maeda, Y. Sakata, S. Okunaka, H. Tokudome, M. Katayama, S. Akiyama, H. Nishiyama, Y. Inoue, T. Takewaki, T. Setoyama, T. Minegishi, T. Takata, T. Yamada and K. Domen, *Joule*, 2018, **2**, 509–520.

22 T. Hisatomi and K. Domen, *Nat. Catal.*, 2019, **2**, 387–399.

23 T. Takata and K. Domen, *ACS Energy Lett.*, 2019, **4**, 542–549.

24 X. Wang, L. Chen, S. Y. Chong, M. A. Little, Y. Wu, W.-H. Zhu, R. Clowes, Y. Yan, M. A. Zwijnenburg, R. Sebastian Sprick and A. I. Cooper, *Nat. Chem.*, 2018, **10**, 1180.

25 M. Schröder, K. Kailasam, J. Borgmeyer, M. Neumann, A. Thomas, R. Schomäcker and M. Schwarze, *Energy Technol.*, 2015, **3**, 1014–1017.

26 A. Xiong, G. Ma, K. Maeda, T. Takata, T. Hisatomi, T. Setoyama, J. Kubota and K. Domen, *Catal. Sci. Technol.*, 2014, **4**, 325–328.

27 G. Balasubramanian, D. D. Dionysiou, M. T. Suidan, I. Baudin and J. M. Laîné, *Appl. Catal. B Environ.*, 2004, **47**, 73–84.

28 J. Hou, X. Hou, Y. Tong, J. Liang, J. Feng, J. Li and L. Wang, *Sustain. Mater. Technol.*, 2018, **19**, e00089.

29 M. Addamo, V. Augugliaro, A. Di Paola, E. García-López, V. Loddo, G. Marcì and L. Palmisano, *Thin Solid Films*, 2008, **516**, 3802–3807.

30 M. Li, K. Gao, X. Wan, Q. Zhang, B. Kan, R. Xia, F. Liu, X. Yang, H. Feng, W. Ni, Y. Wang, J. Peng, H. Zhang, Z. Liang, H. L. Yip, X. Peng, Y. Cao and Y. Chen, *Nat. Photonics*, 2017, **11**, 85–90.

31 C. T. Bolger, R. A. Farrell, G. M. Hughes, M. A. Morris, N. Petkov and J. D. Holmes, *ACS Nano*, 2009, **3**, 2311–2319.

32 S. Park, S. H. Ahn, H. J. Lee, U. S. Chung, J. H. Kim and W. G. Koh, *RSC Adv.*, 2013, **3**, 23673–23680.

33 Y. Liu, Q. Gan, S. Baig and E. Smela, *J. Phys. Chem. C*, 2007, **111**, 11329–11338.

34 N. Allard, R. B. Aïch, D. Gendron, P. L. T. Boudreault, C. Tessier, S. Alem, S. C. Tse, Y. Tao and M. Leclerc, *Macromolecules*, 2010, **43**, 2328–2333.

35 R. S. Sprick, M. Hoyos, J. J. Morrison, I. M. Grace, C. Lambert, O. Navarro and M. L. Turner, *J. Mater. Chem. C*, 2013, **1**, 3327–3336.

36 Z. Li and R. H. Yoon, *J. Colloid Interface Sci.*, 2013, **392**, 369–375.

37 Y. Ito, A. A. Virkar, S. Mannsfeld, H. O. Joon, M. Toney, J. Locklin and Z. Bao, *J. Am. Chem. Soc.*, 2009, **131**, 9396–9404.

38 Y. R. Liu, P. T. Lai, R. H. Yao and L. F. Deng, *IEEE Trans. Device Mater. Reliab.*, 2011, **11**, 60–65.

39 R. S. Sprick, M. Hoyos, M. S. Wrackmeyer, A. V. Sheridan Parry, I. M. Grace, C. Lambert, O. Navarro and M. L. Turner, *J. Mater. Chem. C*, 2014, **2**, 6520–6528.

40 E. F. Manley, J. Strzalka, T. J. Fauvell, T. J. Marks and L. X. Chen, *Adv. Energy Mater.*, 2018, **8**, 1800611.

41 L. Krapf, M. Dezi, W. Reichstein, J. Köhler and S. Oellerich, *Colloids Surfaces B Biointerfaces*, 2011, **82**, 25–32.

42 N. Nalajala, K. K. Patra, P. A. Bharad and C. S. Gopinath, *RSC Adv.*, 2019, **9**, 6094–6100.

43 W. X. Xianyu, M. K. Park and W. I. Lee, *Korean J. Chem. Eng.*, 2001, **18**, 903–907.

44 C. Y. Wu, Y. L. Lee, Y. S. Lo, C. J. Lin and C. H. Wu, *Appl. Surf. Sci.*, 2013, **280**, 737–744.

45 V. Subramanian, E. E. Wolf and P. V Kamat, *Langmuir*, 2003, **19**, 469–474.

46 A. R. Malagutti, H. A. J. L. Mourão, J. R. Garbin and C. Ribeiro, *Appl. Catal. B Environ.*, 2009, **90**, 205–212.

47 K. J. Kumar, N. R. C. Raju and A. Subrahmanyam, *Appl. Surf. Sci.*, 2011, **257**, 3075–3080.

48 S. Shoaee, M. Stolterfoht and D. Neher, *Adv. Energy Mater.*, 2018, **8**, 1703355.

49 P. Guiglion, C. Butchosa and M. A. Zwijnenburg, *Macromol. Chem. Phys.*, 2016, **217**, 344–353.

50 O. V. Mikhnenko, H. Azimi, M. Scharber, M. Morana, P. W. M. Blom and M. A. Loi, *Energy Environ. Sci.*, 2012, **5**, 6960–6965.

51 A. Bruno, L. X. Reynolds, C. Dyer-Smith, J. Nelson and S. A. Haque, *J. Phys. Chem. C*, 2013, **117**, 19832–19838.

52 M. T. Sajjad, A. J. Ward, A. Ruseckas, A. K. Bansal, S. Allard, U. Scherf and I. D. W. Samuel, *Phys. Status Solidi - Rapid Res. Lett.*, 2019, **13**, 13–17.

53 J. Yao, C. Yu, Z. Liu, H. Luo, Y. Yang, G. Zhang and D. Zhang, *J. Am. Chem. Soc.*, 2016, **138**, 173−185.

54 Y. Long, G. J. Hedley, A. Ruseckas, M. Chowdhury, T. Roland, L. A. Serrano, G. Cooke and I. D. W. Samuel, *ACS Appl. Mater. Interfaces*, 2017, **9**, 14945–14952.

55 L. Bian, E. Zhu, J. Tang, W. Tang and F. Zhang, *Prog. Polym. Sci.*, 2012, **37**, 1292–1331.

56 T. Nakamura, D. K. Sharma, S. Hirata and M. Vacha, *J. Phys. Chem. C*, 2018, **122**, 8137–8146.

57 G. Zeng, W. L. Yu, S. J. Chua and W. Huang, *Macromolecules*, 2002, **35**, 6907–6914.

58 S. Y. Leblebici, T. L. Chen, P. Olalde-Velasco, W. Yang and B. Ma, *ACS Appl. Mater. Interfaces*, 2013, **5**, 10105–10110.

59 G. Yu, J. Gao, J. C. Hummelen, F. Wudl and A. J. Heeger, *Science (80-.).*, 1995, **270**, 1789–1791.

60 F. Etzold, I. A. Howard, R. Mauer, M. Meister, T. D. Kim, K. S. Lee, N. S. Baek and F. Laquai, *J. Am. Chem. Soc.*, 2011, **133**, 9469–9479.

61 X. Zhang, F. Shen, Z. Hu, Y. Wu, H. Tang, J. Jia, X. Wang, F. Huang and Y. Cao, *ACS Sustain. Chem. Eng.*, 2019, **7**, 4128–4135.

62 C. H. Wu, C. C. Chueh, Y. Y. Xi, H. L. Zhong, G. P. Gao, Z. H. Wang, L. D. Pozzo, T. C. Wen and A. K. Y. Jen, *Adv. Funct. Mater.*, 2015, **25**, 5326–5332.

63 H. C. Liao, C. C. Ho, C. Y. Chang, M. H. Jao, S. B. Darling and W. F. Su, *Mater. Today*, 2013, **16**, 326–336.

64 J. Jo, S. S. Kim, S. I. Na, B. K. Yu and D. Y. Kim, *Adv. Funct. Mater.*, 2009, **19**, 866–874.

65 K. Maeda, *ACS Catal.*, 2013, **3**, 1486–1503.

66 A. Carella, F. Borbone and R. Centore, *Front. Chem.*, 2018, **6**, 1–24.

67 J. Qin, J. Huo, P. Zhang, J. Zeng, T. Wang and H. Zeng, *Nanoscale*, 2016, **8**, 2249–2259.

68 A. Marzec, Z. Boruszczak, J. Rogowski and M. Zaborski, *Polym. Test.*, 2017, **62**, 392–401.

69 A. Marzec, *The effect of dyes, pigments and ionic liquids on the properties of elastomer composites*. Université Claude Bernard - Lyon I, 2014.

70 Y. Litman, H. B. Rodríguez and E. San Román, *Photochem. Photobiol. Sci.*, 2016, **15**, 80–85.

71 W. Zhu, Y. Wu, S. Wang, W. Li, X. Li, J. Chen, Z. S. Wang and H. Tian, *Adv. Funct. Mater.*, 2011, **21**, 756–763.

72 W. Li, Y. Wu, Q. Zhang, H. Tian and W. Zhu, *ACS Appl. Mater. Interfaces*, 2012, **4**, 1822–1830.

73 L. Cabau, L. Pellejà, J. N. Clifford, C. V. Kumar and E. Palomares, *J. Mater. Chem. A*, 2013, **1**, 8994–9000.

74 W. Li, B. Liu, Y. Wu, S. Zhu, Q. Zhang and W. Zhu, *Dye. Pigment.*, 2013, **99**, 176–184.

75 S. Feng, Q. S. Li, P. P. Sun, T. A. Niehaus and Z. S. Li, *ACS Appl. Mater. Interfaces*, 2015, **7**, 22504–22514.

76 F. B. Dias, M. Maiti, S. I. Hintschich and A. P. Monkman, *J. Chem. Phys.*, 2005, **122**, 054904.

77 M. Jørgensen, K. Norrman, S. A. Gevorgyan, T. Tromholt, B. Andreasen and F. C. Krebs, *Adv. Mater.*, 2012, **24**, 580–612.

78 T. L. Andrew and T. M. Swager, *Macromolecules*, 2008, **41**, 8306–8308.

79 M. Salvador, N. Gasparini, J. D. Perea, S. H. Paleti, A. Distler, L. N. Inasaridze, P. Troshin, L. Lüer, H.-J. Egelhaaf and C. J. Brabec, *Energy Environ. Sci.*, 2017, **10**, 2005–2016.

80 F. Caffy, N. Delbosc, P. Chávez, P. Lévêque, J. Faure-Vincent, J. P. Travers, D. Djurado, J. Pécaut, B. Grévin, N. Lemaitre, N. Leclerc and R. Demadrille, *Polym. Chem.*, 2016, **7**, 4160–4175.

81 K. L. Chan, M. J. McKiernan, C. R. Towns and A. B. Holmes, *J. Am. Chem. Soc.*, 2005, **127**, 7662–7663.

82 S. Holze, B. Krüger, T. Hoffmann, A. Bück and M. Schwidder, *Chem. Eng. Technol.*, 2017, **40**, 1084–1091.

83 G. A. Blengini, M. Busto, M. Fantoni and D. Fino, *Waste Manag.*, 2012, **32**, 1000–1008.

84 A. Elhage, B. Wang, N. Marina, M. L. Marin, M. Cruz, A. E. Lanterna and J. T. Scaiano, *Chem. Sci.*, 2018, **9**, 6844–6852.

85 W. Huang, B. C. Ma, D. Wang, Z. J. Wang, R. Li, L. Wang, K. Landfester and K. A. I. Zhang, *J. Mater. Chem. A*, 2017, **5**, 3792.

86 L. Wengeler, M. Schmitt, K. Peters, P. Scharfer and W. Schabel, *Chem. Eng. Process. Process Intensif.*, 2013, **68**, 38–44.

87 M. I. Maldonado, A. López-Martín, G. Colón, J. Peral, J. I. Martínez-Costa and S. Malato, *Appl. Catal. B Environ.*, 2018, **229**, 15–23.

88 M. Schröder, K. Kailasam, S. Rudi, K. Fündling, J. Rieß, M. Lublow, A. Thomas, R. Schomäcker and M. Schwarze, *RSC Adv.*, 2014, **4**, 50017–50026.

89 B. Schmatz, Z. Yuan, A. W. Lang, J. L. Hernandez, E. Reichmanis and J. R. Reynolds, *ACS Cent. Sci.*, 2017, **3**, 961–967.

90 U. Scherf and D. Neher, *Polyfluorene*, Springer-Verlag Berlin Heidelberg, 2008.

91 L. Yao, A. Rahmanudin, N. Guijarro and K. Sivula, *Adv. Energy Mater.*, 2018, **8**, 1802585.

Chapter 4

Forming Heterostructures with Solution-Processable Polymer Photocatalysts

4.1. Contributions to this Chapter

FS-TEG/TiO_2 composites were prepared and characterised by David De Souza. SEM images were captured by Catherine Aitchison. All other work was performed by the thesis author.

4.2. Background

In most cases, photocatalytic performance is at least partially expected to be limited by the lifetimes of charge carriers.[1] Significantly enhanced excited state lifetimes are particularly required to overcome the sluggish kinetics of overall water splitting.[2] The formation of semiconductor heterojunctions can enhance performance by simultaneously broadening the light-harvesting region and suppressing electron-hole recombination. Certain criteria must be met in order to fabricate heterostructures that can enhance photocatalytic rates.

4.2.1. Requirements of Heterostructures

Consideration of band alignment is essential when fabricating semiconductor composites. Different alignments lead to different types of heterostructures, classified as Type I, Type II or Type III composites (**Figure 4.1**).[3] Identification of the heterostructure type is important so that suitable co-catalysts for hydrogen or oxygen evolution can be added to the appropriate components.

In Type I heterostructures, the band edges of a narrow band-gap material are straddled by a wider band-gap material. Electrons and holes are therefore both transferred from the wide band-gap material to the narrow band-gap material. In the context of OWS, this means hydrogen and oxygen evolution would occur on the same material which is not favourable. Type II composites meanwhile possess overlapping offset band structures. In these heterostructures, holes and electrons are directed to different components and so hydrogen and oxygen evolution may be spatially separated. This type is generally considered to be the most suitable type of semiconductor heterojunction for photocatalysis.[1] In Type III heterostructures holes and electrons are also directed to different components but in this case there is no overlap of band structures. Very high driving forces are therefore required for charge transfer and Type III heterostructures have therefore not been widely studied.[4,5]

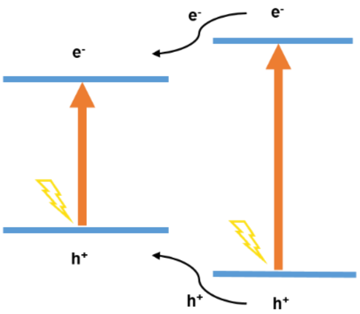

Type I

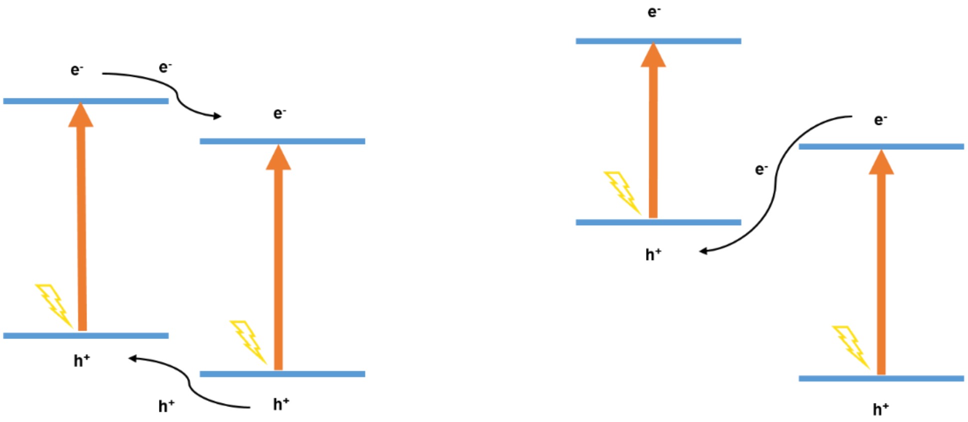

Type II

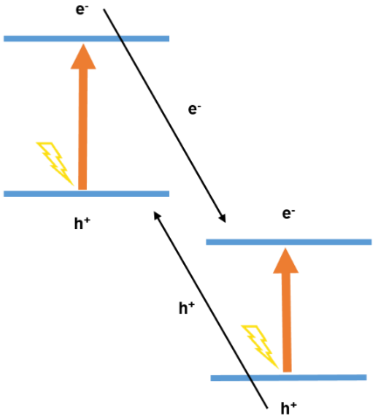

Type III

Figure 4.1. Different types of semiconductor heterojunctions. Excitation of electrons indicated by orange arrows with the direction of flow of electrons and holes indicated by black arrows.

Achieving good interfacial contact between heterojunction components is necessary to achieve efficient charge transfer. At the same time, contact of photocatalysts with the aqueous mixture must be maintained and light-harvesting components should not be prohibitively blocked by coating them with other materials. This can be challenging in complex multi-component systems of materials with poor processability.

The relative success of composites is often measured by comparison of photocatalytic performance with the components in isolation. However, it is important to ensure improved activity is not due to other factors such as altered morphologies of materials in the composite. Deconvoluting these factors is challenging but can be done by conducting control experiments. For instance, composites can be fabricated with one component replaced by a non-semiconducting material with a similar morphology. As well as improvements in photocatalytic rates, reduced charge carrier recombination can also be confirmed by reduced PL intensities.[6]

4.2.2. Literature Precedents

As detailed in **Chapter 1**, forming composites is a common strategy used to enhance the performance of inorganic systems. For example, a heterostructure of cobalt phosphide and black phosphorus recently achieved a record STH efficiency for photocatalytic hydrogen production from water of 5.4%.[7]

Meanwhile, the formation of organic-inorganic heterostructures can combine the advantageous properties of polymers and inorganic materials. A number of organic-inorganic composites have been prepared, mostly using C_3N_4.[8–11] For example, a nanocomposite of C_3N_4 and tungsten oxide was prepared for hydrogen evolution with good interfacial contact ensured by embedding WO_3 nanocuboids into the C_3N_4 matrix.[10] The present chapter will focus on forming heterostructures of **FS-TEG** with TiO_2 in an effort to improve photocatalytic performance.

4.3. Polymer-TiO_2 Heterostructures

4.3.1. Background

TiO_2 is regarded as the benchmark semiconductor in the field of photocatalysis [12] and is used in a number of the composites discussed in **Chapter 4.1.2**. The poor performance of TiO_2 under visible light can be enhanced by forming a composite with a narrower band-gap semiconductor with greater visible light absorption. Moreover, a recent study investigating the poor oxygen-evolving ability of TiO_2 suggested this can be mainly attributed to the low concentration of holes on the surface.[13] Polymers are typically better suited to hole transport and so could act to bring holes to the surface and facilitate overall water splitting.

The choice of polymer to be used in composite materials is important. Solubility is desirable as it can enable facile preparation of composite materials. However, large solubilising alkyl side chains are expected to prevent intimate contact and charge transfer between polymers and TiO_2, resulting in poor photocatalytic performance. Yang *et al.* attempted to avoid this problem by post-processing cleavage of solubilising *t*-butoxycarbonyl groups.[14] This step could, however, be averted by using solubilising groups that can also interact well with TiO_2. Poly(ethylene glycol) is known to bind strongly to TiO_2[15] so polymers with hydrophilic oligo(ethylene glycol) OEG side chains may therefore interact sufficiently with TiO_2 to form stable composites with good interfacial contact.

The expected band alignment of an **FS-TEG / TiO_2** composite is shown in **Figure 4.2**. According to this approximation, a Type II heterojunction will be formed, with **FS-TEG** effectively acting as a photosensitiser to improve the activity of TiO_2 under visible light. Hydrogen evolution experiments will be performed using methanol as a sacrificial electron donor, as has previously been used for polymer-TiO_2 composites.[16] Moreover, the band positions of the two components appear to be suitable for OWS so this will also be attempted.

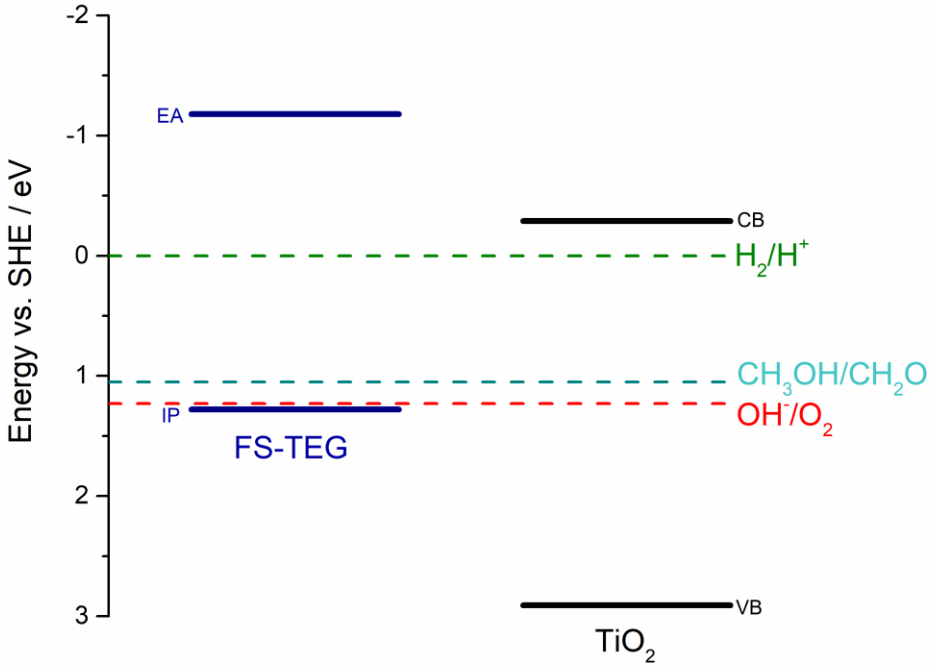

Figure 4.2. Approximate band alignment of **FS-TEG** and TiO_2. Positions of **FS-TEG** IP and EA were estimated from PESA and UV-vis absorption onset measurements performed in **Chapter 2**. Values for the band positions of TiO_2[17] and oxidation potential of methanol[18] were obtained from literature.

4.3.2. Preparation and Characterisation

FS-TEG was loaded onto P25 TiO_2 nanoparticles; a mixture of anatase and rutile that is commercially available and has high photocatalytic performance.[17] A recent investigation found an optimum polymer loading of 2.5 wt. % C_3N_4 on P25.[19] Composites of TiO_2 with 2 and 5 wt. % **FS-TEG** loading were prepared using a simple method. A solution of **FS-TEG** dissolved in chloroform was added to a dispersion of TiO_2 in chloroform before evaporation of the solvent to give **FS-TEG / TiO_2** composites. SEM images showed TiO_2 and the **FS-TEG / TiO_2 2 wt. %** composite to have similar morphologies (**Figure 4.3**) with the composite seemingly forming larger aggregates.

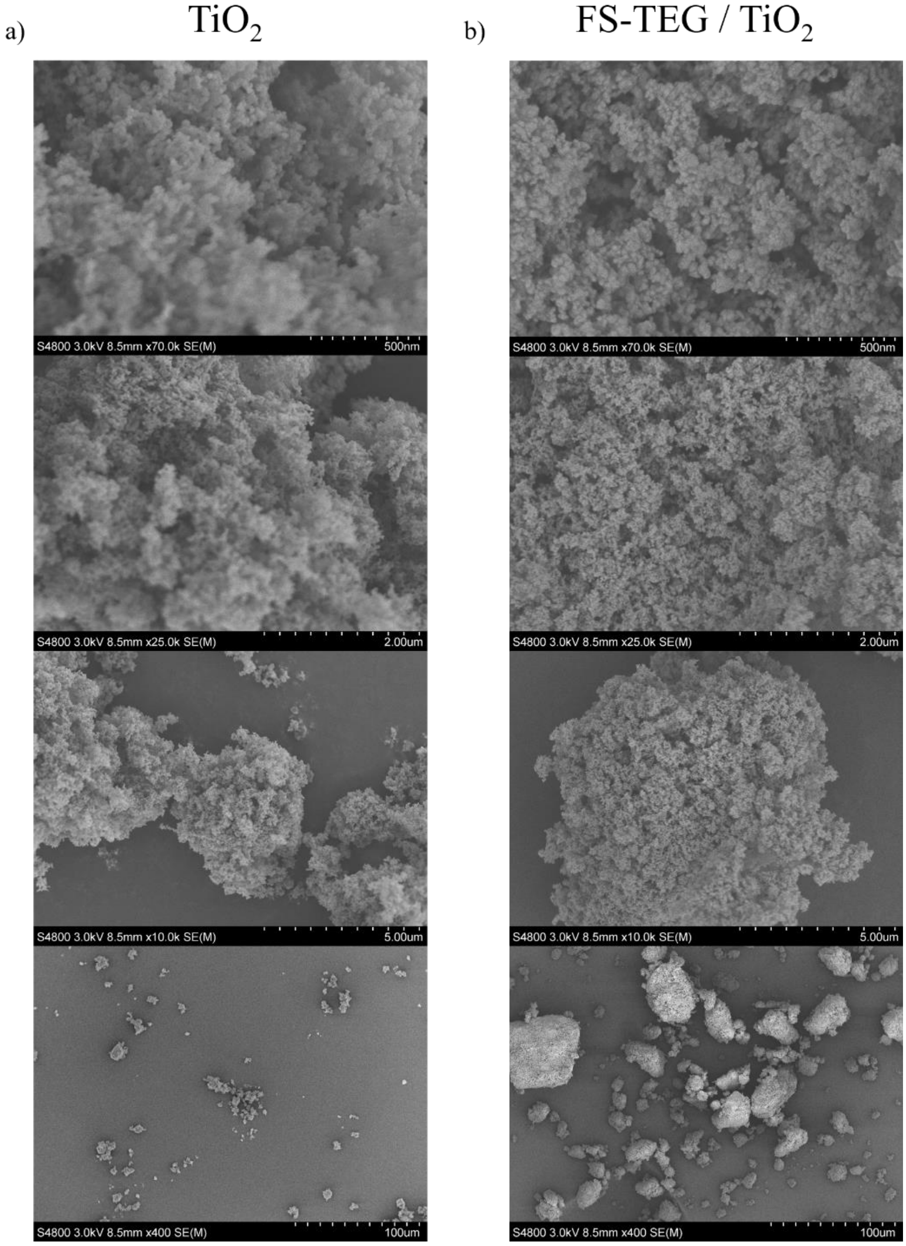

Figure 4.3. SEM images of **a) TiO_2** and **b) FS-TEG / RGO / TiO_2** at different magnifications.

FS-TEG appeared to be uniformly distributed on the surface of the TiO_2 particles (**Figure 4.4a**) with a deeper yellow colour observed in the composite with higher **FS-TEG** loading. FT-IR spectra display the stretching frequencies characteristic of TiO_2 (**Figure 4.4b**).[20] Weaker **FS-TEG** signals are visible in the spectra of composites, especially in the fingerprint region. These signals are more prominent at higher loadings as anticipated. UV-vis absorption spectra clearly show the broadened absorption spectra of the composites (**Figure 4.4c**), with the addition of **FS-TEG** extending the absorption of composites into the visible region.

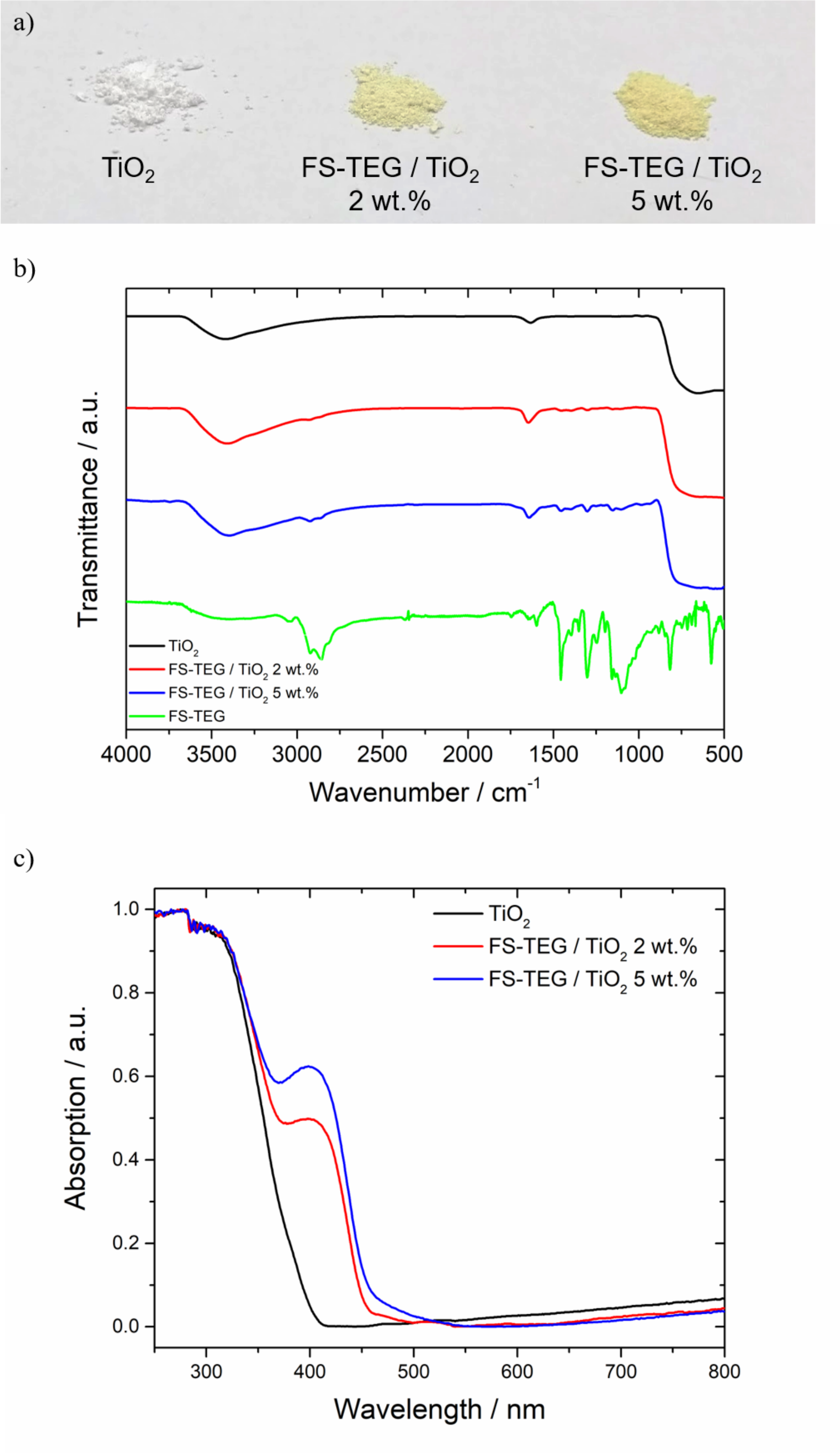

Figure 4.4. a) Images of **TiO_2**, **FS-TEG / TiO_2 2 wt. %** and **FS-TEG / TiO_2 5 wt. %** in air. **b)** FT-IR spectra of **TiO_2**, **FS-TEG / TiO_2 2 wt. %**, **FS-TEG / TiO_2 5 wt. %** and **FS-TEG** polymer**. c)** UV-vis absorption spectra of **TiO_2**, **FS-TEG / TiO_2 2 wt. %** and **FS-TEG / TiO_2 5 wt. %.**

The TGA trace of TiO_2 shows it possesses excellent stability to temperatures in excess of 600 °C (**Figure 4.5a**). In the composites, thermal degradation of **FS-TEG** is observed, with weight loss corresponding to 2.7 and 4.1 wt. % of the composite at 600 °C, similar to the expected 2 and 5 wt. % polymer loadings. The amorphous nature of **FS-TEG** means it is not observable in the PXRD patterns of composites (**Figure 4.5b**), which are instead dominated by the highly crystalline TiO_2.

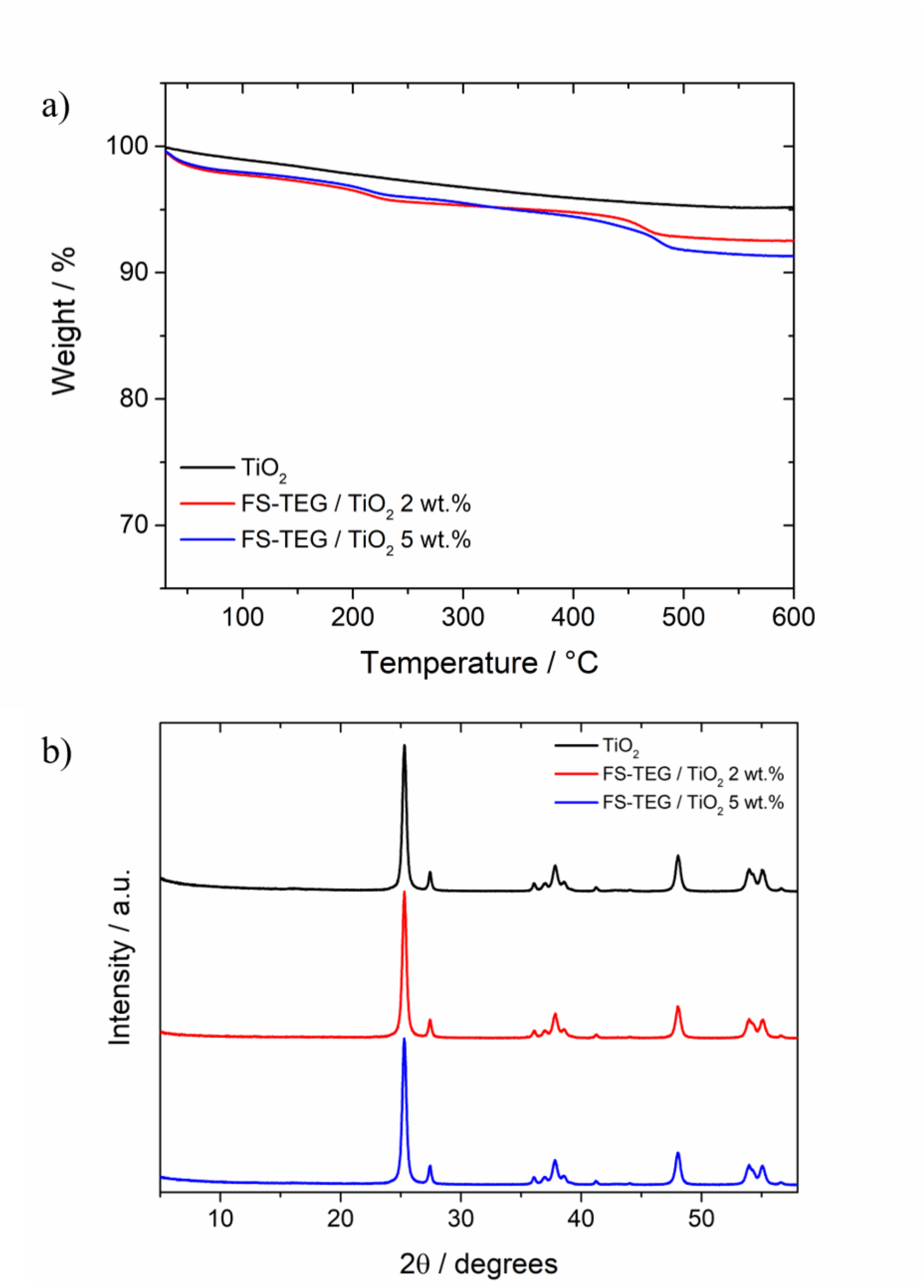

Figure 4.5. a) TGA traces of **TiO_2**, **FS-TEG / TiO_2 2 wt. %** and **FS-TEG / TiO_2 5 wt. %** in air. **b)** PXRD patterns of **TiO_2**, **FS-TEG / TiO_2 2 wt. %** and **FS-TEG / TiO_2 5 wt. %.**

PL spectra were measured by exciting at different wavelengths to probe charge transfer in the composite materials. The PL spectra of the individual components were first measured (**Figure 4.6a** and **b**). TiO_2 displays sharper emission peaks than **FS-TEG**, which has a consistently broad emission profile over the range of excitation wavelengths studied here. **FS-TEG** displays emission over a wider range of excitation wavelengths than TiO_2 in accordance with the UV-vis absorption spectra. TiO_2 is so poorly emissive when excited at wavelengths above 380 nm that the PL spectrum is buried in the baseline and is therefore not presented in **Figure 4.6a**. The PL spectra of the 2 wt. % and 5 wt. % composites are shown in **Figure 4.6c** and **4.6d** respectively. A variation in the emission spectra of composites is apparent upon changing the excitation wavelength. Excitation at shorter wavelengths results in emission predominantly from TiO_2 whereas emission from the polymer dominates at longer excitation wavelengths. This dependence on excitation wavelength is particularly prevalent in the spectrum of the 5 wt. % composite.

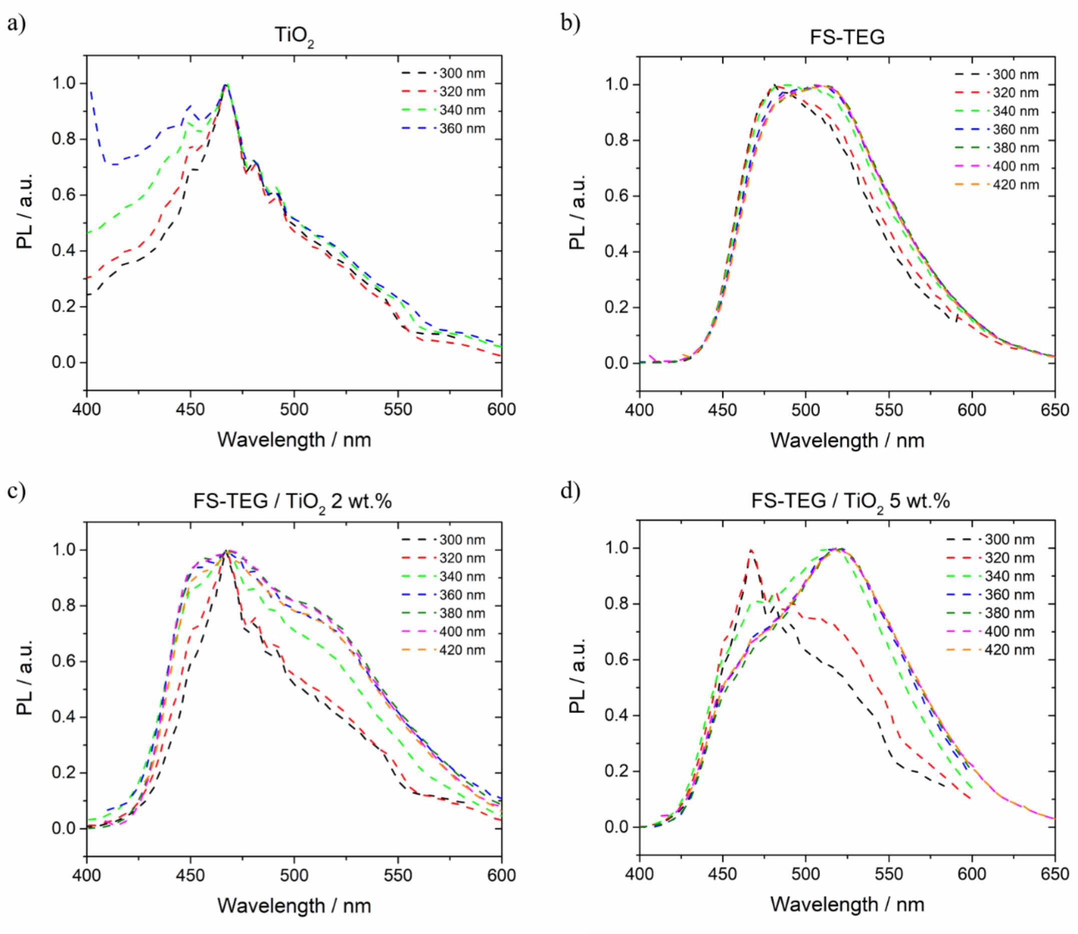

Figure 4.6. PL spectra of **a) TiO_2**, **b) FS-TEG c) FS-TEG / TiO_2 2 wt. %** and **d) FS-TEG / TiO_2 5 wt. %** with the excitation wavelengths varied as shown.

These PL spectra can be used to indicate charge transfer in a composite material. This was done by comparing unnormalised spectra obtained using an excitation wavelength which does not lead to emission from TiO_2 on its own (λ_{exc} = 420 nm, **Figure 4.7**). The spectrum of the 2 wt. % composite appears to show strong emission at the wavelength previously observed in the TiO_2 spectrum (λ_{em} = 467 nm) whereas the PL spectrum of the polymer is dominated by higher wavelength emissions (λ_{em} > 475 nm). Moreover, the reduction in PL intensity of the composite suggests electron transfer from the polymer to TiO_2.[10] The intensity of emission from the 5 wt. % composite is higher than the 2 wt.% composite as a result of the higher polymer loading, although still notably less than the polymer on its own.

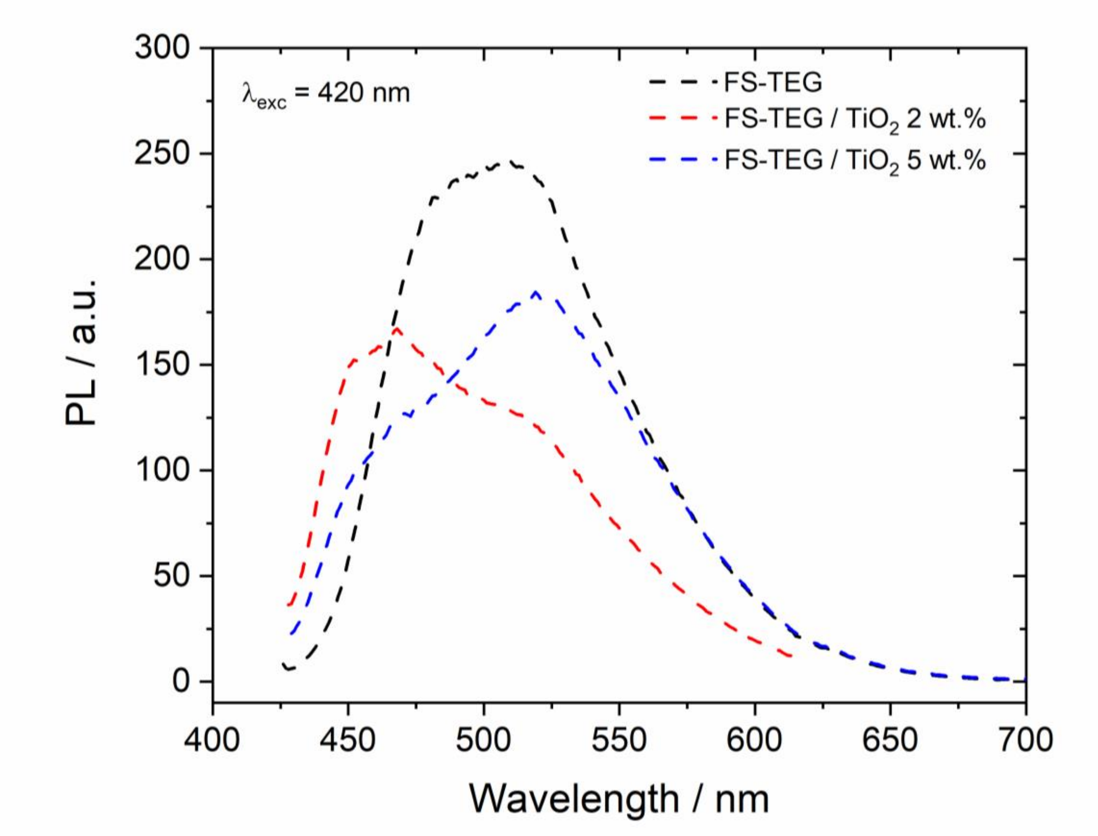

Figure 4.7. Unnormalised PL spectra of **FS-TEG**, **FS-TEG / TiO_2 2 wt. %** and **FS-TEG / TiO_2 5 wt. %** with λ_{exc} = 420 nm.

4.3.3. Photocatalysis Experiments

Hydrogen evolution experiments were performed using methanol as a sacrificial electron donor. Although oxidation of methanol to methanaldehyde produces hydrogen, this has been found not to significantly contribute to the overall rate of hydrogen evolution (< 8% over the course of 10 hours).[21] The photocatalytic performance of composites was compared to equivalent amounts of polymer in the composites (0.50 and 1.25 mg) and TiO_2 (25 mg).

The hydrogen evolution performance of the composites appear to be notably higher than the individual TiO_2 and **FS-TEG** (**Figure 4.8a**, **Table 4.1**). The 2 wt. % and 5 wt. % composites have very similar HERs (10.1 ± 0.2 and 10 ± 1 µmol h^{-1}). This suggests that HER does not increase with polymer loading above 2 wt. % and is therefore possibly further indication of the synergistic behaviour of the composite. The **FS-TEG / TiO_2 2 wt. %** composite was found to be photocatalytically stable over 60 hours (**Figure 4.8b**). Significantly more hydrogen was evolved than is present in the polymer (535 *vs.* 15.6 µmol), suggesting that hydrogen evolution is not due to degradation of the polymer by TiO_2.

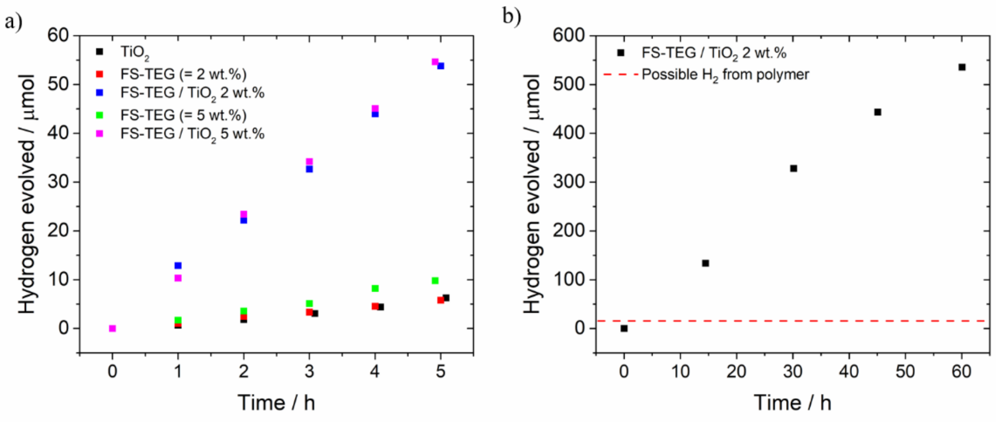

Figure 4.8. **a)** Hydrogen evolution of **TiO_2** (25 mg), **FS-TEG / TiO_2 2 wt. %** (25 mg), **FS-TEG / TiO_2 5 wt. %** (25 mg) and equivalent amounts of **FS-TEG** to the amounts present in the two composites (0.50 and 1.25 mg respectively) in 20 vol. % methanol (22.5 mL) under broadband irradiation by a 300 W Xe light source. **b)** Hydrogen evolution of **FS-TEG / TiO_2 2 wt. %** (25 mg) in 20 vol. % methanol (22.5 mL). The red dash indicates the amount of dihydrogen molecules that could be formed from the hydrogen atoms present in the polymer.

Table 4.1. Hydrogen evolution of various materials, composites and mixture in 20 vol. % methanol under broadband irradiation with a 300 W Xe light source.

Material	FS-TEG loading / wt. %	HER / µmol h^{-1}
FS-TEG	n/a	1.0 ± 0.1
TiO_2	n/a	1.2 ± 0.1
FS-TEG / TiO_2 2 wt. %	2	10.1 ± 0.2
FS-TEG / TiO_2 5 wt. %	5	10 ± 1

The composite was expected to perform markedly better than TiO_2 under visible light irradiation. However, no hydrogen was evolved by the composite under visible light ($\lambda > 420$ nm) irradiation over 20 hours. The performance was therefore investigated using a $\lambda > 395$ nm band-pass filter to increase activity. **FS-TEG / TiO_2 2 wt. %** does evolve hydrogen at a greater rate than TiO_2 (1.88 ± 0.04 *vs.*1.47 ± 0.08 µmol h^{-1}, **Figure 4.9**). However, the increase in performance of the composite is not as great as under broadband ($\lambda > 295$ nm) irradiation. This is surprising given the red-shifted absorption on-set of the composite.

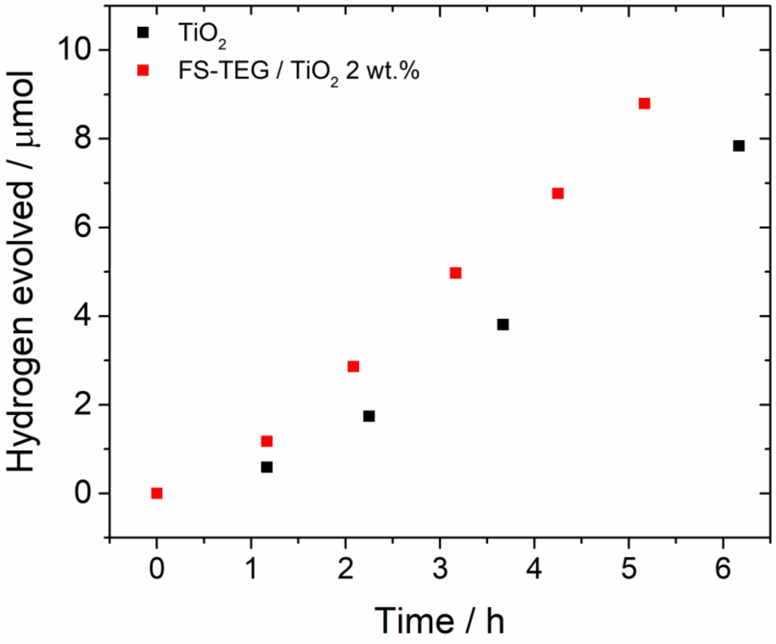

Figure 4.9. Hydrogen evolution of **TiO_2** (25 mg) and **FS-TEG / TiO_2 2 wt. %** (25 mg) in 20 vol. % methanol (22.5 mL) under irradiation by a 300 W Xe light source with a $\lambda > 395$ nm band-pass filter.

The photocatalytic experiments under broadband irradiation seem to suggest photocatalytic performance can be increased by forming polymer-TiO_2 composites. However, comparisons of this kind should be made with caution as other properties are altered in these heterostrructures. The thin layer of polymer coating in particular differs significantly in morphology to the bulk material obtained after synthesis. Furthermore, factors such as the non-linearity of light absorption can artificially enhance the photocatalytic performance of composites.[22] Control experiments were therefore also performed by coating the polymer on non-semiconducting silica. Reduced photocatalytic performance of the **FS-TEG / SiO_2** composite relative to the **FS-TEG / TiO_2** composite would further support heterojunction formation as a useful means of enhancing activity.

4.3.4. Control Experiments: Polymer-SiO_2 Heterostructures

An **FS-TEG / SiO_2 2 wt. %** composite was prepared and compared to the TiO_2 composite. The silica composite was prepared using an analogous procedure with SiO_2 of a similar particle size to P25 TiO_2 (25 nm *vs.* 21 nm). Interestingly, the HER of the control composite (0.088 ± 0.008 μmol g^{-1} h^{-1}) was much lower than the equivalent mass of as-synthesised polymer (1.15 ± 0.03 μmol g^{-1} h^{-1}) and notably inferior to the TiO_2 composite (10.1 ± 0.2 μmol h^{-1}).

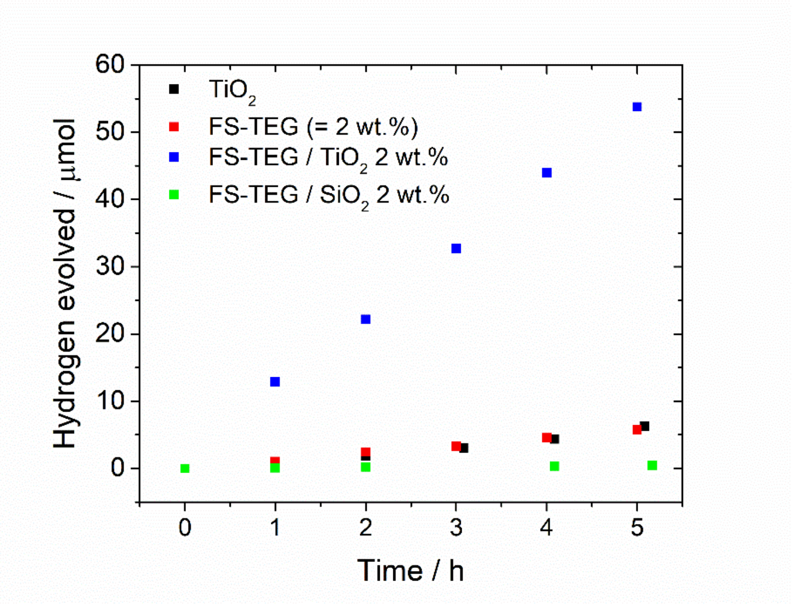

Figure 4.10. Hydrogen evolution of TiO_2 (25 mg), **FS-TEG** (0.50 mg), **FS-TEG / TiO_2 2 wt. %** (25 mg) and **FS-TEG / SiO_2 2 wt. %** in 20 vol. % methanol (22.5 mL) under broadband irradiation by a 300 W Xe light source.

4.3.5. Overall Water Splitting Attempts

The band positions of **FS-TEG** and TiO_2 were shown to be suitable for overall water splitting if a 'direct' Z-scheme can be formed between the two materials. In a direct Z-scheme, water oxidation and proton reduction takes place on different semiconductors, with electron transfer taking place without the use of an electron mediator.[23] The composites and their components were tested for overall water splitting using a high throughput method. Samples (5 mg) were placed in water and irradiated with a solar simulator. The amounts of hydrogen evolved from each sample after 18 hours of irradiation are shown in **Figure 4.11**.

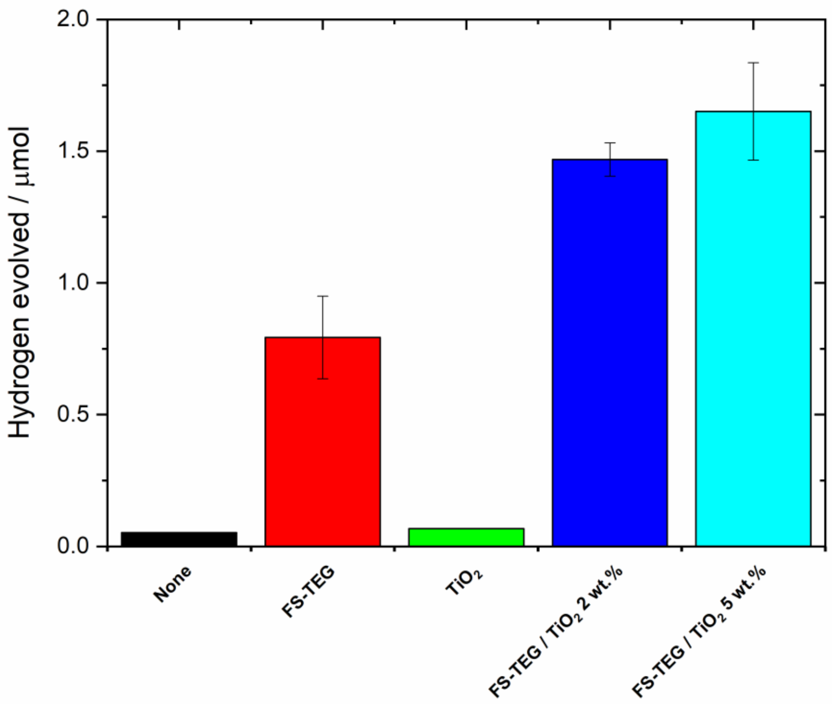

Figure 4.11. Amount of hydrogen evolved by the specified materials (5 mg) in water under irradiation by a solar simulator (AM1.5G, 1 Sun) after 18 hours. Errors given are the standard deviation associated with repeat samples.

Whilst higher than the polymer and TiO_2 individually (0.8 ± 0.2 and 0.067 ± 0.001 µmol), the amounts of hydrogen produced by the composites in water are low (1.47 and 1.65 µmol respectively). Furthermore, whereas OWS should result in the stoichiometric evolution of hydrogen and oxygen, oxygen levels in all samples were found to be below the baseline detected in 'blank' water samples containing no photocatalyst. Oxygen evolution is notoriously difficult to measure accurately due to the presence of atmospheric oxygen. However, if OWS was taking place, some increase in the level of detected oxygen would be expected. These results therefore suggest the composites studied here have no appreciable OWS activity under simulated sunlight.

4.3.6. Summary

The present investigation supports composite formation as a means of enhancing the performance of photocatalysts. The HER of the composite is notably higher than its constituent components, with some evidence of charge transfer taking place between the polymer and TiO_2. Excitation at wavelengths absorbed by the polymer leads to emission from TiO_2 while PL also appears to be quenched.

However, some issues exist with these composites that must be addressed, most notably the lack of OWS activity despite the apparent suitability of the band structure. The composite also displays poor hydrogen evolution activity under visible light. It is possible that the improved activity of the composite under broadband irradiation may be due to residual palladium in the polymer acting as a co-catalyst for hydrogen evolution from TiO_2. This could be investigated by forming composites with the twice-washed polymer from **Chapter 2.4.3** (**FS-TEG-w2**). The reduction in Pd content may also reduce trapping of electrons and encourage charge transfer between the heterostructure components. Charge transfer could also be improved with the use of an electron mediator.[24] These strategies will be employed in **Chapter 4.4** in an effort to improve the performance of these composites.

4.4. Polymer-TiO_2 Heterostructures with Electron Mediators

4.4.1. Background

Conventionally, Z-scheme photocatalysts make use of ionic electron mediators dissolved in the aqueous mixture. However, suitable adsorbing and desorbing properties of ionic electron mediators on photocatalysts are required and backward reactions can inhibit electron transfer.[25] Electron transfer by solid state electron mediators may therefore lead to higher efficiencies than transfer by redox mediators dissolved in solution.[26]

Materials based on graphene—conducting 2-D sheets of sp^2-hybridised carbon atoms—have been identified as suitable materials for use as solid-state electron mediatiors.[27] As well as promoting electron transfer, graphene-like materials can also act as macromolecular photosensitisers.[28] Graphene is prone to defect formation[27] and so the more stable reduced graphene oxide (RGO) has been more commonly employed in recent years.[29-32]

RGO can be used as a support for a single photocatalyst. The rate at which WO_3/RGO photocatalytically degraded an organic pollutant was double that of pure WO_3 under visible light irradiation.[32] Meanwhile, using RGO as an electron mediator in a composite of C_3N_4 and Bi_2WO_6 was found to enhance the rate of degradation of organic pollutants.[30] RGO has also reportedly facilitated OWS in a purely organic composite of CMP nanosheets.[24] These studies give confidence that RGO may further enhance performance of the polymer-TiO_2 heterostructures investigated here.

4.4.2. Preparation and Characterisation

The P90 grade of TiO_2 was used in this case as the higher specific surface area of this grade (91 vs 50 m^2 g^{-1} for P25) has been shown to enhance photocatalytic performance.[33] Graphene oxide (GO) was reduced to RGO by *in situ* photoreduction on TiO_2. TiO_2 (0.5 g) and GO (0.025 g) were placed in a 50 vol. % mixture of methanol and water and irradiated under broadband irradiation until a steady rate of hydrogen evolution was observed, signifying the formation of **RGO / TiO_2**

The FT-IR spectrum of **RGO / TiO_2** displays similar features to TiO_2 but with additional peaks at around $\upsilon = 1600$ cm^{-1} and $\upsilon = 1050$ cm^{-1}, corresponding to the C=C and C-O stretching frequencies of RGO (**Figure 4.12a**).[34] The absence of a sizeable peak at 1700 cm^{-1}, denoting the presence of carbonyl functionalities confirms that reduction of GO to RGO has taken place. The addition of RGO did not notably alter the crystallinity or absorption profile of TiO_2 (**Figure 4.12b** and **c**).

Composites of **RGO / TiO_2** with 2 wt. % loading of **FS-TEG** and the twice-washed **FS-TEG** with reduced palladium content from **Chapter 2.4.3** (**FS-TEG-w2**) were prepared using the method outlined in **Chapter 2.3.2**, with the addition of polymer again observed by FT-IR and UV-vis absorption spectra (**Figure 4.12a** and **b**). SEM images show the morphology of **RGO / TiO_2** and **FS-TEG / RGO / TiO_2** (**Figure 4.13**). The composite again seems to form larger aggregates than **RGO / TiO_2** which suggests some inhomogeneity in the composite formed using this method of fabrication.

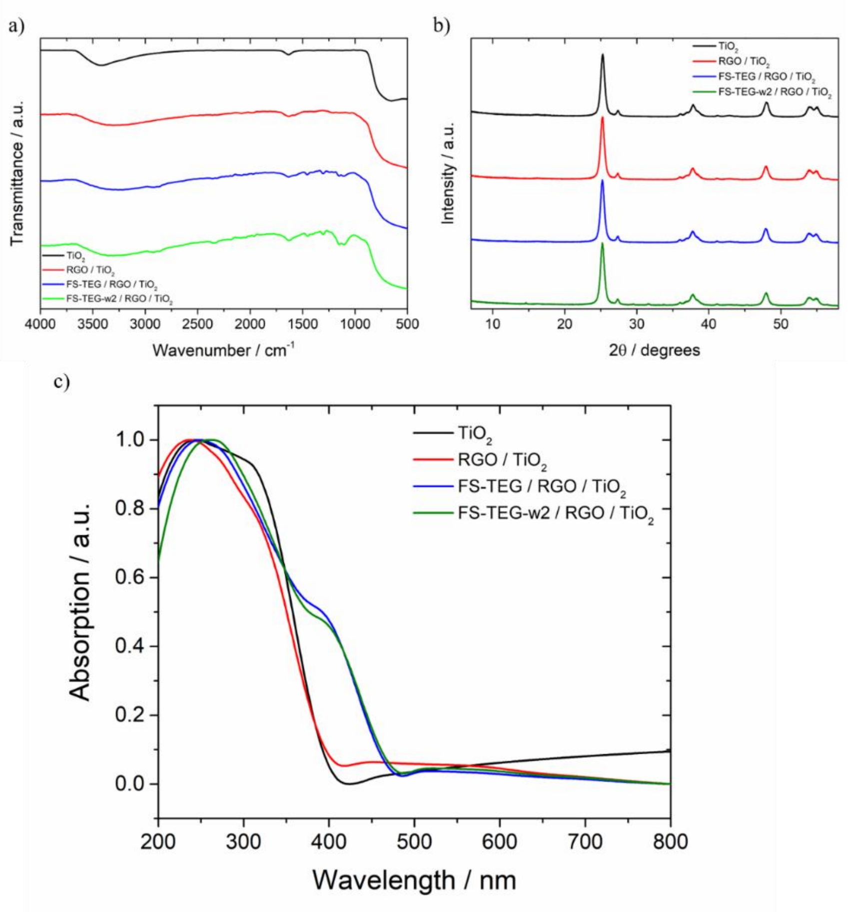

Figure 4.12. a) FT-IR spectrum, **b)** PXRD patterns and **c)** UV-vis absorption spectra of **TiO_2**, **RGO / TiO_2**, **FS-TEG / RGO / TiO_2** and **FS-TEG-w2 / RGO / TiO_2**.

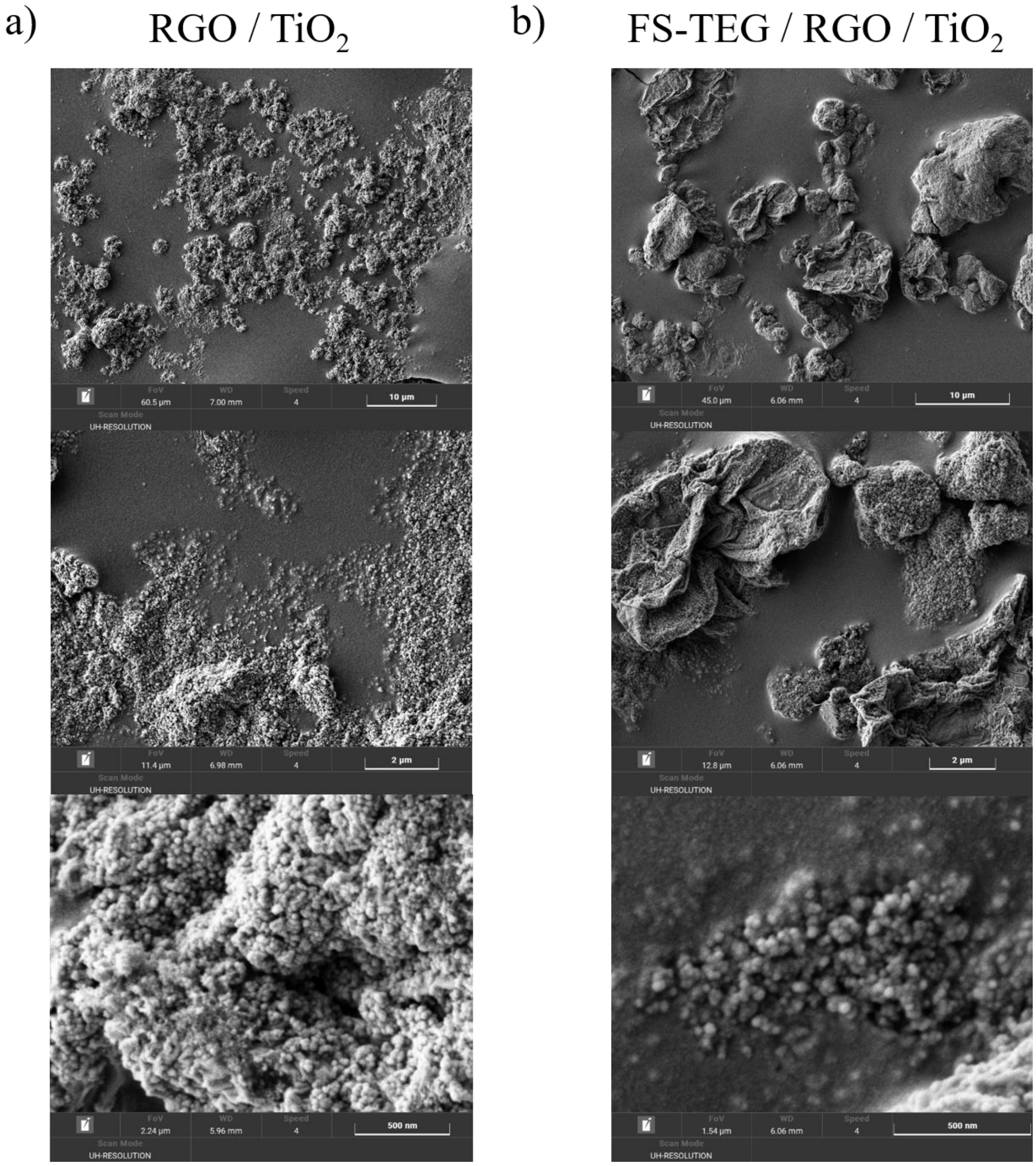

Figure 4.13. SEM images of **a) RGO / TiO_2** and **b) FS-TEG / RGO / TiO_2** at different magnifications.

4.4.3. Photocatalysis Experiments

Hydrogen evolution experiments were conducted in 20 vol. % solutions of methanol in water (**Figure 4.14**, **Table 4.2**). Coating TiO_2 with RGO was found to enhance its photocatalytic activity considerably from 1.2 ± 0.1 to 7.2 ± 0.6 µmol h^{-1}. A further improvement was observed by forming a composite with **FS-TEG** (**FS-TEG / RGO / TiO_2** = 14.1 ± 0.1 µmol h^{-1}). The addition of RGO at the polymer-TiO_2 interface enabled higher activity than the composite in **Chapter 4.3** (**FS-TEG / TiO_2** = 10.1 ± 0.2 µmol h^{-1}) although it should be noted that a different grade of TiO_2 was used in this case.

The palladium content of the polymer appears to affect the photocatalytic performance of these composites; the HER of the composite containing the washed polymer (**FS-TEG-w2 / RGO / TiO_2** = 10.5 ± 0.1 µmol h^{-1}) was not only lower than the **FS-TEG / RGO / TiO_2** composite but also lower than a mixture of as-synthesised polymer and **RGO / TiO_2** (**FS-TEG + RGO / TiO_2** = 11.3 ± 0.5 µmol h^{-1}), suggesting that residual palladium plays an important role in the hydrogen evolution activity of these composites. However, while this composite is clearly not optimised for hydrogen evolution, the anticipated improved charge transfer in **FS-TEG-w2 / RGO / TiO_2** may facilitate overall water splitting.

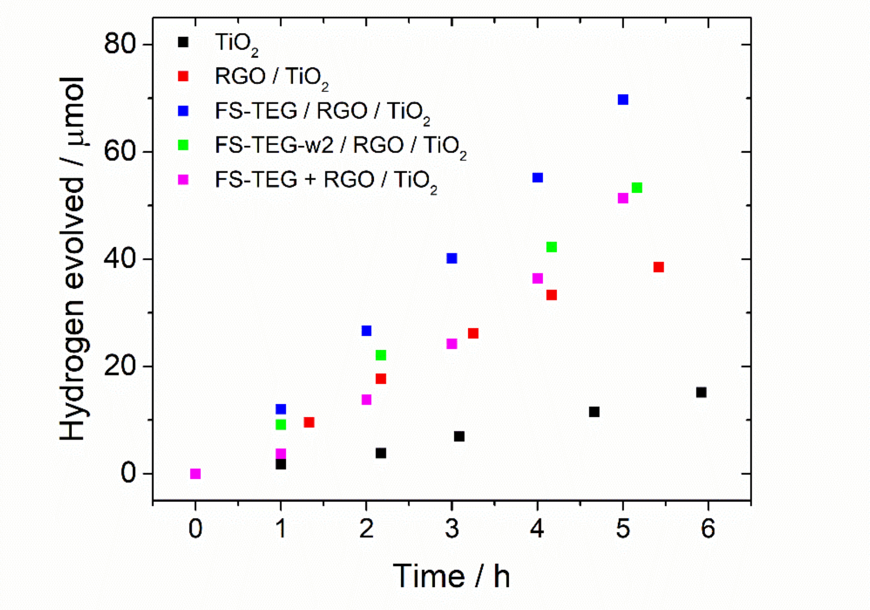

Figure 4.14. Hydrogen evolution of **TiO_2**, **RGO / TiO_2**, **FS-TEG / RGO / TiO_2**, **FS-TEG-w2 / RGO / TiO_2** and the mixture **FS-TEG + RGO / TiO_2** under broadband irradiation with a 300 W Xe light source.

Table 4.2. Hydrogen evolution of various materials, composites and mixtures (25 mg unless stated) in 20 vol. % methanol under broadband irradiation with a 300 W Xe light source.

Material	HER / µmol h^{-1}
FS-TEG[i]	1.0 ± 0.1
TiO_2	1.2 ± 0.1
RGO / TiO_2	7.2 ± 0.6
FS-TEG / RGO / TiO_2	14.1 ± 0.1
FS-TEG-w2 / RGO / TiO_2	10.5 ± 0.1
FS-TEG + RGO / TiO_2	11.3 ± 0.5

[i] Equivalent to the amount of polymer in composite (2 wt. % = 0.5 mg)

4.4.4. Hydrogen Production from Water

FS-TEG-w2 / RGO / TiO_2 was placed in pure water and irradiated with a broadband light source. Hydrogen production from water was observed over 71 hours (**Figure 4.15**). The rate of hydrogen production appears to be linear over this period after an initial induction period (5.1 ± 0.1 µmol g^{-1} h^{-1}. However, the total amount of hydrogen produced in this time was low (2.1 µmol). This is less than the amount of hydrogen that could be produced as a result of degradation the polymer present in the composite (4.9 µmol) and so this cannot be ruled out as the source of hydrogen. Furthermore, concurrent oxygen evolution was not studied.

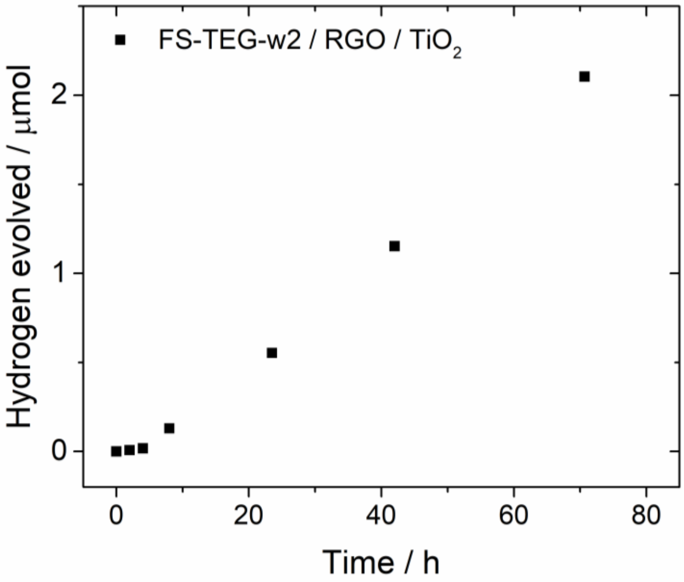

Figure 4.15. Hydrogen evolution of **FS-TEG / RGO / TiO_2** (7.8 mg) in water (8 mL) under broadband irradiation.

4.4.5. Summary

The addition of RGO appears to result in increased hydrogen evolution performance in the materials studied here. **FS-TEG / RGO / TiO_2** outperformed the previously reported composite with no electron mediator. The fact that **RGO / TiO_2** performs notably better than unmodified TiO_2 suggests that perhaps the increased activity of the composite may be due to RGO acting as a photosensitiser rather than enabling more efficient electron transfer. Excited state lifetimes could also be measured to investigate this. Nevertheless, the fact that the performance of **FS-TEG / RGO / TiO_2** was higher than an equivalent mixture of **FS-TEG** and **RGO / TiO_2** again suggests that composite formation is beneficial.

These results also suggest that residual palladium in the polymer appears to contribute to the hydrogen evolution activity of these composites. A reduction in palladium content of the polymer used in the composite notably reduced hydrogen evolution performance. However, as discussed previously, a reduction in these trapping sites may encourage charge transfer and thus enable OWS. The **FS-TEG-w2 / RGO / TiO_2** composite appeared to be capable of hydrogen production from water although amounts produced were low and a more thorough investigation is necessary to confirm the nature of this hydrogen evolution.

4.5. Conclusions

In this chapter, the suitability of solution-processable polymers for the fabrication of composites with inorganic materials was demonstrated. Heterostructures were prepared using a straightforward method. Composite formation was found to enhance photocatalytic performance relative to a control silica composite, suggesting charge transfer between components of the composite. This synergistic behaviour is encouraging for future investigations. Meanwhile, incorporation of RGO as a solid state electron mediator appears to further improve the hydrogen evolution activity of these composites. Future studies should focus on systematically modifying the amounts of these materials in order to optimise performance.

This chapter also illustrates the challenges involved with moving from hydrogen evolution in sacrificial conditions to overall splitting of pure water. **FS-TEG / TiO_2** composites were found to produce less hydrogen from water than TiO_2 in isolation and only small amounts were produced by **FS-TEG-w2 / RGO / TiO_2**. The poor activity of these systems suggest that overall water splitting using organic-inorganic heterostructures is a challenging task that requires careful consideration of a host of factors from band position alignment and interfacial contact to the addition of electron mediators and co-catalysts. Optimisation of these variables is a sizeable challenge and beyond the remit of the current study. However, this preliminary investigation has indicated some of the potential benefits of heterostructure fabrication. Overall water splitting by composites incorporating organic polymers remains a long term goal of this field.

4.6. Experimental

4.6.1. Preparation Methods

FS-TEG / TiO_2 2 wt. %: TiO_2 (P25, Degussa, 1.0005 g) were heated at 120 °C for 5.5 hours. **FS-TEG** (21.7 mg) was dissolved in chloroform (100 mL). The activated TiO_2 was dispersed in chloroform (100 mL) using an ultrasonic bath for 15 minutes, with the polymer solution to ensure complete dissolution. Once fully dispersed, the polymer solution was added slowly to the TiO_2 suspension under stirring. The solvent was evaporated and the resultant composite, **FS-TEG / TiO_2 2 wt. %**, was dried under vacuum and obtained as a light-yellow powder (0.9686 g).

FS-TEG / TiO_2 5 wt. %: The same procedure was repeated using TiO_2 (100.2 mg) and FS-TEG (5.01 mg), initially dispersed and dissolved in 10 mL of chloroform, to yield the composite (82.0 mg).

FS-TEG / SiO_2 2 wt. %: The same procedure was repeated using silica nanobeads (101.2 mg) dispersed in chloroform (10 mL) were added to a solution of FS-TEG (2.0 mg) dissolved in chloroform (10 mL). **FS-TEG / SiO_2 2 wt. %** (66.0 mg).

RGO / TiO_2: RGO was deposited using a photoreduction method**.** TiO_2 (P90, Lawrence Industries, 0.5 g) and graphene oxide (Graphenea, 0.025 g) were dispersed in distilled water (25 mL) and methanol (25 cm^3) using an ultrasonic bath. The mixture was degassed with N_2 for 20 minutes and irradiated with a broadband 300 W Xe light source until a steady rate of hydrogen evolution was observed after 5 hours. **RGO / TiO_2** (442 g) was collected by centrifugation, dried under vacuum and was obtained as a grey powder after centrifugation and drying (442 mg).

FS-TEG / RGO / TiO_2: The same procedure was repeated as described previously. **RGO / TiO_2** (100 mg) dispersed in chloroform (10 mL) was added to a solution of FS-TEG (2.0 mg) dissolved in chloroform (10 mL). The **FS-TEG / RGO / TiO_2** composite was obtained (80.3 mg).

FS-TEG-w2 / RGO / TiO_2: The same procedure was repeated as described previously. **RGO / TiO_2** (100 mg) dispersed in chloroform (10 mL) was added to a solution of FS-TEG (2.0 mg) dissolved in chloroform (10 mL). The **FS-TEG-w2 / RGO / TiO_2** composite was obtained (50.4 mg).

4.6.2. Characterisation Methods

The majority of characterisation methods used in this chapter were outlined in **Chapters 2** and **3**. When not previously used, equipment and methods will be outlined in the relevant sections.

4.6.3. Photocatalysis Experiments

Photocatalysis experiments were performed using the same apparatus as in **Chapter 2**. Photocatalysis experiments were performed in 20 vol. % methanol under broadband irradiation unless stated.

Overall Water Splitting Attempts: A HTS method similar to the method outlined in **Chapter 2** was used. Samples (5 mg) were placed in glass vials before water was dispensed under nitrogen. After capping, samples were sonicated for 5 minutes and irradiated for 18 hours by a solar simulator (AM1.5G, 1 Sun). Amounts of hydrogen evolved are reported as an average of duplicate samples.

4.7. References

1 H. Wang, L. Zhang, Z. Chen, J. Hu, S. Li, Z. Wang, J. Liu and X. Wang, *Chem. Soc. Rev.*, 2014, **43**, 5234.

2 T. Hisatomi, K. Takanabe and K. Domen, *Catal. Letters*, 2015, **145**, 95–108.

3 K. Afroz, M. Moniruddin, N. Bakranov and N. Nuraje, *J. Mater. Chem. A*, 2018, **6**, 21696–21718.

4 S. J. A. Moniz, S. A. Shevlin, D. J. Martin, Z. X. Guo and J. Tang, *Energy Environ. Sci.*, 2015, **8**, 731–759.

5 R. Marschall, *Adv. Funct. Mater.*, 2014, **24**, 2421–2440.

6 J. Chen, C.-L. Dong, D. Zhao, Y.-C. Huang, X. Wang, L. Samad, L. Dang, M. Shearer, S. Shen and L. Guo, *Adv. Mater.*, 2017, **29**, 1606198.

7 B. Tian, B. Tian, B. Smith, M. C. Scott, R. Hua, Q. Lei and Y. Tian, *Nat. Commun.*, 2018, **9**, 1–11.

8 J. Qin, J. Huo, P. Zhang, J. Zeng, T. Wang and H. Zeng, *Nanoscale*, 2016, **8**, 2249–2259.

9 S. Cao, J. Low, J. Yu and M. Jaroniec, *Adv. Mater.*, 2015, **27**, 2150–2176.

10 W. Yu, J. Chen, T. Shang, L. Chen, L. Gu and T. Peng, *Appl. Catal. B Environ.*, 2017, **219**, 693–704.

11 S. Chu, C. Wang, J. Feng, Y. Wang and Z. Zou, *Int. J. Hydrogen Energy*, 2014, **39**, 13519–13526.

12 R. Li, Y. Weng, X. Zhou, X. Wang, Y. Mi, R. Chong, H. Han and C. Li, *Energy Environ. Sci.*, 2015, **8**, 2377–2382.

13 D. Wang, T. Sheng, J. Chen, H. F. Wang and P. Hu, *Nat. Catal.*, 2018, **1**, 291–299.

14 L. Yang, Y. Yu, J. Zhang, F. Chen, X. Meng, Y. Qiu, Y. Dan and L. Jiang, *Appl. Surf. Sci.*, 2018, **434**, 796–805.

15 D. Selli and C. Di Valentin, *J. Phys. Chem. C*, 2016, **120**, 29190–29201.

16 H. Yan and H. Yang, *J. Alloys Compd.*, 2011, **509**, 26–29.

17 Y. Fang, Y. Huang, Z. J. Ni, Z. L. Wang, S. Kang, Y. Wang and X. Li, *Int. J. Electrochem. Sci.*, 2017, **12**, 5951–5963.

18 M. Wang, S. Shen, L. Li, Z. Tang and J. Yang, *J. Mater. Sci.*, 2017, **52**, 5155–5164.

19 J. Chen, X. Tao, L. Tao, H. Li, C. Li, X. Wang, C. Li, R. Li and Q. Yang, *Appl. Catal. B Environ.*, 2019, **241**, 461–470.

20 H. Li, B. Liu, S. Yin, T. Sato and Y. Wang, *Nanoscale Res. Lett.*, 2015, **10**, 415.

21 F. Guzman, S. S. C. Chuang and C. Yang, *Ind. Eng. Chem. Res.*, 2013, **52**, 61–65.

22 L. Kunz, B. T. Diroll, C. Wrasman, A. Riscoe, A. Majumdar and M. Cargnello, *Energy Environ. Sci.*, 2019, **12**, 1657–1667.

23 X. Li, J. Yu, J. Low, Y. Fang, J. Xiao and X. Chen, *J. Mater. Chem. A*, 2015, **3**, 2485–2534.

24 L. Wang, X. Zheng, L. Chen, Y. Xiong and H. Xu, *Angew. Chemie - Int. Ed.*, 2018, **57**, 3454–3458.

25 K. Iwashina, A. Iwase, Y. H. Ng, R. Amal and A. Kudo, *J. Am. Chem. Soc.*, 2015, **137**,

604–607.

26 D. J. Martin, P. J. T. Reardon, S. J. A. Moniz and J. Tang, *J. Am. Chem. Soc.*, 2014, **136**, 12568–12571.

27 P. Zhou, J. Yu and M. Jaroniec, *Adv. Mater.*, 2014, **26**, 4920–4935.

28 P. Kumar, R. Boukherroub and K. Shankar, *J. Mater. Chem. A*, 2018, **6**, 12876–12931.

29 R. Amal, A. Iwase, A. Kudo, Y. H. Ng and Y. Ishiguro, *J. Am. Chem. Soc.*, 2011, **133**, 11054–11057.

30 D. Ma, J. Wu, Y. Xin, Y. Sun, T. Ma and M. Gao, *Chem. Eng. J.*, 2016, **290**, 136–146.

31 J. Wan, M. Wei, Z. Hu, Z. Peng, B. Wang, D. Feng and Y. Shen, *Int. J. Hydrogen Energy*, 2016, **41**, 14692–14703.

32 W. Zhu, F. Sun, R. Goei and Y. Zhou, *Appl. Catal. B Environ.*, 2017, **207**, 93–102.

33 W. R. Siah, H. O. Lintang, M. Shamsuddin and L. Yuliati, *IOP Conf. Ser. Mater. Sci. Eng.*, 2016, **107**, 012005.

34 D. Konios, M. M. Stylianakis, E. Stratakis and E. Kymakis, *J. Colloid Interface Sci.*, 2014, **430**, 108–112.

Chapter 5

Summary & Outlook

In this thesis, solution-processable polymers were investigated as an alternative to conventional insoluble photocatalysts for hydrogen evolution from water. Factors affecting the performance of these materials were studied using an array of characterisation techniques and processing methods enabled by solubility.

Structure-property-activity relationships were investigated in **Chapter 2**. The choice of solubilising side-chain was found to have a significant influence on photocatalytic performance. Encouragingly, it was found that solubility can be achieved whilst simultaneously enhancing hydrogen evolution rates by incorporating oligo(ethylene glycol) (OEG) side chains. The tri(ethylene glycol) (TEG)-substituted **FS-TEG** significantly outperformed both alkyl-substituted and unsubstituted analogues and exhibited an EQE (10.0 ± 0.5% at 420 nm) that ranks amongst the highest achieved by linear polymer photocatalysts to date (**Table 1.1**). The polar environment created by hydrophilic OEG side-chains appears to stabilise the electron polaron state formed by the polymer upon quenching by the sacrificial electron donor. The ability of TEG-substituted polymers to swell in aqueous conditions also appears to be beneficial for photocatalysis.

The tunability of organic polymers means there is ample scope for further optimisation of these materials. An increase in the number of solution-processable photocatalysts is needed to identify more factors that determine the photocatalytic efficiency of this class of polymers. This exploration of chemical space could be achieved by performing a high throughput synthesis of polymers and screening of their properties and photocatalytic performances; an approach that has been shown to rapidly accelerate materials discovery in this field.[1] A number of monomers with solubilising alkyl side-chains, which could be used in an investigation of this kind, are commercially available.[2] Additional polymers with OEG side-chains should also be prepared, although the unavailability of OEG-substituted monomers presents a greater synthetic challenge.

OEG side-chains could also be incorporated into network polymers. The inclusion of side-chains in CMPs may be possible without occluding pores[3] and the resultant porosity and hydrophilicity of these structures should enable excellent contact with the aqueous medium, thus improving photocatalytic performance.

Meanwhile, modification of OEG side-chains may further enhance the activity of solution-processable linear photocatalysts. Branched OEG side-chains are likely to result in even greater interaction with water although they may disrupt packing of polymer chains.[4] Meanwhile, chelation of OEG side-chains to metal ions could result in interesting morphologies; polythiophenes with pendant TEG side-chains have been found to complex with K^+ ions resulting in the formation of superhelical structures.[5] Chelation of metal ions to crown ether side-chains can alternatively planarise the polymer backbone.[6] This ionochromism resulted in a red shift in the absorption on-set of polythiophenes and could therefore be used to enhance the photocatalytic performance of polymer photocatalysts under visible light irradiation.

Different polar side groups besides OEG chains could also be investigated. Ionic side-chains have recently been used to achieve good contact with Pt co-catalysts.[7] Like OEG side-chains, ionic side-chains can enhance the dispersibility of polymers in aqueous mixtures.[2] The hydrophilicity of cationic side-chains in conjugated polyelectrolytes (CPEs) was recently found to improve hydrogen evolution rates.[8] Complete solubility in water would enable maximum contact with the aqueous medium although other crucial properties may be affected. For example, a water-soluble inorganic complex was recently shown to catalyse overall water splitting although only in saturated solutions and not when it was fully dissolved in water.[9] The lack of activity of the dissolved photocatalyst was attributed to its inability to harvest light. In water-soluble conjugated polymers, loss of inter-chain charge transfer may also lead to reduced charge carrier lifetimes. Therefore, good dispersibility, rather than complete solubility, in aqueous mixtures appears to be desirable for polymer photocatalysts.

The universality of the bridgehead atom dependence seen in **Chapter 2.4.2** should be tested over a larger sample set and the reasons behind the observed trends more thoroughly investigated. For example, charge transport properties of these materials could be studied by constructing OFET devices.[10] Nevertheless, the high activity of **SiS-Oct** supports the inclusion of silicon atoms in the backbones of future polymer photocatalysts. Based on the present thesis, a copolymer of TEG-substituted silole with DBTS (**SiS-TEG**, **Figure 5.1**) is expected to have high photocatalytic performance and should be synthesised and studied in future investigations.

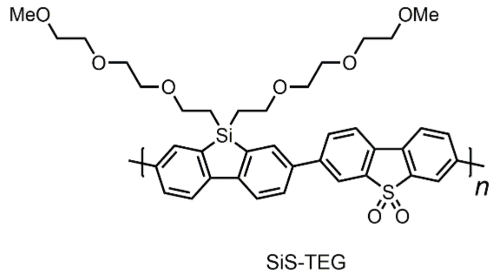

Figure 5.1. Structure of proposed **SiS-TEG** polymer.

Other important parameters were revealed in **Chapter 2**, including the dependence of photocatalytic performance on molecular weight. The photocatalytic activity of **FS-Dodec** seemed to increase with molecular weight up to the effective conjugation length of the polymer. However, this should be validated by further control experiments, for example by equalising the palladium content of the polymers of different molecular weights using the method outlined in **Chapter 2.5.3**. The influence of residual palladium should also be studied more thoroughly in a wider range of polymers to determine if a similar threshold (around 250 ppm) is required to maximise photocatalytic performance in all cases. Other important factors such as pH-dependence and scavenger-dependence should also be considered in more detail in future investigations as these have been shown to significantly affect performance.[11,12]

In **Chapter 3,** a range of morphologies were investigated in an attempt to maximise the photocatalytic performance of **FS-TEG**, with particular focus on casting from solution onto different substrates. Each substrate was found to possess advantages and disadvantages. For instance, deposition on roughened glass slides resulted in high areal performance while spin-coating on OTS-functionalised glass enabled more precise control over film thickness. The activity of films prepared using the latter method was improved to a rate of 9.6 ± 0.2 mmol m^{-2} h^{-1} by stacking them in series to enhance light harvesting.

Processing polymers in organic solvents also enabled the formation of blends and incorporation of dyes. Incorporation of small amounts of the visible-light harvesting **LS-1** dye was found to increase the HER of **FS-TEG** films by more than a factor of three. Meanwhile, creating a bulk heterojunction between polymers was expected to encourage exciton separation and therefore improve photocatalytic activity[15] although the **FP-TEG + FS-TEG** polymer blend in this study did not show a significant performance increase. Future investigations should focus on optimising these blends by varying the amounts of polymers and the polymers themselves and looking for evidence of charge transfer between the components.

A thick free-standing **FS-TEG** film displayed excellent photocatalytic stability over 141 hours. However, the photocatalytic stability of thin polymer films must be improved. Strategies to improve resistance to photobleaching should be investigated, including ensuring removal of residual organic impurities[16] and addition of antioxidants.[17] In this study, $^1O_2$-chelating Ni(dtc)$_2$ appeared to improve the photostability of **FS-TEG** although this should be investigated in greater detail with varied loading of Ni(dtc)$_2$. Meanwhile, while delamination did not appear to take place in the majority of cases in this study, the mechanical stability of films could be ensured by chemically anchoring silanised polymers to glass substrates.[18]

The choice of solvent used to process these materials should also be considered. Chloroform was used as the processing solvent throughout this chapter although the use of more environmentally benign, non-toxic solvents such as anisole is desirable.[13] **FS-TEG** can dissolve in anisole up to a concentration of 0.4 mg mL^{-1}, suggesting non-halogenated solvents could be used for the processing of these polymers. Alternatively, it was shown in **Chapter 3.3** that nanoparticles of **FS-TEG** can be formed by precipitation which could then be processed in aqueous conditions.[14]

Arguably the greatest challenge in this field lies in the construction of heterojunctions for overall water splitting (OWS). In **Chapter 4**, **FS-TEG / TiO$_2$** heterojunctions were prepared and found to evolve hydrogen at a notably higher rate than their individual components. However, none of the composites prepared appeared to be capable of OWS to any appreciable extent, despite the apparently suitable band structures and inclusion of electron-mediating RGO. This investigation underlines the difficulty associated with OWS in comparison to hydrogen evolution in sacrificial conditions, and the different requirements of materials for this application.

Nevertheless, the suitability of solution-processable polymer photocatalysts for incorporation into heterojunctions warrants further investigation. Electron transfer between components should be investigated in more detail, for example by observing differences in excited state lifetimes,[19] while the addition of co-catalysts for hydrogen and oxygen evolution should also be considered. Future heterojunctions could also utilise materials more well-known for their oxygen-evolving abilities such as $BiVO_4$

or WO_3.[20] The procedure used to prepare composites could also be improved to achieve better contact between the polymer and metal oxide as, in the present study, SEM images suggested inhomogeneous coating of **FS-TEG** on TiO_2.

In the long-term, incorporating solution-processed polymer photocatalysts into intricate layered structures, akin to Nocera's 'artificial leaf' concept,[21] is envisaged. Such devices could be prepared by depositing thin layers of metal oxides using techniques such as atomic layer deposition (ALD)[22] onto polymer films. In OPV cells, interfacial layers play a crucial role in the extraction of charges, thereby preventing charge recombination and substantially boosting performance.[23] Charge transporting layers could similarly be used in photocatalytic Z-scheme sheets to achieve electron-hole separation and spatial separation of hydrogen and oxygen evolution. Naturally, the requirements of materials to be used in photocatalytic devices—such as high resistance to degradation in aqueous environments—are arguably even more stringent than in OPV devices. However, it is conceivable that these layered OWS devices could be produced and that, eventually, forming a heterostructure of this kind with an oxygen-evolving polymer could result in OWS using a purely organic system.

In summary, solution-processable polymer photocatalysts appear to be promising materials for photocatalytic applications because of their high activities and controllable morphologies. However, significant challenges lie ahead before photocatalytic hydrogen evolution using these materials becomes a commercially viable alternative to PV-electrolysis as a method of renewable hydrogen production. This will require significant improvements in quantum yields and incorporation into systems capable of overall water splitting. However, the numerous strategies outlined here present opportunities for improving performance. It is hoped that the findings of this thesis will encourage the field of solution-processable photocatalysts to expand in the forthcoming years and, ultimately, enable the production of devices for efficient, scalable and cheap solar hydrogen production.

References

1 Y. Bai, L. Wilbraham, B. J. Slater, M. A. Zwijnenburg, R. S. Sprick and A. I. Cooper, *J. Am. Chem. Soc.*, 2019, **141**, 9063–9071.

2 J. Mei and Z. Bao, *Chem. Mater.*, 2014, **26**, 604–615.

3 A. I. Cooper, *Adv. Mater.*, 2009, **21**, 1291–1295.

4 J. J. Bryant, *Oligo(Ethylene Glycol) Chains: Applications and Advancements in Biosensing*, MSc dissetation, Georgia Institute of Technology, 2010.

5 E. Lee, B. Hammer, J. K. Kim, Z. Page, T. Emrick and R. C. Hayward, *J. Am. Chem. Soc.*, 2011, **133**, 10390–10393.

6 M. Leclerc, A. Boldea and I. Le, *J. Mater. Chem.*, 1999, **9**, 2133–2138.

7 Z. Hu, X. Zhang, Q. Yin, X. Liu, X. fang Jiang, Z. Chen, X. Yang, F. Huang and Y. Cao, *Nano Energy*, 2019, **60**, 775–783.

8 C. Dai, M. Panahandeh-Fard, X. Gong, C. Xue and B. Liu, *Sol. RRL*, 2018, **3**, 1800255.

9 Y. H. Li, Y. Wang, L. R. Zheng, H. J. Zhao, H. G. Yang and C. Li, *Appl. Catal. B Environ.*, 2017, **209**, 247–252.

10 Y. Ito, A. A. Virkar, S. Mannsfeld, H. O. Joon, M. Toney, J. Locklin and Z. Bao, *J. Am. Chem. Soc.*, 2009, **131**, 9396–9404.

11 D. J. Martin, P. J. T. Reardon, S. J. A. Moniz and J. Tang, *J. Am. Chem. Soc.*, 2014, **136**, 12568–12571.

12 Y. Pellegrin and F. Odobel, *Comptes Rendus Chim.*, 2017, **20**, 283–295.

13 M. Yavari, M. Mazloum-Ardakani, S. Gholipour, M. M. Tavakoli, S.-H. Turren-Cruz, N. Taghavinia, M. Grätzel, A. Hagfeldt and M. Saliba, *Adv. Energy Mater.*, 2018, **8**, 1800177.

14 B. Schmatz, Z. Yuan, A. W. Lang, J. L. Hernandez, E. Reichmanis and J. R. Reynolds, *ACS Cent. Sci.*, 2017, **3**, 961–967.

15 K. Takanabe, *ACS Catal.*, 2017, **7**, 8006–8022.

16 B. J. Tremolet De Villers, K. A. O'Hara, D. P. Ostrowski, P. H. Biddle, S. E. Shaheen, M. L. Chabinyc, D. C. Olson and N. Kopidakis, *Chem. Mater.*, 2016, **28**, 876–884.

17 T. L. Andrew and T. M. Swager, *Macromolecules*, 2008, **41**, 8306–8308.

18 Y. Liu and M. C. Messme, *Comparison of Contact Angle Measurements Using Various Probe Liquids on Incomplete OTS SAMS. In: Thin Films: Preparation, Characterization, Applications.* Springer, Boston, MA, 2002.

19 W. Yu, J. Chen, T. Shang, L. Chen, L. Gu and T. Peng, *Appl. Catal. B Environ.*, 2017, **219**, 693–704.

20 X. Chen, S. Shen, L. Guo and S. S. Mao, *Chem. Rev.*, 2010, **110**, 6503–6570.

21 D. G. Nocera, *Acc. Chem. Res.*, 2012, **45**, 767–776.

22 H. C. Guo, E. Ye, Z. Li, M. Y. Han and X. J. Loh, *Mater. Sci. Eng. C*, 2016, **70**, 1182–1191.

23 L. Yao, A. Rahmanudin, N. Guijarro and K. Sivula, *Adv. Energy Mater.*, 2018, **8**, 1802585.

Appendix

Table A-1. Structures and properties of all polymers discussed in **Chapter 2**.

Name	**Structure**	**Solubility in $CHCl_3$**	**M_n[a] / g mol^{-1}**	**M_w[a] / g mol^{-1}**	**Đ[a]**	**Optical gap[b] / eV**	**ε[c] / 10^5 m^2 mol^{-1}**	**Contact angle (H_2O)[d] / °**	**HER[e] / µmol g^{-1} h^{-1}**	**HER[f] / µmol mmol^{-1} h^{-1}**
P4	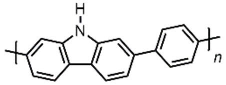	Insoluble	n/a	n/a	n/a	2.72	n/a	n/a	224 ± 8	54 ± 2
P8-s	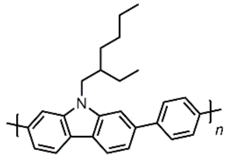	Soluble	1500	2100	1.4	2.71	-	97.4 ± 0.7	72 ± 1	25.5 ± 0.4
P8-i		Insoluble	n/a	n/a	n/a	2.77	n/a	n/a	124 ± 1	43.8 ± 0.3
P9-s	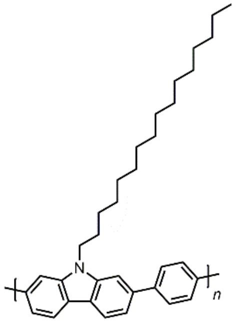	Soluble	3800	5100	1.3	2.49	-	103.1 ± 0.9	20 ± 0.4	9.3 ± 0.2
P9-i		Insoluble	n/a	n/a	n/a	2.94	n/a	n/a	36 ± 2	16.8 ± 0.7
PFO	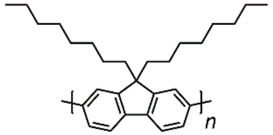	Soluble	44,600	144,000	3.23	3.00	3.04	99 ± 2	0	0
FS-1	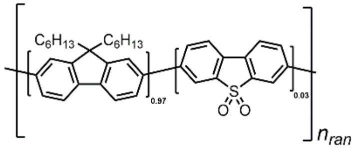	Soluble	14,800	51,700	3.49	3.00	6.79	88 ± 1	5	3

Name	**Structure**	**Solubility in $CHCl_3$**	**M_n[a] / g mol^{-1}**	**M_w[a] / g mol^{-1}**	**Đ[a]**	**Optical gap[b] / eV**	**ε[c] / 10^5 m^2 mol^{-1}**	**Contact angle (H_2O)[d] / °**	**HER[e] / µmol g^{-1} h^{-1}**	**HER[f] / µmol mmol^{-1} h^{-1}**
FS-2	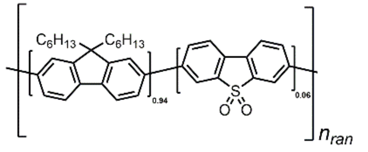	Soluble	16,800	74,500	4.43	2.98	5.28	96 ± 1	18	12
FS-3	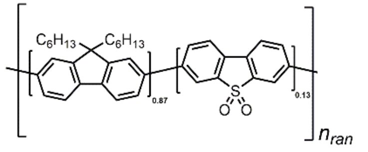	Soluble	18,900	97,800	5.17	2.95	5.73	93 ± 1	15	10
FS-4	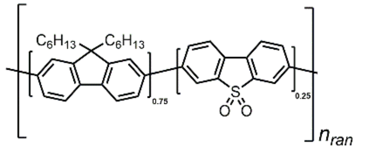	Soluble	11,100	50,900	4.59	2.92	4.27	86 ± 8	238	144
FS-Hex / FS-5	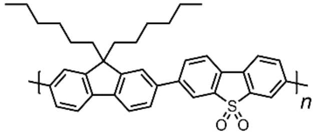	Soluble	3800	8200	2.16	2.80	3.71	88 ± 1	1370 ± 20	750 ± 20
FP-Me	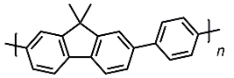	Insoluble	n/a	n/a	n/a	2.86	n/a	94 ± 8	8.3 ± 0.2	2.3 ± 0.1
FP-Hex	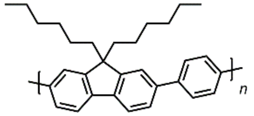	Soluble	18,200	43,200	4.4	2.97	3.34	93 ± 1	0	0
FP-EtHex	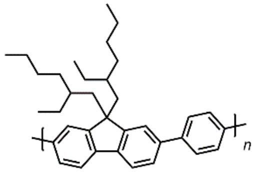	Soluble	14,600	39,000	2.67	3.02	2.47	103.9 ± 0.3	4.3 ± 0.2	2.0 ± 0.1

Name	Structure	Solubility in $CHCl_3$	M_n[a] / g mol^{-1}	M_w[a] / g mol^{-1}	$Đ$[a]	Optical gap[b] / eV	ε[c] / 10^5 m^2 mol^{-1}	Contact angle (H_2O)[d] / °	HER[e] / µmol g^{-1} h^{-1}	HER[f] / µmol mmol^{-1} h^{-1}
FP-Oct	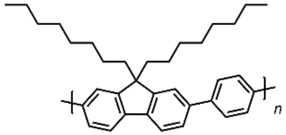	Soluble	16,300	57,900	3.55	2.98	4.16	100 ± 1	5.2 ± 0.3	2.4 ± 0.1
FP-Dodec	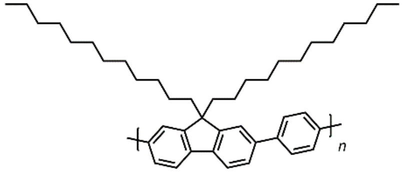	Soluble	6600	12,900	1.95	2.99	3.20	97 ± 2	6 ± 1	4 ± 1
FS-Me	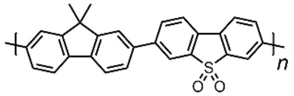	Insoluble	n/a	n/a	n/a	2.59	n/a	77 ± 3	840 ± 20	340 ± 10
FS-EtHex	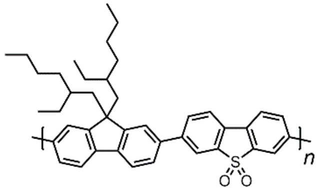	Soluble	19,000	36,900	1.94	2.80	5.34	86 ± 1	535 ± 3	323 ± 2
FS-Oct	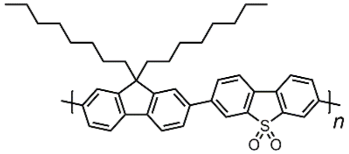	Soluble	18,900	31,900	1.69	2.84	4.98	92 ± 2	680 ± 7	410 ± 20
FS-Dodec	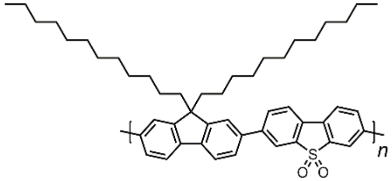	Soluble	14,900	25,400	1.71	2.83	4.74	97 ± 1	577 ± 5	413 ± 4

Name	Structure	Solubility in $CHCl_3$	M_n[a] / g mol^{-1}	M_w[a] / g mol^{-1}	$Đ$[a]	Optical gap[b] / eV	ε[c] / 10^5 m^2 mol^{-1}	Contact angle (H_2O)[d] / °	HER[e] / µmol g^{-1} h^{-1}	HER[f] / µmol mmol^{-1} h^{-1}
FP-TEG	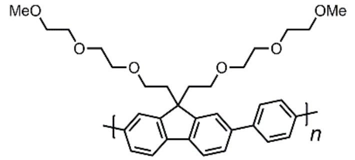	Soluble	8200	12,300	1.51	2.94	3.79	73 ± 1	306 ± 6	163 ± 3
FS-TEG	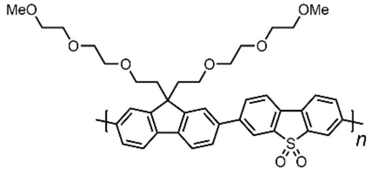	Soluble	8700	11,500	1.35	2.79	5.61	69.6 ± 0.3	2,900 ± 100	1,980 ± 70
FS-DEG	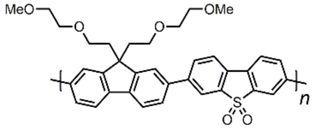	Soluble	4900	7700	1.59	2.79	4.72	73.9 ± 0.7	2100 ± 80	2100 ± 80
FS-TeEG	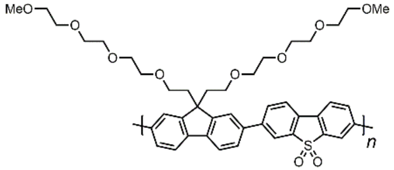	Soluble	15,200	30,400	2.00	2.79	7.86	67.2 ± 0.7	1,220 ± 50	1,220 ± 50
SiS-Oct	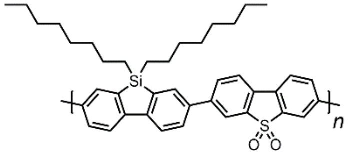	Soluble	5900	14,000	2.36	2.76	4.81	95 ± 1	1520 ± 30	940 ± 20
GeS-Oct	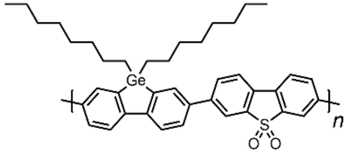	Soluble	7900	16,900	2.14	2.79	4.12	89 ± 1	0.70 ± 0.08	0.46 ± 0.05

Name	**Structure**	**Solubility in $CHCl_3$**	**M_n[a] / g mol^{-1}**	**M_w[a] / g mol^{-1}**	**Đ[a]**	**Optical gap[b] / eV**	**ε[c] / 10^5 m^2 mol^{-1}**	**Contact angle (H_2O)[d] / °**	**HER[e] / µmol g^{-1} h^{-1}**	**HER[f] / µmol $mmol^{-1}$ h^{-1}**
CzS-Oct	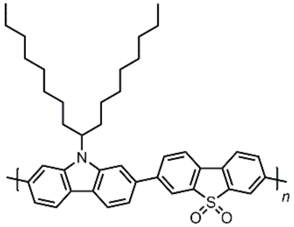	Soluble	4800	7800	1.64	2.90	3.90	89 ± 1	670 ± 30	410 ± 20

[a] Obtained from GPC in chloroform, calibrated to polystyrene standards, 40 °C, flow rate 1.0 mL min^{-1}

[b] Obtained from UV-vis absorption spectra of spin-coated films of soluble materials and powders of insoluble materials

[c] Obtained from UV-vis absorption spectra of solutions of polymer dissolved in chloroform

[d] Obtained from UV-vis absorption spectra of spin-coated films of soluble materials and powders of insoluble materials

[e] HER of polymer (25 mg) in water/methanol/TEA (22.5 mL), irradiated with 300 W Xe light source with a $\lambda > 420$ nm band-pass filter. Rate taken from linear gradient over 5 hours after initial induction period

[f] HER of polymer normalised to molecular weight of the repeating unit